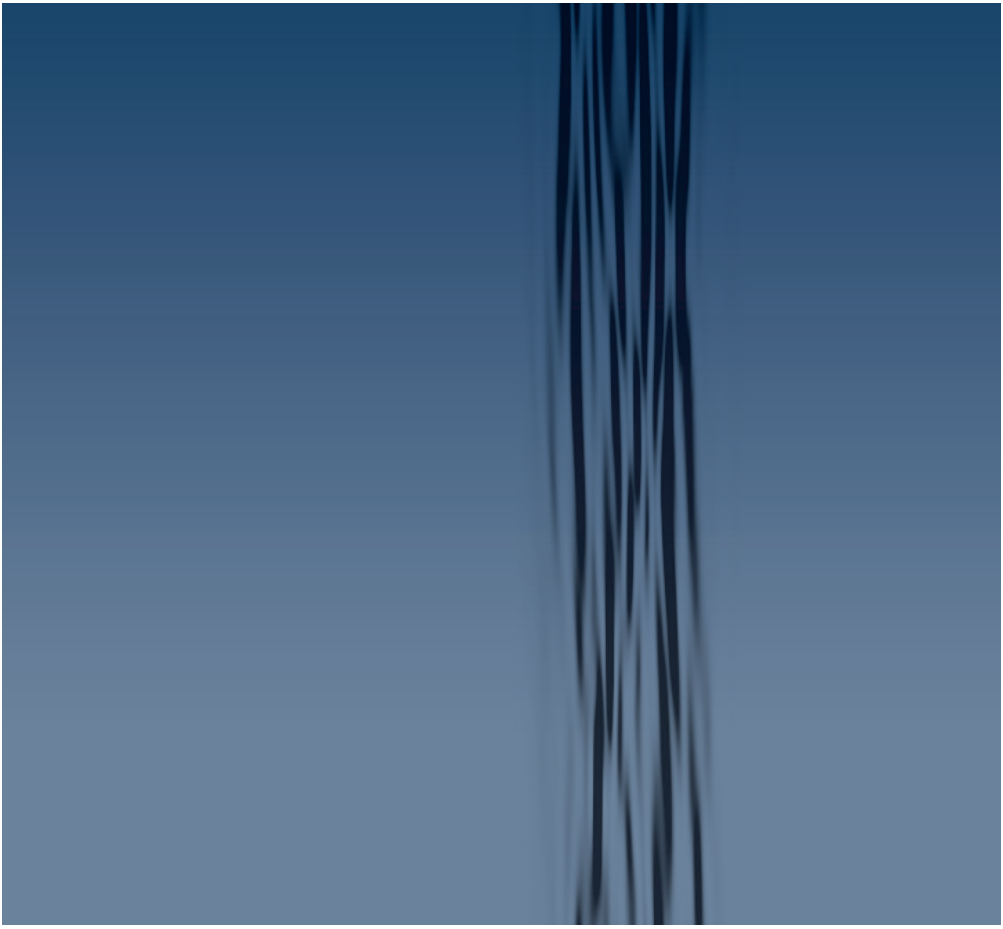

Modeling of the Lateral Emission Characteristics of High-Power Edge-Emitting Semiconductor Lasers

Carlo Holly

Fraunhofer ILT

LLT Chair for Laser Technology | RWTH AACHEN UNIVERSITY

Modeling of the Lateral Emission Characteristics of High-Power Edge-Emitting Semiconductor Lasers

Modellierung der lateralen Abstrahlcharakteristik von Hochleistungsdiodenlaser-Kantenemittern

Von der Fakultät für Maschinenwesen der Rheinisch-Westfälischen Technischen Hochschule Aachen zur Erlangung des akademischen Grades eines Doktors der Naturwissenschaften genehmigte Dissertation

vorgelegt von

Carlo Holly

Berichter: Univ.-Prof. Dr. rer. nat. Reinhart Poprawe
Univ.-Prof. Dr. rer. nat. Günther Tränkle

Tag der mündlichen Prüfung: 15. April 2019

Berichte aus der Lasertechnik

Carlo Holly

Modeling of the Lateral Emission Characteristics of High-Power Edge-Emitting Semiconductor Lasers

Shaker Verlag
Düren 2019

Bibliographic information published by the Deutsche Nationalbibliothek
The Deutsche Nationalbibliothek lists this publication in the Deutsche Nationalbibliografie; detailed bibliographic data are available in the Internet at http://dnb.d-nb.de.

Zugl.: D 82 (Diss. RWTH Aachen University, 2019)

Printed in Germany.

ISBN 978-3-8440-6923-5
ISSN 0945-084X

Shaker Verlag GmbH • Am Langen Graben 15a • 52353 Düren
Phone: 0049/2421/99011-0 • Telefax: 0049/2421/99011-9
Internet: www.shaker.de • e-mail: info@shaker.de

Acknowledgements

The initiative for this work, and for the development of numerical models for the design and analysis of semiconductor lasers was given at the Fraunhofer-Institute for Laser Technology (ILT) and the Chair of Laser Technology (LLT) at the Rheinisch-Westfälische Technische Hochschule (RWTH) Aachen University in the scope of the projects *SpektraLas* (Contract 13N9729) and *FreeLas* (Contract 13N10849), which where both supported by the German Federal Ministry of Education and Research (German: Bundesministerium für Bildung und Forschung, BMBF). In close cooperation between TRUMPF Photonics Inc., the Chair of Laser Technology (LLT-RWTH), and the Fraunhofer ILT the simulation software was further extended with the goal to reproduce and predict lateral emission characteristics for industrial high-power semiconductor lasers. I continued the development and finished this dissertation at TRUMPF Photonics Inc. in Cranbury (New Jersey) in parallel to my role as Semiconductor Laser Design Engineer. I would like to thank my colleagues at TRUMPF Photonics Inc., my former colleagues at the Chair of Laser Technology (LLT-RWTH), and Fraunhofer ILT for the friendly work environment and inspiration for this thesis.

I would like to express my sincere gratitude to Univ.-Prof. Dr. rer. nat. Reinhart Poprawe for the supervision of this thesis, his trust in my research- and teaching-activities, and his positive, inspiring guidance. In addition, I thank Univ.-Prof. Dr. rer. nat. Günther Tränkle for taking over the role as the second reader, and his insightful comments to this work, and to Univ.-Prof. Ph. D. Marek Behr for taking over the role of the chair of the dissertation committee.

My sincere thanks also goes to Dr. rer. nat. Hagen Zimer, Dr. Stewart McDougall, and Dr. rer. nat. Stefan Heinemann for their support, the opportunity to continue the work on this thesis and semiconductor laser modeling at TRUMPF Photonics Inc., and for hours of valuable scientific and technical discussions, which greatly pushed me and this thesis forward.

For the scientific freedom and trust to start the modeling activities and their support in initiation and acquisition of the initial diode laser modeling project, my sincere thanks to Dipl.-Ing. Hans-Dieter Hoffmann and Dipl.-Ing. Dipl.-Wirt.-Ing. Martin Traub. In addition, I thank M. Sc. Martin Adams, M. Sc. Florian Rackerseder, Dipl.-Phys. Thomas Schwarz, and M. Sc. Simon Rauch for their great scientific contributions and many stimulating discussions about simulation of diode lasers.

For their constant support and encouragement I would like to sincerely thank my parents, and my sisters. I express my deep gratitude to my wife - Thank you for moving halfway around the world to support me.

New York, April 2019 Carlo Holly

Abstract

In this work, numerical methods for the simulation of broad-area edge-emitting semiconductor lasers are presented. Frequency-domain and time-domain models are employed to predict the propagation of the filamented optical field in the semiconductor laser and determine emission characteristics including near-field and far-field profiles, beam width, divergence angle, and power over current. The models utilize wave-optical beam propagation and account for the interaction of the optical field with the spatial (and temporal) varying carrier and temperature distributions inside the semiconductor laser cavity. Once calibrated, the frequency-domain model is utilized to predict emission characteristics of single emitters and laser arrays, which differ in geometrical properties (contact width, cavity length or emitter pitch), epitaxial structure or facet reflectivity. By comparison with experimental data for eight laser designs, which include single-emitter and laser arrays it is demonstrated that the frequency-domain model allows computation of lateral far-field angles and near-field widths as a function of current and thermal state for edge-emitting diode lasers.

An opto-mechanical model is derived to compute the degree of polarization for packaged single emitter or laser arrays. The mechanical strains, induced by the soldering process, heating of the device during operation and intrinsic lattice mismatch in the device, are considered. The ratio of the shear strain and the lateral (and vertical) strain component(s) determines the degree of polarization.

In addition to the frequency-domain model, a time-domain model based on the traveling-wave method is implemented and employed to compute the optical propagation in the QW-plane of an edge-emitting diode laser, including carrier- and temperature-induced refractive index changes. The evolution of the optical field along the cavity is computed iteratively for transverse slices. Alongside with the optical propagation, the carrier diffusion equation and an auxiliary equation for the material polarization are solved. The results obtained with the time-domain model obey similar filamented field profiles like the ones obtained with the frequency-domain model.

In summary, the numerical model acts as a *digital-twin* of the real device and with the simulation tools presented in this work the lateral emission characteristics for edge-emitting laser devices can be predicted to the extent needed to make design decisions.

Zusammenfassung

Im Rahmen dieser Arbeit werden numerische Methoden zur Simulation von Breitstreifen-Kantenemitter Halbleiterlasern entwickelt und untersucht. Dazu werden Modelle in der Frequenz-Domäne und in der Zeit-Domäne herangezogen, um die Propagation des filamentierten optischen Feldes im Halbleiterlaser vorherzusagen und Abstrahlcharakteristiken, wie Nah- und Fernfeldprofile, Strahlbreite, Divergenzwinkel und Ausgangsleistung über Betriebsstrom zu bestimmen. Für die Modelle werden wellenoptische Propagationsmethoden eingesetzt und die Kopplung des optischen Feldes mit dem räumlich (und zeitlich) variierenden Ladungsträger- und Temperatur-Verteilungen in der Kavität des Halbleiterlasers berechnet. Nach Kalibration werden, basierend auf dem Model in der Frequenz-Domäne, Abstrahlcharakteristiken von Einzelemittern und von Emittern aus Laserbarren berechnet, die sich in geometrischen Eigenschaften (Injektionskontaktbreite, Kavitätslänge oder Emitterabstand), der epitaktischen Struktur oder der Facettenreflektivität unterscheiden. Durch Vergleich mit experimentellen Daten von acht unterschiedlichen Diodenlasern wird demonstriert, dass das Model in der Frequenz-Domäne die Vorhersage von lateralen Fernfeldwinkeln und Nahfeldbreiten in Abhängigkeit des Betriebsstroms und der Temperatur des Kantenemitters erlaubt.

Um den Polarisationsgrad von Einzelemittern oder Laserbarren zu berechnen, wird ein opto-mechanisches Model entwickelt. Unter denen in Betracht gezogenen mechanischen Einflüssen sind Verspannungen durch den Lötprozess, Aufheizen des Lasers im Betrieb und durch unterschiedliche Gitterkonstanten im Halbleiter. Das Verhältnis von Scherspannung zu lateralen (und vertikalen) Spannungskomponenten bestimmt den Polarisationsgrad des emittierten Feldes.

Zusätzlich zum Model in der Frequenz-Domäne, wird basierend auf der *traveling-wave* Methode ein Zeit-Domänen Model implementiert und angewendet, um die räumliche und zeitliche Entwicklung des optischen Feldes in der Quantengraben-Ebene eines Halbleiterlaser-Kantenemitters zu berechnen. Dabei umfassen die Berechnungen die durch Ladungsträger und Temperatur induzierten Brechungsindexvariationen. Die Evolution des optischen Feldes entlang der Laserkavität erfolgt iterativ für transversale Querschnitte. Die Ergebnisse, die mit dem Model in der Zeit-Domäne berechnet werden, gleichen denen des Frequenz-Domänen Modells im Hinblick auf Filamentierung des optischen Feldes.

Zusammenfassend agiert das numerische Modell als *Digitaler-Zwilling* des realen optoelektronischen Bauteils. Mit den Simulationswerkzeugen, die im Rahmen dieser Arbeit vorgestellt werden, können die lateralen Abstrahlcharakteristiken von Hochleistungsdiodenlaser-Kantenemittern so präzise vorhergesagt werden, dass in Zukunft Entscheidungen für neue Designs aus der Simulation abgeleitet werden können.

Contents

List of Figures

List of Tables

Abbreviations

AlGaAs	**Al**uminum **Ga**llium **As**enid
AR	**A**nti **R**eflective
AlN	**Al**uminum **N**itride
Au	**Au**rum (Gold)
AuSn	**Au**rum **S**tannum (Gold-tin)
BADL	**B**road-**A**rea **D**iode **L**aser
BPM	**B**eam **P**ropagation **M**ethod
BPP	**B**eam **P**arameter **P**roduct
CAD	**C**omputer-**A**ided **D**esign
COMD	**C**atastrophic **O**ptical **M**irror **D**amage
COD	**C**atastrophic **O**ptical **D**amage
CPU	**C**entral **P**rocessing **U**nit
CTE	**C**oefficient of **T**hermal **E**xpansion
CuW	**C**opper-Tungsten
CW	**C**ontinuous **W**ave
DDM	**D**rift-**D**iffusion **M**odel
DOE	**D**esign **O**f **E**xperiment
DOP	**D**egree **O**f **P**olarization
DOS	**D**ensity **O**f **S**tates
DUT	**D**evice **U**nder **T**est
DRT	**D**iscontinuous **R**aviart-**T**homas
DWM	**D**ense **W**avelength **M**ultiplexing
EIM	**E**ffective **I**ndex **M**ethod
EOS	**E**xternal **O**ptical **S**ystem
FA	**F**ast-**A**xis

FD	**F**requency **D**omain
FDM	**F**inite-**D**ifferences **M**ethod
FEM	**F**inite-**E**lement **M**ethod
FDTD	**F**inite-**D**ifferences **T**ime **D**omain
FF	**F**ar-**F**ield
FFT	**F**ast-**F**ourier **T**ransformation
FVM	**F**inite-**V**olume **M**ethod
GaAs	**Ga**llium **As**senid
GB	**G**iga**B**yte
GPU	**G**raphics **P**rocessing **U**nit
GRIN	**GR**aded **IN**dex
GRINSCH	**G**raded **I**ndex **S**eparate **C**onfinement **H**eterostructures
HH	**H**eavy-**H**ole
HPDL	**H**igh-**P**ower **D**iode **L**aser
HR	**H**igh **R**eflective
InGaAs	**In**dium **Ga**llium **As**senid
ICN	**I**terated **C**rank-**N**icolson
LA	**L**aser **A**rray
LH	**L**ight-**H**ole
LOC	**L**arge **O**ptical **C**avity
LSHB	**L**ongitudinal **S**patial **H**ole **B**urning
NF	**N**ear-**F**ield
P.I.	**P**ower **I**nclusion
PMM	**P**rimal **M**ixed **M**ethod
Pt	**Pla**tinum
QW	**Q**uantum **W**ell
SA	**S**low-**A**xis
SAD	**S**low-**A**xis **D**ivergence
SBE	**S**emiconductor **B**loch **E**quation
SCH	**S**eparate **C**onfinement **H**eterostructure
SE	**S**ingle **E**mitter
SiN	**Si**licon **Nitride**
SO	**S**plit-**O**ff

SRH	**S**hockley **R**ead **H**all
SVE	**S**lowly **V**arying **E**nvelope
SVEA	**S**lowly **V**arying **E**nvelope **A**pproximation
TD	**T**ime **D**omain
TDTW	**T**ime-**D**omain **T**raveling **W**ave
TEM	**T**ransverse **E**lectro-**M**agnetic
TE	**T**ransverse **E**lectric
Ti	**Ti**tanium
TM	**T**ransverse **M**agnetic
VBG	**V**olume **B**ragg **G**rating
WA	**W**ide **A**ngle

Physical Constants

Speed of light in vacuum	c_0	=	$2.997\,924\,58 \cdot 10^{8}\,\mathrm{m\,s^{-1}}$
Elementary charge	q_{el}	=	$1.602\,176\,487 \cdot 10^{-19}\,\mathrm{A\,s}$
Electron mass	m_0	=	$9.109\,382\,15 \cdot 10^{-31}\,\mathrm{kg}$
Planck constant	h	=	$6.626\,069\,572\,9 \cdot 10^{-34}\,\mathrm{J\,s}$
Planck constant (reduced)	$\hbar = \frac{h}{2\pi}$	=	$1.054\,571\,726\,47 \cdot 10^{-34}\,\mathrm{J\,s}$
Vacuum permittivity	ε_0	=	$8.854\,187\,817 \cdot 10^{-12}\,\mathrm{CV^{-1}m^{-1}}$
Vacuum permeability	μ_0	=	$4\pi \cdot 10^{-7}\,\mathrm{kgmA^{-2}s^{-2}}$
Boltzmann constant	k_{B}	=	$1.380\,648\,8 \cdot 10^{-23}\,\mathrm{JK^{-1}}$
		=	$8.617 \cdot 10^{-5}\,\mathrm{eVK^{-1}}$
Absolute zero temperature	T_0	=	$273.15\,\mathrm{K}$

Symbols

Symbol	Name	Unit
a_c	Deformation potential for conduction band	eV
a_v	Deformation potential for valence band	eV
a_{lc}	Lattice constant	m
A_{nr}	(Ambipolar) non-radiative recombination rate	s^{-1}
b	Shear deformation potential	eV
$\vec{B}$	Magnetic flux density	T
B_{sp}, C_{sp}	Coefficient of spontaneous emission	$\mathrm{m}^3\,\mathrm{s}^{-1}$
c_{ijkl}	Elastic stiffness constants	Nm^{-2}
C_{11}, C_{12}, C_{44}	Elastic stiffness constants	Nm^{-2}
C_{A}	Coefficient of (ambipolar) Auger recombination	m^6/s
$C_{n/p}$	Coefficient of Auger recombination for electrons / holes	m^6/s
d	Shear deformation potential	eV
d_{qw}	Quantum well thickness	m
D	(Ambipolar) diffusion coefficient	m^2/s
$\vec{D}$, $\vec{J_\phi}$	Electric displacement field	Cm^{-2}
$D_{n/p}$	Diffusion coefficient for electrons / holes	$\mathrm{m}^2\mathrm{s}^{-1}$
$\vec{E}$	Electric field	Vm^{-1}
E	Energy	eV
E	Elastic modulus	Nm^{-2}
E_{c}	Conduction band edge	eV
E_{F}	Fermi energy	eV
E_{g}	Bandgap	eV
E_{hh}	Heavy-holes energy	eV
E_{lh}	Light-holes energy	eV

E_{SO}	Split-off-holes energy	eV
E_{v}	Valence band edge	eV
g	Material gain (amplitude)	m^{-1}
G	Material gain (intensity)	m^{-1}
g_0	Gain coefficient (amplitude)	m^{-1}
$g_{0,T}$	Linear thermal gain change (amplitude)	$\mathrm{m}^{-1}\mathrm{K}^{-1}$
g_{hs}	Heatsink boundary flux	$\mathrm{Wm}^{-2}\mathrm{K}^{-1}$
G_0	Gain coefficient (intensity)	m^{-1}
$G_{0,T}$	Linear thermal gain change (intensity)	$\mathrm{m}^{-1}\mathrm{K}^{-1}$
H	Magnetic field	Am^{-1}
I	Current	A
I	Optical intensity	$\mathrm{W/m}^2$
J	Current density	$\mathrm{A/m}^2$
$\vec{J}_{n/p}$	Current density of electrons / holes	$\mathrm{A/m}^2$
J_{th}	Threshold current density	Am^{-2}
$\vec{k}$	Wavevector	m^{-1}
k	Wavenumber	m^{-1}
k_{ref}	Reference wavenumber	m^{-1}
k_T	Thermal conductivity	$\mathrm{Wm}^{-1}\mathrm{K}^{-1}$
l_z	Cavity length	m
$\lvert L\rvert^2$	Relative intensity in linear polarization	
m_{c}	Mass of conduction band electrons	m_0
m_{v}	Mass of valence band electrons	m_0
$\vec{n}$	Surface normal	
n_{2d}	Density of confined carriers	m^{-3}
n_{3d}	Density of bulk carriers	m^{-3}
n_{bg}	Background refractive index	
n_{i}	Intrinsic carrier density	m^{-3}
n_{ref}	Reference index of refraction	
n_{qw}	(Ambipolar) carrier density in Quantum well	m^{-3}
N_{A}	Acceptor impurity concentration	m^{-3}
N_{c}	Effective density of states in conduction band	m^{-3}
N_{D}	Donator impurity concentration	m^{-3}

N_{th}	Threshold carrier density	m^{-3}
N_{tr}	Transparency carrier density	m^{-3}
$N_{\mathrm{tr},T}$	Linear thermal transp. carrier density change	$\mathrm{m}^{-3}\mathrm{K}^{-1}$
N_{v}	Effective density of states in valence band	m^{-3}
$\vec{p}$	Momentum vector	$\mathrm{N\,m}$
P	Power	W
P	Material polarization	Cm^{-2}
p_{ijkl}	Photo-elastic coefficients	$\mathrm{m}^2\mathrm{N}^{-1}$
P_{11}, P_{12}, P_{44}	Photo-elastic coefficients	$\mathrm{m}^2\mathrm{N}^{-1}$
P_{cv}	Interband momentum matrix element	eV
q	Heat source density	Wm^{-3}
Q	Heat power	W
R	Recombination rate density	$\mathrm{m}^{-3}\mathrm{s}^{-1}$
R_0	Front facet reflectivity	
R_l	Rear facet reflectivity	
R_{A}	Auger recombination rate density	$\mathrm{m}^{-3}\mathrm{s}^{-1}$
R_{sp}	Spontaneous recombination rate density	$\mathrm{m}^{-3}\mathrm{s}^{-1}$
R_{SRH}	Shockley-Read-Hall recombination rate density	$\mathrm{m}^{-3}\mathrm{s}^{-1}$
R_{st}	Stimulated recombination rate density	$\mathrm{m}^{-3}\mathrm{s}^{-1}$
R_{Th}	Thermal resistance	KW^{-1}
s_{ij}	Strain components	
S	Photon flux	$\mathrm{m}^{-2}\mathrm{s}^{-1}$
t	Time	s
T	Temperature	K
u	Displacement field	m
$\lvert V\rvert^2$	Relative intensity in circular polarization	
w_{c}	Contact width	m
$\vec{x}$	Position	m
x	Vertical coordinate	m
y	Lateral coordinate	m
z	Longitudinal coordinate	m
α_{CTE}	Coefficient of thermal expansion	K^{-1}
α_{fc}	Free-carrier absorption	m^{-1}

α_{m}	Modal absorption	m^{-1}
α_N	Linear carrier induced refractive index change	m^3
α_T	Linear thermally induced refractive index change	K^{-1}
β	Inverse thermal voltage	V^{-1}
β_{sp}	Contribution of spontaneous emission	
γ	Dephasing frequency	$\mathrm{rad\,s}^{-1}$
$\gamma_1, \gamma_2, \gamma_3$	Luttinger parameter	
Γ	Optical confinement factor	
δE_{lh}	Light-hole band offset	eV
δE_{hh}	Heavy-hole band offset	eV
δE_{v}	Valence band offset	eV
δE_{c}	Conduction band offset	eV
δn	Refractive index perturbation	
δn_N	Carrier induced refractive index perturbation	
δn_T	Temperature induced refractive index perturbation	
δn_t	Trench induced refractive index perturbation	
ΔE_{c}	Conduction band offset	eV
Δ_{SO}	Split-off energy	eV
Δt	Time discretization	s
ΔT	Temperature difference	K
Δp	Material polarization envelope	Cm^{-2}
Δx	Vertical discretization	m
Δy	Lateral discretization	m
Δz	Longitudinal discretization	m
$\Delta\varepsilon$	Permittivity perturbation	$\mathrm{CV}^{-1}\mathrm{m}^{-1}$
ε	Permittivity	$\mathrm{CV}^{-1}\mathrm{m}^{-1}$
ε_{r}	Relative permittivity	
η_{tr}	Transport efficiency	
θ	Angle	$^\circ$
λ	Wavelength	m
λ_0	Vacuum wavelength	m
μ	Permeability	$\mathrm{kgmA}^{-2}\mathrm{s}^{-2}$
$\mu_{\vec{k}}$	Dipole-matrix elements	

$\mu_{n/p}$	Mobility for electrons / holes	$\mathrm{m^2V^{-1}s^{-1}}$
μ_r	Relative permeability	
ν	Poisson's ratio	
ρ	Charge density	C
ρ	Degree of polarization	
ρ_y	TE polarization purity	
σ_{ij}	Stress components	$\mathrm{Nm^{-2}}$
$\sigma_{n/p}$	Conductivity for electrons / holes	$\Omega^{-1}\mathrm{m^{-1}}$
τ_nr	(Ambipolar) Non-radiative lieftime	s
$\tau_{n/p}$	Non-radiative lieftime of electrons / holes	s
$\sigma_{n/p}$	Free-carrier abs. cross section	$\mathrm{m^2}$
ϕ	Electric potential	V
ϕ	Envelope of electric field	$\mathrm{Vm^{-1}}$
$\phi_{n/p}$	Quasi-Fermi potential for electrons / holes	V
χ	Electric susceptibility	
χ_el	Electron affinity	eV
ψ	One-particle wave function	
ω	Angular frequency	$\mathrm{rad\,s^{-1}}$
ω_ref	Reference angular frequency	$\mathrm{rad\,s^{-1}}$
Ω	Spatial domain	
i	Imaginary unit	
∂	Partial derivative	
δ_{ij}	Kronecker delta	
$\mathbb{1}$	Identity matrix	
$\mathbb{R}$	Real numbers	
$\mathbb{C}$	Complex numbers	
H^1	Sobolov space of order one	

The Einstein summation convention is used for repeated indices.

Chapter 1

Introduction

1.1 Motivation

High-Power Diode Lasers (HPDLs) are widely established as versatile tools for pumping of solid-state lasers, measurement applications and for direct materials processing. During the past ten years, these lasers gained market shares from other laser types like CO_2- or lamp pumped solid state lasers. Pump applications on the one hand side and direct applications on the other profit from a steady increase of the brightness and spectral brightness for frequency stabilized diode laser systems. The constantly increasing demand for higher beam quality, efficiency and output power is reached by continuous improvement of individual emitters and new design concepts for power scaling on the system side. These concepts typically include spatial, polarization and spectral multiplexing with optional frequency stabilized Single Emitters (SEs) or diode Laser Arrays (LAs) due to external feedback. Based on Dense Wavelength Multiplexing (DWM) direct diode laser systems offering 4 kW of power out of a 150 µm fiber with a beam parameter product of 5 mm mrad are realized [1]. The output power of these high-power direct diode lasers is scaled up into the kW-regime to address applications with high demands on brightness, such as sheet metal cutting with a market share of 1.2 billion Dollars and additive manufacturing with an expected annual growth of about 30 % [2]. In this regime, the market is shared by competing gas-, fiber-, and direct diode laser sources. The key requirements for diode laser-based systems to enter industries are reliability, costs per Watt of output power and cost of ownership. Application regimes with brilliance greater than $1 \cdot 10^7\,\mathrm{Wmm^{-2}sr^{-1}}$ are currently covered by solid-state laser sources. Either for direct diode laser systems or as part of pump modules for disk lasers the individual diode laser emitter is the very first component in a chain of product integrations. The disk lasers are typically integrated into laser machine tools, which constitute the final product. On that score, since the semiconductor laser is at the very beginning of the value-added chain, every improvement made to the individual diode laser emerges into a cascade of improvements and enablers for the entire laser machine tool whether in respect of efficiency, costs, power or beam quality. State of the art high-power SE or emitters in LAs typically have 4 to 5 mm long cavities and current injection widths between 90 and 200 µm. A SE with 100 µm contact opening and 4 mm long cavity is operated around 12 to 16 W output power at approximately 13 to 18 A with an electro-optical efficiency around 55 %. Although the devices can be operated at power levels up to 18 W without thermal roll-over or Catastrophic Optical (Mirror) Damage (CO(M)D), in products, the

lasers are usually operated at lower currents to maintain reliability, increase the lifetime and keep the lateral divergence angle at a reasonably low value. Typical values of internal COMD power densities are over $18\,\mathrm{MWcm^{-2}}$ for 100 µm stripe lasers [3]. The

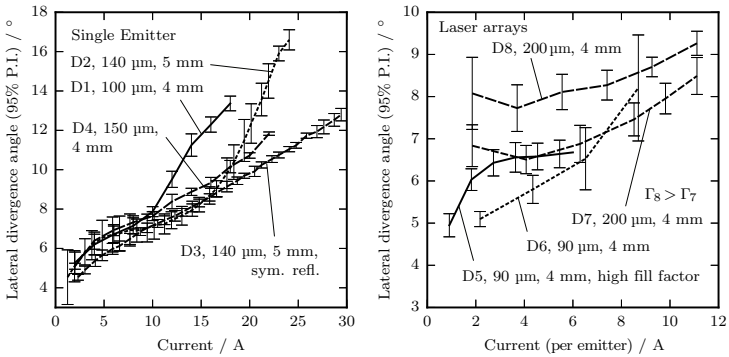

FIGURE 1.1: Measured far-field divergence over current for various single emitter (left) and laser array (right) devices. For the laser arrays, the current displayed is the current per emitter. Specifics of the devices are listed in Tb. C.2 and C.3. The numbers attached to the device label are contact width and device length. Despite D3, all devices have asymmetric facet coatings, with 98 % back facet and 2 % front facet reflectivity. Device D3 is a symmetric cavity with respect to the facet coatings. Both front and back facet reflectivity are 10 %. Laser array D8 has a higher optical confinement factor than D7. The array fill factor of device D5 is higher as the one of D6.

trend of Slow-Axis Divergence (SAD) over current for gain-guided SEs usually separates in two regimes: One below and one above the operating current at which thermal lensing dominates. The transition is characterized by a substantial increase in SAD with the current. The onset of thermal *blooming* can be shifted to higher currents with an increase in the emitter width or length in conjunction with lower dissipated power and temperature, see Fig. 1.1 at 10 A for D1 and more than 20 A for D4. Specifics of the devices D1-D8 are listed in Tb. C.2 and C.3 in the appendix. Between D1 and D4 the contact width changes from 100 µm to 150 µm, while the epitaxy is equal. Analogue, the change in both contact width and cavity length between D1 and D2, again both devices have identical epitaxial structure, shifts the onset of thermal blooming towards a higher current for device D2. An even greater change in SAD is realized by equalization of the reflectivities for the front and rear facet. To symmetrize temperature and intensity distributions in the cavity coatings with 10 % reflectivity are applied for both front and back facet of device D3, which leads to significantly different SAD compared to the corresponding device D2 (same contact width and length) with asymmetric coatings of 2 % and 98 % for front and back facet respectively [4]. The difference in SAD becomes prominent for currents above 20 A. The SAD of D3 stays below the divergence angle of D2, see Fig. 1.1. Emitters in LAs are usually operated at lower currents (per emitter) than SEs. Mainly below currents where the thermal lens dominates. However, based on emitter pitch, contact width (compare D5 and D6 against D7 and D8) and changes to the epitaxial structure characteristic trends over current and the magnitude of SAD of LAs can differ significantly, compare Fig. 1.1 (right). Devices D5 and D6 have identical epitaxial structure, contact width, and length but differ in the pitch between adjacent emitters. LA D5 has a higher fill factor [5] than LA D6, the resulting difference in the

thermal profile leads to the observed change in SAD. In addition to the changes in the lateral structure variations in epitaxial design (changes in the vertical device direction) influence the lateral emission characteristics. The asymmetry of the waveguide and as a consequence, the optical confinement factor is changed between devices D7 and D8 [6]. The design of D8 results in a larger confinement factor than for D7 and a larger SAD over the entire current range, compare trends in Fig. 1.1 (right). Alongside with the changes in SAD between the devices the Near-Field (NF) profile, especially the near-field width over current undergoes variations. The resulting near-field profiles are of equal importance as the Far-Field (FF) width since both determine the lateral Beam Parameter Product (BPP) of the device. Details about the near-field profiles are given in Chapter Fig.8, where modeling results for devices D1-D8 are presented. In addition to the lateral BPP, the Degree Of Polarization (DOP), which accounts for the fraction of the emitted light polarized parallel to the Quantum Well (QW)-plane corresponding to the Transverse Electric (TE) mode, is a crucial property of the laser device. Diode laser systems, which rely on polarization combining demand high DOP to deliver the overall power at sufficient electro-optical efficiency. Both the efficiency and power of the system or diode laser module decrease with decreasing DOP of either the individual emitters or the diode LAs. With respect to mounting conditions, the DOP of packaged LAs can decrease down to 90 % (for the entire array). The spatially resolved DOP decrease can follow systematic trends, for example, lower DOP towards the edges of the array, or occur randomly distributed with variations of several percents between adjacent emitters, see Fig. 5.17.

Currently, the knowledge about SAD, near-field width and DOP over current is mainly gathered by experiment. The lateral emission characteristics cannot be predicted by any simulation tool (known to the author) to the extent needed to make design decisions and in some cases after evaluation of experiments emerging differences in the characteristics (SAD, NF, DOP) between devices remain unexplained. The total duration for epitaxial growth, processing, the packaging on submounts and heat sinks, and finally execution of measurements can take from several weeks up to months. On top of this, it is often hard to isolate specific effects or correlations in experimental findings since the device remains a *black-box* and internal processes, for example, the evolution of the filamented light field inside the cavity are not directly observable. To realize the requirements for future applications, several aspects of high-power diode lasers, as such as lateral mode dynamics, far-field emission, and damage mechanisms have to be investigated and understood in more detail. A key component alongside experimental studies leading to this understanding is the development of models for Computer-Aided Design (CAD).

The aim of this thesis is the investigation of theoretical models and the development of a simulation software package to support future design improvements of high-power semiconductor laser emitters, especially with respect to lateral beam quality. In this thesis, a numerical model is presented which is capable of calculating SAD and NF over current for high-power edge-emitting diode lasers. The model is demonstrated and validated by calculation of device characteristics, such as near- and far-field profiles and optical output power for the eight devices D1–D8 (Fig. 1.1). Alongside with the numerical study, the mechanisms driving those lateral emission characteristics are theoretically investigated. In addition, an opto-mechanical model is presented, which is employed to calculate polarization rotations in mechanically strained semiconductor lasers.

1.2 State of the Art

1.2.1 High-Power Edge-Emitting Diode Lasers

First semiconductor lasers were realized in 1962. These devices were p-n homojunctions with high threshold current densities, and output power for single-mode beams was limited to a few milliwatts. Within the following twenty years, development and research lead to devices with a diffraction limited beam and output powers above 30 mW which are mainly used in communication, measurement, and sensing applications, optical data storage and printing. Double-heterostructures play an important role in the development of optoelectronic devices with low threshold current, high output power, and electro-optical efficiency. The concept of a separate carrier and photon confinement enables efficient Continuous Wave (CW) operation of semiconductor lasers at room temperature. HPDL with emission wavelengths around 980 nm for optical pumping and telecommunication were among the main drivers for this development. [7] In the late 1990s, HPDLs with tens of watts optical output power were introduced. Since then the brilliance of HPDLs increases exponentially since today, Fig. 1.2. In 2014 diode laser systems based on edge-emitters with output powers of 40 kW and beam parameter product of 40 mm mrad where demonstrated [2]. In these systems, the output power is increased by wavelength multiplexing without a significant increase in the beam parameter product. Applications for edge-emitting diode lasers in the range of $1 \cdot 10^5\,\mathrm{Wmm^{-2}sr^{-1}}$ are soft soldering (500 W, 20 mm mrad) and heat treatment of steels with powers up to 12 kW and BPP of 100 mm mrad. Semiconductor lasers addressing transparent plastic welding typically have a brilliance in the range of $1 \cdot 10^3$ to $1 \cdot 10^4\,\mathrm{Wmm^{-2}sr^{-1}}$. Employing semiconductor lasers as beam sources in the field of additive manufacturing offers great potential for future applications. Single fiber-coupled diode laser modules with powers of 200 W and brightness of 10 mm mrad or multi-spot configurations [8] can lead to increased build-up rates and part volumes. [2] Today limiting factors are power linearity

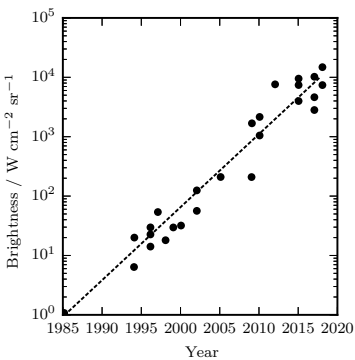

FIGURE 1.2: Development of high-power semiconductor laser brightness from 1985 till today, after [9].

(suppression of thermal roll-over), beam quality (in the lateral direction), reliability and lifetime. A long lifetime of more than 50,000 hours is crucial for industrial applications. Among other factors like facet passivation and material purity (defect density), local spikes in optical intensity due to high filamentation lead to reduced lifetimes or device

failure. The primary design target for laser development is the combination of power and beam quality, alias the brightness. The brightness [10] of a laser source is defined as

$$B = \frac{P}{A\Omega} = \frac{P}{\lambda_0^2 M^2} \tag{1.1}$$

where P is the optical power, M^2 the beam propagation parameter, λ_0 is the wavelength in vacuum, A the emission area (mode field size in focus of laser beam) and Ω is the solid angle (far-field) into which the power is emitted. Edge-emitting diode lasers considered

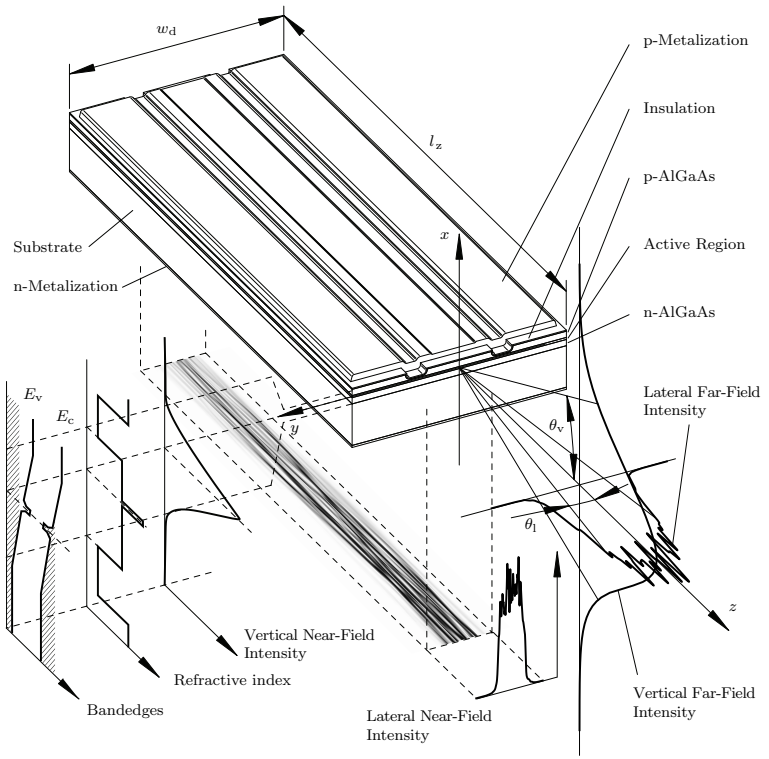

FIGURE 1.3: Schematic of high-power diode laser device.

in the scope of this work exhibit the structure illustrated in Fig. 1.4 and are produced in the following steps: An epitaxial structure which forms a p-i-n heterojunction including a (single) QW in the intrinsic region is grown on a n-doped Gallium Arsenid (GaAs) substrate. After the growth process lateral features, such as index trenches or ridges are etched into the epitaxial stack. A Silicon Nitride (SiN) insulation layer (thickness approximately 0.2 µm) is applied on top of the semiconductor and partially removed with a photolithographic etching process to define contact openings (injection stripe). After the insulating layer is deposited, the p-side is covered by a metallization stack

typically consisting of Titanium (Ti), Platinum (Pt) and Gold (Au) to form an ohmic contact with the semiconductor in the areas where the insulation is removed. The Pt layer acts as a diffusion barrier for the Au. The thickness of the metal stack amounts to around 2 to 3 µm. The contact opening is pulled back 30 µm from both facets to prevent current injection near the facets and thus, reduce the surface recombination. After thinning-down of the GaAs substrate, the n-side metallization is applied to supply the n-side electrical contact. The devices are singulated (cleaved along a crystallographic direction), either to SEs or LAs and facet coatings, either High reflective (HR) or Anti Reflective (AR), are deposited at the front and rear facets of the device. Finally, the devices are soldered on submounts, made of Aluminum Nitride (AlN) or Copper-Tungsten (CuW), or directly on heatsinks. The devices in the scope of this work, are soldered with Gold-tin (AuSn) solder with a thickness of approximately 4 µm facing p-side down. Wire-bonds are attached to the n-side metallization to supply electrical contact. The devices considered in this work incorporate a single Indium Gallium Arsenid (InGaAs) QW emitting at 950 nm, which is embedded in an asymmetric Aluminum Gallium Arsenid (AlGaAs) waveguide with a total thickness around 2 µm and Aluminum concentration in the waveguide layers around 20 % [11]. Carbon is utilized as the acceptor for p-doping and Silicon as the donator for n-doping.

Broad-Area Diode Lasers (BADLs) show an asymmetric beam profile with a large divergence angle in Fast-Axis (FA) in combination with high beam quality in the vertical direction and a smaller divergence angle in Slow-Axis (SA) together with smaller beam quality in the lateral direction, see illustration in Fig. 1.3. Typical SA divergence angles (at 95% P. I.) of SE with 100 µm contact opening range from 4 - 14° for operation currents from 2 - 20 A. FA divergence angles (the full angle at 95% P. I.) range from 30° for Large Optical Cavity (LOC) lasers [12] to 40 - 60° and higher for typical BADL [10]. The asymmetric emission of the BADL arises from the two conceptional different forms of light guidance inside the cavity: BADLs show a high beam quality in the vertical direction due to waveguiding based on the refractive index steps between the epitaxial layers which alternate along this vertical direction. A stable vertical eigenmode of the waveguide travels inside the cavity and results in a Gaussian-like beam profile in the vertical far-field. Due to the absence of refractive index steps in the lateral direction for gain-guided devices the only confinement for the light field in this direction arises from the injection current stripe area. Injected carriers are concentrated in under the injection window and form a channel of high material gain along the longitudinal direction of the cavity. This concept is called gain-guiding and is usually accompanied by lateral instabilities of the light field. Typical field evolutions for the lateral mode intensity and carrier density inside a device are illustrated in Fig. 1.3. Operation with only one lateral mode is not achieved with broad-area gain-guided lasers. A filamented near-field is observed for stripe widths larger than 10 µm [13]. The multi-mode near-field fills the area under the injection stripe and shows aperiodic ripples (filaments). This many lobed near-field builds up from a superposition of high-order lateral modes which result in large lateral far-field angles and reduced beam quality in the lateral direction. The gain of the QW is broad around tens of nanometer, and the wavelength difference between longitudinal modes in the Fabry-Perot cavity is small so that the devices without frequency stabilization operate with multiple longitudinal modes. State-of-the-art research and developments with the aim to reduce lateral filamentation and far-field divergence are mainly driven by Design Of Experiments (DOEs) with large numbers of experimental laser designs and long turnaround times of several weeks or month per experiment. Although some laser tools include lateral modes in the calculations [14] or even the

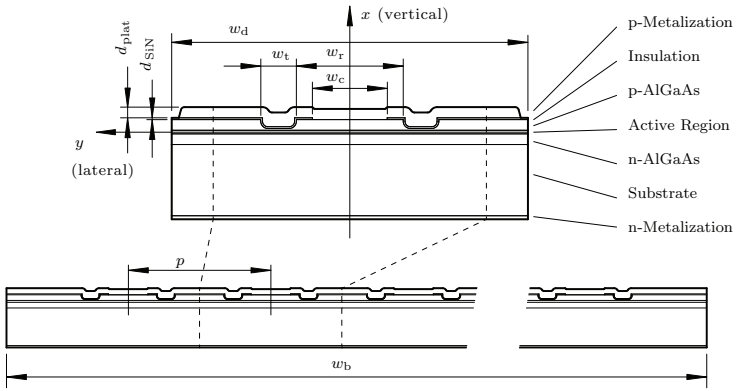

FIGURE 1.4: Schematic of the transverse cross-section of a high-power diode laser device including lateral index trenches, insulation (SiN) and contact metalization.

longitudinal propagation of the light field, there is no commercial tool available, which is capable of predicting the lateral emission characteristics of high-power edge-emitting semiconductor lasers to the extent presented in this work.

1.2.2 Semiconductor Laser Simulation Software

In order to maintain the trend of brightness improvement for HPDLs new design tools have to be integrated into the semiconductor laser design process. The objective of past and current research activities is the development of models describing the dynamics of the electromagnetic field in semiconductor lasers, either free-running or with coupled external resonators for frequency stabilization. Based on wave-optical numerical simulations the propagation of light inside the waveguide of the optoelectronic device and in external optical systems is analyzed. Design guidelines and directives can be drawn from the CAD approach, regarding emission and device characteristics, as such as voltage, power, near- and far-field patterns and operation under external feedback for wavelength stabilization.

Cross-sectional (transverse) semiconductor laser design tools (for example [14]) are employed to design QW band structures and gain, in addition to electrical and thermal properties for voltage or efficiency improvements. However, models not including the longitudinal light propagation are not sufficient to predict the filamented beam profile and emission angles for BADLs. Coupled simulations including the longitudinal and lateral dimension demand large computational resources and computational time. Additionally, the evolution of the lateral light field is a highly nonlinear process. The nonlinearity emerges from the fact that the light field induced changes to the medium which themselves influence the light fields evolution. Consequently, solutions for models including the lateral dimension cannot be found (yet) by solving a fully coupled set of equations. The first models which self-consistently described light propagation in semiconductor lasers were reported in the 80s by G. P. Agrawal [15, 16, 17] and were followed by works of G. R. Hadley [18, 19]. Instead of searching for a closed solution of a set

of eigenmodes for an optical waveguide the models employ iterative Beam Propagation Methods (BPMs), in the beginning, based on Fast-Fourier Transformation (FFT)-BPM, to propagate the light field iteratively along the waveguide. These models belong to the class of iterative FD models, which aim to find time-harmonic (stationary) solutions for the light field. In contrast, models which are based on eigenmode solutions of the optical field are suited for index-guided devices with small refractive index perturbations and weak coupling between material and optical equations. However, to deal with high-power gain-guided stripe geometry diode lasers with (lateral) spatial hole burning and carrier-induced anti-guiding, models were developed in which the lateral optical profile is propagated back and forth along the waveguide to obtain self-consistent solutions. Due to the step-wise propagation gain, refractive index and temperature distributions can be iteratively updated for each longitudinal slice and influences on the light propagation are considered. Hadley et al. applied this class of models to calculate far-field patterns for gain-guided LAs. Based on the consistent coupling of the nonlinear carrier equation, thermal equations and optical equations phenomena like self-focusing and anti-guiding, which lead to filamentation in broad-area lasers can be described. The emerge and spatial evolution of filaments were investigated by R. Lang in the early 90s [20, 21] followed by later works reported by Z. Dai in [22], where iterative FD models were applied to calculate optical propagation in tapered amplifiers. L. Borruel et al. [23] present a FD model for the quasi three-dimensional simulation of high-brightness tapered lasers. Besides the FD models, several groups [24, 25, 26, 27] (and more) developed TD models, which are employed to investigate the dynamics of the longitudinal and lateral field evolution. Similar to the FD models, the TD models account for the coupling of the nonlinear carrier-, thermal- and optical equations.

The initiative for the development of numerical models and simulation tools for design and analysis of semiconductor lasers at Fraunhofer Institute for Laser Technology (ILT) and Chair of Laser Technology (LLT) at the Rheinisch-Westfälische Technische Hochschule (RWTH) Aachen University was given in the scope of the projects *SpektraLas* (Contract 13N9729) and *FreeLas* (Contract 13N10849), which where both supported by the German Federal Ministry of Education and Research (German: Bundesministerium für Bildung und Forschung, BMBF). The first version of a *MatLab* based broad-area edge-emitting diode laser simulation tool is presented in [28]. The main objective for this version is the modeling of spectral stabilization by frequency selective feedback due to Volume Bragg Gratings (VBGs) positioned in external resonators. Additionally, the wave-optical analysis of external feedback concepts for frequency stabilization is presented in [29]. Different optical setups, like self-imaging, inverse self-imaging or biaxial divergent feedback from VBGs in external resonators are demonstrated and analyzed with respect to stabilization efficiency and sensitivity to the *smile-error*. In cooperation between the Chair of Laser Technology (LLT), the Fraunhofer ILT and TRUMPF Photonics Inc. the simulation tool is further extended to reproduce and predict lateral near- and far-field patterns. In particular the increase of the lateral divergence angle with high injection currents (called far-field *blooming*) in conjunction with high lateral near-field filamentation. In this work, the temperature is not calculated just for transverse slices along the cavity but on a three-dimensional domain including the device, solder, and submount and thus, accounting for longitudinal heat flow. The thermal profile is crucial for the prediction of the lateral emission characteristics. A novelty of this work lies in the calculation of the DOP based on a transverse opto-mechanical model, and the close relation between experiment, model development, and model calibration for the prediction of the lateral emission characteristics of various HPDLs.

1.3 Objectives and Outline of this Thesis

This thesis is organized as follows: In Chapters 2–6 the underlying physics and models for the optical gain and carrier-induced refractive index change (Chapter 2), thermal properties (Chapter 3), the light field dynamics (Chapter 4), photo-elastic properties of a strained waveguide (Chapter 5), and the electrical properties of the device (Chapter 6) are introduced (Fig 1.6). In Chapter 7 these individual models are combined into one FD and one TD model for edge-emitting semiconductor lasers. The FD model is applied to compute the lateral emission characteristics (NF and FF profiles over current) for the laser devices D1-D8. The results are presented in Chapter 8. Alongside with the simulation of the SE and LA devices the lateral guiding mechanisms, which lead to the respective SAD and NF widths for the individual devices are discussed. In the last section of Chapter 8, the TD model is demonstrated by the example of device D1. In Appendix B, an Finite Differences Method (FDM) discretization scheme is

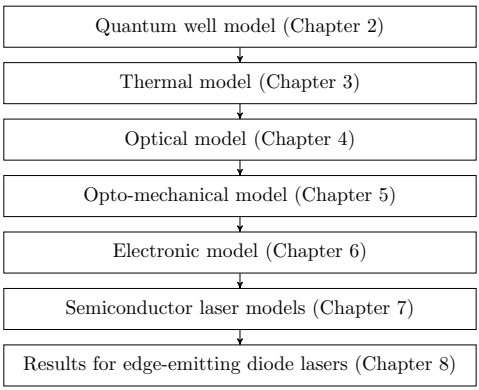

FIGURE 1.5: Organization of the thesis and physical models.

presented, which is applied for numerical solution of the differential equations arising from Schrödinger's equation for band structure calculations in Chapter 2, the optical BPM, Time-Domain Traveling Wave (TDTW) method in Chapter 4, for the carrier diffusion equation and (with modifications) for the Drift-Diffusion Model (DDM) in Chapter 6. The heat diffusion equation in Chapter 3, the linear elastic mechanical model in Chapter 5 and the drift-diffusion equations in conjunction with the Primal Mixed Method (PMM) in Chapter 6 are solved with the Finite-Element Method (FEM). In Chapter 2, the quantum mechanical calculation of semiconductor band structures are utilized to compute the optical gain for TE and TM polarized light and carrier-induced refractive index changes for strained QWs. Additionally, the free-carrier absorption is determined. The thermal model is presented next in Chapter 3. The steady state thermal profiles based on the heat source distribution in the device are computed, and the resulting thermal lens profiles are analyzed in Section 3.2. The temperature increase over current is calculated for devices D1-D8. The chapter closes with the investigation of induced Catastrophic Optical Damage (COD) by external heating of a SE device. In this section, the thermal model is employed to calculate the temperature increase at the front facet due to an external heat source. In Chapter 5, the optical polarization is calculated based on photo-elasticity according to the mechanical strain state of the waveguide. In

the first part of the chapter, an analytical model for the Degree Of Polarization (DOP) as a function of the strain components is derived. The model is extended for interaction with a medium with anisotropic gain, and the full-vectorial BPM is employed to confirm the findings by analysis of light propagation in a birefringent waveguide. The influence of thin-film stress and packaging induced stress on the DOP are analyzed in Sections 5.4 and 5.5. The study of the electronic properties (distribution of charge carriers and currents in the device) in Chapter 6 mainly serves the following purposes: Prediction of the transverse current-flow through the active laser diode with focus on the current distribution injected into the QW, calculation of optical power and voltage over current, determination of modal free-carrier losses and determination of heat sources, which serve as input for the thermal solver. An overview of the main physical interactions and governing equations which are considered in the scope of this work is given in Fig 1.6.

The objectives of this thesis are:

1. Development of a model for edge-emitting semiconductor lasers, which can describe multi-mode lateral emission characteristics including near-field and far-field profiles and far-field divergence angles dependent on the injection current.

2. Demonstration of this model by simulation of the lateral emission characteristics of the experimental investigated devices D1-D8 which are summarized in Fig. 1.1.

3. Explain the guiding mechanisms influencing the observed trends of the far-field widths and near-field widths over current for broad-area diode lasers.

4. Development of an opto-mechanical model, which describes depolarization due to mechanical stress in the device.

5. Explain the deterioration of the degree of polarization in packaged laser arrays.

6. Comparison between results for the evolution of the optical field obtained by Frequency-Domain (FD) and Time-Domain (TD) models for edge-emitting laser diodes.

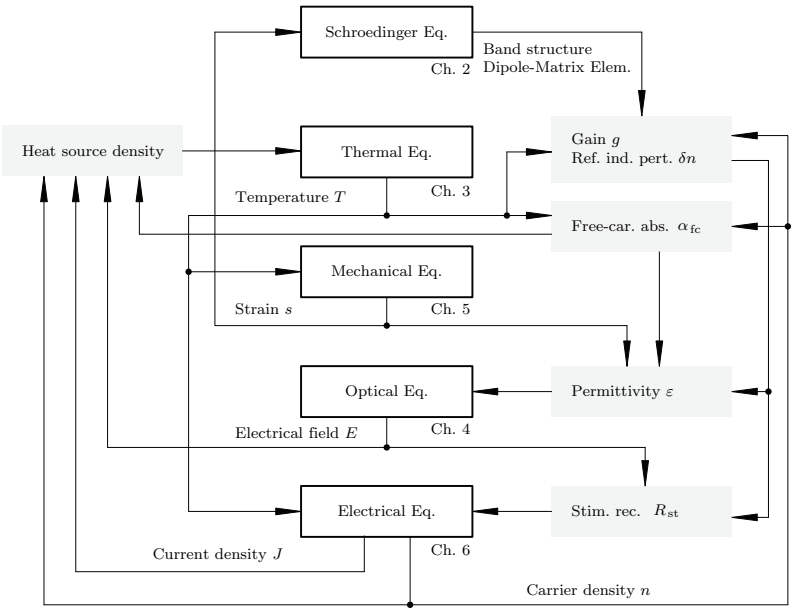

FIGURE 1.6: Overview of (main) interactions and governing equations.

Chapter 2

Electronic Band Structures and Optical Interactions in Semiconductors

To predict optical interactions with semiconductor nanostructures the band structure, the quasi-continuous one-particle energy in solids, as well as the wavefunctions of the particles bound in the energy states of the nanostructure have to be computed. The wavefunctions are needed to calculate the matrix elements of the inter- and intra-band transitions for quantum mechanical operators such as the dipole-matrix operator and the operator for Coulomb interactions. A common approach for the calculation of band structures for transitions with energies close to the bandgap of the semiconductor and for the corresponding range of optical frequencies is the $k \cdot p$ method, see Section 2.2 and [30]. In combination with the envelope-formalism, this method can be applied to predict band structures of nanostructures with different numbers of quantum mechanically confined dimensions for various semiconductor materials. The order of the $k \cdot p$ method denominates the number of basis functions in which the electron wavefunction is developed. In general, the accuracy of the method increases with increasing order. The solution of Schrödinger's equation with 4×4, 6×6 and 8×8 band $k \cdot p$ method is used in research and commercial applications. Nevertheless, reasons for the implementation of a band structure solver are: Seamless integration into the modeling package *SEMSIS*, which includes the coupling to a mechanical solver for strain calculations and execution of parametric studies, extent-ability (for example: inclusion of new materials) and control over subtle implementation details, which influence numerical stability and accuracy of the solutions. For several material combinations application of a standard FDM scheme leads to unphysical solutions, which manifest in false dispersions of the band structure or wavefunctions with high-frequency oscillations. These *spurious solutions* can be suppressed by an adequate choice of the discretization scheme, in this case, the FDM scheme with box-integration as presented in Chapter B in combination with a specific order of the differential operators and rescaling of material parameters [31]. To take into account the coupling of conduction and valence bands, which results in non-parabolic energy dispersions for the conduction bands (see, for example, Fig. 2.5), the order of the $k \cdot p$ method has to be increased to at least 8×8. In the 8×8 scheme, the wavefunctions of the conduction band are included in the calculations. For several material systems, the form of the conduction band has a significant influence on the gain and absorption spectra calculated based on the optical Bloch equations. The objective

of this chapter is the numerical solution of $k \cdot p$ Schrödinger equations with the envelope formalism for the calculation of band structures and wavefunctions for semiconductor nanostructures. An initial implementation of the band structure solver is presented in [32]. In addition to the band structure, the complex electric susceptibility as a function of the frequency of the interacting light field, temperature and carrier density is calculated based on the microscopic description.

In the binary compound of the group III-V semiconductor GaAs, the Gallium and Arsenide atoms form a zinc-blende structure. The investigation of the optical properties in the relevant spectral regime is carried out by evaluation of the band structure in a small region (in momentum space) around points of high symmetry. In the case of GaAs, these are Γ_8 for the Light-Holes (LHs) and Heavy-Holes (HHs), Γ_7 for the Split-Off (SO) holes and Γ_6 for the conduction band electrons [33]. Calculation of the band structure requires the solution of Schrödinger's equation for electrons in a crystal. The crystal is made up of a grid generated by the vectors $\vec{a}_i$ and a basis. Therefore, the semiconductor lattice fulfills the translational symmetry of the crystal. The potential $V(\vec{x})$ of the crystal lattice made up of atom cores, and the bound electrons is consequently invariant under translations of integer multiples of n_i of the lattice vectors $\vec{a}_i$.

2.1 Schrödinger's Equation and Bloch Theorem

For an electron exposed to a periodic potential $V(\vec{x})$ with wavefunction $\psi_n(\vec{x})$, energies E_n and including spin-orbit interaction the stationary one-particle Schrödinger equation

$$(H + H_{SO})\,\psi_n(\vec{x}) = \left(\frac{p^2}{2m_0} + V(\vec{x}) + \frac{\hbar}{4m^2c^2}\left[\nabla V \times \vec{p}\right]\cdot\vec{\sigma}\right)\psi_n(\vec{x}) = E_n\psi_n(\vec{x}) \qquad (2.1)$$

holds. Here, the momentum operator $p = -i\hbar\nabla$ is given in position space. In (2.1) the term

$$H_{\mathrm{SO}} = \frac{\hbar}{4m^2c^2}\left[\nabla V \times \vec{p}\right]\cdot\vec{\sigma}, \qquad (2.2)$$

accounts for the spin-orbit interaction, where $\vec{\sigma} = (\sigma_1, \sigma_2, \sigma_3)^T$ is Pauli's spin-matrix-vector with the components

$$\sigma_1 = \begin{pmatrix} 0 & 1 \\ 1 & 0 \end{pmatrix}, \quad \sigma_2 = \begin{pmatrix} 0 & -i \\ i & 0 \end{pmatrix}, \quad \sigma_3 = \begin{pmatrix} 1 & 0 \\ 0 & -1 \end{pmatrix}, \qquad (2.3)$$

which are Pauli's matrices. The Hamiltonian H fulfills the symmetry of the semiconductor crystal and is consequently invariant under translations of multiples of the lattice vector $\vec{R}$. If $\psi_n(\vec{x})$ is a solution of (2.1) then due to the symmetry of the lattice also $\psi_n(\vec{x} + \vec{R})$ solves the stationary Schrödinger equation for a periodic potential. Both eigensolutions $\psi_n(\vec{x} + \vec{R})$ and $\psi_n(\vec{x})$ only differ by a complex phase factor. According to Bloch's theorem with the Bloch factors $u_{n,\vec{k}}(\vec{x}) = u_{n,\vec{k}}(\vec{x} + \vec{R})$, which exhibit the periodicity of the crystal, the solutions $\psi_{n,\vec{k}}(\vec{x})$ of (2.1) are written in the form

$$\psi_{n,\vec{k}}(\vec{x}) = e^{i\vec{k}\cdot\vec{x}}u_{n,\vec{k}}(\vec{x}). \qquad (2.4)$$

The functions $\psi_{n,\vec{k}}(\vec{x})$ are denominated as Bloch functions. Insertion of the Bloch functions (2.4) into Schrödinger's equation (2.1) results in the eigenvalue equation for the

Bloch factors

$$\left(-\frac{\hbar^2}{2m_0}\nabla^2 + V(\vec{x}) + \frac{\hbar}{4m^2c^2}\left[\nabla V \times \vec{p}\right]\cdot\vec{\sigma}\right) e^{i\vec{k}\cdot\vec{x}} u_{n,\vec{k}}(\vec{x}) = E_n(\vec{k}) e^{i\vec{k}\cdot\vec{x}} u_{n,\vec{k}}(\vec{x}) \tag{2.5}$$

and equivalent

$$\begin{aligned}\Bigg(\frac{p^2}{2m_0} + \frac{\hbar^2}{2m_0}k^2 + \frac{\hbar}{m_0}\vec{k}\cdot\vec{p} + \frac{\hbar^2}{4m^2c^2}\left[\nabla V \times \vec{k}\right]\cdot\vec{\sigma} \\ + \frac{\hbar}{4m^2c^2}\left[\nabla V \times \vec{p}\right]\cdot\vec{\sigma} + V(\vec{x})\Bigg) u_{n,\vec{k}}(\vec{x}) = E_n(\vec{k}) u_{n,\vec{k}}(\vec{x}),\end{aligned} \tag{2.6}$$

where $k^2 = |\vec{k}|^2$. The fourth term in the second row of (2.6) is much smaller than the fifth term and is consequently neglected [30], so that the eigenvalue equation for the Bloch factors with spin-orbit coupling becomes

$$\left(\frac{p^2}{2m_0} + \frac{\hbar^2}{2m_0}k^2 + \frac{\hbar}{m_0}\vec{k}\cdot\vec{p} + V(\vec{x}) + \frac{\hbar}{4m^2c^2}\left[\nabla V \times \vec{p}\right]\cdot\vec{\sigma}\right) u_{n,\vec{k}}(\vec{x}) = E_n(\vec{k}) u_{n,\vec{k}}(\vec{x}). \tag{2.7}$$

For an arbitrary wavenumber $\vec{k}_0$, the Bloch factors $u_{n,\vec{k}_0}$ build a complete orthonormal basis

$$\int_{\text{unit cell}} u_{\mu,\vec{k}_0}(\vec{x}) u^*_{\nu,\vec{k}_0}(\vec{x})\,\mathrm{d}^3\vec{x} = \delta_{\mu\nu}. \tag{2.8}$$

Based on this the Bloch factors for arbitrary wavenumber $\vec{k}$ can be expanded with respect to the Bloch factors at $\vec{k}_0$

$$u_{n,\vec{k}}(\vec{x}) = \sum_{\mu} c_{n\mu,\vec{k}-\vec{k}_0}\, u_{\mu,\vec{k}_0}(\vec{x}). \tag{2.9}$$

Additionally, the Bloch factors $u_{n,\vec{k}_0}$ are eigensolutions of

$$H(\vec{k}_0) u_{n,\vec{k}_0}(\vec{x}) = E_n(\vec{k}_0) u_{n,\vec{k}_0}(\vec{x}), \tag{2.10}$$

with

$$H(\vec{k}_0) = \frac{p^2}{2m_0} + \frac{\hbar}{m_0}\vec{k}_0\cdot\vec{p} + \frac{\hbar^2}{2m_0}k_0^2 + V(\vec{x}). \tag{2.11}$$

Multiplication of (2.6) with $u^*_{\nu,\vec{k}_0}(\vec{x})$, integration of the product and insertion of equations (2.8), (2.9) and (2.11) leads to

$$\begin{aligned}&\int_{\text{u.c.}} u^*_{\nu,\vec{k}_0}(\vec{x})\left[H(\vec{k}_0) + \frac{\hbar}{m_0}(\vec{k}-\vec{k}_0)\cdot\vec{p} + \frac{\hbar^2}{2m_0}\left(k^2 - k_0^2\right) + H_{SO}\right] \\ &\times \sum_{\mu} u_{\mu,\vec{k}_0}(\vec{x}) c_{n\mu,\vec{k}-\vec{k}_0}\,\mathrm{d}^3\vec{x} \\ &= \int_{\text{u.c.}} E_n(\vec{k}) \sum_{\mu} u_{\mu,\vec{k}_0}(\vec{x}) c_{n\mu,\vec{k}-\vec{k}_0} u^*_{\nu,\vec{k}_0}(\vec{x})\,\mathrm{d}^3\vec{x}.\end{aligned} \tag{2.12}$$

Insertion of (2.10) results in the eigenvalue equation

$$\sum_{\mu} \underbrace{\left\{ \left[E_\nu(\vec{k}_0) + \frac{\hbar^2}{2m_0}\left(k^2 - k_0^2\right) \right] \delta_{\nu\mu} + H_{SO,\nu\mu} + \frac{\hbar}{m_0}(\vec{k} - \vec{k}_0)\cdot\vec{p}_{\nu\mu} \right\}}_{\equiv H_{\nu\mu}(\vec{k})} \times c_{n\mu,\vec{k}-\vec{k}_0} = E_n(\vec{k}) c_{n\nu,\vec{k}-\vec{k}_0}, \tag{2.13}$$

for the coefficients $c_{n\mu,\vec{k}-\vec{k}_0}$ of the series. The infinite-dimensional matrix $H_{\nu\mu}(\vec{k})$ couples bands based on the momentum-matrix elements

$$\vec{p}_{\nu\mu} = \langle u_{\nu,\vec{k}_0} | \, \vec{p} \, | u_{\mu,\vec{k}_0} \rangle, \tag{2.14}$$

which are non-vanishing and non-diagonal with respect to the band indices.

2.2 $k \cdot p$ Method

The $k \cdot p$ method is a perturbative treatment, which can be applied in the cases, where band structures in the vicinity of a local extremum are computed. The calculation of these sections of the band structure is reduced to the solution of an algebraic eigenvalue problem which depends on the wavevector $\vec{k}$. For the development of the single-particle wavefunctions (2.4) based on the order of the method employed, 1, 4, 6, or 8 basis wavefunctions are included in the calculations. For the 8-band $k \cdot p$ method, two spin-degenerate LH, two spin-degenerate HH, two spin-degenerate SO, and two spin-degenerate conduction band states are employed. Thus, the coupling between valence band states and conduction band states which lead to non-parabolic conduction bands are treated in the 8-band method.

In the following the time-independent perturbation theory, which treats the $\vec{k}\cdot\vec{p}$ term as a perturbation is employed in conjunction with the Löwdin renormalization technique [34, 30] to acquire a finite-dimensional representation of the Hamiltonian from (2.13). The bands included in the Hamiltonian are denominated as class A bands and all other bands, the class B bands are included in the calculations as perturbations to the Hamiltonian. The properties of class B bands are represented in the form of constant material parameters and thus, implicitly take influence on the Hamiltonian and the calculated band structures. To realize this the coupling terms, the non-diagonal entries of the momentum matrix

$$\frac{\hbar}{m_0}(\vec{k} - \vec{k}_0)\cdot\vec{p}_{\nu\mu} \tag{2.15}$$

between the bands of class A and B are treated as perturbations [31]. To summarize: The nonlinear, finite-dimensional Hamilton-operator which is the result of the renormalization technique is linearized with the help of the perturbation theory.

2.2.1 8-Band Hamiltonian

For the 8×8 method, additionally to the valence bands of the 6×6 method, the lowest conduction band is also treated as a class A band and included in the calculations. The

Hamilton operator $H^{8\times8}_{|jm\rangle}$ given in the angular momentum states

$$|S,\uparrow\rangle,\ |\frac{3}{2},\frac{3}{2}\rangle,\ |\frac{3}{2},\frac{1}{2}\rangle,\ |\frac{1}{2},-\frac{1}{2}\rangle,\ |S,\downarrow\rangle,\ |\frac{3}{2},-\frac{3}{2}\rangle,\ |\frac{3}{2},-\frac{1}{2}\rangle,\ |\frac{1}{2},-\frac{1}{2}\rangle \tag{2.16}$$

is [35]

$$H^{8\times8}_{|jm\rangle} = \begin{pmatrix} H^{8\times8}_{U} & H^{8\times8}_{UL} \\ H^{8\times8}_{LU} & H^{8\times8}_{L} \end{pmatrix} \tag{2.17}$$

with the upper block

$$H^{8\times8}_{U} = \begin{pmatrix} E_c + A & -\sqrt{3}V & \sqrt{2}U & U \\ -\sqrt{3}V^* & E_v - P - Q & S & \frac{1}{\sqrt{2}}S \\ \sqrt{2}U & S^* & E_v - P + Q & \sqrt{2}Q \\ U & \frac{1}{\sqrt{2}}S^* & \sqrt{2}Q & E_v - P - \Delta_{\mathrm{SO}} \end{pmatrix}, \tag{2.18}$$

the lower block

$$H^{8\times8}_{L} = \begin{pmatrix} E_c + A & \sqrt{3}V^* & \sqrt{2}U & -U \\ \sqrt{3}V & E_v - P - Q & -S^* & \frac{1}{\sqrt{2}}S^* \\ \sqrt{2}U & -S & E_v - P + Q & -\sqrt{2}Q \\ -U & \frac{1}{\sqrt{2}}S & -\sqrt{2}Q & E_v - P - \Delta_{\mathrm{SO}} \end{pmatrix}, \tag{2.19}$$

and the off-diagonal blocks

$$H^{8\times8}_{UL} = \begin{pmatrix} 0 & 0 & V^* & \sqrt{2}V^* \\ 0 & 0 & -R & -\sqrt{2}R \\ -V^* & -R & 0 & -\sqrt{\frac{3}{2}}S \\ \sqrt{2}V^* & \sqrt{2}R & -\sqrt{\frac{3}{2}}S & 0 \end{pmatrix}, \tag{2.20}$$

and

$$H^{8\times8}_{LU} = \begin{pmatrix} 0 & 0 & -V & \sqrt{2}V \\ 0 & 0 & -R^* & \sqrt{2}R^* \\ V & -R^* & 0 & -\sqrt{\frac{3}{2}}S^* \\ \sqrt{2}V & -\sqrt{2}R^* & -\sqrt{\frac{3}{2}}S^* & 0 \end{pmatrix}. \tag{2.21}$$

The parameters inserted into the matrix blocks are

$$A = A_k + A_\epsilon, \tag{2.22}$$
$$P = P_k + P_\epsilon, \tag{2.23}$$
$$Q = Q_k + Q_\epsilon, \tag{2.24}$$
$$R = R_k + R_\epsilon, \tag{2.25}$$
$$S = S_k + S_\epsilon, \tag{2.26}$$
$$V = \frac{1}{\sqrt{6}}P_{cv}\left(k_y + ik_z\right), \tag{2.27}$$
$$U = \underbrace{\frac{1}{\sqrt{3}}P_{cv}}_{\equiv U_{k,1}}k_x, \tag{2.28}$$

with

$$A_k = \underbrace{\frac{\hbar^2}{2m_c}\left(k_y^2+k_z^2\right)}_{\equiv A_{k,0}} + \underbrace{\frac{\hbar^2}{2m_c}}_{\equiv A_{k,2}} k_x^2, \tag{2.29}$$

$$P_k = \left(\frac{\hbar^2}{2m_0}\right)\gamma_1\left(k_x^2+k_y^2+k_z^2\right), \tag{2.30}$$

$$Q_k = \left(\frac{\hbar^2}{2m_0}\right)\gamma_2\left(k_y^2+k_z^2-2k_x^2\right), \tag{2.31}$$

$$S_k = \sqrt{3}\left(\frac{\hbar^2}{m_0}\right)\gamma_3 k_z\left(k_y - ik_z\right), \tag{2.32}$$

$$R_k = \sqrt{3}\left(\frac{\hbar^2}{2m_0}\right)\left[-\gamma_2\left(k_y^2-k_z^2\right)+2i\gamma_3 k_y k_z\right] \tag{2.33}$$

where m_c is the effective mass of conduction band electrons and

$$P_{cv} = \sqrt{\frac{\hbar^2}{2m_0}E_P}, \tag{2.34}$$

is the interband momentum-matrix element

$$P_{cv} = -i\frac{\hbar}{m_0}\left\langle iS\right|p_x\left|X\right\rangle, \tag{2.35}$$

which is related to the Kane parameter. The Pikus-Bir deformation potential

$$A_\epsilon = a_c\left(s_{11}+s_{22}+s_{33}\right) \tag{2.36}$$

and the additional strain dependent quantities

$$P_\epsilon = -a_v\left(s_{11}+s_{22}+s_{33}\right), \tag{2.37}$$

$$Q_\epsilon = -\frac{b}{2}\left(s_{22}+s_{33}-s_{11}\right), \tag{2.38}$$

$$R_\epsilon = \frac{\sqrt{3}}{2}b\left(s_{22}-s_{33}\right) - ids_{23}, \tag{2.39}$$

$$S_\epsilon = -d\left(s_{12}-is_{31}\right). \tag{2.40}$$

are calculated based on the strain components s_{ij}. The rescaled mass of the conduction band electrons is

$$\frac{m_0}{m_c'} = \frac{m_0}{m_c} - E_P\frac{E_g+\frac{2}{3}\Delta_{\mathrm{SO}}}{E_g\left(E_g+\Delta_{\mathrm{SO}}\right)} \tag{2.41}$$

and according to

$$\begin{aligned}
\gamma_1'' &= \gamma_1 - \frac{E_P}{3E_g+\Delta_{\mathrm{SO}}},\\
\gamma_2'' &= \gamma_2 - \frac{1}{2}\frac{E_P}{3E_g+\Delta_{\mathrm{SO}}},\\
\gamma_3'' &= \gamma_3 - \frac{1}{2}\frac{E_P}{3E_g+\Delta_{\mathrm{SO}}},
\end{aligned} \tag{2.42}$$

the Luttinger parameters inserted into the 8×8 Hamiltonian are rescaled. The Luttinger parameters γ_i in the 8×8 Hamiltonian are replaced by the rescaled parameters $\gamma_i \to \gamma_i''$ defined in (2.42). The presented Hamiltonian depends on both in-plane momentums k_y and k_z. However, the solution of the system of equations can be simplified by applying the axial approximation by averaging the properties in the QW plane and introduction of the transverse (in-plane) wave number k_t with $k_\mathrm{t}^2 = k_y^2 + k_z^2$.

Application of the unitary transformation U in combination with the axial approximation transfers $H_{|jm\rangle}^{8\times8}$ into block-diagonal form

$$UH_{|jm\rangle}^{8\times8}U^\dagger = \begin{pmatrix} H_{U,\mathrm{axial}}^{8\times8} & 0 \\ 0 & H_{L,\mathrm{axial}}^{8\times8} \end{pmatrix}, \tag{2.43}$$

which consists of two 4×4 matrices $H_U^{8\times8}$ and $H_L^{8\times8}$. With

$$V_\rho = \frac{1}{\sqrt{6}} P_{cv} k_t \tag{2.44}$$

the upper block of the matrix for the 8×8 Hamiltonian in axial approximation reads [35]

$$H_{U,\mathrm{axial}}^{8\times8} = \begin{pmatrix} E_c + A & -\sqrt{3}V_\rho & -V_\rho + i\sqrt{2}U & -\sqrt{2}V_\rho - iU \\ -\sqrt{3}V_\rho & E_v - P - Q & -|R_k| + i|S_k| & -\sqrt{2}|R_k| - i\frac{1}{\sqrt{2}}|S_k| \\ -V_\rho - i\sqrt{2}U & -|R_k| - i|S_k| & E_v - P + Q & -\sqrt{2}Q - i\sqrt{\frac{3}{2}}|S_k| \\ -\sqrt{2}V_\rho + iU & -\sqrt{2}|R_k| + i\frac{1}{2}|S_k| & -\sqrt{2}Q + i\frac{3}{2}|S_k| & E_v - P - \Delta_\mathrm{SO} \end{pmatrix}, \tag{2.45}$$

and

$$H_{L,\mathrm{axial}}^{8\times8} = \begin{pmatrix} E_c + A & -\sqrt{3}V_\rho & -V_\rho - i\sqrt{2}U & -\sqrt{2}V_\rho + iU \\ -\sqrt{3}V_\rho & E_v - P - Q & -|R_k| - i|S_k| & -\sqrt{2}|R_k| + i\frac{1}{\sqrt{2}}|S_k| \\ -V_\rho + i\sqrt{2}U & -|R_k| + i|S_k| & E_v - P + Q & -\sqrt{2}Q + i\sqrt{\frac{3}{2}}|S_k| \\ -\sqrt{2}V_\rho - iU & -\sqrt{2}|R_k| - i\frac{1}{2}|S_k| & -\sqrt{2}Q - i\frac{3}{2}|S_k| & E_v - P - \Delta_\mathrm{SO} \end{pmatrix}. \tag{2.46}$$

is the lower block of the matrix. In the axial approximation, the angular dependence of the Hamiltonian in the k_y-k_z-plane is neglected. The quantities P and Q depend only on the magnitude of the transverse wavevector k_t, while R and S are functions of the angle $\phi = \arctan(k_z/k_y)$

$$\begin{aligned} R_k &= -\sqrt{3}\left(\frac{\hbar^2}{2m_0}\right)\left[\left(\frac{\gamma_2+\gamma_3}{2}\right)\exp(-2i\phi) + \left(\frac{\gamma_2-\gamma_3}{2}\right)\exp(2i\phi)\right]k_t^2 \\ S_k &= 2\sqrt{3}\left(\frac{\hbar^2}{2m_0}\right)\gamma_3 k_t k_x \exp(-2i\phi)\,. \end{aligned} \tag{2.47}$$

If the assumption $\gamma_1 \approx \gamma_2$ is made the Hamiltonian in block-diagonal form becomes independent of ϕ since both

$$\begin{aligned} |R_k| &= \sqrt{3}\left(\frac{\hbar^2}{2m_0}\right)\cdot\frac{\gamma_2+\gamma_3}{2}\cdot k_t^2 \\ |S_k| &= 2\sqrt{3}\left(\frac{\hbar^2}{2m_0}\right)\gamma_3 k_t k_x \end{aligned} \tag{2.48}$$

are no functions of the in-plane angle of the wavevector.

2.2.2 Envelope Formalism

The formerly presented derivations in the scope of the $k \cdot p$ method for the eigenvalue equation

$$H\psi_n(\vec{x}) = E_n^{(0)}\psi_n(\vec{x}) \tag{2.49}$$

are deducted under the assumption of a bulk lattice with infinite spatial extent and therefore, for a perfect periodic potential $V(\vec{x})$. If the semiconductor structure exhibits an additional non-periodic potential $U(\vec{x})$ the translation symmetry of the Hamilton operator is broken. The perturbation of the potential $U(\vec{x})$ can emerge from various sources: Defects in the crystal lattice, external applied potentials or discontinuities at heterointerfaces. It is assumed that these perturbative potentials vary slowly over spatial regions in the order of magnitude of the lattice constants of the employed semiconductor crystal. The Schrödinger equation

$$\left[H + U(\vec{x})\right]\psi_n(\vec{x}) = E_n\psi_n(\vec{x}) \tag{2.50}$$

is solved by the wave function

$$\psi_n(\vec{x}) = \sum_\mu F_{n,\mu}(\vec{x})u_{\mu,\vec{k}_0}(\vec{x}) \tag{2.51}$$

if the envelope function

$$F_{n,\mu}(\vec{x}) = \frac{e^{i\vec{k}_\perp\cdot\vec{x}_\perp}}{\sqrt{A}}g_n^{(\mu)}(\vec{x}_\parallel), \tag{2.52}$$

is an eigensolution of

$$\sum_\mu \left[H_{\nu\mu}(\vec{k} = -i\nabla) + U(\vec{x})\delta_{\nu\mu}\right]F_{n,\mu}(\vec{x}) = \left(E_n - E_n^{(0)}\right)F_{n,\nu}(\vec{x}), \tag{2.53}$$

where $E_n^{(0)}$ are the energies of the non-disturbed potential and A is a factor chosen to normalize the envelope functions. Due to the broken translational symmetry of the Hamilton operator, the wavevectors $\vec{k}$ are no longer suitable quantum numbers. To solve (2.53), the eigenvalue equation is transferred to position space by introducing the operator $\vec{k} = -i\nabla$. The wavefunctions in (2.51) are superpositions of products of envelope functions and Bloch-functions. In the scope of the applied envelope function approximation (EFA) it is assumed that the same Bloch-functions are employed for all materials present in the heterostructure under investigation, which is valid if the materials are similar to each other. In Eq. (2.52) the envelope function is separated into a factor which depends upon the transverse coordinates $\vec{x}_\perp$ and wavenumbers $\vec{k}_\perp$ and the functions $g_n^{(\mu)}(\vec{x}_\parallel)$. The coordinates $\vec{x}_\parallel$ are those spatial directions, which are parallel to the direction of the translation symmetry that is broken by the potential $U(\vec{x}_\parallel)$. The remaining coordinates $\vec{x}_\perp$ are perpendicular to the directions $\vec{x}_\parallel$. Insertion of the envelope functions (2.52) into (2.53) yields

$$\sum_\mu \left[H_{\nu\mu}(\vec{k}_\perp, \vec{k}_\parallel = -i\nabla_\parallel) + U(\vec{x}_\parallel)\delta_{\nu\mu}\right]g_n^{(\mu)}(\vec{x}_\parallel) = \left(E_n - E_n^{(0)}\right)g_n^{(\nu)}(\vec{x}_\parallel), \tag{2.54}$$

a partial differential equation in the spatial directions $\vec{x}_\parallel$. In case of a QW-structure with the z-axis as the growth direction of the QW layer, this direction has a broken translational symmetry so that the $x_\parallel = x$, $k_\parallel = -i\partial_x$ and $\vec{x}_\perp = (y, z)^{\mathrm{T}}$, $\vec{k}_\parallel = (k_y, k_z)^{\mathrm{T}}$. Exemplary, envelope functions for the QW-structure studied in Section 2.4 are displayed

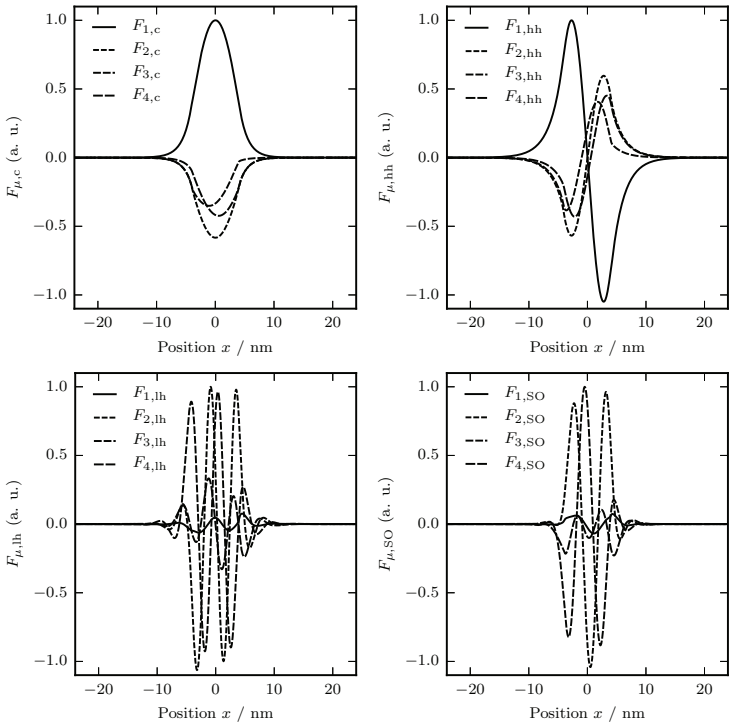

FIGURE 2.1: Calculated envelope functions of the conduction band (top, left), (1^{st}) HH (top, right), (2^{nd}) LH (lower, left) and (3^{rd}) SO (bottom, right) valence band states at wave number $k_t = 1.5\,\mathrm{nm}^{-1}$ for $\mathrm{In_{0.2}Ga_{0.8}As}$ / $\mathrm{Al_{0.2}Ga_{0.8}As}$ / $\mathrm{Al_{0.3}Ga_{0.7}As}$ QW-structure as investigated in Section 2.4 without external strain applied.

in Fig. 2.1 for the case without additional external strain applied.

2.2.3 Hamilton Operator for Nanostructures

According to [31] and [32] the total operator matrix $\hat{H}^{\mu\nu}$ is split up into the matrices $H_{ij}, H^{\mu\nu}_{i\rightarrow}, H^{\mu\nu}_{i\leftarrow}$ for $i,j \leq d$ and $H^{\mu\nu}_0$

$$\begin{aligned}\hat{H}^{\mu\nu} =& -\sum_{i,j=1}^{d} \partial_i H^{\mu\nu}_{ij}(\vec{x})\partial_j \\ & - i\sum_{i=1}^{d}\left[\partial_i H^{\mu\nu}_{i\rightarrow}(\vec{x}) + H^{\mu\nu}_{i\leftarrow}(\vec{x})\partial_i + \sum_{j>d}^{D}\left(\partial_i H^{\mu\nu}_{ij}(\vec{x})k_j + k_j H^{\mu\nu}_{ij}(\vec{x})\partial_i\right)\right] \\ & + i\sum_{i>d}^{D}\left[k_i H^{\mu\nu}_{i\rightarrow}(\vec{x}) + H^{\mu\nu}_{i\leftarrow}(\vec{x})k_i\right] \\ & + \sum_{i,j>d}^{D} k_i H^{\mu\nu}_{ij} k_j + H^{\mu\nu}_0(\vec{x}) \end{aligned} \tag{2.55}$$

with respect to the order and position of the differential operators. The quantization, which is the substitution of the wave number $k_\alpha \rightarrow -i\partial_\alpha, \alpha \leq d$ in the Hamiltonian operator $\hat{H}^{\mu\nu}$ is performed in d of the total D spatial dimensions. The resulting coupled linear 2nd order eigenvalue equation is discretized and solved by the methods presented in Chapter B. For quantum wells, which are heterostructures with one quantized dimension, the Hamiltonian for the 8-band model in axial approximation is

$$\begin{aligned} H^{8\times8}_{U,\text{axial}} =& \frac{\hbar^2}{2m_0}\begin{pmatrix} -s & 0 & 0 & 0 \\ 0 & \gamma_1 - 2\gamma_2 & 0 & 0 \\ 0 & 0 & \gamma_1 + 2\gamma_2 & -2\sqrt{2}\gamma_2 \\ 0 & 0 & -2\sqrt{2}\gamma_2 & \gamma_1 \end{pmatrix}\partial_x^2 \\ &+ \begin{pmatrix} 0 & 0 & \sqrt{\frac{2}{3}}P_0 & -\sqrt{\frac{1}{3}}P_0 \\ 0 & 0 & \frac{\hbar^2}{2m_0}2\sqrt{3}\gamma_3 k_t & -\frac{\hbar^2}{2m_0}\sqrt{6}\gamma_3 k_t \\ -\sqrt{\frac{2}{3}}P_0 & -\frac{\hbar^2}{2m_0}2\sqrt{3}\gamma_3 k_t & 0 & -\frac{\hbar^2}{2m_0}3\sqrt{2}\gamma_3 k_t \\ \sqrt{\frac{1}{3}}P_0 & \frac{\hbar^2}{2m_0}\sqrt{6}\gamma_3 k_t & \frac{\hbar^2}{2m_0}3\sqrt{2}\gamma_3 k_t & 0 \end{pmatrix}\partial_x \\ &+ \begin{pmatrix} E_c + \frac{\hbar^2}{2m_0}sk_t^2 & -\frac{1}{\sqrt{2}}P_0 k_t & -\frac{1}{\sqrt{6}}P_0 k_t & -\frac{1}{\sqrt{3}}P_0 k_t \\ -\frac{1}{\sqrt{2}}P_0 k_t & E_v - \frac{\hbar^2}{2m_0}(\gamma_1+\gamma_2)k_t^2 & -\frac{\hbar^2}{2m_0}\frac{\sqrt{3}}{2}(\gamma_2+\gamma_3)k_t^2 & -\frac{\hbar^2}{2m_0}\sqrt{\frac{3}{2}}(\gamma_2+\gamma_3)k_t^2 \\ -\frac{1}{\sqrt{6}}P_0 k_t & -\frac{\hbar^2}{2m_0}\frac{\sqrt{3}}{2}(\gamma_2+\gamma_3)k_t^2 & E_v - \frac{\hbar^2}{2m_0}(\gamma_1-\gamma_2)k_t^2 & -\frac{\hbar^2}{2m_0}\sqrt{2}\gamma_2 k_t^2 \\ -\frac{1}{\sqrt{3}}P_0 k_t & -\frac{\hbar^2}{2m_0}\sqrt{\frac{3}{2}}(\gamma_2+\gamma_3)k_t^2 & -\frac{\hbar^2}{2m_0}\sqrt{2}\gamma_2 k_t^2 & E_v - \Delta - \frac{\hbar^2}{2m_0}\gamma_1 k_t^2 \end{pmatrix}. \end{aligned} \tag{2.56}$$

where the matrix operators are separated and sorted with respect to the order of the derivatives ∂_x along the quantized direction. To derive a band structure including a conduction band in the scope of the 4- and 6-band theory, the conduction band is calculated with a 1-band method in a calculation separate from the coupled valence band problem. Schrödinger's equation for the $k\cdot p$ method (2.6)

$$\left(-\frac{\hbar^2}{2m^*}\nabla^2 + V_c(\vec{x})\right)\psi(\vec{x}) = E\psi(\vec{x}). \tag{2.57}$$

is employed for one class A conduction band, and all other bands are treated as class B bands. Their influence reflects in the effective conduction band electron mass m^*. The terms of the Hamilton operator (2.55) are

$$H_{ij}(\vec{x}) = -\left(\frac{1}{m^*}\right)_{ij}, \tag{2.58}$$

$$H_0(\vec{x}) = V_c(\vec{x}) \tag{2.59}$$

and for a one-dimensional nanostructure quantized along the z-direction

$$\tilde{H}_{33}(\vec{x}) = -\frac{\hbar^2}{2m_c}, \tag{2.60}$$

$$\tilde{H}_0(\vec{x}) = \frac{\hbar^2 k_t^2}{2m_c} + V_c(\vec{x}) + \delta E_c. \tag{2.61}$$

are the non-vanishing coefficients of the operator matrix. In contrast to the 1-band theory, which results in a parabolic conduction band, the coupling of the conduction band states to valence band states in the 8-band theory leads to lower curvature of the conduction band. Altering the conduction band dispersion leads to changes in the resulting optical gain calculated from the band structure [31, 32].

2.3 Optical Properties of Semiconductors

The optical properties of a semiconductor nanostructure, which are gain [1] g and refractive index change δn dependent on temperature, the frequency of the interacting optical field and the carrier density (density of electrons and holes) are calculated based on the Semiconductor Bloch Equations (SBEs). The electric susceptibility of a semiconductor is given by [36, 37, 38]

$$\begin{aligned}
\chi &= \chi' + i\chi'' \\
&= n_{\mathrm{bg}}^2 - 1 - \frac{1}{\varepsilon_0 \hbar \gamma V} \sum_{\mu,\nu} \sum_{\vec{k}} |\mu_{\vec{k}}|^2 \left(f_{e,\mu,\vec{k}} + f_{h,\nu,\vec{k}} - 1 \right) L\left(\omega_{\vec{k}} - \omega\right) \left(i + \frac{\omega_{\vec{k}} - \omega}{\gamma} \right) \\
&= n_{\mathrm{bg}}^2 - 1 - \frac{1}{\varepsilon_0 \hbar \gamma V} \sum_{\mu,\nu} \sum_{\vec{k}} |\mu_{\vec{k}}|^2 \left(f_{e,\mu,\vec{k}} + f_{h,\nu,\vec{k}} - 1 \right) L\left(\omega_{\vec{k}} - \omega\right) \left(\frac{\omega_{\vec{k}} - \omega}{\gamma} \right) \\
&\quad -i \frac{1}{\varepsilon_0 \hbar \gamma V} \sum_{\mu,\nu} \sum_{\vec{k}} |\mu_{\vec{k}}|^2 \left(f_{e,\mu,\vec{k}} + f_{h,\nu,\vec{k}} - 1 \right) L\left(\omega_{\vec{k}} - \omega\right),
\end{aligned} \tag{2.62}$$

with summation over all wavevectors $\vec{k}$ and related angular frequency $\omega_{\vec{k}}$ and over $\mu = 1, \ldots, M_{\mathrm{c}}$ and $\nu = 1, \ldots, M_{\mathrm{v}}$ the number of conduction N_{c} and valence bands N_{v}. Gain broadening is modeled with a Lorentzian lineshape function $L(\omega)$, $\mu_{\vec{k}}$ are the dipole-matrix elements, n_{bg} is the frequency independent *background* index of refraction, V the spatial volume in m^3, γ a dephasing parameter in rads^{-1}. Additionally, the Fermi-Dirac

[1] In the scope of this thesis the term *gain* for g refers to the *amplitude gain* - the change of the magnitude of the electric field amplitude along the propagation direction. Several authors use the term *gain* for the *material gain* $G = 2g$, which is the change in optical intensity along the propagation direction

functions are evaluated for the electrons and holes

$$f_{e/h,\mu,\vec{k}} = \frac{1}{1+\exp\left(\frac{E_{c/v,\mu,\vec{k}}-E_{\mathrm{F},n/p}}{k_{\mathrm{B}}T}\right)} \tag{2.63}$$

with the Fermi energy for electron or holes $E_{\mathrm{F},n/p}$ and band structure $E_{c/v,\mu/\nu,\vec{k}}$. The amplitude gain is defined by the complex part of the susceptibility

$$g = -\frac{k_0}{2n_{\mathrm{bg}}}\chi'', \tag{2.64}$$

where $k_0 = \frac{\omega}{c_0}$ is the vacuum wavenumber. The deviation from the background refractive index due to inter-band transitions is

$$\delta n^{\mathrm{inter}} = \frac{1}{2n_{\mathrm{bg}}}\left(\chi' + 1 - n_{\mathrm{bg}}^2\right). \tag{2.65}$$

If one or multiple dimensions of the structure are quantized, and energy bands are not approximated by effective parabolic bands to evaluate the expressions for the gain, spontaneous emission and refractive index change the energy dispersion for each band, and the dipole-matrix elements $\mu_{\vec{k}}$ have to be known to evaluate the optical susceptibility. Alongside with the calculation of the eigenvalues of the $k\cdot p$-Schrödinger equation, which give the band energies for different transverse wave numbers k_{t}, the dipole transitions between conduction and valence band states are calculated by evaluation of the corresponding electron wave functions. The envelope functions $g_m^{(i)}$ are used to calculate the squared magnitudes (since only they enter into the expression for the gain evaluation) of the Transverse-Electric (TE) and Transverse-Magnetic (TM) dipole-matrix elements $|\mu_{mn}^{\mathrm{TE}}|^2$ and $|\mu_{mn}^{\mathrm{TM}}|^2$ according to

$$\begin{aligned}
|\mu_{mn}^{\mathrm{TE}}|^2 &= \frac{|\mu_{\mathrm{Bulk}}^{\mathrm{TE}}|^2}{12}\left|\langle g_m^{(1)}|\sqrt{3}g_n^{(2)} + g_n^{(3)} + \sqrt{2}g_n^{(4)}\rangle + \langle\sqrt{3}g_m^{(2)} + g_m^{(3)} + \sqrt{2}g_m^{(4)}|g_n^{(1)}\rangle\right|^2, \\
|\mu_{mn}^{\mathrm{TM}}|^2 &= \frac{|\mu_{\mathrm{Bulk}}^{\mathrm{TM}}|^2}{3}\left|\langle g_m^{(1)}|\sqrt{2}g_n^{(3)} - g_n^{(4)}\rangle - \langle\sqrt{2}g_m^{(3)} - g_m^{(4)}|g_n^{(1)}\rangle\right|^2
\end{aligned} \tag{2.66}$$

for the transition between bands m and n for the (upper) U-block in the 8-band theory, see [35, 32]. In the software package *SEMSIS* gain and refractive index change can be calculated based on three different models:

1. Free-carrier theory (no many-body interactions),
2. screened Hartree-Fock (inclusion of Hartree-Fock contributions),
3. time evolution of microscopic polarizations of SBEs,

which distinguish themselves in the treatment of many-body effects. The Coulomb effects that are explicitly given are called Hartree-Fock contributions. Correlation contributions from carrier-carrier scattering (electron-phonon scattering also contributes and dominates at low inversion levels) yield the correct (homogenous) lineshape broadening and corrections to the Hartree-Fock contributions due to plasma screening effects. Details on the implementation and derivation of the models including many-body effects are given in [38]. The formulas presented in the following sections are valid for the evaluation of the free-carrier gain [36]. In the scope of the model of free-carriers, many-body

effects and Coulomb interactions are neglected, and quasi-equilibrium distributions are assumed for electrons and holes since the inter-band relaxation times are high compared to the intra-band relaxation times. Calculation of the gain with the free-carrier theory is straightforward and relatively simple regarding implementation compared to theories including higher order contributions. Although the gain spectra calculated with more advances theories can show significant differences for the free-carrier theory trends and magnitudes for the QW structure can be analyzed with the latter.

The coefficient of spontaneous emission is [37, 39]

$$\tilde{r}_{\mathrm{sp}}(\omega) = \frac{k_0}{2n_{\mathrm{bg}}\varepsilon_0\hbar\gamma V}\sum_{m,n}\sum_{\vec{k}}|\mu_{\vec{k}}|^2 f_{e,m,\vec{k}} f_{h,n,\vec{k}} L\left(\omega_{\vec{k}}-\omega\right) \tag{2.67}$$

Prior to multiplication with the optical mode density, the spontaneous emission coefficient $\tilde{r}_{\mathrm{sp}}$ has the unit m^{-1}. To evaluate the spontaneous emission spectrum per volume per time per energy $r_{\mathrm{sp}} = \tilde{r}_{\mathrm{sp}}\rho_{\mathrm{opt}}$ in units $\mathrm{J}^{-1}\mathrm{m}^{-3}\mathrm{s}^{-1}$, (2.67) is multiplied with the optical mode density [40, 41]

$$\rho_{\mathrm{opt}} = \frac{n_{\mathrm{bg}}^2(\hbar\omega)^2}{\pi^2\hbar^3 c_0^2}. \tag{2.68}$$

The total spontaneous recombination rate per unit volume and time $\mathrm{m}^{-3}\mathrm{s}^{-1}$ is calculated by integration over the frequency (spectral) space

$$R_{\mathrm{sp}} = \hbar\int_0^\infty r_{\mathrm{sp}}(\omega)\,\mathrm{d}\omega. \tag{2.69}$$

The Fermi energies for electrons and holes are connected to the respective carrier density and temperature so that also R_{sp} and r_{sp} are functions of carrier densities and temperature.

In addition to *inter-band* transitions leading to absorption or gain by stimulated processes in the QW, which are included in (2.62), free-carrier absorption occurs due to *intra-subband* transitions. A free-carrier (electron or hole) in the conduction or valence bands absorbs a photon and is transferred to a higher energy level within the same band. The absorption coefficient increases with carrier density and wavelength. Free-carrier absorption is determined by the multiplication of the cross-section with the carrier density. It can be separated into contributions from unconfined (bulk) electrons n_{3d} and holes p_{3d} in the waveguide and confined electrons $n_{2\mathrm{d}}$ and holes $p_{2\mathrm{d}}$ in the QW

$$\begin{aligned}\alpha_{\mathrm{fc}} &= \sigma_n n + \sigma_p p \\ &= \alpha_{\mathrm{fc,wg}} + \alpha_{\mathrm{fc,qw}} \\ &= \sigma_n n_{3d} + \sigma_p p_{3d} + \sigma_{n,\mathrm{qw}} n_{2\mathrm{d}} + \sigma_{p,\mathrm{qw}} p_{2\mathrm{d}}\end{aligned} \tag{2.70}$$

Free-carrier absorption cross-sections are approximated with Drude's model [42]

$$\sigma_n(\lambda, \varepsilon_{\mathrm{r}}, m_n, \mu_n) = \frac{\lambda^2 q_{\mathrm{el}}^3}{4\pi^2 c_0^3\sqrt{\varepsilon_{\mathrm{r}}}\varepsilon_0 m_n^2\mu_n}, \tag{2.71}$$

$$\sigma_p(\lambda, \varepsilon_{\mathrm{r}}, m_p, \mu_p) = \frac{\lambda^2 q_{\mathrm{el}}^3}{4\pi^2 c_0^3\sqrt{\varepsilon_{\mathrm{r}}}\varepsilon_0 m_p^2\mu_p}. \tag{2.72}$$

The cross-sections depend on wavelength λ, permittivity ε_{r}, effective masses $m_{n/p}$ and mobilities $\mu_{n/p}$. The cross-sections can either be approximated by constants throughout

the domain with values for GaAs reported in the literature [43, 44] of $\sigma_n = 3 \cdot 10^{-22}\,\mathrm{m}^2$ and $\sigma_p = 7 \cdot 10^{-22}\,\mathrm{m}^2$ or the expressions in Eq. (2.72) are evaluated with spatial resolved material parameters. Variations in semiconductor alloy composition and spatial profile of the vertical mode $|E|^2$ influence the modal losses

$$\begin{aligned}\alpha_{\mathrm{fc,m}} &= \alpha_{\mathrm{fc,m,wg}} + \alpha_{\mathrm{fc,m,qw}} \\ &= \frac{\int_{\Omega_\mathrm{v}} (\sigma_n n_{3d} + \sigma_p p_{3d})\,|E|^2\,\mathrm{d}x}{\int_{\Omega_\mathrm{v}} |E|^2\,\mathrm{d}x} + \Gamma\,(\sigma_{\mathrm{qw},n} n_{2\mathrm{d}} + \sigma_{\mathrm{qw},p} p_{2\mathrm{d}})\end{aligned} \tag{2.73}$$

which obey contributions from the unconfined carriers in the waveguide and confined carriers in the QW. The optical confinement Γ accounts for the overlap of the vertical mode with the QW. Band-to-band absorption in the AlGaAs waveguide layers is not included since contributions should be small due to the relatively large energy gap compared to the photon energy. Kramers-Kronig relation links real and imaginary part of the permittivity (refractive index and gain). Since there is absorption due to free carriers (Drude model) based on the Kramers-Kronig relation, there is also a refractive index change [45]

$$\delta n_{\mathrm{fc}}(E) = \frac{2c\hbar}{q_{\mathrm{el}}^2} P \int_0^\infty \frac{\delta\alpha_{\mathrm{fc}}(E')}{E' - E}\,\mathrm{d}E' \tag{2.74}$$

associated with the free-carrier absorption. Here, P is the principal value of the integral and $\delta\alpha_{\mathrm{free}}$ is the change in free-carrier absorption. The coefficient is related to the refractive index change induced by carrier density N via [39, 46]

$$\delta n_{\mathrm{fc}} = \frac{\mathrm{d}n_{\mathrm{fc}}}{\mathrm{d}N} N = \alpha_{\mathrm{fc}} N = -\frac{q_{\mathrm{el}}^2}{2\varepsilon_0 \sqrt{\varepsilon_r} m_{\mathrm{c/v}} \omega^2} N. \tag{2.75}$$

The total carrier-induced refractive index change is the sum of contributions from unconfined (free) carriers in the bulk material and from inter-band transitions and intra-band transitions of confined carriers in the QW [47]

$$\begin{aligned}\delta n_N &= \delta n_{\mathrm{inter}} + \delta n_{\mathrm{intra}} \\ &= \delta n_{\mathrm{inter}} + \delta n_{\mathrm{inter-sub}} + \delta n_{\mathrm{intra-sub}} \\ &\approx \delta n_{\mathrm{inter}} + \delta n_{\mathrm{inter-sub}} + \delta n_{\mathrm{fc}} \\ &= \delta n_{\mathrm{inter,2d}} + \delta n_{\mathrm{inter-sub,2d}} + \delta n_{\mathrm{fc,2d}} + \delta n_{\mathrm{inter,3d}} + \delta n_{\mathrm{fc,3d}}.\end{aligned} \tag{2.76}$$

The intra-band contributions split up into two contributions: inter-subband transitions between band number i and j for $i \neq j$, which are transitions between different subbands and intra-subband transitions for $i = j$, which are transitions within the one subband. For the TE-modes the intra-subband transitions can be transferred to the classical Drude formula and therefore be expressed in terms of free carriers. For parabolic band approximation for TE the inter-subband components and for TM the intra-subband components vanish [47]. Thus, $\delta n_{\mathrm{inter-sub,3d}} \approx 0$ is neglected, since two parabolic bands are assumed for the bulk semiconductors. The free-carrier contributions occur for both the QW and the surrounding waveguide layers. For the current state of the model also $\delta n_{\mathrm{inter-sub,2d}}$ is neglected, although there are subbands present. For short wavelengths this assumption is reasonable [47]. The modal refractive index change

$$\delta n_{N,\mathrm{m}} = \delta n_{\mathrm{fc,3d,m}} + \Gamma(\delta n_{\mathrm{inter,2d}} + \delta n_{\mathrm{fc,2d}}), \tag{2.77}$$

accounts for contributions from the QW and surrounding waveguide. Inter-band transitions in the waveguide are neglected $\delta n_{\mathrm{inter,3d,m}} \approx 0$ since for the investigated InGaAs QW in AlGaAs waveguide the photon energy is well below the bandgap energy of the waveguide.

2.3.1 Three-Dimensional Structures

The Density Of States (DOS) for bulk semiconductors is determined by summation over all states including spins σ and energy bands m [36]

$$n/p_{\mathrm{3d}} = \frac{1}{2\pi^2} \sum_{m} \sum_{\sigma=\uparrow,\downarrow} \int_0^\infty k^2 f_{e/h,m}(k)\,\mathrm{d}k, \tag{2.78}$$

where the Fermi-Dirac functions are evaluated for the respective carrier species

$$f_{e/h,m}(k) = \frac{1}{1+\exp\left(\frac{E_{c/v,m}(k)-E_{\mathrm{F},n/p}}{k_{\mathrm{B}}T}\right)} \tag{2.79}$$

with the Fermi energy for electron or holes $E_{\mathrm{F},n/p}$ and band structure $E_{\mathrm{c/v},m}(k)$ as a function of the wavenumber k. It is assumed that the energy dispersion relation is spherically symmetric in the wavenumber k. For a three dimensional structure (bulk material) the gain is

$$g_{3d}\,(\omega) = \frac{\omega\gamma}{\hbar c_0 \varepsilon_0 n_{\mathrm{bg}} 2\pi^2} \sum_{\eta=\uparrow,\downarrow} \sum_{\sigma=U,L} \sum_{ij} \int_0^\infty k^2 |\mu_{ij}^{\eta\sigma}(k)|^2 \frac{f_{e,i}(k)+f_{h,j}(k)-1}{\left(\frac{E_{\mathrm{c},i}(k)+E_{\mathrm{v},j}(k)}{\hbar}-\omega\right)^2+\gamma^2}\,\mathrm{d}k, \tag{2.80}$$

with the dipole-matrix elements $\mu_{ij}^{\eta\sigma}(k)$ as functions of the wavenumber. Here, η labels the two spin states and σ labels the two blocks, the (upper) U-block and (lower) L-block of the respective Hamiltonian after application of the axial approximation for the 8-band theory, see [31] and [32]. The spontaneous recombination spectrum is

$$r_{\mathrm{sp,3d}}\,(\omega) = \frac{\omega^3 n_{\mathrm{bg}}\gamma}{2\hbar^2 c_0^3 \varepsilon_0 \pi^4} \sum_{\eta=\uparrow,\downarrow} \sum_{\sigma=U,L} \sum_{ij} \int_0^\infty k^2 |\mu_{ij}^{\eta\sigma}(k)|^2 \frac{f_{e,i}(k) f_{h,j}(k)}{\left(\frac{E_{\mathrm{c},i}(k)+E_{\mathrm{v},j}(k)}{\hbar}-\omega\right)^2+\gamma^2}\,\mathrm{d}k, \tag{2.81}$$

and the carrier-induced refractive index change is

$$\delta n_{\mathrm{inter,3d}}\,(\omega) = -\frac{1}{2\pi^2\hbar\varepsilon_0 n_{\mathrm{bg}}} \sum_{\eta=\uparrow,\downarrow} \sum_{\sigma=U,L} \sum_{ij} \int_0^\infty k^2 |\mu_{ij}^{\eta\sigma}(k)|^2 \times \frac{(f_{e,i}(k)+f_{h,j}(k)-1)\left(\frac{E_{\mathrm{c},i}(k)+E_{\mathrm{v},j}(k)}{\hbar}-\omega\right)}{\left(\frac{E_{\mathrm{c},i}(k)+E_{\mathrm{v},j}(k)}{\hbar}-\omega\right)^2+\gamma^2}\,\mathrm{d}k \tag{2.82}$$

for bulk material.

2.3.2 Two-Dimensional Structures

For a two-dimensional quantum gas with confined states in the z-direction the density of carriers (number of states per volume V) is

$$\begin{aligned} n/p_{2d} &= \frac{1}{V}\sum_{\sigma=\uparrow,\downarrow}\sum_{m}\sum_{k_x}\sum_{k_y} f_{e/h,m,\vec{k}_t} \\ &= \frac{1}{2\pi d_{\mathrm{qw}}}\sum_{\sigma=\uparrow,\downarrow}\sum_{m}\int k_t f_{e/h,m}(k_t)\,\mathrm{d}k_t. \end{aligned} \tag{2.83}$$

where $\vec{k}_t = (k_x, k_y)$ is the transverse wavevector with $k_t = |\vec{k}_t|^2$ and the sum over σ accounts for spin degeneracy of the states. The DOS (per energy) in units $\mathrm{m}^{-3}\mathrm{J}^{-1}$ is

$$\rho_{n/p,2d}(E) = \frac{1}{\pi d_{\mathrm{qw}}}\sum_{m} H(E \mp E_{\mathrm{c/v},m}(0))k_t(E)\frac{\partial k_t}{\partial E_{\mathrm{c/v},m}}(E), \tag{2.84}$$

with the Heaviside function $H(x)$, where $H(x) = 1$ for $x > 0$ and $H(x) = 0$ else. The free-carrier gain for a two-dimensional quantum gas (confined states in one direction) is calculated with the help of

$$g_{2d}(\omega) = \frac{\omega\gamma}{\hbar c_0\varepsilon_0 n_{bg} 2\pi d}\sum_{\eta=\uparrow,\downarrow}\sum_{\sigma=U,L}\sum_{ij}\int_0^\infty k|\mu_{ij}^{\eta\sigma}(k)|^2\frac{f_{e,i}(k)+f_{h,j}(k)-1}{\left(\frac{E_{\mathrm{c},i}(k)+E_{\mathrm{v},j}(k)}{\hbar}-\omega\right)^2+\gamma^2}\,\mathrm{d}k. \tag{2.85}$$

Analogue to the three-dimensional case, η labels the two spin states and σ labels the two blocks, the (upper) U-block and (lower) L-block of the respective Hamiltonian after application of the axial approximation for the 8-band theory, see [31] and [32]. The spontaneous recombination spectrum is

$$r_{\mathrm{sp,2d}}(\omega) = \frac{\omega^3 n_{bg}\gamma}{2\hbar^2 c_0^3\varepsilon_0\pi^3 d}\sum_{\eta=\uparrow,\downarrow}\sum_{\sigma=U,L}\sum_{ij}\int_0^\infty k|\mu_{ij}^{\eta\sigma}(k)|^2\frac{f_{e,i}(k)f_{h,j}(k)}{\left(\frac{E_{\mathrm{c},i}(k)+E_{\mathrm{v},j}(k)}{\hbar}-\omega\right)^2+\gamma^2}\,\mathrm{d}k, \tag{2.86}$$

and the carrier-induced refractive index change is

$$\begin{aligned} \delta n_{\mathrm{inter,2d}}(\omega) = -\frac{1}{\hbar\varepsilon_0 n_{bg} 2\pi d}\sum_{\eta=\uparrow,\downarrow}\sum_{\sigma=U,L}\sum_{ij}\int_0^\infty k|\mu_{ij}^{\eta\sigma}(k)|^2\times \\ \frac{(f_{e,i}(k)+f_{h,j}(k)-1)\left(\frac{E_{\mathrm{c},i}(k)+E_{\mathrm{v},j}(k)}{\hbar}-\omega\right)}{\left(\frac{E_{\mathrm{c},i}(k)+E_{\mathrm{v},j}(k)}{\hbar}-\omega\right)^2+\gamma^2}\,\mathrm{d}k. \end{aligned} \tag{2.87}$$

The linewidth enhancement factor is defined by

$$\alpha_{\mathrm{H}} = \frac{\frac{\partial\chi'}{\partial n}}{\frac{\partial\chi''}{\partial n}}. \tag{2.88}$$

It is a measure for carrier-induced increase of emission linewidth and for carrier-induced lateral filamentation [48]. Carrier-induced lateral refractive index variations are, for example, observed in Figs. 8.1 and 8.2 in Chapter 8.

2.4 Influence of External Stress on Gain Characteristics of Strained Quantum Well Structures

Due to mechanical strain s_{ij}, which acts on the semiconductor lattice, the band edges are shifted. The strain component due to lattice mismatch perpendicular to the growth direction of the epitaxial structure (also called the in-plane strain) is

$$s_\perp = \frac{a_{\mathrm{lc},0} - a_{\mathrm{lc}}}{a_{\mathrm{lc}}}, \tag{2.89}$$

and the strain parallel to the growth direction is

$$s_\parallel = -2\frac{C_{12}}{C_{11}} s_\perp. \tag{2.90}$$

The strain due to lattice mismatch is called intrinsic strain in the following. Note that

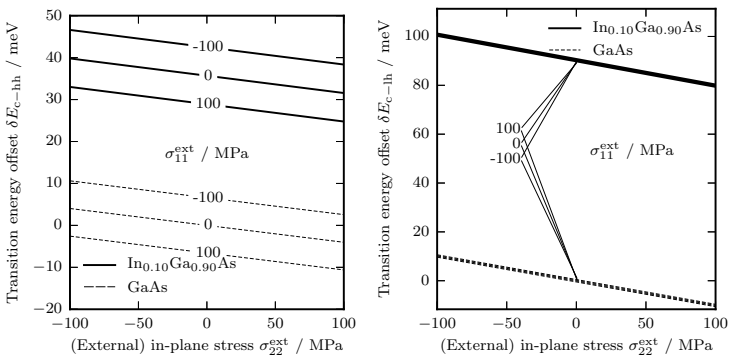

FIGURE 2.2: Perturbation of transition energies for conduction band to heavy-hole transitions (left) and conduction band to light hole transitions (right) dependent on external stress for the materials $In_{0.10}Ga_{0.90}As$ and GaAs.

the lattice constant a_{lc} and material parameters such as stiffness constants C_{11}, C_{12} and C_{44} can potentially vary spatially if the structure consists of different materials or contains graded sections. The reference lattice constant $a_{\mathrm{lc},0}$ is the lattice constant of the substrate. Additional to the intrinsic strain due to lattice mismatch, the semiconductor device can be under thermo-mechanical strain due to heating of the device and external mechanical strain due to packaging or deposition of metallization layers. The potentials and strain components are marked by the superscript *int* to associate the contributions to the intrinsic strain due to lattice mismatch and the superscript *ext* is used for the contributions due to externally applied stress [2]

$$s_{11} = s_{11}^{\mathrm{ext}} + s_{11}^{\mathrm{int}} = s_{11}^{\mathrm{ext}} - 2\frac{C_{12}}{C_{11}} s_\perp, \tag{2.91}$$

$$s_{22} = s_{33} = s_{22}^{\mathrm{ext}} + s_{22}^{\mathrm{int}} = s_{33}^{\mathrm{ext}} + s_{33}^{\mathrm{int}} = s_{22}^{\mathrm{ext}} + s_\perp. \tag{2.92}$$

[2]The signs of the intrinsic stress components are inverted when the (initial) intrinsic strain is utilized to calculate the initial stress which acts on the structure due to a compressive or tensile quantum well.

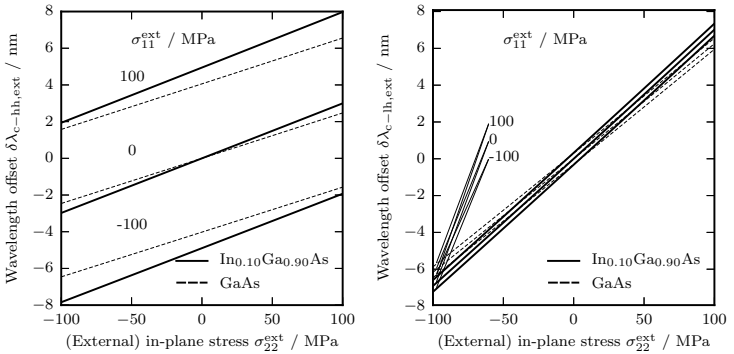

FIGURE 2.3: Change of wavelength for conduction band to heavy-hole transitions (left) and conduction band to light hole transitions (right) dependent on external stress for the materials $In_{0.10}Ga_{0.90}As$ and GaAs.

To study the effect of external stress on the band edges Hook's law is inverted to find the strain components dependent on the stress components for the biaxial case $s_{22}^{\text{ext}} = s_{33}^{\text{ext}}$

$$s_{11}^{\text{ext}} = \frac{\sigma_{22}^{\text{ext}}}{C_{12}} - \frac{(C_{11}+C_{12})\left(\sigma_{11}^{\text{ext}} - \frac{C_{11}}{C_{12}}\sigma_{22}^{\text{ext}}\right)}{2C_{12}^2 - C_{11}(C_{11}+C_{12})}, \tag{2.93}$$

$$s_{22}^{\text{ext}} = \frac{C_{12}\sigma_{11}^{\text{ext}} - C_{11}\sigma_{22}^{\text{ext}}}{2C_{12}^2 - C_{11}(C_{11}+C_{12})}. \tag{2.94}$$

The (total) deformation potentials are

$$A_\varepsilon = A_\varepsilon^{\text{ext}} + A_\varepsilon^{\text{int}} = a_c(s_{11}+s_{22}+s_{33}), \tag{2.95}$$

$$P_\varepsilon = P_\varepsilon^{\text{ext}} + P_\varepsilon^{\text{int}} = -a_v(s_{11}+s_{22}+s_{33}), \tag{2.96}$$

$$Q_\varepsilon = Q_\varepsilon^{\text{ext}} + Q_\varepsilon^{\text{int}} = -\frac{b}{2}(-2s_{11}+s_{22}+s_{33}). \tag{2.97}$$

For the simplified biaxial strain model with an infinite extension of the quantum well the intrinsic energy offsets become

$$A_\varepsilon^{\text{int}} = 2a_c\left(1 - \frac{C_{12}}{C_{11}}\right)s_\perp, \tag{2.98}$$

$$P_\varepsilon^{\text{int}} = -2a_v\left(1 - \frac{C_{12}}{C_{11}}\right)s_\perp, \tag{2.99}$$

$$Q_\varepsilon^{\text{int}} = -b\left(1 + 2\frac{C_{12}}{C_{11}}\right)s_\perp. \tag{2.100}$$

Finally, the band edges are shifted according to

$$\delta E_{\text{c}} = A_\varepsilon, \tag{2.101}$$

$$\delta E_{\text{hh}} = -P_\varepsilon - Q_\varepsilon, \tag{2.102}$$

$$\delta E_{\text{lh}} = -P_\varepsilon + Q_\varepsilon. \tag{2.103}$$

Note that for InGaAs, AlGaAs, and GaAs the deformation potentials are $a_c < 0$, $a_v > 0$, $b < 0$ and for compressively strained InGaAs QWs the following relations hold

$$s_\parallel > 0, \quad s_\perp < 0, \quad A_\varepsilon > 0, \quad P_\varepsilon > 0, \quad Q_\varepsilon < 0. \tag{2.104}$$

Consequently, compressive strain leads to a shift of the conduction band edge to higher energies. The valence band edges shift to lower energies to due P_ε and the HH and LH energies are split by $2Q_\varepsilon$, compare to (2.103). The offsets in transition energy from conduction to LH and HH bands and change in the corresponding wavelength due to externally applied stress for $In_{0.10}Ga_{0.90}As$ on a GaAs substrate are plotted in Fig. 2.2 and Fig. 2.3, respectively.

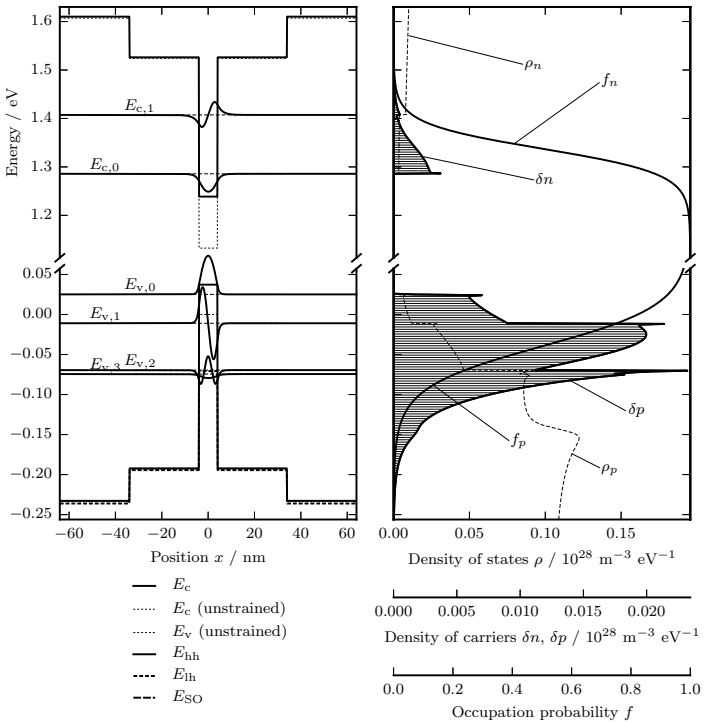

FIGURE 2.4: Band edges, zone-center ($k_t = 0$) wavefunctions, density of states, density of carriers and Fermi-distributions plotted for a carrier density of $n_{(2)} = 3 \cdot 10^{24}\,\mathrm{m}^{-3}$ for an $In_{0.2}Ga_{0.8}As$ / $Al_{0.2}Ga_{0.8}As$ / $Al_{0.3}Ga_{0.7}As$ QW-structure without external strain applied $s_{11}^{\mathrm{ext}} = s_{22}^{\mathrm{ext}} = s_{33}^{\mathrm{ext}} = 0$. The conduction band offsets due to strain in the barriers is $\delta E_{c,b} = 2.07\,\mathrm{meV}$ and $\delta E_{c,qw} = 106\,\mathrm{meV}$ in the QW, heavy-holes band offsets due to strain $\delta E_{hh,b} = 0.66\,\mathrm{meV}$, $\delta E_{hh,qw} = 37.28\,\mathrm{meV}$, light-holes band offsets due to strain $\delta E_{lh,qw} = -70.73\,\mathrm{meV}$ and $\delta E_{lh,b} = -1.52\,\mathrm{meV}$. The bandgap energy is $E_{g,qw} = 1.132\,\mathrm{eV}$ in QW and $E_{g,b} = 1.717\,\mathrm{eV}$ in the barriers.

The external strain adds up to the intrinsic strain (due to lattice mismatch) in the QW and influences the band structure of the active region. To study this influence the band structure (Fig. 2.5), gain characteristics (Fig. 2.6), carrier-induced refractive index

change (Fig. 2.8) are calculated for a Separate Confinement Heterostructure (SCH) with an introduction of additional external strain. The structure under study is a single 8 nm InGaAs QW with InAs concentration of $x_{\mathrm{qw}} = 0.2$ surrounded by AlGaAs barriers with AlAs concentration of $x_{\mathrm{b}} = 0.2$ on a GaAs substrate. The intrinsic strain in growth direction in the QW amounts to $s_{\mathrm{qw},11} = 1.343\,\%$, the strain in growth direction in the barriers to $s_{\mathrm{b},11} = 0.025\,\%$ and the strain perpendicular to the growth direction in the QW is $s_{\mathrm{qw},22} = -1.413\,\%$ and $s_{\mathrm{b},22} = -0.028\,\%$ in the barriers. The band edges for the SCH with and without intrinsic strain and (dominant) zone-center electron wavefunctions together with the resulting DOS are displayed in Fig. 2.4. The valence band edge without intrinsic or external strain is aligned with the origin of the energy scale. The band structure is calculated for transverse wavenumbers up to $1.8\,\mathrm{nm}^{-1}$ for two conduction and four valence bands, see Fig. 2.5. Compressive (intrinsic) strain leads to an increased gain in TE emission, see the gain spectrum in Fig. 2.6. For the investigation, the external in-plane strain $s_{22} = s_{33}$ is varied from $7 \cdot 10^{-4}$ to $-7 \cdot 10^{-4}$ and the out-of-plane (in growth direction) component s_{11} is varied from $-2.26 \cdot 10^{-4}$ to $2.26 \cdot 10^{-4}$. These strains correspond to external stress in the lateral direction of approximately $\pm 55.56\,\mathrm{MPa}$ and no additional stress in the vertical direction (force-free). The stiffness constants for $\mathrm{In_{0.2}Ga_{0.8}As}$ are $C_{11} = 114.3\,\mathrm{GPa}$, $C_{12} = 54.3\,\mathrm{GPa}$ and $C_{44} = 55.9\,\mathrm{GPa}$, see material values in Tb. A.6. A homogeneous spatial profile for the external strain in the active region and the case of biaxial strain $s_{22} = s_{33}$ is assumed. The external strain shifts the peak-gain wavelength (Fig. 2.7) and changes the ratio between TE and TM gain. The results are summarized in Tb. 2.1. Gain coefficients

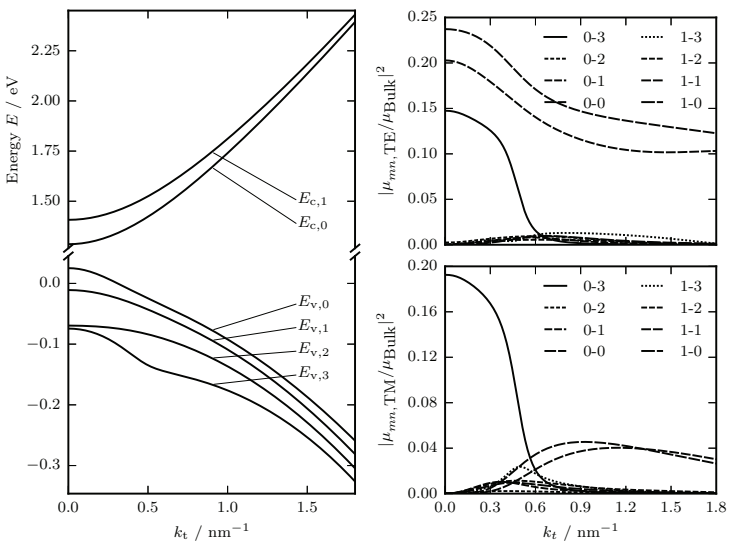

FIGURE 2.5: Band structure (left) and dipole-elements (right) for an $\mathrm{In_{0.2}Ga_{0.8}As}$ / $\mathrm{Al_{0.2}Ga_{0.8}As}$ / $\mathrm{Al_{0.3}Ga_{0.7}As}$ QW-structure without external strain applied $s_{11}^{\mathrm{ext}} = s_{22}^{\mathrm{ext}} = s_{33}^{\mathrm{ext}} = 0$.

and transparency carrier density are determined based on a fit of the gain dependence on carrier density at the peak-gain wavelength, see Fig. 2.9 for the structure with intrinsic

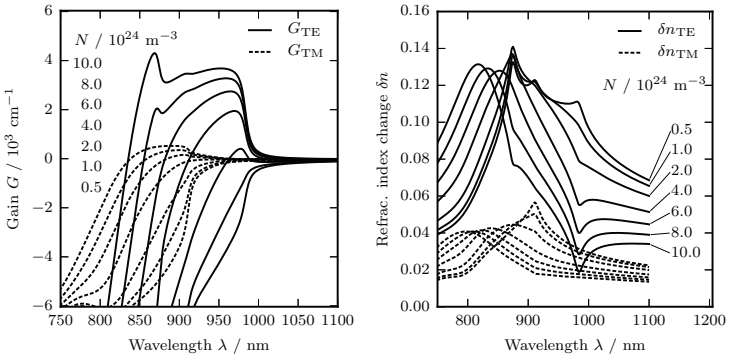

FIGURE 2.6: Gain spectrum (left) and refractive index change (right) over wavelength for multiple carrier densities calculated by free-carrier theory for $In_{0.2}Ga_{0.8}As$ / $Al_{0.2}Ga_{0.8}As$ / $Al_{0.3}Ga_{0.7}As$ QW-structure without external strain applied.

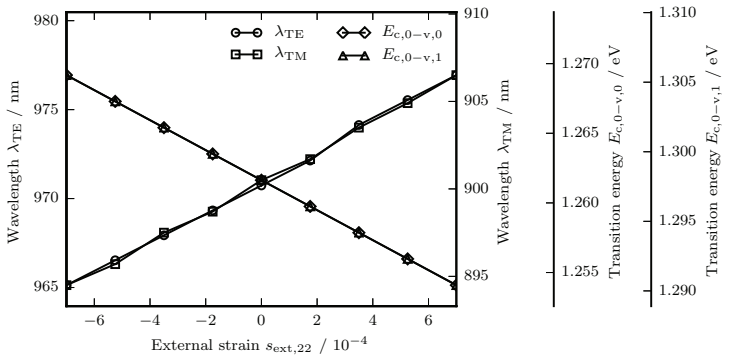

FIGURE 2.7: Wavelength (at gain peak) and transition energies for TE and TM transitions for 8 nm thick $In_{0.2}Ga_{0.8}As$ / $Al_{0.2}Ga_{0.8}As$/ $Al_{0.3}Ga_{0.7}As$ QW-structure on a GaAs substrate with external strain applied external strain applied along the QW in-plane direction in addition to the intrinsic strain due to lattice mismatch.

strain. For higher compressive strain $s_{22} = s_{33} < 0$ TM gain is suppressed further by an additional splitting of the HH and LH subbands, see band edges in Fig. 2.4. For external tensile strain in the in-plane direction, the intrinsic strain due to lattice mismatch is partially compensated. In this case, the TM gain increases compared to the case with only intrinsic strain. The threshold carrier density is determined with the model of a logarithmic gain dependence [49] on carrier density

$$N_{\mathrm{th}} = N_{\mathrm{tr}} \exp\left(\frac{\alpha_{\mathrm{int}} + \alpha_{\mathrm{mir}}}{\Gamma g_0}\right). \tag{2.105}$$

and the threshold current density is

$$J_{\mathrm{th}} = q_{\mathrm{el}} d_{\mathrm{qw}} \left(A_{\mathrm{nr}} N_{\mathrm{th}} + B_{\mathrm{sp}} N_{\mathrm{th}}^2 + C_{\mathrm{A}} N_{\mathrm{th}}^3\right). \tag{2.106}$$

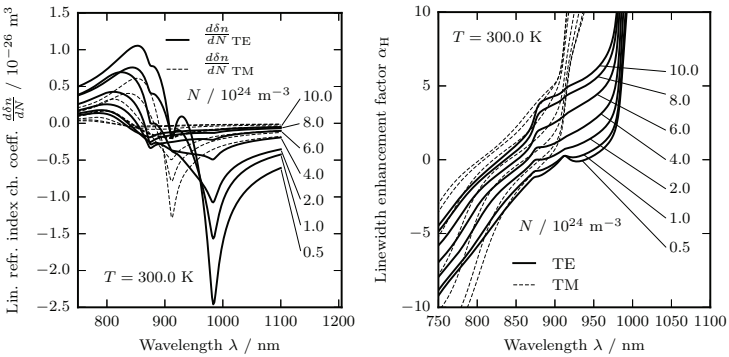

FIGURE 2.8: Linearized refractive index change (left) and linewidth enhancement factor (right) over wavelength for multiple carrier densities calculated by free-carrier theory for $In_{0.2}Ga_{0.8}As$ / $Al_{0.2}Ga_{0.8}As$ / $Al_{0.3}Ga_{0.7}As$ QW-structure without external strain applied. The refractive index dependence on the carrier density is linearized around the transparency carrier density.

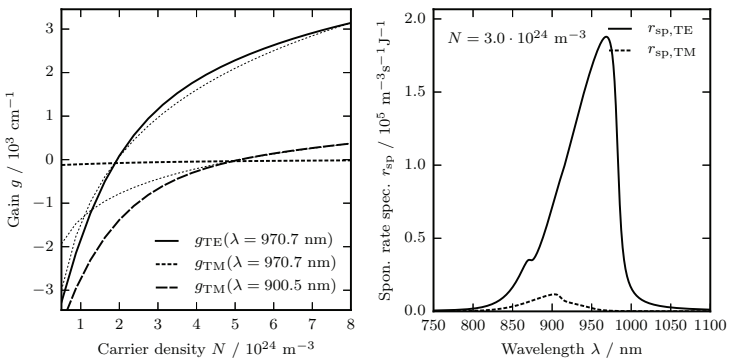

FIGURE 2.9: Gain over carrier density (left) and spontaneous recombination spectrum (right, for a carrier density of $n_{(2)} = 3 \cdot 10^{24}\,\mathrm{m}^{-3}$) for an $In_{0.2}Ga_{0.8}As$ / $Al_{0.2}Ga_{0.8}As$ / $Al_{0.3}Ga_{0.7}As$ QW-structure without external strain applied $s_{11}^{ext} = s_{22}^{ext} = s_{33}^{ext} = 0$. In the plot on the left, the gain curves for TE- and TM-radiation at the TE-wavelength of 970.7 nm, and the gain curve for TM-radiation at the TM-wavelength of 900.5 nm are displayed. Additionally, logarithmic fits to the gain curves for the TE-wavelength are shown as dotted lines.

Parameter	intrinsic strain		external stress (compressive)		external stress (tensile)	
	well	barrier	well	barrier	well	barrier
σ_{22}^{ext} / MPa	0		-55.56		55.56	
s_{11}^{int} / %	1.343	0.025	1.365	0.048	1.320	0.002
s_{22}^{int} / %	-1.413	-0.028	-1.483	-0.098	-1.343	0.042
δE_{c} / meV	106	2.07	114.7	10.13	97.90	-5.99
δE_{hh} / meV	27.28	0.66	37.77	0.90	36.79	0.43
δE_{lh} / meV	-70.73	-1.52	-73.87	5.10	-67.59	2.05
λ_{TE} / nm	970.735		965.133		976.938	
λ_{TM} / nm	900.500		894.497		906.503	
$g_{0,\text{TE}}$ / $1 \cdot 10^3\,\text{cm}^{-1}$	2.215		2.249		2.161	
$g_{0,\text{TM}}$ / $1 \cdot 10^3\,\text{cm}^{-1}$	0.831		0.815		0.850	
$N_{\text{tr,TE}}$ / $1 \cdot 10^{24}\,\text{m}^{-3}$	1.938		1.934		1.930	
$N_{\text{tr,TM}}$ / $1 \cdot 10^{24}\,\text{m}^{-3}$	5.121		5.203		5.044	

TABLE 2.1: Comparison of energy offsets and gain characteristics for $In_{0.2}Ga_{0.8}As/Al_{0.2}Ga_{0.8}As$ QW on GaAs substrate without and with compressive and tensile external strain applied. The bandgap energies without any strain applied are $E_{\text{g,qw}} = 1.132\,\text{eV}$ in QW and $E_{\text{g,b}} = 1.717\,\text{eV}$ in the barriers.

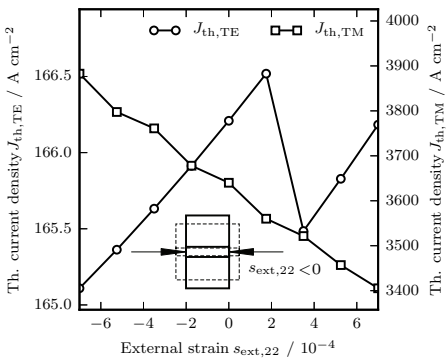

FIGURE 2.10: Threshold current density for TE and TM transitions for 8 nm thick $In_{0.2}Ga_{0.8}As/Al_{0.2}Ga_{0.8}As/\ Al_{0.3}Ga_{0.7}As$ QW-structure on GaAs substrate with external strain applied along the QW in-plane direction in addition to the intrinsic strain due to lattice mismatch.

The threshold carrier density depends on the gain coefficient g_0, the internal optical loss α_{int} and the mirror loss α_{mir}, see Appendix C.9. These values are calculated for a structure with front facet reflectivity of 2% and back facet reflectivity of 98%. Threshold current density for TE decreases slightly and increases for TM with increasing lateral compressive strain, Fig. 2.10.

2.5 Analysis of Quantum Well Structures

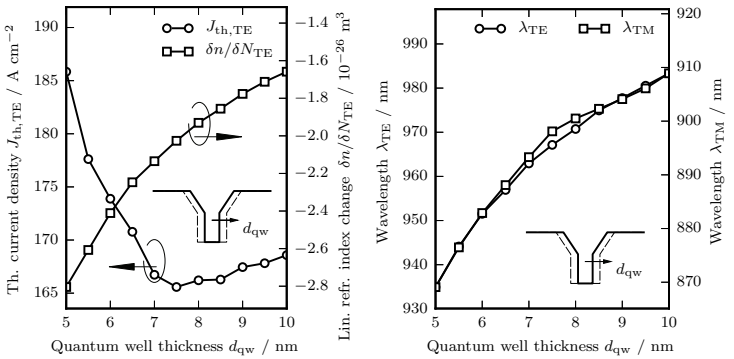

FIGURE 2.11: Results for an $In_{0.2}Ga_{0.8}As$ / $Al_{0.1}Ga_{0.9}As$ / $Al_{0.2}Ga_{0.8}As$ GRINSCH structure on a GaAs substrate for various well widths.

The barrier height and width of the QW for a Graded Index Separate Confinement (GRINSCH) with an $In_{0.2}Ga_{0.8}As$ QW surrounded by graded AlGaAs barriers are varied to investigate the correlation to threshold carrier density for TE and TM modes and resulting (linearized) carrier-induced refractive index change. Adjacent to the QW is $Al_{x_b}Ga_{1-x_b}As$ which is graded to $Al_{0.2}Ga_{0.8}As$ towards the confinement layers. The well width is varied between 5-10 nm and the barrier height between $x_b = 0$ and $x_b = 0.2$. In the extreme case $\Delta x_b = 0$, the GRINSCH disappears, and the structure is a $In_{0.2}Ga_{0.8}As$ QW embedded in $Al_{0.2}Ga_{0.8}As$ layers. Alongside with the calculation of the band structure and free-carrier gain, for each set of parameters, the vertical waveguide eigenmode is determined to extract the optical confinement factor. The transparency carrier density, gain coefficient, and confinement are inserted into (2.105) and (2.106) to yield the threshold current density for the specific structure. The goal is to reduce threshold carrier densities for TE modes while increasing threshold for TM modes, so that TE modes start lasing before the TM modes and the latter are suppressed sufficiently. The threshold current increases with the threshold carrier density. Carrier-induced refractive index changes play a crucial role for near-field filamentation and far-field divergence. The (linearized) change of refractive index with carrier density is determined for a variation of the well width (Fig. 2.11) and barrier height (Fig. 2.12). Both an increase in width of the well and an increase in barrier concentration lead to a smaller magnitude in carrier-induced refractive index change (evaluated at the wavelength with the highest gain). Overall, an increasing barrier height drop for this structure leads to a reduction of the threshold carrier density (Fig. 2.12). The decrease of the gain coefficient and transparency density is countered by an increase in confinement factor. For the investigated structure, a QW width of about 7.5 nm leads to a minimum threshold current density for the TE modes (Fig. 2.11). The changes in barrier height and well width are accompanied by a change of the emission wavelength for both TE and TM emission, see Fig. 2.12 (right) and 2.11 (right).

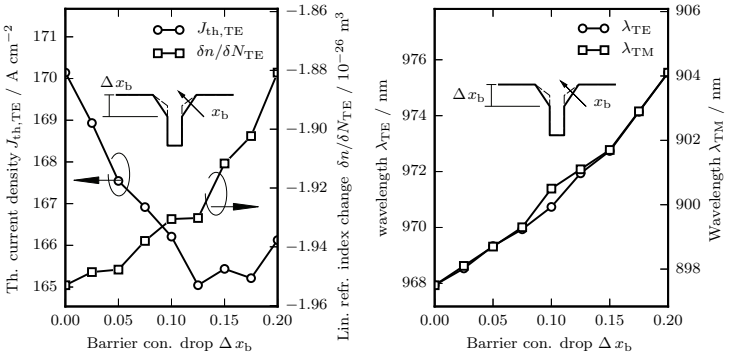

FIGURE 2.12: Results for an $In_{0.2}Ga_{0.8}As$ / $Al_{x_b}Ga_{1-x_b}As$ / $Al_{0.2}Ga_{0.8}As$ GRINSCH structure for various barrier heights with a QW thickness of 8 nm. The barrier heights are changed symmetrically $\Delta x_{\mathrm{b}} = \Delta x_{n,\mathrm{b}} = \Delta x_{p,\mathrm{b}}$.

2.6 Chapter Summary

The band structure and dipole-matrix elements of single InGaAs QWs surrounded by AlGaAs barriers are calculated with the help of the 8-band $k \cdot p$-method. Based on the free-carrier theory, the gain and carrier-induced refractive index change are computed. The results are either stored in data tables for the simulation models (Chapter 7 and Chapter 8), or the characteristics are computed and then approximated by analytical dependencies, which, for example, are a logarithmic dependence of the gain on the carrier-density (6.89) and a linearized relation between carrier-induced refractive index change and carrier density.

External strain induced by packaging or heating, adds up to the intrinsic strain (due to lattice mismatch) and influences the band structure of the active region. Compressive (intrinsic) strain leads to an increased gain for TE emission. The external strain shifts the peak-gain wavelength (Fig. 2.7) and changes the ratio between TE and TM gain. The influence of the anisotropy in the gain on the DOP for an edge-emitting HPDL is discussed in Chapter 5.

By the example of a GRINSCH structure, it is demonstrated that the carrier-induced refractive index change in the QW is a function of the width of the QW and barrier height. A change in the width of the QW from 5 nm to 10 nm leads to a change of the linearized carrier-induced refractive index variation from approximately $-2.8 \cdot 10^{-26}\,\mathrm{m}^3$ to $-1.75 \cdot 10^{-26}\,\mathrm{m}^3$ (Fig. 2.11). This finding offers the potential for a reduction of the filamentation and SAD due to a thicker QW.

Chapter 3

Thermal Model

3.1 Heat Sources in Semiconductor Lasers

The instationary heat equation governs the spatial and temporal evolution of the temperature $T(\vec{x},t)$

$$\rho c_p \partial_t T - \nabla \cdot (k_T \nabla T) = q, \tag{3.1}$$

based on the distribution of the local heat source density q in units $\mathrm{W\,m^{-3}}$. The parameters in (3.1) are the thermal conductivity k_T in $\mathrm{W\,m^{-1}\,K^{-1}}$, the density ρ in $\mathrm{kg\,m^{-3}}$, the specific heat capacity c_p in $\mathrm{J\,kg^{-1}\,K^{-1}}$. The thermal diffusivity κ in $\mathrm{m^2\,s^{-1}}$, density, specific heat capacity and thermal conductivity are related $\kappa = {}^{k_T}/_{\rho c_p}$. The material parameters and the heat source distribution in the above equation can be functions of position and time. For stationary problems (3.1) reduces to the Fourier heat-equation

$$\nabla \cdot (k_T \nabla T) = -q \tag{3.2}$$

for the temperature $T(\vec{x})$. The weak-form for the heat equation is obtained by multiplication of (3.2) with a test function v, integration over the domain $\Omega \subset \mathbb{R}^3$, and integration by parts of the divergence term

$$-\int_\Omega k_T \nabla T \cdot \nabla v \,\mathrm{d}^3x + \int_{\delta\Omega_\mathrm{N}} g_\mathrm{N} v \,\mathrm{d}s + \int_{\delta\Omega_\mathrm{R}} g_\mathrm{R}(T - T_\mathrm{R}) v \,\mathrm{d}s = -\int_\Omega q v \,\mathrm{d}^3x \tag{3.3}$$

where $\vec{n}$ is the surface normal and the boundary integral is split up into contributions from Neumann boundaries

$$g_\mathrm{N} = k_T \nabla T \cdot \vec{n}, \quad \text{on} \quad \delta\Omega_\mathrm{N}, \tag{3.4}$$

and Robin boundaries

$$g_\mathrm{R}(T - T_\mathrm{R}) = k_T \nabla T \cdot \vec{n} \quad \text{on} \quad \delta\Omega_\mathrm{R}. \tag{3.5}$$

The parameter g_N equals a heat flux density in units $\mathrm{Wm^{-2}}$ and g_R equals a heat flux density per temperature difference with respect to the reference temperature T_R in units $\mathrm{Wm^{-2}K^{-1}}$. The Dirichlet boundaries are imposed on the temperature $T \in V$, which is in the function space $V = \{v \in H^1(\Omega) : v = T_\mathrm{D} \,\mathrm{on}\, \delta\Omega_\mathrm{D}\}$ and on the test function $v \in \hat{V}$ which is in the function space $\hat{V} = \{v \in H^1(\Omega) : v = 0 \,\mathrm{on}\, \delta\Omega_\mathrm{D}\}$. The total heat source

density

$$q = q_{\text{Joule},n} + q_{\text{Joule},p} + q_{\text{SRH}} + q_{\text{sp}} + q_{\text{A}} + q_{\text{abs}} \tag{3.6}$$

consists of the contributions

$$\begin{aligned} q_{\text{Joule},n} &= \frac{\vec{J}_n^{\,2}}{\sigma_n}, \\ q_{\text{Joule},p} &= \frac{\vec{J}_p^{\,2}}{\sigma_p}, \\ q_{\text{SRH}} &= R_{\text{SRH}} E_{\text{g}}, \\ q_{\text{sp}} &= (1 - \beta_{\text{sp}})\, R_{\text{sp}} E_{\text{g}}, \\ q_{\text{A}} &= R_{\text{A}} E_{\text{g}}, \\ q_{\text{abs}} &= I_{\text{opt}} \alpha_{\text{opt}}, \end{aligned} \tag{3.7}$$

for the dissipated Joule heat from currents densities, non-radiative SRH recombination, reabsorption of spontaneous emission (emitted from the QW), non-radiative Auger recombination, and reabsorption of optical intensity I_{opt} [50]. The electrical conductivities are denoted by $\sigma_{n/p}$, and the factor β_{sp} accounts for contributions of the spontaneous emission to the amplified optical field. The recombination rate densities R_{SRH}, R_{sp}, and R_{A} are defined in Chapter 6 in (6.23) and E_{g} is the bandgap energy. The heat source density depends on the optical absorption coefficient $\alpha_{\text{opt}} = \alpha_{\text{int}} + \alpha_{\text{fc}}$, which consists of free-carrier absorption and constant background absorption α_{int}.

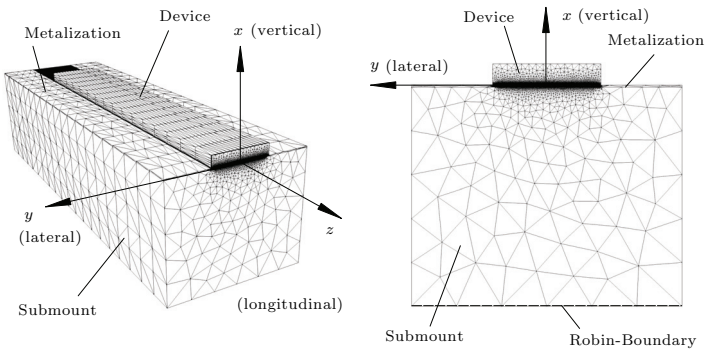

FIGURE 3.1: Mesh for the three-dimensional thermal domain including submount metalization, submount, solder and device.

The thermal model is employed to predict the temperature profiles for the devices D1–D8. The devices are modeled on the FEM domain displayed in Fig. 3.1, and the cavity length, contact width, and trench distance is adapted for each device respectively. All devices are soldered with the p-side down onto the submount. For the SEs D1–D4, the domain consists of an AlN submount with Au metalization layer, an AuSn solder layer, a p-side metalization layer (modeled with properties of Au), the insulating SiN layer, the epitaxial layers, the GaAs substrate, and a n-side metalization layer (Au). A detailed view of the mesh at the solder interface is shown in Fig. 3.7. In case of the simulation of individual emitters out of the LAs D5–D8 the submount material is CuW, and the width

of the submount, width of the emitter-section of the device, and therefore the width of the entire thermal domain are equal to the pitch of the emitters. A summary of the layer thicknesses used for the model is given in Tb. C.6 for the SEs and Tb. C.7 for the LAs. The material properties for AlN, CuW, Au, AuSn, and SiN are given in the Appendix C in Tbs. A.12, A.7, A.9, A.8, and A.10. For GaAs, AlGaAs, and InGaAs the material parameters are listed in Tbs. A.1, A.5, and A.6. The thermal conductivity is calculated based on Eq. (A.24) [1] given in the appendix in Section A.6. The inputs for the thermal simulations, the heat source densities, are evaluated in the FD simulations. The FD model is discussed in Section 7.2 and details and results for the performed simulations are presented in Chapter 8.

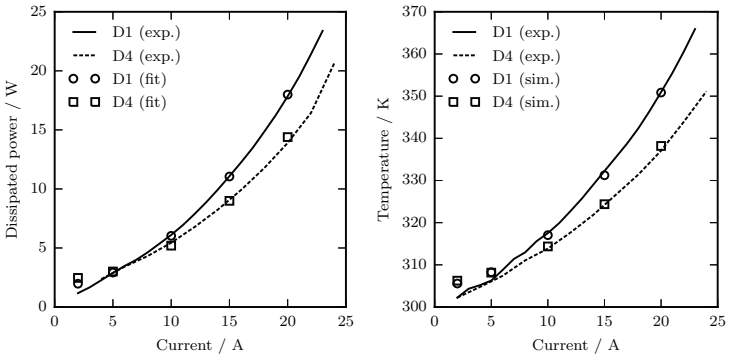

FIGURE 3.2: Calculated temperature over current for SE devices. The experimental temperatures are determined by the measured spectral drift. The comparison is performed for two different laser designs D1 and D4 with 100 µm and 150 µm contact opening, respectively. Details about the devices are listed in Tb. C.2. Due to the larger contact area the dissipated power for D4 (left) and temperature change (right) with current is lower compared to the ones of D1.

The results for the SEs D1, D4, and D2, D3 are shown in Figs. 3.2, and 3.3. The results for LAs D5, D6, and D7, D8 are shown in Figs. 3.4, and 3.5. The experimental measurements are determined from the drift of the spectrum assuming a tuning coefficient of $0.31\,\mathrm{nmK^{-1}}$. The calculated temperatures are averaged over the active region under the contact opening. To resemble the measurements the total (calculated) input heat source is rescaled to match the experimental value. The measured dissipated powers over current are fitted by quadratic functions (Figs. 3.2, 3.3, 3.4, and 3.5). Except for the bottom surface of the submount, homogeneous Neumann boundaries $\vec{n} \cdot \nabla T = 0$ are applied, so that the heat flux over the adiabatic surfaces vanishes. The heat generated in the domain is extracted at the bottom surface of the submount by the attached heatsink. Since this heatsink is excluded from the simulation the limited heat flux through the bottom surface is modeled by a Robin boundary condition with $g_\mathrm{R} = g_\mathrm{hs}$. The parameter g_hs in units $\mathrm{Wm^{-2}K^{-1}}$ is a specific property of the individual heatsink and $T_\mathrm{R} = T_\mathrm{hs}$ is the heatsink temperature. For each device, it is fitted so that the measured temperature matches the calculated one. Strictly speaking, it cannot be concluded that the calculated temperature is correct in its spatial profile. Nevertheless, the predicted

[1] All conducitivities are evaluated for $T = 300\,\mathrm{K}$ and not updated iteratively, so that the conductivity is not a function of the temperature in the simulations.

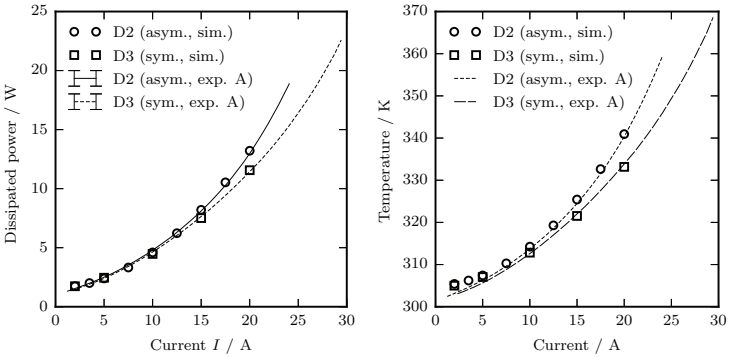

FIGURE 3.3: Calculated temperature over current for SE devices. The experimental temperatures are determined by the measured spectral drift. The comparison is performed for two different laser designs D2 and D3 with 140 µm contact opening and asymmetric coating (D2) and symmetric coating (D3). Details about the devices are listed in Tb. C.2.

averaged temperatures, and the change of the temperature with input heat power are reproduced.

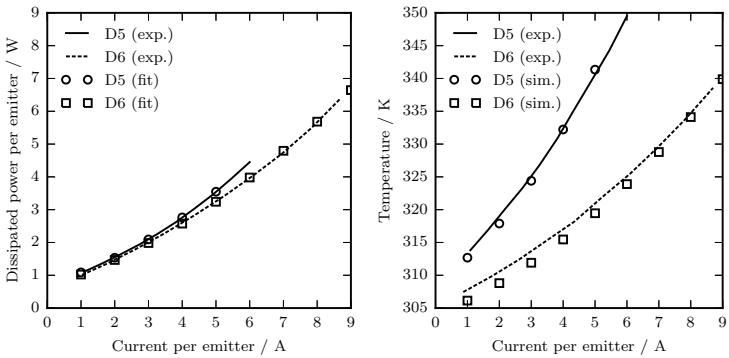

FIGURE 3.4: Calculated temperature in (central) emitter of a 55 emitter diode laser array (D5) and a 23 emitter laser array (D6). Both emitters have a 90 µm contact width. The experimental temperatures are determined by the measured spectral drift. Details about the devices are listed in Tb. C.3.

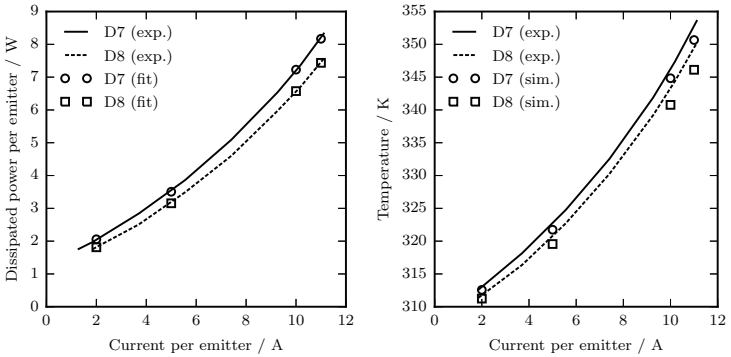

FIGURE 3.5: Calculated temperature in (central) emitter of 27 emitter diode laser arrays D7 and D8. Both emitters have a 200 µm contact width and differ in optical confinement factor with 0.62 % for D7 and 0.85 % for D8. The experimental temperatures are determined by the measured spectral drift. Details about the devices are listed in Tb. C.3.

3.2 Application: Thermal Lens Profile in Broad-Area Diode Lasers

The thermal lens plays a crucial role for the slow-axis divergence of diode lasers, primary when they are operated under high injection currents. Under common operating conditions (above 10 A for a 4 mm long device with 100 µm contact width) the thermal lens can be so high that the equivalent focal length is only a fraction of the cavity length. The parabolic refractive index profile leads to light propagation comparable to the one in a Graded-Index (GRIN) fiber or lens, which results in light filaments being continuously focused towards the center of the injection stripe. Due to gain and refractive index nonlinearities, higher filamentation is evoked with thermal lensing and the SAD increases. In this section, the thermal model is employed to investigate the change of thermal lensing by variation of the injection stripe width. The heat source distribution is linked to the curvature of the refractive index profile, which is proportional to the magnitude of the thermal lens, Fig. 3.7.

For the numerical study, the total dissipated heat Q is kept constant so that the local heat source density (under the injection stripe) is inversely proportional to the contact width $q_{\mathrm{h},0} = \frac{Q}{w_c l_z}$. A decrease in the magnitude of the curvature is observed with increasing contact width, see Fig. 3.7. Since the lateral gradient of the temperature is proportional to the heat flux, the slope of the heat flux gives the magnitude of the thermal lens, compare slopes for different contact widths in Fig. 3.6. The calculated heat flux densities reveal two characteristics: One is a nearly linear slope in the central part (inside the contact width), the other is a rapid increase in magnitude towards the edge of the contact opening, see Fig. 3.6. To approximate the curvature in the central part of the waveguide the expression $c_n = \partial_y \left(\frac{\partial_y n}{n} \right)$ with $n = n_0 + \alpha_T (T - T_0)$ is numerically evaluated. The local value is averaged along the lateral direction where only the region inside the stripe width is taken into account so that only a part of the spikes of the heat flux densities at the contact edges are included for the determination of the

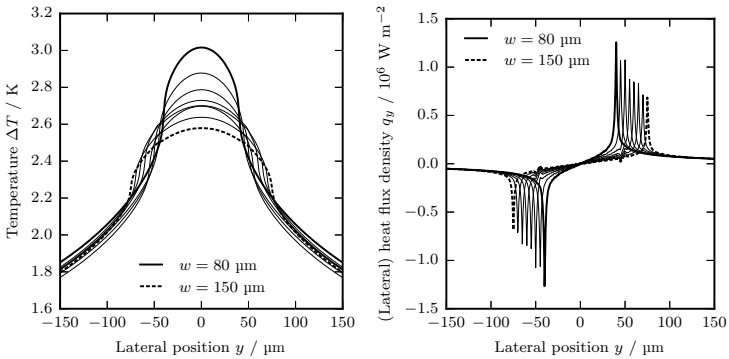

FIGURE 3.6: Temperature increase for total dissipated heat of 1 W at front of device (left) and corresponding heat flux density in lateral direction (right) for contact widths 80, 90, 100, 110, 120, 130, 140, 150 µm.

average curvature. Although, these regions influence the optical field evolution as high gradients in the refractive index manifest in high spatial frequencies of the light field. For this analysis, it is assumed that the light field approximately follows the contour of the contact opening. The observations made in this section are recited in Chapter 8 where SAD angles for devices with different contact openings are compared. For the same amount of dissipated heat thermal slow-axis *blooming* occurs at higher currents for devices with wider contact openings. Additionally, a larger contact area decreases the devices series resistance so that less power is dissipated at the same operating current. Both, the reduction of the dissipated heat and the wider contact width reduce thermal lensing and thus the SAD.

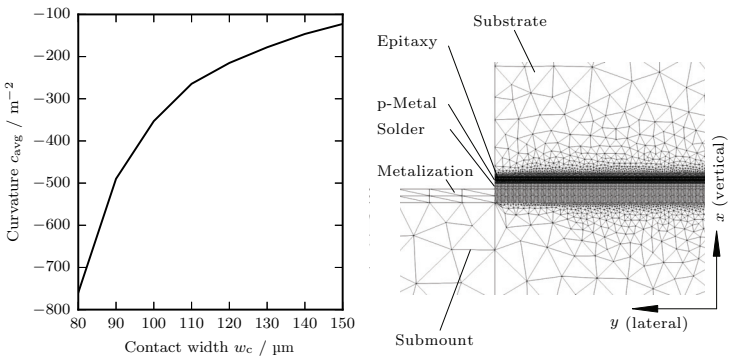

FIGURE 3.7: Left: Curvature of refractive index profile along lateral direction under injection stripe. Right: Detailed view of the mesh around the solder interface at the left edge of the device. The SiN insulation layer is included in the mesh but not labeled in the figure due to the small size.

3.3 Application: COD by Misaligned Optical Feedback

If feedback light for spectral stabilization is misaligned with respect to the vertical waveguide, it can be absorbed by layers surrounding the active region. A drawback of this misaligned is not only that the back-coupled light does not contribute to the stabilization, but its absorption introduces additional heat sources, which are cause for accelerated gradual degradation as well as COMD. Light with wavelengths below 870 nm is absorbed in the GaAs-substrate and p-cap layers due to interband absorption. For InGaAs/AlGaAs diode lasers with emission wavelengths in the range from 880 to 1060 nm, there is no interband absorption in the epitaxial layers, so that the epitaxial layers despite the active region are transparent to the lasing wavelength except for other absorption mechanisms, such as free-carrier absorption in highly doped regions. However, also for these devices misalignment leads to the described drawbacks. A method of emulating misaligned feedback experimentally by injection of light from a heating laser into a Device Under Test (DUT) is presented in [51]. This study concludes that for InGaAs/AlGaAs-based devices misalignment towards the p-side lowers the threshold for CO(M)D significantly while these devices are robust against displacement towards the n-side in contrast to devices emitting below 870 nm. The author contributed a numerical study which supports the interpretation of the experimental findings.

The properties of the DUT are listed in Tb. C.2 as D1. The device is soldered p-side down on an AlN submount. The AuSn solder is 4 µm thick, and the heating laser is operated CW at 1.03 W. Since the vertical intensity distribution injected onto the facet of the DUT cannot be measured directly a wave-optical analysis is performed resulting in a vertical width of 1.83 µm (for 90 % P. I.) for a Gaussian distribution. In lateral direction, a top-hat profile with a width of 100 µm corresponding to the contact opening is assumed. In the numerical study, see results in Fig. 3.11, this intensity distribution is displaced along the vertical direction, and temperature profiles are evaluated for the probing position in the experiments, which is located 15 µm away from the QW in the substrate. Except for the metallization layer, the absorption coefficient for all other materials is set to zero. For the study, absorption in the metal only is not vanishing to demonstrate that the measured front facet temperature observed in the experiment emerges mainly due to absorption of the external heating radiation in these metal layers or the adjacent solder layer. The heat due to Joule heating and non-radiative recombinations are generated by the DUT and are set for a CW operation point at 14 A. At 59 % electro-optical efficiency the output power is 13.25 W, and the remaining dissipated heat is 9.2 W. The heat sources due to reabsorption are distributed along the laser cavity according to the longitudinal optical intensity approximated by the one-dimensional model presented in Chapter 7. An absorption coefficient of $0.9\,\mathrm{cm}^{-1}$ is assumed [11] so that 26 % of the dissipated heat is contributed to re-absorption. The increasing intensity towards the front facet leads to an increased temperature in the front of the device. The remaining fraction of the dissipated heat is contributed to Joule heating and non-radiative reabsorption and is homogeneously distributed laterally inside the width of the contact opening. Although the internally dissipated heat of a free-running diode laser exceeds 10 W at 15 A and above, about 1 W of externally back coupled light into the device can cause severe damage and lead to CO(M)D. The main reason that such a relatively small fraction of back-coupled power can cause this damage lies in the spatial concentration and therefore high local heat source density. In an aligned system, the focal spot of the feedback light is placed at the front facet of the device. The vertical size of the back-coupled mode is comparable to the size of the waveguides

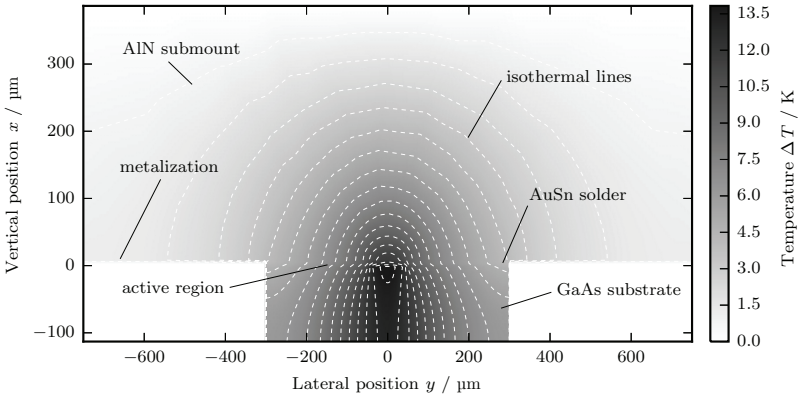

FIGURE 3.8: Temperature in the transverse plane (slice out of three-dimensional domain) at front facet of the device without external heating. In the case of external heating, the location of maximal temperature (in the plane) shifts towards the p-side metal, where the external heat is introduced. The device is displayed with the n-side facing downwards. The QW is located at $x = 0\,\mu\text{m}$.

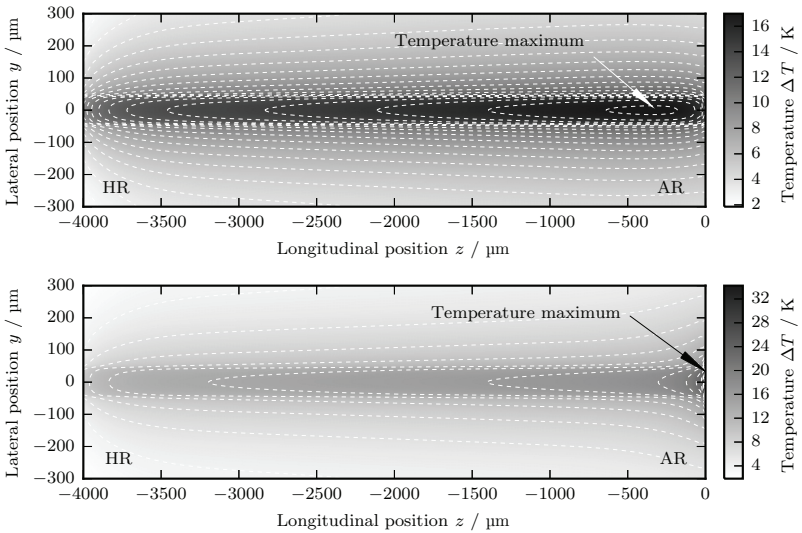

FIGURE 3.9: Temperature in QW plane without external heating (top) and external heating power of 0.363 W (bottom). The location of maximal temperature (in the plane) shifts to the facet in case of external heating.

eigenmode. However, when the light is coupled into a layer with a high absorption coefficient the penetration depth of the light into the corresponding layer is small. In the investigated case of absorption in the metalization or solder, the penetration depth for wavelengths around 950 nm is below 100 nm [52] leading to high local heat source densities at the impact location. For the simulation, the longitudinal resolution is larger than the penetration depth, so that instead of handling the reabsorbed heat source as a volume density, it is introduced as a surface heat source density into the calculations. The surface heat source is applied as a Neumann boundary (3.4) to the front surface of the domain, where the boundary term g_N equals the surface heat source. The shape and magnitude of the surface heat source correspond to the back-coupled light intensity. Due to the reflectivity of the metal, only a fraction of this power penetrates the metal. The optical absorption coefficient (at the utilized wavelength) and the reflectivity are unknown so that the simulation is calibrated by setting the total external heat power to 0.363 W and the calculated maximum temperature aligns with the maximum measured temperature, Fig. 3.11. The temperature increase induced by an external heating power

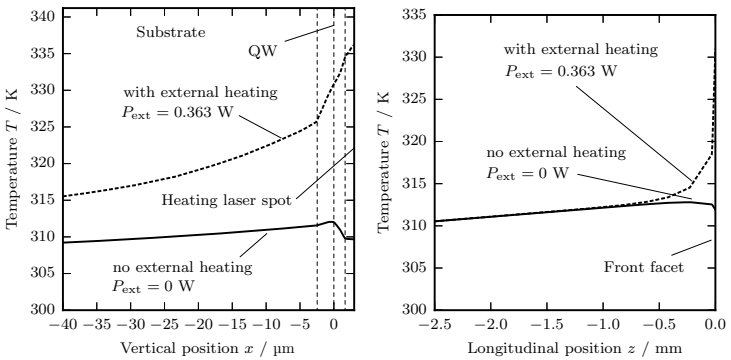

FIGURE 3.10: Temperature with and without external heating at front facet. Cross section in the vertical direction (left) and longitudinal direction (right) through the center of the device. The focus position of the heating laser is located 3 µm above the QW. The results are published in [51].

of 1.03 W incident on the solder (corresponding vertical position is 3 µm) is about two times as high inside the QW compared to the temperature increase at the measurement position 15 µm above the QW on the substrate. Since the temperature increase at the epitaxy or QW location cannot be accessed with the measurement setup presented in [51], the simulation gives insights into the extrapolated temperature QW temperature at the front facet. To reduce facet heating due to carrier recombination, the contact opening is offset by 30 µm from the back and front facets, so that carrier injection is suppressed there. The absence of current in the front section leads to a shift of the maximum temperature of about 100 µm away from the front facet, see Fig. 3.9 and 3.10. This situation changes when an additional external heat source is included, and the maximum temperature is at the front facet. High temperatures in the QW seed the thermal run-away process which leads to device degradation. Besides, high temperatures at the facet coatings cause Catastrophic Optical Mirror Damage (COMD) [53, 54]. It is concluded that absorption of spatially concentrated feedback light in the p-side of the semiconductor or the adjacent metals initiates the origination of COMD. Panchromatic cathodoluminescence images of devices with and without feedback that failed due

to COD are presented in [51] and support this conclusion. The temperature increase

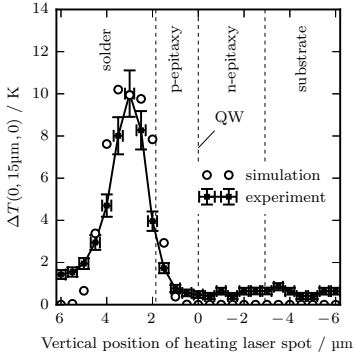

FIGURE 3.11: Comparison of experimental temperature rise (at the probing position on the substrate 15 µm above the QW) as a function of the vertical heating laser spot position on the front facet of the DUT and simulated values. The results are published in [51]. The heating laser is operated at 1.03 W at 970 nm with 100 µm lateral spot width and 1.83 µm vertical spot width on the front facet of the DUT. Probe laser for temperature measurement with 14 mW at 785 nm incident on substrate 15 µm above the QW.

as a function of the vertical spot position results from folding the (vertical) Gaussian intensity distribution with the absorption profile, which is a constant in the metal layer and zero everywhere else. The maximum occurs if the feedback position aligns with the absorbing layer at position 3 µm in Fig. 3.11. Displacement leads to a reduction of the temperature since the overlap of the intensity distribution and the layer decreases together with the total absorbed power. Possible reasons for the deviation of the simulated and measured profile can be due to simplified geometry of solder and metal layers in the simulation or deviations from the actual beam profile at the diode facet in the experiment. For InGaAs/AlGaAs-based semiconductor lasers misaligned feedback with a back coupling strength between 4-10 % can lead to a reduction of the threshold for COD when the high absorbing metalization layers are hit. A similar temperature increase in the simulation could as well be reached if the absorption of the highly p-doped epitaxial layers is included. From the conducted experiment and simulations it cannot be distinguished between absorption in the p-doped regions or the adjacent metallization or solder. By design, the vertical misalignment, especially towards the p-side, has to be reduced to circumvent reduction of COD threshold.

3.4 Chapter Summary

The computation of the temperature by the FEM on a three-dimensional domain, which is coupled to the edge-emitting laser simulation model in Chapter 7 is introduced. The heat source density is calculated based on the current density, carrier density, optical intensity, and the bandgap which potentially dependents on the temperature (from a previous iteration step). The temperature profiles for the devices D1–D8 are obtained from the coupled computations (Chapter 8) with the FD laser model (Chapter 7). The

heat flux through the bottom of the submount is modeled with a Robin boundary condition, and the parameter for the boundary condition is calibrated for each device so that the computed temperature aligns with the measurements.

Under common operating conditions (above 10 A for a 4 mm long device with 100 µm contact width) the thermal lens can be so high that the equivalent focal length is only a fraction of the cavity length. The parabolic refractive index profile results in light filaments which are continuously focused towards the center of the injection stripe. The calculated heat flux densities reveal two characteristics: A nearly linear slope in the central part (inside the contact width), and an increase in magnitude towards the edge of the contact opening, see Fig. 3.6. These steep gradients at the edges influence the optical field as high gradients in the refractive index manifest in high spatial frequencies of the light field and therefore increased SAD.

The temperature increase due to misaligned optical feedback [51] is computed, and results are compared to experiments. This study concludes that for InGaAs/AlGaAs-based devices misalignment towards the p-side lowers the threshold for CO(M)D of the device while these devices are robust against displacement towards the n-side in contrast to devices emitting below 870 nm. The numerical study which supports the interpretation of the experimental findings is presented in Section 3.3. It is concluded that absorption of spatially concentrated feedback light in the p-side of the semiconductor or the adjacent metals initiates the origination of COMD by increasing the temperature at the front facet.

Chapter 4

Optical Model

In this chapter, the equations governing the evolution of the electromagnetic field are introduced. Since full space-time calculations are resource and time-consuming, several approximations are made to simplify the wave equation. For the optical models it is distinct between three different types of equations: The Time-Domain (TD) and Frequency-Domain (FD) methods and the equations for eigenmodes, see the separated boxes in Fig. 4.1. In the presented models all temporal derivatives are of the first-order (at some point second-order derivatives in time are neglected), so that when applying forward derivatives or the Crank-Nicolson scheme for the discretization only the field values from the preceding time step are needed to calculate the values for the next step. Expressing the fields with the help of a Fourier series, the time-dependent equations can be transformed from the time into the frequency domain. Then the variables of the equations are the coefficients of the Fourier series for the discrete frequencies, for example, the longitudinal frequencies of the laser resonator. The FD approach is utilized to compute beam propagation through optical waveguides and investigate the change of the electric field along the propagation direction. For the FD-BPM only the field values from the previous (in longitudinal direction) transverse slice needs to be known to calculate the values for the next transverse slice. This benefits the calculation of the propagation through long waveguides like optical fibers. The memory requirements are smaller compared to the TD methods. The FD-BPM can also be applied to evaluate the propagation of the forward and backward traveling fields in a semiconductor laser resonator. The solution obtained with the FD propagation in combination with a Fox-Li iteration is only valid if the fields converge after a certain number of round-trips. Due to the nonlinearities of material parameters and the strong coupling between the electric field and the material properties, the propagation in the semiconductor waveguide is unstable and convergence (regarding the reproduction of field values after one or multiple round-trips) is not observed, even after a large number of round trips (> 200). Although the fields do not converge for broad-area edge-emitting laser models, conclusions on the output characteristics (power, divergence, near-field width) of the device can be drawn from the FD Fox-Li method.

The derivations and approximations presented in this chapter are performed under the requirements:

1. Prediction of (transverse) polarization of electric field for propagation in birefringent waveguides,

2. either TD or FD propagation through waveguides with spatial dimensions in the order of $400\,\mu m \cdot 10\,\mu m \cdot 4000\,\mu m$ for a large number of time steps or round trips (> 1000),

3. transverse (and temporal) varying susceptibility (refractive index and gain),

4. frequency dependent susceptibility (to model gain and refractive index spectrum).

Large changes (relative to the wavelength) of material properties in the propagation direction are not taken into account in this work, although they can be relevant for different types of diode lasers, for example, Distributed FeedBack (DFB) lasers. An overview of the relations between the optical models, equations and the approximations is given in Fig. 4.1. Beginning from Maxwell's equations the full-vectorial wave equation for the electric field is formulated. This step eliminates the need for the calculation of the magnetic field in the governing equations. To fulfill requirement 2 the concept of a Slowly Varying Envelope (SVE) for the electric field and the non-static part of the material polarization is applied. The SVE Approach (SVEA) reduces the required mesh resolution and time discretization. Splitting of the fields into transverse and longitudinal components brings along two benefits: First, this formulation enables the choice of two sets of finite elements when applying the FEM to solve, for example, the eigenmode problem for the transverse plane. The elements chosen are curl-conforming (Nédélec) [55] vector elements for the transverse field vector and Lagrange elements of the first-order for the longitudinal component. This approach guarantees the stability of the numerical scheme and is described in Section 4.5. The second reason is the elimination of the longitudinal component from the SVE wave equation, which leads to the formulation of the TDTW and BPM method. For a charge-free space (no unbound free charges) a relation between the longitudinal electric field component and the transverse component can be drawn from the divergence of the dielectric displacement field. After expression of the longitudinal electric field component through the transverse components the SVE wave equation reduces to a set of two partial differential equations for the two transverse field components. This formulation enables to model the electric polarization rotations in anisotropic dielectric waveguides, see requirement 1. For the TDTW model, the discretization is performed along characteristic lines, which result from a coordinate transformation into a moving *light-cone* frame. To apply this discretization second-order derivatives along the propagation direction and in time are neglected. In contrast to the TDTW model, for the BPM the second-order derivatives do not need to be neglected. Due to the transformation into frequency space, the time derivatives transform into $\partial_t \rightarrow -i\omega$, multiplications with the frequency of the time-harmonic field component. The neglection of the second-order derivative along the propagation direction leads to the paraxial approximation of the wave equation. The application of the first-order Padé approximation results in the Wide-Angle (WA) FD-BPM, which allows higher divergence angles and propagation through media with steep variations of the refractive index in transverse directions (see requirement 3). To model the dispersion of the susceptibility (requirement 4) in the TDTW model, at least one auxiliary equation for the material polarization updates is employed. The material polarization is also treated with the concept of the SVE and calculated as a dynamical variable in the time stepping. In the FD the susceptibility is directly evaluated for the corresponding frequency of the field component.

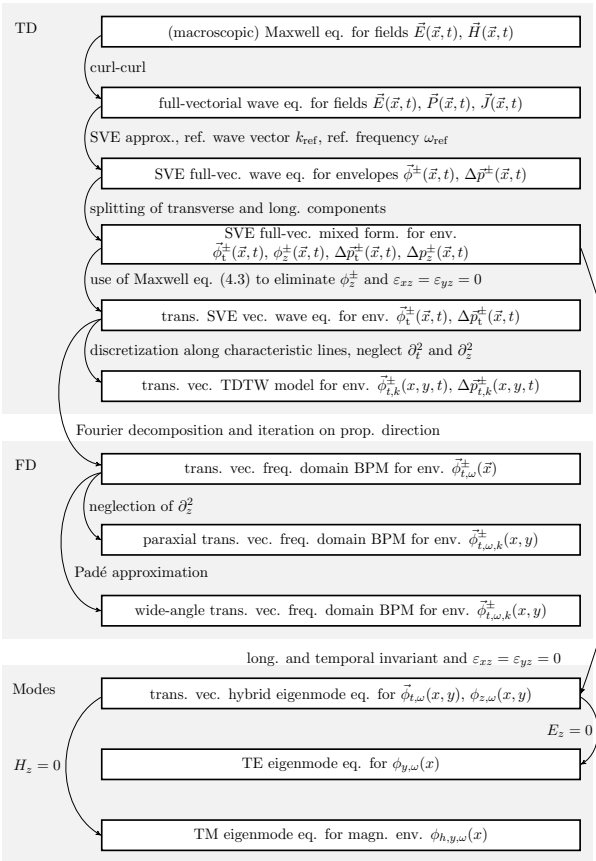

FIGURE 4.1: Overview of optical models, equations and the underlying approximations.

4.1 Maxwell's Equations

The spatio-temporal dynamics of the electric field $\vec{E}(\vec{x},t)$, electric displacement $\vec{D}(\vec{x},t)$, magnetic field $\vec{H}(\vec{x},t)$ and magnetic flux density $\vec{B}(\vec{x},t)$ are described by the (macroscopic) Maxwell's equations [56]

$$\nabla\times\vec{E}=-\partial_t\vec{B}, \tag{4.1}$$

$$\nabla\times\vec{H}=\partial_t\vec{D}+\vec{J}, \tag{4.2}$$

$$\nabla\cdot\vec{D}=\rho, \tag{4.3}$$

$$\nabla\cdot\vec{B}=0. \tag{4.4}$$

Macroscopic material properties are incorporated into the (free) charge density $\rho(\vec{x},t)$ and the (free) current density $\vec{J}(\vec{x},t)$. In general, all fields, the charge density, and

current density are functions of position $\vec{x} = (x, y, z)^{\mathrm{T}}$ and time t. The electric displacement and magnetic flux density are related to the electric field, and magnetic field via the constitutive equations

$$D_i(\vec{x}, t) = \int_{-\infty}^{t} \varepsilon_{ij}(\vec{x}, t-\tau) E_j(\vec{x}, \tau)\, \mathrm{d}\tau, \tag{4.5}$$

$$B_i(\vec{x}, t) = \int_{-\infty}^{t} \mu_{ij}(\vec{x}, t-\tau) H_j(\vec{x}, \tau)\, \mathrm{d}\tau, \tag{4.6}$$

with the permeability $\mu_{ij} = \mu_0 \mu_{r,ij}$ and the permittivity $\varepsilon_{ij} = \varepsilon_0 \varepsilon_{r,ij}$ which both are rank two tensors. The permittivity tensor is related to the (electric) susceptibility tensor χ

$$\varepsilon_{ij}(\vec{x}, t) = \varepsilon_0 \left(I_{ij} \delta(t) + \chi_{ij}(\vec{x}, t) \right), \tag{4.7}$$

which in the general case both have space and time dependency. The (time) delta-function $\delta(t)$ is inserted to model a direct material response, and the Kronecker-delta δ_{ij} is equivalent to the identity tensor. The constitutive relations (4.6) are explicitly written as temporal convolutions of the time-dependent material properties and the corresponding fields to account for dispersive media in the following derivations. Similar to the constitutive relation for the electric displacement the material polarization P is given by

$$P_i(\vec{x}, t) = \varepsilon_0 \int_{-\infty}^{t} \chi_{ij}(\vec{x}, t-\tau) E_j(\vec{x}, \tau)\, \mathrm{d}\tau, \tag{4.8}$$

so that the electric displacement can be expressed by

$$D_i(\vec{x}, t) = \varepsilon_0 E_i(\vec{x}, t) + P_i(\vec{x}, t). \tag{4.9}$$

In the scope of this work, only non-magnetic media are considered, so that the magnetic permeability equals the vacuum permeability times the identity tensor

$$\mu_{ij} = \mu_{\mathrm{r}} \mu_0 \delta_{ij} \tag{4.10}$$

with $\mu_{\mathrm{r}} = 1$. This reduces the convolution of the magnetic flux density and the magnetic field in Eq. (4.6) to a multiplication and the magnetic flux density in the first Maxwell's Eq. (4.1) is expressed by the magnetic field. Taking the curl of (4.1), insertion of the curl of the magnetic field from the second Maxwell's Eq. (4.2), followed by the insertion of the expression for the electric displacement (4.9) leads to

$$\nabla \times \left(\mu^{-1} \nabla \times \vec{E} \right) + \varepsilon_0 \partial_t^2 \vec{E} = -\partial_t^2 \vec{P} - \partial_t \vec{J}, \tag{4.11}$$

the full-vectorial wave equation for the electric field. This formulation is the starting point for the derivations of the TD- and FD-BPM, and eigenmode equations in this chapter.

4.2 Slowly Varying Envelope Method for Full-Vectorial Wave Equation

For the slowly varying complex envelope approach, the electric field is separated into a slowly varying and a fast oscillating part

$$\begin{aligned}\vec{E}(x,y,z,t) = \vec{\phi}^{+}(x,y,z,t)\exp(ik_{\mathrm{ref}}z)\exp(-i\omega_{\mathrm{ref}}t) \\ +\vec{\phi}^{-}(x,y,z,t)\exp(-ik_{\mathrm{ref}}z)\exp(-i\omega_{\mathrm{ref}}t).\end{aligned} \tag{4.12}$$

The oscillation takes place along the propagation direction, which here is the z-axis. Additionally, the forward $\vec{\phi}^{+}$ and backward $\vec{\phi}^{-}$ traveling parts of the electric field with respect to the axis of propagation are separated. The total field is the superposition of these two parts. If the changes of the permittivity along the propagation direction are small, which must hold for the SVEA to be valid, the equations for the forward and backward parts are decoupled. The fields are only coupled at domain boundaries (the facets). The (full) permittivity tensor reads

$$\varepsilon = \begin{pmatrix} \varepsilon_{xx} & \varepsilon_{xy} & \varepsilon_{xz} \\ \varepsilon_{yx} & \varepsilon_{yy} & \varepsilon_{yz} \\ \varepsilon_{zx} & \varepsilon_{zy} & \varepsilon_{zz} \end{pmatrix}. \tag{4.13}$$

To make the following derivations more compact, two subsets of the components are defined

$$\varepsilon_{\mathrm{t}} = \begin{pmatrix} \varepsilon_{xx} & \varepsilon_{xy} \\ \varepsilon_{yx} & \varepsilon_{yy} \end{pmatrix}, \quad \varepsilon_{z,\mathrm{t}} = \begin{pmatrix} \varepsilon_{xz} \\ \varepsilon_{yz} \end{pmatrix} \tag{4.14}$$

The subset ε_{t} holds only the transverse components of the permittivity tensor. For the derivation of the governing beam propagation equation, the transverse x, y components are separated from the longitudinal component z of the electric field

$$\vec{E} = \begin{pmatrix} \vec{E}_{\mathrm{t}} \\ E_z \end{pmatrix} = \begin{pmatrix} E_x \\ E_y \\ E_z \end{pmatrix}. \tag{4.15}$$

The vector $\vec{E}_s$ and corresponding envelopes $\vec{\phi}_s$ hold only the transverse components x, y of the electric field in a three-component vector

$$\vec{E}_s = \begin{pmatrix} E_x \\ E_y \\ 0 \end{pmatrix}, \quad \vec{\phi}_s^{\pm} = \begin{pmatrix} \vec{\phi}_{\mathrm{t}}^{\pm} \\ 0 \end{pmatrix} = \begin{pmatrix} \phi_x^{\pm} \\ \phi_y^{\pm} \\ 0 \end{pmatrix} \tag{4.16}$$

For the Nabla operator ∇_{t} in transverse directions, the transverse parts embedded in a three component vector ∇_s and the longitudinal part of the Nabla operator ∇_z the notations

$$\nabla_{\mathrm{t}} = \begin{pmatrix} \partial_x \\ \partial_y \end{pmatrix}, \quad \nabla_s = \begin{pmatrix} \partial_x \\ \partial_y \\ 0 \end{pmatrix}, \quad \nabla_z = \begin{pmatrix} 0 \\ 0 \\ \partial_z \end{pmatrix} \tag{4.17}$$

are defined so that in sum

$$\nabla = \nabla_s + \nabla_z. \tag{4.18}$$

The wave equation (4.11) is rewritten with the aim to separate the transverse and longitudinal components of the electric field. First, (4.18) is inserted into (4.11)

$$\nabla \times \left(\mu^{-1}\nabla_s \times \vec{E} + \mu^{-1}\nabla_z \times \vec{E}\right) + \varepsilon_0 \partial_t^2 \vec{E} = -\partial_t^2 \vec{P} - \partial_t \vec{J} \tag{4.19}$$

which leads to

$$\begin{aligned}&\nabla_s \times \nabla_s \times \vec{E} + \nabla_s \times \nabla_z \times \vec{E} + \nabla_z \times \nabla_s \times \vec{E} + \nabla_z \times \nabla_z \times \vec{E} \\ &+ \mu_0 \varepsilon_0 \partial_t^2 \vec{E} = -\mu_0 \partial_t^2 \vec{P} - \mu_0 \partial_t \vec{J}\end{aligned} \tag{4.20}$$

and

$$\begin{aligned}&\nabla_s \times \nabla_s \times \vec{E}_s - \left(\partial_x^2 + \partial_y^2\right) E_z \vec{e}_z + \vec{e}_z \partial_z \nabla_s \cdot \vec{E}_s + \partial_z \nabla_s E_z - \partial_z^2 \vec{E}_s \\ &+ \mu_0 \varepsilon_0 \partial_t^2 \vec{E} = -\mu_0 \partial_t^2 \vec{P} - \mu_0 \partial_t \vec{J},\end{aligned} \tag{4.21}$$

where $\vec{e}_z = (0, 0, 1)^{\mathrm{T}}$ is the unit vector in the longitudinal direction. Note that the above procedure may seem to make the notation more complex in the first place but provides two decoupled equations, one for all terms proportional to $\vec{e}_z$ (which would correspond to the third row of the three equations) and one for the remaining terms.

To account for dispersion of the material, the susceptibility in the frequency domain is split up into two contributors: A part with the static susceptibility at a reference frequency ω_{ref} and the frequency dependency for first-order (linear) dispersion, and a second frequency dependent part to model nonlinear (gain) dispersion. For the first part the second time derivative of the respective polarization can be evaluated and then inserted into the wave equation. For the nonlinear gain dispersion an evolution equation for (the envelope of) the corresponding polarization of the gain medium is introduced and solved in addition to the wave equation. This approach for the incorporation of linear dispersion and nonlinear (gain) dispersion into the TWTD model follows the models presented in [57, 25, 58, 59]. The susceptibility, split up into the two contributions, reads $\tilde{\chi}(\omega) = \tilde{\chi}_{\mathrm{L}}(\omega) + \Delta\tilde{\chi}(\omega)$ and likewise the material polarization is separated into $\vec{P}(t) = \vec{P}_{\mathrm{L}}(t) + \Delta\vec{P}(t)$.

Linear dispersion is induced by the polarization $\vec{P}_{\mathrm{L}}$ and leads to the introduction of the group velocity in Section 4.3. To insert the polarization contributions into the wave equation, the second-order time derivative has to be evaluated. The transformation of $\mu_0 \partial_t^2 \vec{P}_{\mathrm{L}}(t)$ into the frequency domain and expansion of the dielectric function up to the first-order yields

$$\begin{aligned}(-i\omega)^2 \mu_0 \vec{\tilde{P}}_{\mathrm{L}}(\omega) &= (-i\omega)^2 \mu_0 \varepsilon_0 \tilde{\chi}_{\mathrm{L}}(\omega) \vec{\tilde{E}}(\omega) \\ &= \frac{1}{c_0^2}(-i\omega)^2 \left(\tilde{\varepsilon}_{\mathrm{r,L}}(\omega) - 1\right) \vec{\tilde{E}}(\omega) \\ &\approx \frac{1}{c_0^2}(-i\omega)^2 \left(\tilde{\varepsilon}_{\mathrm{r,L}}(\omega_{\mathrm{ref}}) + \left.\frac{\mathrm{d}\tilde{\varepsilon}_{\mathrm{r,L}}(\omega)}{\mathrm{d}\omega}\right|_{\omega_{\mathrm{ref}}} (\omega - \omega_{\mathrm{ref}}) - 1\right) \vec{\tilde{E}}(\omega).\end{aligned} \tag{4.22}$$

A similar derivation with the expansion of the dielectric function up to the second-order is given in [24]. To keep the notation short, from here on the value of the permittivity $\varepsilon = \tilde{\varepsilon}_{\mathrm{L}}(\omega_{\mathrm{ref}})$ and its derivative $\varepsilon' = \tilde{\varepsilon}'_{\mathrm{L}}(\omega_{\mathrm{ref}})$ are the values at the reference frequency, and the tildes are omitted. The same holds for the corresponding relative permittivies.

Separation of the terms in the above equation gives

$$(-i\omega)^2\mu_0\vec{\tilde{P}}_{\mathrm{L}}(\omega) \approx -\frac{1}{c_0^2}(-i\omega)^2\vec{\tilde{E}}(\omega) + \frac{1}{c_0^2}\left((-i\omega)^2\left(\varepsilon_{\mathrm{r}} - \omega_{\mathrm{ref}}\varepsilon_{\mathrm{r}}'\right) + i(-i\omega)^3\varepsilon_{\mathrm{r}}'\right)\vec{\tilde{E}}(\omega). \tag{4.23}$$

The equation is transformation back into the time domain, the SVEA is inserted, and the third-order $\partial_t^3\vec{\phi}^{\pm}$ time derivatives of the electric field envelopes are dropped

$$\begin{aligned}\mu_0\partial_t^2\vec{P}_{\mathrm{L}}^{\pm} + \frac{1}{c_0^2}\partial_t^2\vec{E}^{\pm} &\approx \frac{1}{c_0^2}\left(\left(\varepsilon_{\mathrm{r}} - \omega_{\mathrm{ref}}\varepsilon_{\mathrm{r}}'\right)\partial_t^2 + i\varepsilon_{\mathrm{r}}'\partial_t^3\right)\vec{E}^{\pm} \\ &= e^{\pm ik_{\mathrm{ref}}z - i\omega_{\mathrm{ref}}t}\Bigg(-\varepsilon_{\mathrm{r}}\frac{\omega_{\mathrm{ref}}^2}{c_0^2} - 2i\overbrace{\frac{\omega_{\mathrm{ref}}}{c_0^2}\left(\varepsilon_{\mathrm{r}} + \frac{1}{2}\omega_{\mathrm{ref}}\varepsilon_{\mathrm{r}}'\right)}^{=\frac{k_{\mathrm{ref}}}{v_{\mathrm{g}}}}\partial_t \\ &\quad + \frac{1}{c_0^2}\left(\varepsilon_{\mathrm{r}} + 2\omega_{\mathrm{ref}}\varepsilon_{\mathrm{r}}'\right)\partial_t^2\Bigg)\vec{\phi}^{\pm}.\end{aligned} \tag{4.24}$$

The term in-front of the first-order time derivative is related to the group velocity[1] v_{g}. Finally, the second-order time derivative of the linear polarization is expressed in terms of the electric field envelopes.

To incorporate the nonlinear dispersion of the gain medium in combination with the SVEA, the direct convolution method [37] is employed. Starting from the relation between the polarization and the electric field in (4.8) the SVEA is inserted

$$\begin{aligned}\Delta\vec{P}^{\pm}(t) &= \varepsilon_0 e^{\pm ik_{\mathrm{ref}}z}\int_{-\infty}^{t}\Delta\chi(t-\tau)\vec{\phi}^{\pm}(\tau)e^{-i\omega_{\mathrm{ref}}\tau}\,\mathrm{d}\tau \\ &= e^{\pm ik_{\mathrm{ref}}z}e^{-i\omega_{\mathrm{ref}}t}\underbrace{\varepsilon_0\int_{-\infty}^{t}\Delta\chi(t-\tau)\vec{\phi}^{\pm}(\tau)e^{-i\omega_{\mathrm{ref}}(\tau-t)}\,\mathrm{d}\tau}_{=\Delta\vec{p}^{\pm}(t)}\end{aligned} \tag{4.25}$$

to arrive at the definition of the time-dependent polarization envelope $\Delta\vec{p}^{\pm}(t)$. The total polarization is split up into forward and backward propagating components $\Delta\vec{P}(t) = \Delta\vec{P}^{+}(t) + \Delta\vec{P}^{-}(t)$. In the next step the complex envelope approach defined in (4.12) is inserted. Together with the expressions (4.24) and (4.25) for the polarization, this leads to

$$\begin{aligned}&\nabla_s\times\nabla_s\times\vec{\phi}_s^{\pm} - \left(\partial_x^2+\partial_y^2\right)\phi_z^{\pm}\vec{e}_z + \vec{e}_z\partial_z\nabla_s\cdot\vec{\phi}_s^{\pm} \\ &\pm ik_{\mathrm{ref}}\vec{e}_z\nabla_s\cdot\vec{\phi}_s^{\pm} + \partial_z\nabla_s\phi_z^{\pm} \pm ik_{\mathrm{ref}}\nabla_s\phi_z^{\pm} + k_{\mathrm{ref}}^2\vec{\phi}_s^{\pm} \mp 2ik_{\mathrm{ref}}\partial_z\vec{\phi}_s^{\pm} - \partial_z^2\vec{\phi}_s^{\pm} \\ &+\frac{1}{c_0^2}(\varepsilon_{\mathrm{r}}+2\omega_{\mathrm{ref}}\varepsilon_{\mathrm{r}}')\partial_t^2\vec{\phi}_s^{\pm} - 2i\frac{k_{\mathrm{ref}}}{v_{\mathrm{g}}}\partial_t\vec{\phi}_s^{\pm} - \frac{\omega_{\mathrm{ref}}^2}{c_0^2}\varepsilon_{\mathrm{ref}}\vec{\phi}_s^{\pm} \\ &+\frac{1}{c_0^2}(\varepsilon_{\mathrm{r}}+2\omega_{\mathrm{ref}}\varepsilon_{\mathrm{r}}')\partial_t^2\phi_z^{\pm}\vec{e}_z - 2i\frac{k_{\mathrm{ref}}}{v_{\mathrm{g}}}\partial_t\phi_z^{\pm}\vec{e}_z - \frac{\omega_{\mathrm{ref}}^2}{c_0^2}\varepsilon_{\mathrm{ref}}\phi_z^{\pm}\vec{e}_z \\ &= \mu_0\partial_t^2\Delta\vec{p}^{\pm} - 2i\omega_{\mathrm{ref}}\mu_0\partial_t\Delta\vec{p}^{\pm} - \omega_{\mathrm{ref}}^2\mu_0\Delta\vec{p}^{\pm} - \underbrace{\mu_0 e^{i(\mp k_{\mathrm{ref}}z+\omega_{\mathrm{ref}}t)}\partial_t\vec{J}}_{=\vec{S}_J}\end{aligned} \tag{4.26}$$

[1] For a dispersive medium with refractive index $n(\omega)$ the group velocity at reference frequency ω_{ref} is defined as $v_{\mathrm{g}} = \left(\frac{\mathrm{d}k}{\mathrm{d}\omega}\big|_{\omega_{\mathrm{ref}}}\right)^{-1} = \left(\frac{1}{c_0}\left.\frac{\mathrm{d}(\omega n(\omega))}{\mathrm{d}\omega}\right|_{\omega_{\mathrm{ref}}}\right)^{-1} = \frac{c_0}{n(\omega_{\mathrm{ref}})+\omega_{\mathrm{ref}}n'(\omega_{\mathrm{ref}})}$.

Additionally, the source term $\vec{S}_J$ is introduced. In the SVEA the second derivative, as well as the first derivative of the polarization envelope, are dropped under the assumption that $|\partial_t^2 \Delta\vec{p}^{\pm}| \ll |\omega_{\mathrm{ref}} \partial_t \Delta\vec{p}^{\pm}|$ and $|\partial_t \Delta\vec{p}^{\pm}| \ll |\omega_{\mathrm{ref}} \Delta\vec{p}^{\pm}|$ so that only the terms proportional to $\Delta\vec{p}^{\pm}$ remain in the wave equation. In the formulation (4.26) of the wave equation, the electric field components are separated into terms proportional to the transverse component and terms proportional to the longitudinal component. For the derivation of hybrid eigenmode weak-forms in Section 4.5.1 this formulation enables the separate application of different finite-element spaces for the (transverse) vector components and the longitudinal component.

Media with axial symmetry around the z-axis are investigated to derive a differential equation with only the transverse field components. The permittivity tensor for this type of material includes five independent entries and takes the form

$$\varepsilon = \begin{pmatrix} \varepsilon_{xx} & \varepsilon_{xy} & 0 \\ \varepsilon_{yx} & \varepsilon_{yy} & 0 \\ 0 & 0 & \varepsilon_{zz} \end{pmatrix}. \tag{4.27}$$

To separate (4.26) into two decoupled equations, one for the transverse field $\vec{\phi}_{\mathrm{t}}$ and one for the longitudinal component ϕ_z, the 3$^{\mathrm{rd}}$ Maxwell's equation under the assumption of a charge free space is used to express $\phi_z^{\pm}$ in terms of the transverse field [60]. Transformation of the electric displacement (4.6) into frequency domain $\vec{\tilde{D}}$ gives

$$\begin{aligned} 0 = \nabla \cdot \vec{\tilde{D}} = \nabla_{\mathrm{t}} \cdot (\tilde{\varepsilon}_{\mathrm{t}} \vec{\tilde{E}}_{\mathrm{t}}) + \tilde{E}_z \underbrace{\partial_z \tilde{\varepsilon}_{zz}}_{\approx 0} + \tilde{\varepsilon}_{zz} \partial_z \tilde{E}_z \\ \Leftrightarrow \partial_z \tilde{E}_z = -\frac{1}{\tilde{\varepsilon}_{zz}} \nabla_{\mathrm{t}} \cdot (\underbrace{\tilde{\varepsilon}_{\mathrm{t}} \vec{\tilde{E}}_{\mathrm{t}}}_{= \varepsilon_0 \vec{\tilde{E}}_{\mathrm{t}} + \vec{\tilde{P}}_{\mathrm{t}}}), \end{aligned} \tag{4.28}$$

where all quantities with tilde symbol are the respective frequency domain counterparts for the time domain fields. A slowly varying permittivity $|\partial_z \tilde{\varepsilon}_{zz}| \ll k_{\mathrm{ref}}$ along the propagation with respect to the reference wavelength is assumed. With the approximation that the dispersion in the longitudinal permittivity component is negligible so that $\tilde{\varepsilon}_{zz}(\omega) \approx \tilde{\varepsilon}_{zz}(\omega_{\mathrm{ref}}) = \varepsilon_{zz}$ Eq. (4.28) can be transformed back into the time domain

$$\partial_z E_z(t) = -\frac{1}{\varepsilon_{zz}} \nabla_{\mathrm{t}} \cdot (\varepsilon_0 \vec{E}_{\mathrm{t}}(t) + \vec{P}_{\mathrm{t}}(t)) \tag{4.29}$$

and the SVEA is inserted

$$\partial_z \phi_z^{\pm} \pm i k_{\mathrm{ref}} \phi_z^{\pm} = -\frac{1}{\varepsilon_{zz}} \nabla_{\mathrm{t}} \cdot (\varepsilon_{\mathrm{t}} \vec{\phi}_{\mathrm{t}}^{\pm} + \Delta\vec{p}_{\mathrm{t}}^{\pm}), \tag{4.30}$$

where analog to the transverse electrical field, $\Delta\vec{p}_{\mathrm{t}}^{\pm}$ is the transverse dynamic polarization. Finally, (4.30) is inserted into (4.26), so that by elimination of the longitudinal

field component (4.26) splits up into a set of two (instead of three) coupled equations

$$\begin{aligned}
&\partial_z^2\vec{\phi}_{\mathrm{t}}^{\pm} \pm 2ik_{\mathrm{ref}}\partial_z\vec{\phi}_{\mathrm{t}}^{\pm} - \frac{1}{c_0^2}(\varepsilon_{\mathrm{r,t}} + 2\omega_{\mathrm{ref}}\varepsilon'_{\mathrm{r,t}})\partial_t^2\vec{\phi}_{\mathrm{t}}^{\pm} + 2i\overbrace{\frac{\omega_{\mathrm{ref}}}{c_0^2}(\varepsilon_{\mathrm{r,t}} + \frac{1}{2}\omega_{\mathrm{ref}}\varepsilon'_{\mathrm{r,t}})}^{=\frac{k_{\mathrm{ref}}}{v_{\mathrm{g,t}}}}\partial_t\vec{\phi}_{\mathrm{t}}^{\pm} \\
&+ \left(\varepsilon_{\mathrm{r,t}}\frac{\omega_{\mathrm{ref}}^2}{c_0^2} - k_{\mathrm{ref}}^2\right)\vec{\phi}_{\mathrm{t}}^{\pm} + \nabla_{\mathrm{t}}^2\vec{\phi}_{\mathrm{t}}^{\pm} - \nabla_{\mathrm{t}}\left(\nabla_{\mathrm{t}}\cdot\vec{\phi}_{\mathrm{t}}^{\pm} - \frac{1}{\varepsilon_{zz}}\nabla_{\mathrm{t}}\left(\varepsilon_{\mathrm{r,t}}\vec{\phi}_{\mathrm{t}}^{\pm} + \Delta\vec{p}_{\mathrm{t}}^{\pm}\right)\right) \\
&= \omega_{\mathrm{ref}}^2\mu_0\Delta\vec{p}_{\mathrm{t}}^{\pm} + \vec{S}_{J,\mathrm{t}}
\end{aligned} \tag{4.31}$$

for the transverse components of the electric field.

4.3 Traveling-Wave Model in Time-Domain

In the TDTW model, an iterative approach is used to solve (4.31). To incorporate gain and refractive index dispersion alongside with the dynamics of the electric field an auxiliary polarization equation is employed. Coupling of Maxwell's equations and SBEs to model semiconductor lasers, including an update equation for the material polarization, is reported in [57]. In this model, the transverse directions are not considered so that no lateral mode patterns are obtained. Ning et al. [58] take into account dispersion of gain and refractive index of semiconductor medium and add carrier density and frequency dependence of the medium to the model. The effective Bloch equations are employed for the interaction of the medium and optical field in the models presented in [58, 61, 62]. Based on the works in [58], Moloney, Indik and Ning present a model [25] with full time, longitudinal and lateral space dependencies and apply it to simulate a Master-Oscillator Power-Amplifier (MOPA). In this model, polarization dynamics are included by a Lorentzian pole, and polarization, carrier diffusion equation and BPM are connected to a comprehensive TD-model. Similarly, in [62], a TDTW model is applied to investigate semiconductor optical amplifiers. The Lorentzian pole is fitted to the semiconductor's susceptibility spectrum. The TDTW formulation enables the computation

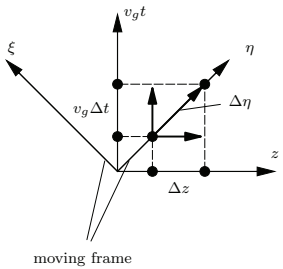

FIGURE 4.2: Schematic of moving frame.

of the temporal evolution for an electromagnetic field, which travels along a distinct direction with a SVE. The transformation of variables from the reference frame with three

space coordinates plus one time coordinate to the light-cone frame (Fig. 4.2) is utilized. This frame moves along with a light pulse, which travels at a constant group velocity (similar approaches are used in [63]). As described in (4.12), the complex electric field is separated into a fast oscillating phase along the propagation direction, the z-axis, and a fast oscillating phase in time and the complex envelope. Between the Cartesian frame with coordinates

$$\underline{x} = (x, y, z, t)\,, \tag{4.32}$$

and the light-cone frame with the coordinates

$$\underline{\zeta} = \left(x', y', \xi, \eta\right), \tag{4.33}$$

the coordinate transformation

$$\begin{aligned} x &= x', \\ y &= y', \\ \xi &= -z + v_\mathrm{g}\,(x, y)\,t, \\ \eta &= z + v_\mathrm{g}\,(x, y)\,t \end{aligned} \tag{4.34}$$

is performed. The partial derivatives transform according to

$$\partial_{x_i} = \partial_{x_i}\zeta_j \cdot \partial_{\zeta_j} \tag{4.35}$$

so that

$$\begin{aligned} \partial_x &= \partial_x x' \cdot \partial_{x'} + \partial_x \xi \cdot \partial_\xi + \partial_x \eta \cdot \partial_\eta + \partial_x y' \cdot \partial_{y'} \\ &= \partial_{x'} + t \cdot \partial_x v_\mathrm{g}\,(x, y) \cdot \partial_\xi + t \cdot \partial_x v_\mathrm{g}\,(x, y) \cdot \partial_\eta, \\ \partial_y &= \partial_y x' \cdot \partial_{x'} + \partial_y \xi \cdot \partial_\xi + \partial_y \eta \cdot \partial_\eta + \partial_y y' \cdot \partial_{y'} \\ &= \partial_{y'} + t \cdot \partial_y v_\mathrm{g}\,(x, y) \cdot \partial_\xi + t \cdot \partial_y v_\mathrm{g}\,(x, y) \cdot \partial_\eta, \\ \partial_z &= \partial_\eta - \partial_\xi, \\ \partial_t &= v_\mathrm{g}\,(x, y)\,\partial_\xi + v_\mathrm{g}\,(x, y)\,\partial_\eta, \end{aligned} \tag{4.36}$$

holds for the first-order derivatives. The second-order derivatives in time and along the propagation direction are

$$\begin{aligned} \partial_t^2 &= v_\mathrm{g}^2 \partial_\xi^2 + 2 v_\mathrm{g}^2 \partial_\xi \partial_\eta + v_\mathrm{g}^2 \partial_\eta^2, \\ \partial_z^2 &= \partial_\xi^2 - 2\partial_\xi \partial_\eta + \partial_\eta^2. \end{aligned} \tag{4.37}$$

The envelopes $\phi^+\,(\underline{x})$ and $\phi^-\,(\underline{x})$ describe the forward and backward traveling part of the light field with respect to the propagation direction. It is assumed that in the light-cone frame the corresponding envelopes are only dependent on three of the four coordinates $\phi^+\,(x', y', \eta)$ and $\phi^-\,(x', y', \xi)$, which means that during propagation the forward and backward fields do not couple to each other. This approximation is only valid if partial reflections for example due to diffraction at refractive index steps in the propagation direction, for example, in DFB lasers, are not taken into account. The reflections at the domain interfaces are treated as boundary conditions, which means that they are imposed on the fields at the respective locations. Since coupling between forward and backward propagating, inside the domain, the mixed derivatives

$$\partial_\xi \partial_\eta \phi^\pm = 0 \tag{4.38}$$

vanish. Insertion of the moving-frame coordinates $\frac{1}{v_g}\partial_t - \partial_z = 2\partial_\xi$ and $\frac{1}{v_g}\partial_t + \partial_z = 2\partial_\eta$, and of (4.37) for the second-order derivatives into the wave equation (4.31) yields

$$\begin{aligned}
&\underbrace{\left(\partial_\eta^2 - 2\partial_\eta\partial_\xi + \partial_\xi^2\right)}_{=\partial_z^2}\phi^\pm - \frac{1}{c_0^2}\left(n^2 + 4\omega_{\mathrm{ref}} n n'\right)\underbrace{v_g^2\left(\partial_\eta^2 - 2\partial_\eta\partial_\xi + \partial_\xi^2\right)}_{=\partial_t^2}\phi^\pm \\
&+ 2ik_{\mathrm{ref}}\left(\frac{1}{v_g}\partial_t \pm \partial_z\right)\phi^\pm - k_{\mathrm{ref}}^2\phi^\pm + \frac{n^2}{c_0^2}\omega_{\mathrm{ref}}^2\phi^\pm \\
&+ \nabla_{\mathrm{t}}^2\phi^\pm - \nabla_{\mathrm{t}}\left(\nabla_{\mathrm{t}}\cdot\phi^\pm - \frac{1}{n^2}\nabla_{\mathrm{t}}\cdot\left(n^2\phi^\pm + \Delta p^\pm\right)\right) \\
&- \omega_{\mathrm{ref}}^2\mu_0\Delta p^\pm - S_J = 0.
\end{aligned} \tag{4.39}$$

In the scope of the TDTW method, scalar fields $\phi^\pm$ in isotropic media with refractive index n and the refractive index dispersion $n' = \frac{\mathrm{d}n(\omega)}{\mathrm{d}\omega}|_{\omega_{\mathrm{ref}}}$ are employed. The reference wavenumber is related to the reference refractive index $k_{\mathrm{ref}} = \frac{\omega_{\mathrm{ref}}}{c_0} n_{\mathrm{ref}}$. As described above, the mixed derivatives drop out so that the equations for the forward and backward propagating fields are[2]

$$\begin{aligned}
&\left(1 - \frac{n_{\mathrm{ref}}^2}{n^2}\right)\partial_{\eta/\xi}^2\phi^\pm + 4ik_{\mathrm{ref}}\partial_{\eta/\xi}\phi^\pm \\
&+ k_0^2\left(n^2 - n_{\mathrm{ref}}^2\right)\phi^\pm + \nabla_{\mathrm{t}}^2\phi^\pm - \nabla_{\mathrm{t}}\left(\nabla_{\mathrm{t}}\cdot\phi^\pm - \frac{1}{n^2}\nabla_{\mathrm{t}}\cdot\left(n^2\phi^\pm + \Delta p^\pm\right)\right) \\
&- \omega_{\mathrm{ref}}^2\mu_0\Delta p^\pm - S_J = 0.
\end{aligned} \tag{4.40}$$

In this formulation, the number of dimensions of the differential equation is reduced by one. The spatial direction z and time t are replaced by one of the coordinates η and ξ. If the reference index is equal to the refractive index n, the second-order terms vanish. However, in the scope of the SVEA, it is assumed that $|\partial_t^2\phi| \ll |\omega_{\mathrm{ref}}\partial_t\phi|$ and $|\partial_z^2\phi| \ll |k_{\mathrm{ref}}\partial_z\phi|$, so that the second-order terms are neglected. The iteration is similar to the one for the BPM. The propagation equation is solved for the transverse spatial directions, which, for the case of the FD-BPM, leads to propagation along the longitudinal direction or, in the case of the TWTD method along the longitudinal direction and forward in time simultaneously. Consequently, in the case of the BPM, the field is not only propagated along the propagation direction but, implicitly, also forward in time. In the FD-BPM, each longitudinal step is accompanied by a forward step in time so that the series of field profiles is a collection of snapshots along an increasing timeline. The drawback of the FD method with Fox-Li iteration emerges from the interaction of forward and backward traveling components with the medium. At each longitudinal position, the field values are valid for different times so that evaluation of the intensity in the Fox-Li iteration (to compute stimulated recombination) is only valid if the solutions converge because in this case, the temporal variation vanishes.

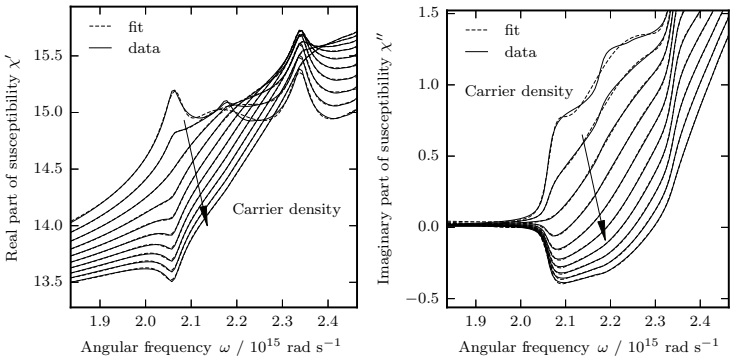

FIGURE 4.3: Fitted real (left) and imaginary (right) part of electrical susceptibility of a semiconductor gain medium with carrier densities $1 \cdot 10^{-5}$, 1.05, 2.11, 3.16, 4.21, 5.26, 6.32, 7.37, 8.42, 9.47 $1 \cdot 10^{24}\,\mathrm{m}^{-3}$ at 325 K. The fit (dashed lines in plots) is performed independently for each value of the carrier density. A number of 4 poles is used.

4.3.1 Complex-Conjugate Pole-Residue Pairs

The dispersion of the susceptibility is modeled by a series of M complex-conjugate pole-residue pairs [64]

$$\begin{aligned}\tilde{\chi}(\omega-\omega_{\mathrm{ref}}) &= \tilde{\chi}(\omega_{\mathrm{ref}}) + \Delta\tilde{\chi}(\omega-\omega_{\mathrm{ref}}) \\ &= \varepsilon_\infty - 1 + \sum_{m=0}^{M} \frac{c_m}{i(\omega-\omega_{\mathrm{ref}})-a_m} + \sum_{m=0}^{M} \frac{c_m^*}{i(\omega-\omega_{\mathrm{ref}})-a_m^*}. \end{aligned} \tag{4.41}$$

Han uses this approach to derive an auxiliary differential equation for the material response in the scope of the Finite-Differences Time-Domain (FDTD) method [64]. With a corresponding choice of the coefficients a_m and c_m both Debye and Lorentz poles are modeled within a unified formulation. With a sufficient number of poles, the expansion (4.41) is suited to resemble both imaginary and real part of the susceptibility of a semiconductor gain medium, see Fig. 4.3. Analog to the susceptibility, the polarization is split up into a sum of contributions from each complex-pole pair. In the numerical model, each of these summands is stored in a separate field. Since the addition of multiple poles is straightforward, the notation is simplified in the following and derivations are performed for only one pole-pair. The Fourier-transform of $\Delta p(t)$ from (4.25) gives

$$\Delta\tilde{p}_\alpha^{\pm}(\omega) = \varepsilon_0 \Delta\tilde{\chi}_{\alpha\beta}(\omega-\omega_{\mathrm{ref}})\tilde{\phi}_\beta^{\pm}(\omega), \tag{4.42}$$

[2]The term in-front of the second-order derivative is approximated by

$$\frac{v_{\mathrm{g}}^2}{c_0^2}(n^2+4\omega_{\mathrm{ref}}nn') = \frac{n^2+4\omega_{\mathrm{ref}}nn'}{(n^2+\omega_{\mathrm{ref}}nn')^2} n_{\mathrm{ref}}^2 \approx \frac{n_{\mathrm{ref}}^2}{n^2} \quad \text{for} \quad \frac{n'}{n} \ll 1.$$

which is the frequency domain relation between electric field and polarization. Inserting (4.41) into (4.42) leads to

$$\begin{aligned}&(-\omega^2 + 2\omega\omega_{\mathrm{ref}} - i\omega a^* - \omega_{\mathrm{ref}}^2 + i\omega_{\mathrm{ref}} a^* - i\omega a + i\omega_{\mathrm{ref}} a + |a|^2)\Delta\tilde{p}^{\pm} \\ &= \varepsilon_0 c(i\omega - i\omega_{\mathrm{ref}} - a^*)\tilde{\phi}^{\pm} + \varepsilon_0 c^*(i\omega - i\omega_{\mathrm{ref}} - a)\tilde{\phi}^{\pm}\end{aligned} \tag{4.43}$$

and transformation back to the time domain gives

$$\begin{aligned}\partial_t^2\Delta p^{\pm} - 2i\omega_{\mathrm{ref}}\partial_t\Delta p^{\pm} - \omega_{\mathrm{ref}}^2\Delta p^{\pm} = 2a'\partial_t\Delta p^{\pm} + \left(-2i\omega_{\mathrm{ref}}a' - |a|^2\right)\Delta p^{\pm} \\ +2c'\varepsilon_0\partial_t\phi^{\pm} + \left(-ca^* - c^*a - 2i\omega_{\mathrm{ref}}c'\right)\varepsilon_0\phi^{\pm}.\end{aligned} \tag{4.44}$$

As stated above, $\partial_t^2\Delta p^{\pm} \to 0$ is neglected so that (4.44) reduces to

$$\begin{aligned}&\partial_t\Delta p^{\pm} + \frac{-\omega_{\mathrm{ref}}^2 + 2i\omega_{\mathrm{ref}}a' + |a|^2}{-2i\omega_{\mathrm{ref}} - 2a'}\Delta p^{\pm} \\ &= \frac{c'\varepsilon_0}{-i\omega_{\mathrm{ref}} - a'}\partial_t\phi^{\pm} + \frac{\left(-ca^* - c^*a - 2i\omega_{\mathrm{ref}}c'\right)\varepsilon_0}{-2i\omega_{\mathrm{ref}} - 2a'}\phi^{\pm}.\end{aligned} \tag{4.45}$$

Eq. (4.45) is the auxiliary material update equation, which is solved in addition to the electric field traveling-wave propagation and carrier rate equation.

4.3.2 Lorentzian Oscillators

The approach presented in [58] is adapted to approximate the frequency dependent susceptibility by a superposition of Lorentzian oscillators. Setting the real part of the coefficient c to zero $c' = 0$ yields a model for Lorentzian oscillators based on the general expression (4.45)

$$\partial_t\Delta p^{\pm} + \frac{\omega_{\mathrm{ref}}^2 - 2i\omega_{\mathrm{ref}}a' - |a|^2}{2i\omega_{\mathrm{ref}} + 2a'}\Delta p^{\pm} = \frac{c''a'\varepsilon_0}{i\omega_{\mathrm{ref}} + a'}\phi^{\pm}. \tag{4.46}$$

In this form, the time derivative of the electric field is removed, which otherwise has to be approximated from past time steps in the numerical model. This simplified the polarization update equation. The susceptibility for a Lorentzian pole is [58]

$$\Delta\tilde{\chi}(\omega) = \frac{A(N,T)}{\omega - \omega_{\mathrm{p}}(N,T) + i\gamma(N,T)}, \tag{4.47}$$

where the parameters for amplitude A, detuning ω_p, and spectral broadening γ are functions of carrier density N and temperature T. However, it is assumed that the carrier density and temperature vary slowly in time and consequently the temporal dependence of the parameters of the Lorentzian pole is neglected [58]. The frequency dependent part of the susceptibility is linked to the differential gain Δg and differential carrier-induced refractive index change $\Delta\delta n$

$$\Delta\tilde{\chi}(\omega) = 2n(\omega_{\mathrm{ref}})\Delta\delta n(\omega,N,T) - \frac{i}{k_{\mathrm{ref}}}n(\omega_{\mathrm{ref}})\Delta g(\omega,N,T). \tag{4.48}$$

Insertion of (4.47) into (4.42) and transformation into the TD gives

$$\partial_t\Delta p^{\pm} = \underbrace{\left(i\omega_{\mathrm{p}}(N,T) + \gamma(N,T)\right)}_{=c_{p,0}}\Delta p^{\pm} + \underbrace{i\varepsilon_0 A(N,T)}_{=c_{p,1}}\phi^{\pm} \tag{4.49}$$

which is equivalent to (4.46). The auxiliary differential equation for the polarization time step is discretized with the Crank-Nicolson scheme

$$\Delta p^{\pm}_{n+1} = \frac{1 + c_{p,0}\frac{\Delta t}{2}}{1 - c_{p,0}\frac{\Delta t}{2}} \Delta p^{\pm}_{n} + \frac{\Delta t c_{p,1}}{1 - c_{p,0}\frac{\Delta t}{2}} \phi^{\pm}_{n+\frac{1}{2}}. \tag{4.50}$$

The update equation for the polarization does not include any spatial derivatives and thus, reduces to an element-wise vector manipulation after discretization.

4.3.3 Discretization of the Time-Domain Traveling-Wave Model

In this section, the discretization for the time marching based on the wave equation (4.40) is presented. With neglection of second-order derivatives Eq. (4.40) is written in short form

$$\partial_{\eta/\xi} \phi^{\pm} = H \phi^{\pm} + \alpha \Delta p^{\pm}, \tag{4.51}$$

with the operator H, which contains only spatial derivatives in the transverse coordinates and the scalar factor $\alpha = -i\omega^2_{\mathrm{ref}}\mu_0/(4k_{\mathrm{ref}})$. The transverse derivatives are discretized with either FDM or FEM. Applying the operator H to the field leads to a propagation of the wave along the characteristics direction η or ξ. The propagation operator H does not differ for the forward or backward propagation. The field values along the z, t, ξ and η coordinates are approximated at discrete points

$$\begin{aligned} z_k &= z_0 + k\Delta z, \\ t_n &= t_0 + n\Delta t, \\ \xi_\mu &= \xi_0 + \mu\Delta\xi, \\ \eta_\nu &= \eta_0 + \nu\Delta\eta, \end{aligned} \tag{4.52}$$

where the coordinates with subscript zero represent the origin. The grid spacings are $\Delta z, \Delta t, \Delta\xi$, and $\Delta\eta$, and the indices $k, n, \mu, \nu \in \mathbb{N}$ iterate over the domain. From the first, second and the last line of (4.52), together with the definition of the moving frame coordinates (4.34), the relation

$$\begin{aligned} \eta_\nu = z_k + v_{\mathrm{g}} t_n &= \underbrace{z_0 + v_{\mathrm{g}} t_0}_{=\eta_0} + k\Delta z + v_{\mathrm{g}} n \Delta t \\ \Leftrightarrow \nu\Delta\eta &= (k+n)\Delta z \end{aligned} \tag{4.53}$$

is derived. The spacing Δ is related to the spatial and temporal discretization, but it is not uniquely defined by the above equation. The grid size is chosen so that a step along the characteristic corresponds to one step in time and one in space

$$(\nu+1)\Delta\eta = (k+1+n+1)\Delta z \Leftrightarrow \Delta\eta = 2\Delta z. \tag{4.54}$$

Based on these relations the spacings are

$$\Delta\xi = \Delta\eta = 2\Delta z = 2v_{\mathrm{g}}\Delta t. \tag{4.55}$$

To discretize (4.51) forward differences for $\partial_{\eta/\xi}$ and an average value for the right-hand side are used

$$\begin{aligned} \frac{\phi^{\pm}_{\nu+1} - \phi^{\pm}_{\nu}}{\Delta\eta} &= H_{\nu+\frac{1}{2}} \frac{\phi^{\pm}_{\nu+1} + \phi^{\pm}_{\nu}}{2} + \alpha \Delta p^{\pm}_{\nu+\frac{1}{2}} \\ \Leftrightarrow \frac{\phi^{\pm}_{n+1,k\pm1} - \phi^{\pm}_{n,k}}{\Delta\eta} &= H_{n+\frac{1}{2},k\pm\frac{1}{2}} \frac{\phi^{\pm}_{n+1,k\pm1} + \phi^{\pm}_{n,k}}{2} + \alpha \Delta p^{\pm}_{n+\frac{1}{2},k\pm\frac{1}{2}}. \end{aligned} \tag{4.56}$$

Rearranging gives

$$\left(1 - \frac{\Delta\eta}{2} H_{n+\frac{1}{2},k\pm\frac{1}{2}}\right) \phi^{\pm}_{n+1,k\pm1} = \left(1 + \frac{\Delta\eta}{2} H_{n+\frac{1}{2},k\pm\frac{1}{2}}\right) \phi^{\pm}_{n,k} + \Delta\eta\alpha\Delta p^{\pm}_{n+\frac{1}{2},k\pm\frac{1}{2}}. \tag{4.57}$$

This equation is similar to the equation for the BPM in the implicit scheme (see Section 4.4.1). The spatial indices of the operator $H_{n+\frac{1}{2},k\pm\frac{1}{2}}$ and polarization envelope $\Delta p_{n+\frac{1}{2},k\pm\frac{1}{2}}$ indicate that the material values used to construct the FDM or FEM matrix are approximated by the values given for the slices between two grid knots. It is assumed that the material properties vary much slower than the fields in time and thus are constant throughout one time step so that the temporal index is

$$H_{n+\frac{1}{2},k\pm\frac{1}{2}} \approx H_{n,k\pm\frac{1}{2}}. \tag{4.58}$$

Eq. (4.57) is the update equation for the field envelope in the implicit scheme. After discretization, the resulting sparse-matrix system is solved by suitable iterative solvers. However, an alternative scheme for the field update is proposed, which yields an explicit update equation and circumvents the need for the solution of a sparse matrix problem. In [65], the Iterated Crank-Nicolson (ICN) (see Appendix C.18) scheme is applied to derive an explicit method for the vectorial beam propagation

$$\phi^{\pm}_{n+1,k\pm1} = \left(\sum_{i=0}^{N} c_i (\Delta\eta H)^i\right) \phi^{\pm}_{n,k} + \left(\sum_{i=0}^{N-1} c_{i+1} (\Delta\eta H)^i\right) \Delta\eta\alpha\Delta p_{n+\frac{1}{2},k\pm\frac{1}{2}}. \tag{4.59}$$

The coefficients for the paraxial approximation are $c = (1, 1, a_2, a_1 a_2)$ and $N = 3$. In Section 4.4.2, the same scheme is applied for the FD-BPM.

4.4 Beam Propagation Method in Frequency-Domain

The evolution of the electric field between transverse slices along the optical axis is computed with the paraxial or WA-BPM [60]. The electric field decomposed into a Fourier series with separated time-harmonic phases, fast oscillating phases in the propagation direction (z-axis), and a time-independent SVE for each frequency m[3]

$$\vec{E}(x, y, z, t) = \sum_{m=1}^{M} \vec{\phi}_m(x, y, z) \cdot \exp(i k_{\mathrm{ref},m} z) \cdot \exp(-i\omega_m t), \tag{4.60}$$

[3]Though the formalism is generalized using a sum of M different fields with frequencies ω_m, in the following the wave equation for a field with one discrete frequency ω is derived to make the notation not too complex. Since the wave equation is linear in the electric field, the solutions for each frequency can be superimposed.

with $j = x, y, z$. Taking the curl of the 1st Maxwell's equation (4.1), elimination of the magnetic field component with the 2nd equation and insertion of (4.60) leads to

$$\begin{aligned} \nabla \times \left(\mu^{-1} \nabla \times \vec{E}\right) &= -\partial_t^2 \left(\varepsilon \vec{E}\right) \\ \Leftrightarrow \nabla \times \left(\mu^{-1} \nabla \times \vec{E}\right) &= \omega^2 \varepsilon \vec{E} \\ \Leftrightarrow \nabla \times \left(\mu_\mathrm{r}^{-1} \nabla \times \vec{E}\right) &= k_0^2 \varepsilon_\mathrm{r} \vec{E}, \end{aligned} \tag{4.61}$$

the time-harmonic wave equation for the electric field. Separation of the transverse and longitudinal components, analog to the derivation of (4.26), leads to the full-vectorial wave equation

$$\begin{aligned} &\nabla_s \times \nabla_s \times \vec{\phi}_s - \left(\partial_x^2 + \partial_y^2\right) \phi_z \vec{e}_z + \vec{e}_z \partial_z \nabla_s \cdot \vec{\phi}_s \\ &+ \vec{e}_z i k_\mathrm{ref} \nabla_s \cdot \vec{\phi}_s + \partial_z \nabla_s \phi_z + i k_\mathrm{ref} \nabla_s \phi_z \\ &+ k_\mathrm{ref}^2 \vec{\phi}_s - 2 i k_\mathrm{ref} \partial_z \vec{\phi}_s - \partial_z^2 \vec{\phi}_s \\ &- k_0^2 \mu_\mathrm{r} \varepsilon_\mathrm{r} \vec{\phi}_s - k_0^2 \mu_\mathrm{r} \varepsilon_\mathrm{r} \phi_z \vec{e}_z = 0 \end{aligned} \tag{4.62}$$

in FD. Transverse anisotropic media with axial symmetry around the propagation axis with a permittivity tensor of the form (4.27) is modeled. The tensor for the transverse components ε_t is defined in (4.14). For the two-dimensional case, the off-diagonal terms $\varepsilon_{xy} = \varepsilon_{yx} = 0$ are set to zero. Analog to the derivation of the transverse wave equation (4.31), the 3rd Maxwell's equation is used to eliminate the longitudinal component ϕ_z in (4.62) and decouple the equations for the transverse field

$$\begin{aligned} &\partial_z^2 \phi_\mu + 2 i k_\mathrm{ref} \partial_z \phi_\mu + \partial_{ii} \phi_\mu + (\varepsilon_{\mathrm{r},\mu\nu} (\omega/c_0)^2 - k_\mathrm{ref}^2 \delta_{\mu\nu}) \phi_\nu \\ &- \partial_\mu \left(\partial_i \phi_i - \frac{1}{\varepsilon_{\mathrm{r},zz}} \partial_j \left(\varepsilon_{\mathrm{r},j\nu} \phi_\nu \right) \right) = 0, \end{aligned} \tag{4.63}$$

where $i, j, \mu, \nu = x, y$ are the indices for the transverse directions. With the operator R (with components given in the Appendix C.13) the short notation reads

$$\partial_z^2 \phi_\mu + 2 i k_\mathrm{ref} \partial_z \phi_\mu + R_{\mu\nu} \phi_\nu = 0. \tag{4.64}$$

To discretize the operator R on a transverse spatial grid, the entries

$$\begin{aligned} H_{ij}^{\mu\nu} &= \delta_{\mu\nu} \delta_{ij} - \delta_{j\mu} \delta_{i\nu} + \delta_{i\mu} \frac{\varepsilon_{\mathrm{r},j\nu}}{\varepsilon_{\mathrm{r},zz}}, \\ H_{i\rightarrow}^{\mu\nu} &= \delta_{i\mu} \frac{1}{\varepsilon_{\mathrm{r},zz}} \partial_j \varepsilon_{\mathrm{r},j\nu}, \\ H_{i\leftarrow}^{\mu\nu} &= 0, \\ H_0^{\mu\nu} &= k_0^2 \left(\varepsilon_{\mathrm{r},\mu\nu} - n_\mathrm{ref}^2 \delta_{\mu\nu} \right). \end{aligned} \tag{4.65}$$

are inserted for the terms in (B.2) and discretized with the FDM as introduced in the Appendix B.

4.4.1 Implicit Method for Beam Propagation

Eq. (4.64) is a second-order partial differential equation, which is formally solved [66] by

$$\vec{\phi}_{\mathrm{t}}(x,y,z) = \exp\left(ik_{\mathrm{ref}}\left(\pm\sqrt{1+\frac{R}{k_{\mathrm{ref}}^2}}-1\right)(z-z_0)\right)\vec{\phi}_{\mathrm{t}}(x,y,z_0). \tag{4.66}$$

Taking the derivative along the propagation direction gives

$$\partial_z\vec{\phi}_{\mathrm{t}}(x,y,z) = ik_{\mathrm{ref}}\left(\pm\sqrt{1+X}-1\right)\vec{\phi}_{\mathrm{t}}(x,y,z), \tag{4.67}$$

with $X = \frac{R}{k_{\mathrm{ref}}^2}$. This first-order differential in z is approximated with the Crank-Nicolson scheme

$$\begin{aligned}\left(1-i\frac{k_{\mathrm{ref}}\Delta z}{2}\left(\sqrt{1+X}-1\right)\right)\vec{\phi}_{\mathrm{t}}(x,y,z+\Delta z)\\ = \left(1+i\frac{k_{\mathrm{ref}}\Delta z}{2}\left(\sqrt{1+X}-1\right)\right)\vec{\phi}_{\mathrm{t}}(x,y,z),\end{aligned} \tag{4.68}$$

where only the positive branch of (4.67) is carried on. To solve the implicit equation, the square-root operator is approximated by a rational fraction of operators [67]

$$\sqrt{1+X}-1 \simeq \frac{N_n}{D_m} \tag{4.69}$$

with n and m denoting the order of the approximation. If the standard Padé approximation is applied evanescent modes are not damped correctly due to the real approximation coefficients [67]. The drawback is overcome by using the modified Padé approximation. Application of the first-order modified Padé rational approximation [68] yields the governing equation for the implicit WA-BPM

$$(1+\zeta R)\,\vec{\phi}_{\mathrm{t}}(x,y,z+\Delta z) = (1+\zeta^* R)\,\vec{\phi}_{\mathrm{t}}(x,y,z) \tag{4.70}$$

with

$$\zeta = \frac{1}{4k_{\mathrm{ref}}^2(1+i\frac{\beta}{2})} - i\frac{\Delta z}{4k_{\mathrm{ref}}} \tag{4.71}$$

According to [68] the damping factor is set to $\beta = 2$. Discretization of (4.70) leads to a sparse-matrix equation, which is solved with the iterative *BiCGStab* algorithm.

4.4.2 Explicit Method for Beam Propagation

Similar to the derivation of the explicit scheme of the field update in the TD formulation (Section 4.3), the ICN scheme [65] is utilized to get an explicit update equation for (4.64)

$$\vec{\phi}_{\mathrm{t}}(x,y,z+\Delta z) = \left(\sum_{i=0}^{N} c_i (H)^i\right)\vec{\phi}_{\mathrm{t}}(x,y,z), \tag{4.72}$$

with the operator

$$H = \frac{\Delta z}{2ik_{\mathrm{ref}}}R. \tag{4.73}$$

The coefficients for the paraxial approximation are $c_{\text{paraxial}} = (1, 1, a_2, a_1 a_2)$ and $N = 3$. For the wide-angle approximation, the coefficients are [65]

$$c_{\text{wide-angle}} = \begin{pmatrix} 1 \\ 1 \\ a_2 - i\frac{1}{2}\beta \\ -\frac{1}{2}\beta^2 - ia_2\beta + a_1 a_2 \\ -a_2\frac{5}{2}\beta^2 - ia_1 a_2\frac{3}{2}\beta \\ ia_2\beta^3 - a_1 a_2\frac{9}{4}\beta^2 \\ a_2\frac{1}{2}\beta^4 + ia_1 a_2\frac{13}{8}\beta^3 \\ a_1 a_2\frac{9}{8}\beta^4 \\ -ia_1 a_2\frac{3}{8}\beta^5 \\ -a_1 a_2\frac{1}{8}\beta^6 \end{pmatrix} \tag{4.74}$$

with $\beta = \frac{1}{k_{\text{ref}}\Delta z}$, $N = 9$ and $a_1, a_2 = 1/2$. For numerical computations, quantities are scaled to dimensionless variables

$$\begin{aligned} \tilde{k}_{\text{ref}} &= x_0 k_{\text{ref}}, & \vec{\tilde{\phi}}_{\text{t}} &= \frac{\vec{\phi}_{\text{t}}}{E_0}, & \partial_{\tilde{z}} &= x_0 \partial_z, \\ \Delta\tilde{z} &= \frac{\Delta z}{x_0}, & \tilde{R} &= x_0^2 R, & \tilde{\zeta} &= \frac{\Delta\tilde{z}}{2i\tilde{k}_{\text{ref}}}, \end{aligned} \tag{4.75}$$

where x_0 is a characteristic length scale and E_0 is a characteristic scale for the field envelope. An example of the propagation of a Gaussian field profile using the explicit scheme is given in Appendix C.14.

4.5 Waveguide Eigenmodes with Polarization

In contrast to the definition of the SVE in (4.12) the envelopes for the eigenmodes $\vec{e}$ and $\vec{h}$ do neither depend on the longitudinal coordinate z nor on time t. The fields are

$$\begin{aligned} \vec{E}(x, y, z, t) &= \vec{e}(x, y) \cdot \exp\left(ik_{\text{ref}} z - i\omega_0 t\right), \\ \vec{H}(x, y, z, t) &= \vec{h}(x, y) \cdot \exp\left(ik_{\text{ref}} z - i\omega_0 t\right). \end{aligned} \tag{4.76}$$

The envelopes for an eigenmode are invariant with respect to propagation. The electric field is time-harmonic but still oscillates corresponding to the eigenmodes reference wavenumber.

4.5.1 Hybrid Modes

The classification of waveguide eigenmodes is based on conditions for the longitudinal electric or the magnetic field components. Transverse Electric (TE) modes fulfill $E_z = 0$ and $H_z \neq 0$, Transverse Magnetic (TM) modes $E_z \neq 0$ and $H_z = 0$, Transverse Electric and Magnetic (TEM) modes $E_z = 0$ and $H_z = 0$. The remaining modes $E_z \neq 0$ and $H_z \neq 0$ are hybrid modes [69]. In [70, 71] the calculation of waveguide eigenmodes based on the FEM is demonstrated (also utilizing the *FEniCS* software package). Here, the work of Lezar and Davidson [71] (who adopted the approach from [72]) is extended, so that the eigenvalue equation includes anisotropic, complex permittivity, which allows to model loss or gain. Insertion of envelopes which only depend on transverse coordinates in (C.105) leads to the vanishing of all terms with time derivatives and derivatives in the

propagation direction. The formulation of the weak problem for (C.105) is given in the Appendix C.17. The eigenmode condition is fulfilled if the derivatives of the envelope along the propagation direction vanish. However, in (C.105) there are still terms of different powers of the propagation wavevector k_{ref} and k_{ref}^2, so that this equation cannot directly be written as an eigenvalue equation. To circumvent this, the longitudinal component $\tilde{\phi}_z = {}^{\phi_z}/_{ik_{\mathrm{ref}}}$ and the corresponding test function $\tilde{v}_z = {}^{v_z}/_{ik_{\mathrm{ref}}}$ are transformed. Insertion of the transformation into (C.105) leads to

$$\begin{aligned}
&\int_\Omega \mathrm{curl_t}(\vec{\phi}_\mathrm{t})\,\mathrm{curl_t}(\vec{v}_\mathrm{t}^*) \\
&- k_0^2\mu_\mathrm{r}\left(\varepsilon_{\mathrm{r,t}}\vec{\phi}_\mathrm{t}\right)\cdot\vec{v}_\mathrm{t}^* \\
&+ k_{\mathrm{ref}}^2\left(\nabla_\mathrm{t}\tilde{\phi}_z\cdot\nabla_\mathrm{t}\tilde{v}_z^* + \vec{\phi}_\mathrm{t}\cdot\nabla_\mathrm{t}\tilde{v}_z^* + \nabla_\mathrm{t}\tilde{\phi}_z\cdot\vec{v}_\mathrm{t}^* + \vec{\phi}_\mathrm{t}\cdot\vec{v}_\mathrm{t}^* - k_0^2\mu_\mathrm{r}\varepsilon_{zz}\tilde{\phi}_z\tilde{v}_z^*\right) \\
&+ ik_{\mathrm{ref}}k_0^2\mu_\mathrm{r}\left(\varepsilon_{z,\mathrm{t}}\cdot\vec{\phi}_\mathrm{t}\tilde{v}_z^* + \varepsilon_{z,\mathrm{t}}\cdot\vec{v}_\mathrm{t}^*\tilde{\phi}_z\right)\mathrm{d}x\,\mathrm{d}y = 0.
\end{aligned} \tag{4.77}$$

In the notation, the complex conjugate of the test functions and the introduced transformation of the longitudinal component of the test function is not altered. But the test functions can be re-defined corresponding to $\vec{v}_\mathrm{t}^* \to \vec{v}_\mathrm{t}$ and $\tilde{v}_z^* \to v_z$ to make the equations more readable. Even after the transformation in Eq. (4.77) there are still terms proportional to ik_{ref} present. To make those vanish, it is required that the components of the vector $(\varepsilon_{z,\mathrm{t}})_i = 0$ are all zero. Otherwise, the above equation cannot be written as an eigenvalue problem. This emerges from the fact that anisotropy of the medium introduced by $\varepsilon_{z,\mathrm{t}}$ leads to a walk-off of the propagating light, transverse to the propagation direction. In this case, there are no invariant field configurations for the structure. The weak-form for the eigenvalue equation of hybrid polarization modes with eigenvalue k_{ref} for the eigenfunctions $\vec{\phi}_\mathrm{t}, \tilde{\phi}_z$ is [70, 71]

$$\int_\Omega s_{\mathrm{tt}} - t_{\mathrm{tt}}\,\mathrm{d}x\,\mathrm{d}y = k_{\mathrm{ref}}^2\int_\Omega -s_{zz} + t_{zz} - b_{\mathrm{tt}} - b_{\mathrm{tz}} - b_{\mathrm{zt}}\,\mathrm{d}x\,\mathrm{d}y. \tag{4.78}$$

The terms read

$$\begin{aligned}
s_{\mathrm{tt}} &= \mathrm{curl_t}(\vec{\phi}_\mathrm{t})\,\mathrm{curl_t}(\vec{v}_\mathrm{t}),\\
t_{\mathrm{tt}} &= k_0^2\mu_\mathrm{r}\left(\varepsilon_{\mathrm{r,t}}\vec{\phi}_\mathrm{t}\right)\cdot\vec{v}_\mathrm{t},\\
s_{zz} &= \nabla_\mathrm{t}\tilde{\phi}_z\cdot\nabla_\mathrm{t}v_z,\\
t_{zz} &= k_0^2\mu_\mathrm{r}\varepsilon_{zz}\tilde{\phi}_z v_z,\\
b_{\mathrm{tt}} &= \vec{\phi}_\mathrm{t}\cdot\vec{v}_\mathrm{t},\\
b_{\mathrm{tz}} &= \nabla_\mathrm{t}\tilde{\phi}_z\cdot\vec{v}_\mathrm{t},\\
b_{\mathrm{zt}} &= \vec{\phi}_\mathrm{t}\cdot\nabla_\mathrm{t}v_z.
\end{aligned} \tag{4.79}$$

The discretization of (4.78) with the FEM leads to an algebraic system of equations

$$\begin{aligned}
\begin{pmatrix} S_{\mathrm{tt}} - T_{\mathrm{tt}} & 0 \\ 0 & 0 \end{pmatrix}\begin{pmatrix} \{\vec{\phi}_\mathrm{t}\} \\ \{\tilde{\phi}_z\} \end{pmatrix} &= k_{\mathrm{ref}}^2\begin{pmatrix} -B_{\mathrm{tt}} & -B_{\mathrm{tz}} \\ -B_{\mathrm{zt}} & -S_{zz} + T_{zz} \end{pmatrix}\begin{pmatrix} \{\vec{\phi}_\mathrm{t}\} \\ \{\tilde{\phi}_z\} \end{pmatrix} \\
&\Leftrightarrow A\{\vec{\phi}\} = \lambda B\{\vec{\phi}\}
\end{aligned} \tag{4.80}$$

which is solved with the *SLEPc* eigensolver [73] for the eigenvalue $\lambda = k_{\mathrm{ref}}^2$. A set of eigenmodes is calculated for the transverse waveguide of device D1, defined in Tb. C.2.

A spatially constant gain is added to the QW in the region under the injection stripe, and the hybrid eigenmodes with the highest gain are computed. The calculation reveals that the waveguide supports both (quasi) TE and (quasi) TM modes. Both sets of

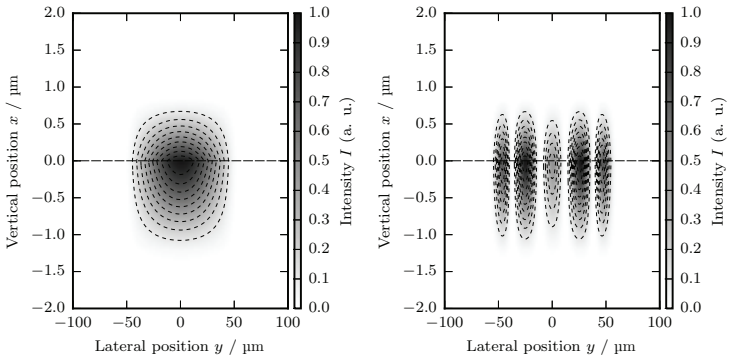

FIGURE 4.4: Intensity of TE eigenmodes number 1 and 3.

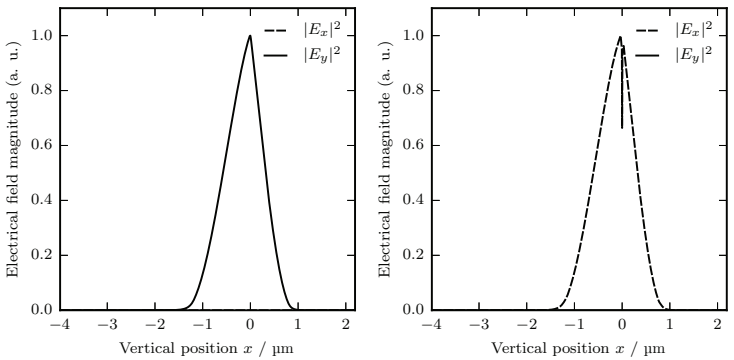

FIGURE 4.5: Vertical intensity of TE eigenmode number 3 (left) and TM eigenmode number 1 (right).

modes are separated with respect to their polarization orientation so that one mode is either TE-like ($\rho_y > 0.99$) or TM-like ($\rho_y < 0.01$), see Fig. 4.6. However, the effective refractive indexes for both TE and TM modes are close (Fig. 4.6), and the modes occur in pairs with similar spatial intensity profiles (Fig. 4.5). This suggests that the coupling, which is induced by an anisotropic permittivity, between pairs of TE and TM modes, is high. Stress-induced polarization rotations are discussed in Chapter 5. Transverse eigenmodes are computed as part of the electro-optical model, which is introduced in Chapter 6.

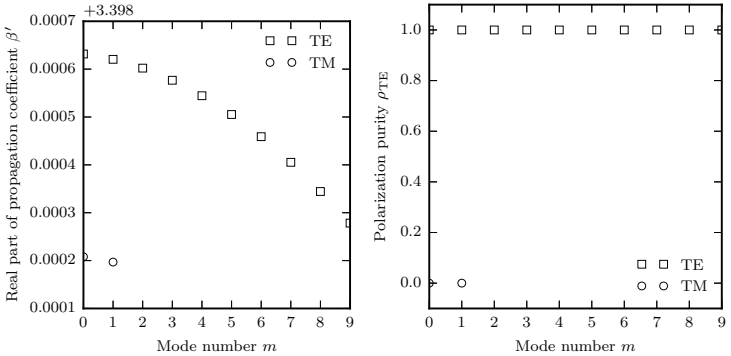

FIGURE 4.6: Real part (left) of complex eigenvalues and polarization purity (right) for TE and TM waveguide modes.

4.5.2 TE and TM Eigenmodes for Vertical Waveguide

In the 1+1 dimensional model (presented in Chapter 8) the beam propagation and carrier updates are reduced to the two-dimensional QW plane. The vertical direction is decoupled from the problem by application of the Effective Index Method (EIM) [74], which means that instead of solving the optical problem in a three-dimensional waveguide it is solved in a plane where the effective refractive index of the (fundamental) mode in the vertical direction is employed for each lateral position. Therefore, structures with ridges or trenches that do not necessarily penetrate through the QW but influence the guidance of the light are included in the 1+1 dimensional model. In this section the governing equations for TE and TM modes are presented, which in the following are employed to determine the effective refractive index of the fundamental mode, optical confinement factor and modal loss for the vertical TE and TM modes. The modal loss is computed from the free-carrier absorption, where contributions from the doping carrier density in the passive waveguide are taken into account. As stated above for TE modes the condition $E_z = 0$ is fulfilled. For a one-dimensional domain with spatial coordinate x (and an infinite extent in y-direction) the TE eigenmode equation for the y-component of the electric field envelope $e_y(x)$ is

$$\partial_x^2 e_y + k_0^2 n^2 e_y = k_{\mathrm{ref}}^2 e_y, \tag{4.81}$$

which is derived from (4.11). For the TM eigenmodes, the wave equation for the y-component of the magnetic field envelope $h_y(x)$

$$\partial_x \left(\frac{1}{n^2} \partial_x h_y \right) + k_0^2 h_y = \frac{k_{\mathrm{ref}}^2}{n^2} h_y \tag{4.82}$$

is solved. The electric and magnetic field components and the refractive index are related $k_z h_y = \omega \varepsilon_0 n^2 e_x$ so that discontinuities in the refractive index transfer to discontinuities in the electric field component. Additionally to the mode properties in the (lateral) center of the waveguide, the change of effective refractive index below the trenches is determined. Under the trench, the semiconductor is insulated with a layer of SiN, which is covered by the p-metallization. For the SiN, an absorption coefficient of $100\,\mathrm{m}^{-1}$ and

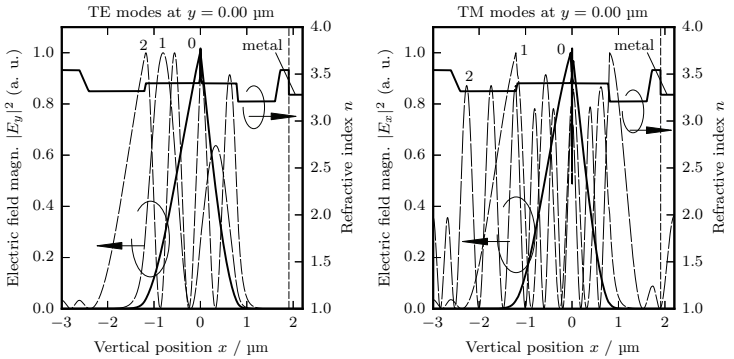

FIGURE 4.7: Vertical TE (left) and TM (right) eigenmodes (first three) for epitaxial structure E1 under the injection contact (lateral position $y = 0\,\mu m$). Details about the structure are summarized in Tb. C.1.

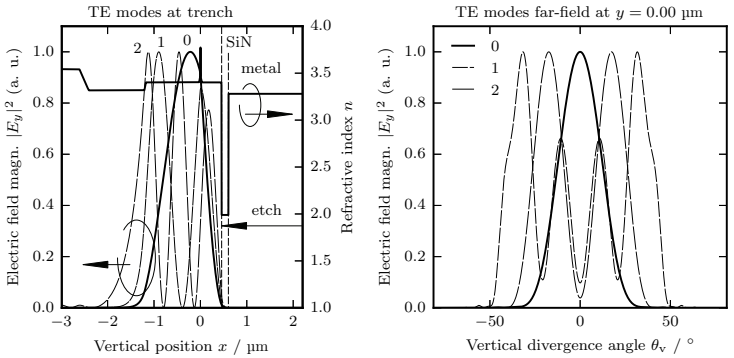

FIGURE 4.8: Left: Vertical TE eigenmodes (first three) for epitaxial structure E1 under a trench with depth 1.45 µm. Right: Far-field for vertical eigenmodes under the injection opening.

a permittivity of 3.958 (at 950 nm) is used, and for the metalization, the properties of Ti, a permittivity of 10.76 and absorption coefficient of 43.5 are inserted. For a 1.45 µm deep trench (Fig. 4.9) the effective refractive index difference for the fundamental mode TE under the contact opening (Fig. 4.7) and below an index trench (Fig. 4.8) amounts to $\delta n_t = 38.4 \cdot 10^{-4}$. The effective refractive index for the fundamental mode TE is 3.3996. These values are utilized in combination with the EIM to reduce the transverse structure to the QW plane in the 1+1 dimensional model. The confinement factor is $7.212 \cdot 10^{-3}$ for the fundamental TE mode and $4.615 \cdot 10^{-3}$ for the fundamental TM mode. For the second TE mode, the confinement is $3.8868 \cdot 10^{-3}$ which is about half the value of the fundamental mode. Additionally, the modal loss increases from $16\,m^{-1}$ for the fundamental TE mode to $107\,m^{-1}$ for the second TE mode. Both the lower confinement and the higher losses damp the second (and higher) TE modes and suppress lasing during operation.

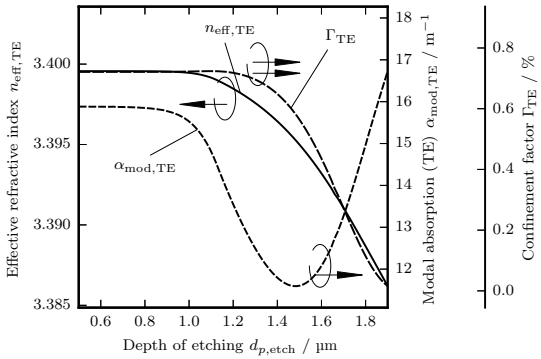

FIGURE 4.9: Effective refractive index, optical confinement factor and modal absorption (due to doping profile) for fundamental vertical TE eigenmode as a function of etch depth under the trench for epitaxial structure E1.

4.6 Chapter Summary

The SVEA is applied to formulate a frequency-domain WA-BPM for transverse anisotropic media and a time-domain traveling-wave method. Both methods employ similar propagation equations, compare Eqs. (4.51) and (4.40) with (4.63) and (4.64). To solve these equations, in addition to the implicit Crank-Nicolson scheme, an explicit update equation in combination with the Iterated Crank-Nicolson (ICN) [65] is used which circumvents the need for the solution of a sparse matrix problem and therefore results in shorter computation times. The propagation equation is solved for the transverse spatial directions, which, for the case of the FD-BPM, leads to propagation along the longitudinal direction or, in the case of the TDTW method along the longitudinal direction and forward in time simultaneously. To incorporate the temporal response of the polarization in the TD model, an auxiliary equation for the SVE of the material polarization resulting from the direct convolution method [37] is employed. In the FD-BPM, each longitudinal step is accompanied by a forward step in time so that the series of field profiles is a collection of snapshots along an increasing timeline. At each longitudinal position, the field values are valid for different times so that evaluation of the intensity in the Fox-Li iteration is only valid if the solutions converge because in this case, the temporal variation vanishes.

The calculation of the hybrid eigenmodes reveals that the waveguide of the device D1 supports both (quasi) TE and (quasi) TM modes, which occur in pairs with similar spatial intensity profiles (Fig. 4.5). Besides the frequency- and time-domain propagation methods, the outcomes of this chapter include the vertical profile for the TE eigenmodes, the optical confinement factor, effective refractive index, vertical FF divergence angle, and the change of the effective refractive index under the trenches. These values are utilized as input parameters in combination with the EIM to reduce the transverse structure to the QW plane in the 1+1 dimensional FD and TD model (Chapter 7).

Chapter 5

Opto-Mechanical Model

Experiments show that packaged SEs and diode LAs yield DOP values between about 90% and 98%. The DOP changes with current and typically decreases by less than 2% over a current range of 20 A per emitter. High DOP is crucial for diode laser systems which rely on polarization combining. The overall electro-optical efficiency of the diode laser system reduces with decreasing DOP, either of individual emitters or diode laser arrays. The motivations for the development of an opto-mechanical model for the computation of DOP in HPDLs are:

1. Significant changes in DOP observed between different diode products.
2. No coherent explanation or understanding for the root causes of DOP reduction on different packaging platforms.
3. Improved and stable (between production runs) DOP is crucial for product performance.
4. DOP is an indicator for stress in the device, which leads to reduced lifetimes.

In diode lasers with compressive strained QWs (InGaAs/AlGaAs wells on a GaAs substrate), the gain for TM-polarized light is significantly reduced compared to the gain for TE-polarized light. Although strain states, which counteract the intrinsic compressive (in-plane) strain by the introduction of tensile strain to the QW, increase the overall gain for TM-modes, the transparency carrier density to raise the TM-modes above lasing threshold remains relatively high compared to the TE threshold. The fact that for devices with (overall) low DOP, the DOP value is already low slightly above the threshold indicates that the reduced DOP cannot be entirely explained by an increase in the gain of the TM-modes since TM-modes would reach the threshold at higher currents. Then, at low currents, only TE emission would be observed. The TM-modes lase at a different wavelength since the TM-gain spectrum is shifted towards lower wavelengths. The shift amounts up to $\approx 70\,\mathrm{nm}$ (Tb. 2.1) for the $In_{0.2}Ga_{0.8}As$ QW from Section 2.4. If up to 10 % of the emitted light is emitted at lower wavelengths, it should be observed in the spectrum, which is not the case in the investigated laser devices. One could argue that when TM-modes reach the threshold, the TM-polarized light emitted at the peak of the TM-gain is reabsorbed by stimulated absorption. While propagating through the device, it would be re-emitted into the TE-mode at the TE-gain peak wavelength, due to the higher value of the TE-gain compared to the TM-gain. This

conversion takes place, but it leads to an increase in the DOP since the re-emitted light is TE-polarized. This suggests that the gain anisotropy alone is not the cause for the measured DOP reduction but that polarization rotation occurs due to stress-induced birefringence. The light which is initially TE polarized undergoes polarization rotation while propagating through a birefringent waveguide. Anisotropic gain still influences the DOP since rotated TE light, which becomes TM polarized, is partially absorbed in the TM transitions. This interplay is analyzed in Section 5.2.5. The goal for this chapter is an opto-mechanical model which describes influences on the DOP based on gain characteristics and anisotropic permittivity. Since both gain and refractive index anisotropies emerge from the mechanical state of the device, the stress and strain play a central role in the root cause analysis for the major influencing factors of the DOP, see Fig. 5.1. The

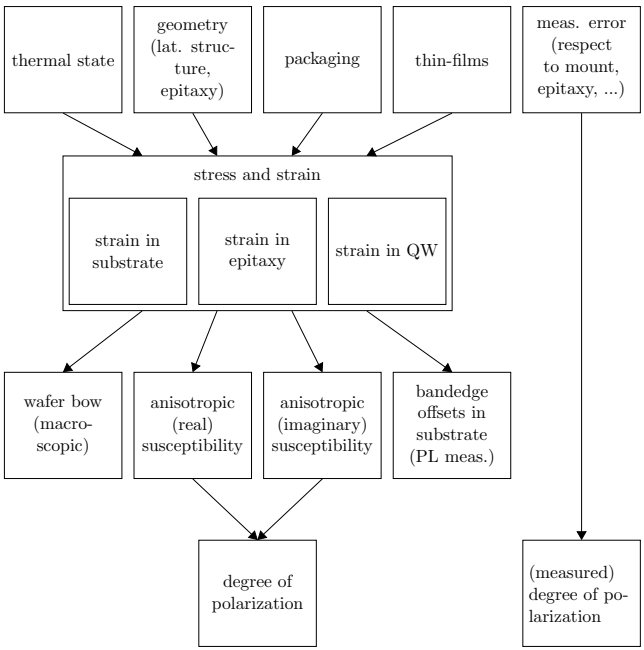

FIGURE 5.1: Root cause analysis for the degree of polarization.

influencing factors of the DOP are clustered into four groups: The *thermal state* of the device, including thermal strains due to heating during device operation in conjunction with different Coefficients of Thermal Expansion (CTEs), for example, between semiconductor and submount or heatsink. The second group *geometry* includes geometric features of the device. These are the thicknesses and compositions of the epitaxial layers and lateral geometries as such as trenches or ridges. The strain accumulates, especially around these geometrical features, and their shape and position influence the emerging birefringence. The third group collects *packaging* influences, such as stress, which results from the soldering process. During wafer-processing stress is built into the deposited *thin-films*, such as SiN or the p-side metallization. This stress partially relaxes and induces strain in the waveguide, especially around trenches or ridges of the waveguide. In the next section, the linear elasticity theory is summarized, which is followed by the

description of refractive index changes based on photoelasticity. An analytical and numerical model, which accounts for interaction with the active media, is introduced to derive the correlation between strain and resulting DOP. In the preceding two sections the opto-mechanical model is applied to investigate the DOP reduction due to thin-film stresses around trenches and due to packaging induced stress in LAs.

5.1 Linear Elasticity

The equation constituting the mechanical equilibrium is

$$\partial_j \sigma_{ij} = f_i, \;\; \vec{x} \text{ in } \Omega, \tag{5.1}$$

where $\sigma_{ij}(\vec{x})$ are the components of the stress tensor (in units Nm^{-2}), and $f_i(\vec{x})$ are the components of an applied force density (in units Nm^{-3}). The indices i, j run over the directions of the spatial domain Ω. For the linear elastic model [75, 76] Hook's law

$$\sigma_{ij} = c_{ijkl} s_{kl} \tag{5.2}$$

gives the relation between stress $\sigma_{ij}(\vec{x})$ and strain $s_{ij}(\vec{x})$ with the stiffness tensor $c_{ijkl}(\vec{x})$. The strain field is denoted with s_{ij} and not with ε_{ij} as it is usually done in literature to not confuse it with the permittivity in the following derivations. The second order differential equation for the displacement field $\vec{u}\,(\vec{x})$ (in units m) reads

$$\partial_i c_{kilj} \partial_j u_l = f_k, \tag{5.3}$$

with $i, j, k, l = 1, 2, 3$. In general, the stiffness tensor is a rank four tensor and thus has $3^4 = 81$ entries. The stress tensor σ_{ij} and strain tensor s_{ij} are both symmetric so that $\sigma_{ij} = \sigma_{ji}$ and $s_{ij} = s_{ji}$. This implies symmetry of the stiffness tensor

$$c_{ijkl} = c_{jikl} = c_{jilk}, \tag{5.4}$$

so that at most 36 of its entries are independent. For sufficient small deformations of a solid body in the scope of the infinitesimal strain theory, the strain tensor

$$s_{ij}\,(u) = \frac{1}{2}\left(\partial_j u_i + \partial_i u_j\right) \tag{5.5}$$

is defined with the help of the gradients of the displacement field u. Dirichlet boundary conditions are applied on the borders $\delta\Omega_\mathrm{D}$ and Neumann boundary conditions on the parts $\delta\Omega_\mathrm{N}$ of the domain.

$$\begin{aligned} \vec{u} &= \vec{u}_\mathrm{D}, \;\; \vec{x} \text{ on } \delta\Omega_\mathrm{D}, \\ \sigma_{ij} n_i &= \sigma_{\mathrm{ext},j}, \;\; \vec{x} \text{ on } \delta\Omega_\mathrm{N}. \end{aligned} \tag{5.6}$$

On the Neumann boundaries, the surface-force density is $\sigma_{\mathrm{ext},j}$ (given in units Nm^{-2}) and $\vec{n}$ denotes the surface normal on the boundary. To compute the unknown displacement field $\vec{u}$ with the FEM, the weak-form of the mechanical equilibrium equation (5.3) is derived. The multiplication of both sites of (5.3) with the vectorial test function $\vec{v} \in \hat{V}$

and integration over the entire spatial domain leads to

$$\begin{aligned}
\int_\Omega f_i v_i \,\mathrm{d}^3x &= \int_{\delta\Omega} c_{ijkl}\partial_l u_k \, v_i n_j \,\mathrm{d}s - \int_\Omega c_{ijk}\partial_l u_k \, \partial_j v_i \,\mathrm{d}^3x \\
&= \int_{\delta\Omega} \sigma_{ij}(\vec{u}) v_i n_j \,\mathrm{d}s - \int_\Omega \sigma_{ij}(\vec{u})\partial_j v_i \,\mathrm{d}^3x \\
&= \int_{\delta\Omega} \sigma_{ij}(\vec{u}) v_i n_j \,\mathrm{d}s - \int_\Omega \frac{1}{2}\left(\sigma_{ij}(\vec{u})\partial_j v_i + \sigma_{ji}(\vec{u})\partial_j v_i\right) \mathrm{d}^3x \\
&= \int_{\delta\Omega} \sigma_{ij}(\vec{u}) v_i n_j \,\mathrm{d}s - \int_\Omega \frac{1}{2}\sigma_{ij}(\vec{u})\left(\partial_j v_i + \partial_i v_j\right) \mathrm{d}^3x \\
\Leftrightarrow \int_\Omega f_i v_i \,\mathrm{d}^3x &= \int_{\delta\Omega_\mathrm{N}} \sigma_{\mathrm{ext},i} v_i \,\mathrm{d}^3x - \int_\Omega \sigma_{ij}(\vec{u}) s_{ij}(\vec{v}) \,\mathrm{d}^3x. \qquad (5.7)
\end{aligned}$$

In the last step, the Neumann boundary condition (5.6) is inserted and n_i are the components of the normal vector on the domain boundaries. Each component of the test function is in the test space $\hat{V} = \{v_i \in H^1(\Omega) : v_i = 0 \,\mathrm{on}\, \delta\Omega\}$, where $H^1(\Omega)$ is the Sobolev space. Details about the solution of PDEs in *FeniCS* are found in [77]. To account for stress and strains that remain after relaxation of a domain which is initially strained, for example, caused by temperature change due to thermal expansion or contraction, the total strain

$$s_{ij}^{(\mathrm{R})} = s_{ij}(\vec{u}) - s_{ij}^{(0)} \qquad (5.8)$$

is split up into the initial strain $s^{(0)}$ and the *resulting* part $s^{(\mathrm{R})}$. In the case of a temperature change, the thermally induced strain is the product of the temperature change and the coefficient of thermal expansion (CTE) of the material $s^{(0)} = s^{(\mathrm{T})} = \alpha_{\mathrm{CTE}}\Delta T$. Analog to the definition of the resulting strain the stress is split into the *resulting*

$$\sigma_{ij}^{(\mathrm{R})} = c_{ijkl} s_{kl}^{(\mathrm{R})} = \sigma_{ij}(\vec{u}) - c_{ijkl} s_{kl}^{(0)} \qquad (5.9)$$

and initial contribution. Due to the symmetry of the strain and stress tensors not all components need to be stored (explicitly) for numerical computations and resources can be reduced by storing only the upper (or lower) triangular part of the tensor. In the three-dimensional case, the components with one index are introduced for the stress

$$(\sigma_1, \sigma_2, \sigma_3, \sigma_4, \sigma_5, \sigma_6) = (\sigma_{11}, \sigma_{22}, \sigma_{33}, \sigma_{23}, \sigma_{13}, \sigma_{12}) \qquad (5.10)$$

and for the strain

$$(s_1, s_2, s_3, s_4, s_5, s_6) = (s_{11}, s_{22}, s_{33}, s_{23}, s_{13}, s_{12}) \qquad (5.11)$$

so that the stiffness tensor can be written as a 6×6 matrix with entries c_{ij}. In this notation, the tensor equation

$$\sigma_{ij} = c_{ijkl} s_{kl}, \qquad (5.12)$$

is written as a matrix and vector multiplication

$$\sigma_i = c_{ij} s_j. \qquad (5.13)$$

For material with cubic symmetry, the 6×6 stiffness matrix [78]

$$c = \begin{pmatrix} C_{11} & C_{12} & C_{12} & 0 & 0 & 0 \\ C_{12} & C_{11} & C_{12} & 0 & 0 & 0 \\ C_{12} & C_{12} & C_{11} & 0 & 0 & 0 \\ 0 & 0 & 0 & 2C_{44} & 0 & 0 \\ 0 & 0 & 0 & 0 & 2C_{44} & 0 \\ 0 & 0 & 0 & 0 & 0 & 2C_{44} \end{pmatrix} \tag{5.14}$$

includes 3 independent entries C_{11}, C_{12} and C_{44}. The independent coefficients and non-vanishing entries of the fourth rank stiffness tensor are related via

$$\begin{aligned} C_{11} &= c_{1111} = c_{2222} = c_{3333}, \\ C_{12} &= c_{1122} = c_{1133} = c_{2233}, \\ C_{44} &= c_{1212} = c_{1313} = c_{2323}, \end{aligned} \tag{5.15}$$

in the introduced notation.

5.2 Photo Elasticity

For the study in this section, the components of the permittivity are real numbers so that there is no gain or loss included in the model. Nevertheless, in Section 5.2.5 additional to the birefringence induced by the photo-elastic effect [79, 80], anisotropic amplification is added to study polarization in active devices. The perturbation of the inverse dielectric tensor is

$$\left(\Delta\varepsilon^{-1}\right)_{ij} = p_{ijkl} s_{kl}. \tag{5.16}$$

The coefficients of the strain tensor are s_{ij}, and the coefficients of the photo-elastic tensor are p_{ijkl}. For the non-zero dielectric tensor entries the contracted notation is introduced

$$(\varepsilon_1, \varepsilon_2, \varepsilon_3, \varepsilon_4, \varepsilon_5, \varepsilon_6) = (\varepsilon_{11}, \varepsilon_{22}, \varepsilon_{33}, \varepsilon_{23}, \varepsilon_{13}, \varepsilon_{12}) \tag{5.17}$$

and analog for the strain entries

$$(s_1, s_2, s_3, s_4, s_5, s_6) = (s_{11}, s_{22}, s_{33}, s_{23}, s_{13}, s_{12}). \tag{5.18}$$

For material with cubic symmetry, the photo-elastic tensor consists of 3 independent entries P_{11}, P_{12} and P_{44} and takes the following form

$$p = \begin{pmatrix} P_{11} & P_{12} & P_{12} & 0 & 0 & 0 \\ P_{12} & P_{11} & P_{12} & 0 & 0 & 0 \\ P_{12} & P_{12} & P_{11} & 0 & 0 & 0 \\ 0 & 0 & 0 & 2P_{44} & 0 & 0 \\ 0 & 0 & 0 & 0 & 2P_{44} & 0 \\ 0 & 0 & 0 & 0 & 0 & 2P_{44} \end{pmatrix} \tag{5.19}$$

In this notation, the coefficients P_{ij} are related to the non-vanishing entries of the photo-elastic tensor by

$$\begin{aligned} P_{11} &= p_{1111} = p_{2222} = p_{3333}, \\ P_{12} &= p_{1122} = p_{1133} = p_{2233}, \\ P_{44} &= p_{1212} = p_{1313} = p_{2323}. \end{aligned} \tag{5.20}$$

The impermeability tensor is the inverse of the permittivity tensor ε^{-1} with the components $\left(\varepsilon^{-1}\right)_{ij}$. The change of the dielectric tensor $\Delta\varepsilon_{ij}$ is related to the change of the inverse dielectric tensor $\left(\Delta\varepsilon^{-1}\right)_{ij}$. The inverse tensor is defined by

$$\left(\varepsilon^{-1}\right)_{ik} \varepsilon_{kj} = \delta_{ij}. \tag{5.21}$$

The variation of (5.21) gives

$$\begin{aligned} &\left(\Delta\varepsilon^{-1}\right)_{ik} \varepsilon_{kj} + \left(\varepsilon^{-1}\right)_{ik} \Delta\varepsilon_{kj} = 0 \\ \Leftrightarrow\ &\left(\varepsilon^{-1}\right)_{ik} \Delta\varepsilon_{kj} = -\left(\Delta\varepsilon^{-1}\right)_{ik} \varepsilon_{kj} \\ \Leftrightarrow\ &\left(\varepsilon^{-1}\right)_{il} \Delta\varepsilon_{lj} = -\left(\Delta\varepsilon^{-1}\right)_{ik} \varepsilon_{kj} \\ \Leftrightarrow\ &\varepsilon_{mi} \left(\varepsilon^{-1}\right)_{il} \Delta\varepsilon_{lj} = -\varepsilon_{mi} \left(\Delta\varepsilon^{-1}\right)_{ik} \varepsilon_{kj} \\ \Leftrightarrow\ &\delta_{ml} \Delta\varepsilon_{lj} = -\varepsilon_{mi} \left(\Delta\varepsilon^{-1}\right)_{ik} \varepsilon_{kj} \\ \Leftrightarrow\ &\Delta\varepsilon_{mj} = -\varepsilon_{mi} \left(\Delta\varepsilon^{-1}\right)_{ik} \varepsilon_{kj} \\ \Leftrightarrow\ &\Delta\varepsilon_{ij} = -\varepsilon_{im} \left(\Delta\varepsilon^{-1}\right)_{mk} \varepsilon_{kj}. \end{aligned} \tag{5.22}$$

In the last step, the indices $m \leftrightarrow i$ are renamed.

The photo-elastic coefficients for the ternary alloys $Al_xGa_{1-x}As$ and $In_xGa_{1-x}As$ are calculated based on material models and measurements proposed by Adachi in [80], [81] and [82]. Similar to the refractive index the photo-elastic coefficients depend on wavelength and alloy concentration x. The resulting values are shown in Fig. 5.2.

5.2.1 Orientation of Crystallographic Lattice

Note that the coordinate system has to correspond to the crystallographic structure. The orientation of the crystals symmetry frame with respect to the propagation direction can be chosen so that the x-, y- and z-axis correspond to the $\langle 100 \rangle$ directions. Or the symmetry frame of the crystal is rotated 45 degrees around the x-axis so that the propagation direction (z-axis) points along the (011) direction. Group III-IV semiconductor laser facets are usually cleaved along the $\{011\}$ planes. If the orientation is such that the propagation direction is parallel to (011) a transformation of the photo-elastic tensor p from the symmetry frame of the crystal to the rotated frame p' is performed. The expression of the dielectric tensor and strain tensor in the so called Kelvin (or Mandel) notation [1] leads to a formulation, in which the transformation of the photo-elastic tensor is expressed by

$$p' = \hat{R}^{\mathrm{T}} p \hat{R}, \tag{5.23}$$

[1] In the Kelvin notation, the components of the $\mathbb{R}^6$ vectors are related to the components of the second rank tensors ε_{ij} by $(\varepsilon_1, \varepsilon_2, \varepsilon_3, \varepsilon_4, \varepsilon_5, \varepsilon_6) = (\varepsilon_{11}, \varepsilon_{22}, \varepsilon_{33}, \sqrt{2}\varepsilon_{23}, \sqrt{2}\varepsilon_{13}, \sqrt{2}\varepsilon_{12})$, and analog for s_{ij} by $(s_1, s_2, s_3, s_4, s_5, s_6) = (s_{11}, s_{22}, s_{33}, \sqrt{2}s_{23}, \sqrt{2}s_{13}, \sqrt{2}s_{12})$ [83]. Here, the non-diagonal components are multiplied by a factor of $\sqrt{2}$ in comparison to the introduction in Eqs. (5.17) and (5.18).

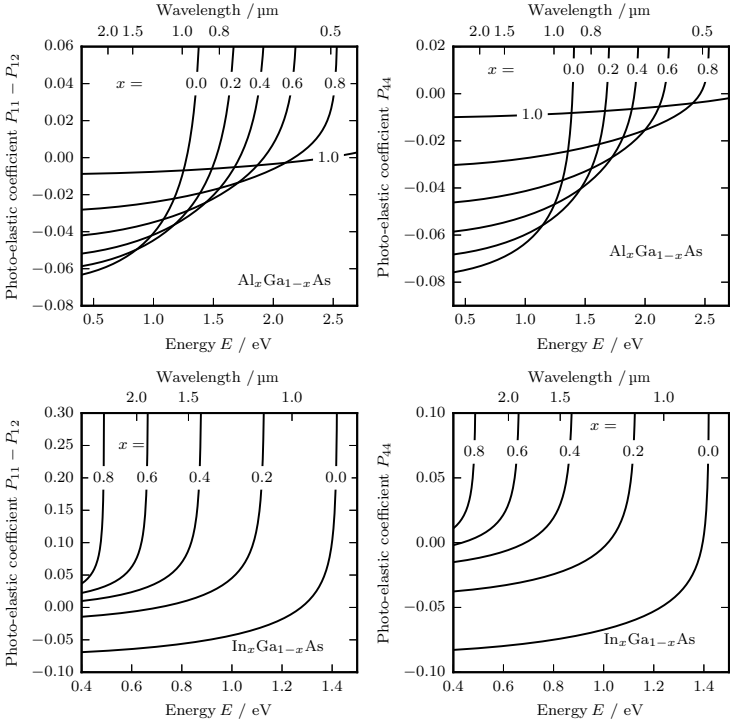

FIGURE 5.2: Photo-elastic coefficients for the ternary semiconductors $Al_xGa_{1-x}As$ (top row) and $In_xGa_{1-x}As$ (bottom row) [80, 81, 82].

Both tensors are written in the contracted Kelvin notation as 6×6 matrices. In this formulation, the transformation matrix $\hat{R}$ is orthogonal and is a second-rank tensor [83]. To perform a rotation around the x-axis, the components of the rotation matrix

$$R = \begin{pmatrix} 1 & 0 & 0 \\ 0 & \cos(\theta) & \sin(\theta) \\ 0 & -\sin(\theta) & \cos(\theta) \end{pmatrix} \tag{5.24}$$

are inserted into the expression for the transformation $\hat{R}$ as given in [83], so that the 6×6 transformation matrix reads

$$\hat{R} = \begin{pmatrix} 1 & 0 & 0 & 0 & 0 & 0 \\ 0 & \cos^2(\theta) & \sin^2(\theta) & \sqrt{2}\sin(\theta)\cos(\theta) & 0 & 0 \\ 0 & \sin^2(\theta) & \cos^2(\theta) & -\sqrt{2}\sin(\theta)\cos(\theta) & 0 & 0 \\ 0 & -\sqrt{2}\sin(\theta)\cos(\theta) & \sqrt{2}\sin(\theta)\cos(\theta) & \cos^2(\theta) - \sin^2(\theta) & 0 & 0 \\ 0 & 0 & 0 & 0 & \cos(\theta) & -\sin(\theta) \\ 0 & 0 & 0 & 0 & \sin(\theta) & \cos(\theta) \end{pmatrix}. \tag{5.25}$$

For a rotation about an angle $\theta = \frac{\pi}{4}$ with $\cos(\frac{\pi}{4}) = \sin(\frac{\pi}{4}) = \frac{1}{\sqrt{2}}$ the matrix yields

$$\hat{R}_{\frac{\pi}{4}} = \begin{pmatrix} 1 & 0 & 0 & 0 & 0 & 0 \\ 0 & \frac{1}{2} & \frac{1}{2} & \frac{1}{\sqrt{2}} & 0 & 0 \\ 0 & \frac{1}{2} & \frac{1}{2} & -\frac{1}{\sqrt{2}} & 0 & 0 \\ 0 & -\frac{1}{\sqrt{2}} & \frac{1}{\sqrt{2}} & 0 & 0 & 0 \\ 0 & 0 & 0 & 0 & \frac{1}{\sqrt{2}} & -\frac{1}{\sqrt{2}} \\ 0 & 0 & 0 & 0 & \frac{1}{\sqrt{2}} & \frac{1}{\sqrt{2}} \end{pmatrix} \tag{5.26}$$

Evaluation of Eq. (5.23) results in the transformed photo-elastic tensor in contracted notation

$$p' = \begin{pmatrix} P'_{11} & P'_{12} & P'_{12} & 0 & 0 & 0 \\ P'_{12} & P'_{22} & P'_{23} & 0 & 0 & 0 \\ P'_{12} & P'_{23} & P'_{22} & 0 & 0 & 0 \\ 0 & 0 & 0 & 2P'_{66} & 0 & 0 \\ 0 & 0 & 0 & 0 & 2P'_{44} & 0 \\ 0 & 0 & 0 & 0 & 0 & 2P'_{44} \end{pmatrix} \tag{5.27}$$

with the entries

$$\begin{aligned} P'_{11} &= P_{11}, \\ P'_{12} &= P_{12}, \\ P'_{22} &= \frac{P_{11} + P_{12} + 2P_{44}}{2}, \\ P'_{23} &= \frac{P_{11} + P_{12} - 2P_{44}}{2}, \\ P'_{44} &= P_{44}, \\ P'_{66} &= \frac{P_{11} - P_{12}}{2}. \end{aligned} \tag{5.28}$$

Finally, the perturbation of the inverse permeability tensor

$$\left(\Delta\varepsilon^{-1}\right)'_{ij} = p'_{ijkl} s'_{kl} \tag{5.29}$$

is given in the frame rotated with respect to the symmetry of the crystal lattice. After transformation of the second-rank and fourth-rank tensors the factor $\sqrt{2}$, which is added in the Kelvin notation, can be dropped since the upper-right and lower-left 3×3 block in (5.27) contains only zeros. The notation given in (5.17) and (5.18) is used for the following analysis.

5.2.2 Isotropic Permittivity

For an isotropic permittivity in the undisturbed case, the permittivity tensor is proportional to the identity tensor

$$\varepsilon_{ij} = \varepsilon_{11} \delta_{ij}, \tag{5.30}$$

and thus, the perturbation of the permittivity reads

$$\Delta\varepsilon_{ij} = -\varepsilon_{11}^2 \left(\Delta\varepsilon^{-1}\right)_{ij} = -\varepsilon_{11}^2 p_{ijkl} s_{kl}. \tag{5.31}$$

For the photo-elastic tensor, the components of a material with cubic symmetry (5.19) are inserted for the diagonal terms

$$\begin{pmatrix} \Delta\varepsilon_{11} \\ \Delta\varepsilon_{22} \\ \Delta\varepsilon_{33} \end{pmatrix} = -\varepsilon_{11}^2 \begin{pmatrix} P_{11} & P_{12} & P_{12} \\ P_{12} & P_{22} & P_{23} \\ P_{12} & P_{23} & P_{22} \end{pmatrix} \cdot \begin{pmatrix} s_{11} \\ s_{22} \\ s_{33} \end{pmatrix}. \tag{5.32}$$

and for the non-diagonal terms

$$\begin{pmatrix} \Delta\varepsilon_{23} \\ \Delta\varepsilon_{13} \\ \Delta\varepsilon_{12} \end{pmatrix} = -2\varepsilon_{11}^2 \begin{pmatrix} P_{66}s_{23} \\ P_{44}s_{13} \\ P_{44}s_{12} \end{pmatrix} \tag{5.33}$$

of the perturbation.

5.2.3 Light Propagation in Anisotropic, Lossless Media

In the following sections, the propagation of light in semiconductor crystals with strain-induced anisotropy is studied. It is of particular interest how the polarization state of the light field changes as a function of the applied strain. The propagation of a plane wave with angular frequency ω through a spatial homogeneous but anisotropic medium is studied to derive this correlation. Therefore in the scope of this section, neither the components of the strain tensor nor the components of the permittivity tensor vary spatially. The permittivity tensor of a strained crystal with monoclinic symmetry is of form

$$\varepsilon = \begin{pmatrix} \varepsilon_{xx} & \varepsilon_{xy} & 0 \\ \varepsilon_{xy} & \varepsilon_{yy} & 0 \\ 0 & 0 & \varepsilon_{zz} \end{pmatrix}. \tag{5.34}$$

This tensor can be diagonalized by a unitary transformation so that the permittivity has only entries on the main diagonal representing the refractive indices along the directions of the principal coordinate system. For biaxial crystals, these refractive indices are pairwise different. If the permittivity is isotropic in case that there is no strain applied, the permittivity tensor of the strained crystal, including perturbations from shear strain only in the xy-directions, has the form as in (5.34). Thus, with the derivations following in this section polarization rotations in (initially isotropic crystals) emerging from the strain with $s_{13} = s_{23} = 0$ and all remaining components not necessarily equal to zero can be studied. Insertion of an electric field $\vec{E}(z)$, which varies only along the propagation direction leads to vanishing spatial derivatives along the transverse directions and due to the form of the permittivity tensor in (5.34) the wave equation (4.61) reduces to the Helmholtz equation for the transverse components

$$\left(\partial_z^2 + \frac{\omega^2}{c_0^2}\varepsilon_{\mathrm{r,t}}\right)\vec{E}_{\mathrm{t}}(z,t) = 0, \tag{5.35}$$

and the transversality condition $E_z(z) = 0$ for the longitudinal component. Only non-permeable media is studied so that $\mu_{\mathrm{r}} = \mathbb{1}$. The transverse electric field in the (original) frame is

$$\vec{E}_{\mathrm{t}} = \begin{pmatrix} E_x \\ E_y \end{pmatrix}. \tag{5.36}$$

If the off-diagonal components of the transverse parts of the permittivity tensor

$$\varepsilon_{\mathrm{t}} = \begin{pmatrix} \varepsilon_{xx} & \varepsilon_{xy} \\ \varepsilon_{xy} & \varepsilon_{yy} \end{pmatrix} \tag{5.37}$$

do not vanish, the solution of (5.35) is not straightforward since the two equations for the field components are coupled. Nevertheless, a solution is obtained by rotating the frame of reference in such a way that the permittivity tensor becomes diagonal, in the rotated reference frame, and the equations decouple. This reference frame is called the principal coordinate system. The transverse permittivity tensor is diagonalized with a unitary matrix U

$$U^{\mathrm{T}} \varepsilon_{\mathrm{t}} U = \begin{pmatrix} \varepsilon_1 & 0 \\ 0 & \varepsilon_2 \end{pmatrix}. \tag{5.38}$$

The entries of the diagonalized tensor

$$\varepsilon_{1/2} = \pm \sqrt{\varepsilon_{xy}^2 + \frac{1}{4}\left(\varepsilon_{xx} - \varepsilon_{yy}\right)^2} + \frac{\varepsilon_{xx} + \varepsilon_{yy}}{2} \tag{5.39}$$

are the eigenvalues of the permittivity matrix and are expressed in terms of the components of the original permittivity tensor. With the rotation angle

$$\tan 2\theta = \frac{2\varepsilon_{xy}}{\varepsilon_{xx} - \varepsilon_{yy}} \tag{5.40}$$

the unitary matrix

$$U = \begin{pmatrix} \cos\theta & -\sin\theta \\ \sin\theta & \cos\theta \end{pmatrix} \tag{5.41}$$

is equivalent to a rotation matrix in the transverse plane. Multiplication of (5.35) with the rotation matrix from the l.h.s and insertion of the identity matrix $U^{\mathrm{T}}U = \mathbb{1}$ yields

$$\begin{aligned} U^{\mathrm{T}} \left(\partial_z^2 U + \frac{\omega^2}{c_0^2} \varepsilon_{\mathrm{r,t}} U \right) U^{\mathrm{T}} \vec{E}_{\mathrm{t}} &= 0 \\ \Leftrightarrow \left(\partial_z^2 + \frac{\omega^2}{c_0^2} \varepsilon'_{\mathrm{r,t}} \right) \vec{E}'_{\mathrm{t}} &= 0 \end{aligned} \tag{5.42}$$

the Helmholtz equation, transformed into the rotated coordinate system. For the decoupled system in the rotated frame, the solution is

$$\begin{aligned} \vec{E}'_{\mathrm{t}}(z,t) &= \begin{pmatrix} e^{ik_1 z} & 0 \\ 0 & e^{ik_2 z} \end{pmatrix} \begin{pmatrix} E'_{x,0} \\ E'_{y,0} \end{pmatrix} e^{-i\omega t} \\ &= \begin{pmatrix} e^{ik_1 z} & 0 \\ 0 & e^{ik_2 z} \end{pmatrix} U^{\mathrm{T}} \vec{E}_{\mathrm{t},0} e^{-i\omega t} \\ &= \begin{pmatrix} \left(\cos\theta E_{x,0} + \sin\theta E_{y,0}\right) e^{ik_1 z} \\ \left(-\sin\theta E_{x,0} + \cos\theta E_{y,0}\right) e^{ik_2 z} \end{pmatrix} e^{-i\omega t} \end{aligned} \tag{5.43}$$

where $\vec{E}_{\mathrm{t},0}$ is the electric field at $z = 0$ in the original frame. The electric field vectors in the original frame and in the rotated frame $\vec{E}'_{\mathrm{t}}$ are related by the rotation

$$\vec{E}_{\mathrm{t}} = U \vec{E}'_{\mathrm{t}} \tag{5.44}$$

so that the solution in the original frame

$$\begin{aligned}\vec{E}_{\mathrm{t}}(z,t) &= U \begin{pmatrix} e^{ik_1 z} & 0 \\ 0 & e^{ik_2 z} \end{pmatrix} U^{\mathrm{T}} \vec{E}_{\mathrm{t},0} e^{-i\omega t} \\ &= e^{ik_2 z - i\omega t} \left\{ \begin{pmatrix} \cos^2\theta E_{x,0} + \cos\theta \sin\theta E_{y,0} \\ \sin\theta\cos\theta E_{x,0} + \sin^2\theta E_{y,0} \end{pmatrix} e^{i\Delta k z} \right. \\ &+ \left. \begin{pmatrix} \sin^2\theta E_{x,0} - \sin\theta\cos\theta E_{y,0} \\ -\cos\theta\sin\theta E_{x,0} + \cos^2\theta E_{y,0} \end{pmatrix} \right\} \end{aligned} \tag{5.45}$$

is obtained by rotating the solution in the transformed frame (5.43) back into the original frame. In the above equation, the wavenumber mismatch $\Delta k = k_1 - k_2$ is introduced.

To illustrate the influence of the shear strain s_{xy} and the initial polarization ρ_0 on the evolution of the polarization state, plots are shown in Fig. 5.3 for a shear strain of $0.01 \cdot 10^{-4}$ in the left column, and for a shear strain of $1.00 \cdot 10^{-4}$ in right column, for the initial polarization degrees of -1 (purely TM-polarized) in the top row, 0 in the central row, and 1 (purely TE-polarized) in the bottom row. The propagation is performed based on (5.45), and the strains in the vertical and lateral direction are set to $s_{xx} = 1.5 \cdot 10^{-4}$, and $s_{yy} = -3.3 \cdot 10^{-4}$. An axis orientation of 0 corresponds to an electric field vector pointing along the vertical direction (TM-polarized) and orientation of $\pm\pi/2$ to an electric field vector oscillating in the lateral direction (TE-polarized). In contrast to the results shown in Fig. 5.3, the medium for this calculations exhibits neither gain nor loss. The lower the shear strain the less the change of the initial polarization state. In the absence of shear strain, the initial (linear) polarization is maintained. For a shear strain of $1.00 \cdot 10^{-4}$ a periodic transfer into the orthogonal polarization with propagation length is observed, compare left and right column in Fig. 5.3. When an initially linear polarized field travels through an anisotropic media with $\varepsilon_{xy} \neq 0$, the amplitudes of the electric field in the two transverse directions oscillate periodically along the propagation direction. However, in the case shown in Fig. 5.3 and in Fig. 5.10 for the results obtained with the BPM, the amplitudes along the propagation direction are not fully modulated, which means that the amplitude in one direction does not reach the same maximum value that the one in the other directions reaches. Thus, the polarization vector is not fully rotated between the two directions in these cases. To illustrate this observation the case of a plane wave traveling through anisotropic media starting with a linear polarization $\vec{E}_1 = \vec{E}(z_1) \sim \vec{e}_y$ along the y-direction at position z_1 is discussed. The scenario is illustrated in Fig. 5.4. The components of the vector $\vec{E}_1$ are projected onto the principal reference frame $(\vec{e}_{x'}, \vec{e}_{y'})$, which is rotated by θ with respect to the original frame $(\vec{e}_x, \vec{e}_y)$. The components along the principal axis are $\vec{E}_{1,y'}$ and $\vec{E}_{1,x'}$ so that $\vec{E}_1 = \vec{e}_{x'}\vec{E}_{1,x'} + \vec{e}_{y'}\vec{E}_{1,y'}$. As shown above, in the principal frame the solutions for the fields are superpositions of linear polarized waves propagating with different wave numbers k_1 and k_2 for the two directions. In this example, $\vec{E}_{1,x'}$ and $\vec{E}_{1,y'}$ oscillate in the $x' - z$ and $y' - z$ plane in the principal frame. At a particular position, which is labeled as z_2, the vector along the x'-axis equals the one at the position z_1 and the one along the y'-direction points in the negative direction with respect to the one at z_1 so that $\vec{E}_{1,x'} = \vec{E}_{2,x'}$ and $\vec{E}_{1,y'} = -\vec{E}_{2,y'}$. Reconstruction of the field at the position z_2 to $\vec{E}_2 = \vec{e}_{x'}\vec{E}_{2,x'} + \vec{e}_{y'}\vec{E}_{2,y'}$ and extraction of $\vec{E}_{2,x}$ shows that the maximum magnitude (for all locations z) in x-direction is smaller than the one in y-direction $|\vec{E}_{2,x}|^2 < |\vec{E}_{1,y}|^2$ if $\theta < \frac{\pi}{4}$. This is the observation described earlier.

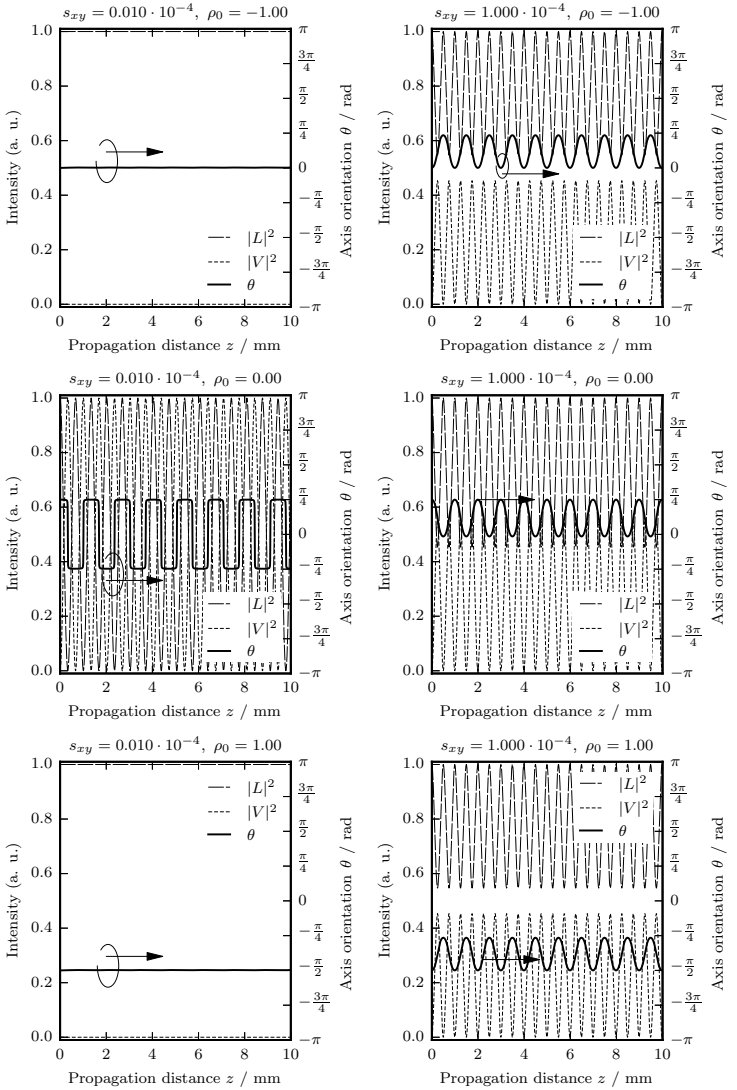

FIGURE 5.3: Relative intensities of linear $|L|^2$ and circular $|V|^2$ polarized light and orientation of polarization ellipses over propagation distance with photo-elastic properties of GaAs A.1. The strains in the vertical and the lateral direction are set to $s_{xx} = 1.5 \cdot 10^{-4}$ and $s_{yy} = -3.3 \cdot 10^{-4}$, and the shear strain is set to $0.01 \cdot 10^{-4}$ (left column) and $1.00 \cdot 10^{-4}$ (right column). Definition of Stokes parameters and $|L|^2$, $|V|^2$ and θ are given in Appendix C.4.

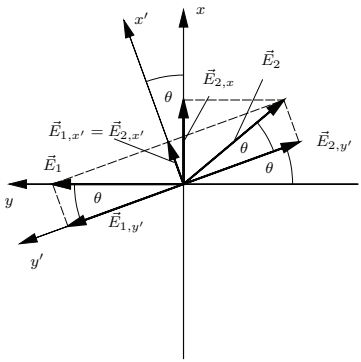

FIGURE 5.4: Polarization vectors in transverse plane for birefringent medium. The reference frame with the primed coordinates x' and y' is the principal system of the anisotropic medium. The field vectors displayed represent the polarization state at two particular positions $\vec{E}_1 = \vec{E}(z_1)$ and $\vec{E}_2 = \vec{E}(z_2)$ and $\vec{E}_{2,x}$ is the projection of the electric field vector $\vec{E}_2$ onto the direction x.

5.2.4 Average Degree of Polarization

The analysis is simplified by assuming that the initial field is linearly polarized in the y-direction so that $E_{0,x} = 0$. This leads to the simplified version of (5.45), from which the intensities in both transverse directions are calculated

$$\vec{E}_{\mathrm{t}}(z,t) = e^{ik_z z - i\omega t} \begin{pmatrix} \cos\theta \sin\theta \left(e^{i(k_1-k_2)z} - 1\right) \\ \sin^2\theta e^{i(k_1-k_2)z} + \cos^2\theta \end{pmatrix} E_{0,y}. \tag{5.46}$$

The time-averaged intensities are proportional to

$$|E_x|^2 = \cos^2\theta \sin^2\theta \, |E_{0,y}|^2 \left(e^{i\Delta kz} - 1\right)\left(e^{-i\Delta kz} - 1\right) \tag{5.47}$$

$$= 2\cos^2\theta \sin^2\theta \, |E_{0,y}|^2 \left(1 - \cos\left(\Delta kz\right)\right) \tag{5.48}$$

and

$$|E_y|^2 = |E_{0,y}|^2 \left(\sin^2\theta e^{i\Delta kz} + \cos^2\theta\right)\left(\sin^2\theta e^{-i\Delta kz} + \cos^2\theta\right) \tag{5.49}$$

$$= |E_{0,y}|^2 \left(\sin^4\theta + \cos^4\theta + 2\cos\left(\Delta kz\right)\sin^2\theta\cos^2\theta\right). \tag{5.50}$$

Since the power is periodically transferred between the two transverse components in the presence of shear strain, the average of the intensities along the propagation directions over one period-length is employed to determine the average normalized intensity of

TE-polarized light

$$\begin{aligned}\rho_y &= \frac{|E_y|^2}{|E_x|^2 + |E_y|^2} \\ &= \frac{\sin^4\theta + \cos^4\theta + 2\cos(\Delta kz)\sin^2\theta\cos^2\theta}{\sin^4\theta + \cos^4\theta + 2\cos(\Delta kz)\sin^2\theta\cos^2\theta + 2(1-\cos(\Delta kz))\cos^2\theta\sin^2\theta} \\ &= \frac{\sin^4\theta + \cos^4\theta + 2\cos(\Delta kz)\sin^2\theta\cos^2\theta}{\sin^4\theta + \cos^4\theta + 2\sin^2\theta\cos^2\theta}. \end{aligned} \tag{5.51}$$

Integration of the cosine term, which includes the propagation coordinate

$$\frac{1}{l}\int_0^l \cos(\Delta kz)\,\mathrm{d}z = \frac{1}{\Delta kl}\int_0^{\Delta kl=2\pi} \cos(\zeta)\,\mathrm{d}\zeta = 0 \tag{5.52}$$

leads to

$$\begin{aligned}\frac{1}{l}\int_0^l \rho_y\,\mathrm{d}z &= \frac{\sin^4\theta + \cos^4\theta + 2\cos(\Delta kz)\sin^2\theta\cos^2\theta}{\sin^4\theta + \cos^4\theta + 2\sin^2\theta\cos^2\theta} \\ &= \frac{\tan^4\theta + 1}{\tan^4\theta + 1 + 2\tan^2\theta}. \end{aligned} \tag{5.53}$$

The DOP

$$\rho = \frac{|E_y|^2 - |E_x|^2}{|E_y|^2 + |E_x|^2} \tag{5.54}$$

is related to the normalized intensity of the TE polarized light by $\rho = 2\rho_y - 1$. The average DOP as a function of the strain components s_{xx}, s_{yy}, and s_{xy} for the photoelastic properties of GaAs is displayed in Fig. 5.5. To calculate the transverse rotation angle

$$\theta = \frac{1}{2}\arctan\left(\frac{2\varepsilon_{xy}}{\varepsilon_{xx} - \varepsilon_{yy}}\right) \tag{5.55}$$

the (perturbed) permittivity components are expressed in terms of the unperturbed permittivity components and the applied strain

$$\begin{aligned}\varepsilon_{xx} &= \varepsilon_{0,xx} - \varepsilon_{0,xx}^2(P'_{11}s_{xx} + P'_{12}s_{yy}), \\ \varepsilon_{yy} &= \varepsilon_{0,yy} - \varepsilon_{0,xx}^2\left(P'_{12}s_{xx} + P'_{22}s_{yy}\right), \\ \varepsilon_{xy} &= \varepsilon_{0,xy} - 2\varepsilon_{0,xx}^2 P'_{44}s_{xy}, \end{aligned} \tag{5.56}$$

where for a rotated crystal orientation the relations

$$\begin{aligned}P'_{11} &= P_{11}, \\ P'_{12} &= P_{12}, \\ P'_{44} &= P_{44}, \\ P'_{22} &= \frac{P_{11} + P_{12} + 2P_{44}}{2} \end{aligned} \tag{5.57}$$

hold. For an isotropic permittivity in the unperturbed case $\varepsilon_{0,xx} = \varepsilon_{0,yy}$ and $\varepsilon_{0,xy} = 0$, insertion of (5.56) into (5.55) gives

$$\begin{aligned}\theta &= \frac{1}{2}\arctan\left(\frac{4P'_{44}s_{xy}}{(P'_{11}-P'_{12})\,s_{xx}-(P'_{22}-P'_{12})\,s_{yy}}\right)\\ &= \frac{1}{2}\arctan\left(\frac{4P_{44}s_{xy}}{(P_{11}-P_{12})\,s_{xx}-\left(\frac{P_{11}-P_{12}}{2}+P_{44}\right)s_{yy}}\right)\end{aligned} \tag{5.58}$$

the angle between the original axes and the principal axes.

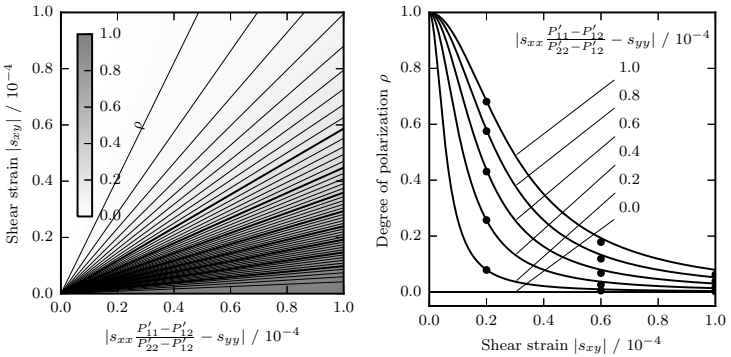

FIGURE 5.5: Average degree of polarization in dependence on strain components. The initial state of the field is entirely TE polarized, which coresponds to $\rho = 1$. Left: DOP over strain components as gray scale plot with contour lines. Right: DOP over shear strain for different values of the diagonal strain components. The markers indicate DOP determined by BPM in a waveguide with corresponding strain. The DOP for the displayed plots is calculated based on the photo-elastic properties of GaAs with $P_{11} = -0.165$, $P_{12} = -0.140$, $P_{44} = -0.072$ [80] and for light traveling along the (011) direction of the crystal.

5.2.5 Light Propagation in Anisotropic Media with Gain or Loss

Additionally to the anisotropy in the real part of the permittivity tensor in this section, anisotropy in the imaginary part is taken into account. For edge-emitting semiconductor lasers, the gain for TE- or TM-polarized light can significantly differ. The complex permittivity

$$\varepsilon = \begin{pmatrix}\varepsilon_{xx} & \varepsilon_{xy} & 0\\ \varepsilon_{xy} & \varepsilon_{yy} & 0\\ 0 & 0 & \varepsilon_{zz}\end{pmatrix} + i\begin{pmatrix}\varepsilon_{(\mathrm{i}),xx} & 0 & 0\\ 0 & \varepsilon_{(\mathrm{i}),yy} & 0\\ 0 & 0 & \varepsilon_{(\mathrm{i}),zz}\end{pmatrix}. \tag{5.59}$$

consists of the real part and an additional complex contribution for the gain or loss of the structure. Here, only the case where the off-diagonal complex entries are zero is studied so that only for the vertical and lateral polarization directions there is gain or loss. One could proceed in the same way as in the previous section and diagonalize the complex permittivity tensor with a unitary transformation. The eigenvalues can be

determined from the same expression (5.39) by substituting the diagonal components with the complex values of (5.59). In the semiconductor laser the TE- and TM-polarized modes couple through the carrier reservoir. Both the gain for TE $g_{\mathrm{TE}}(N)$ and the gain for TM $g_{\mathrm{TM}}(N)$ are functions of the carrier density N. Including the carrier rate equation in the model accounts for the coupling between TE- and TM-polarized light through the carrier reservoir, also in the absence of shear strain, and the decrease of gain with increasing intensity due to depletion of carriers. The model is solved iteratively by successive repetition of the three steps:

1. Propagation of the electric field in the anisotropic media from z_i to z_{i+1}.
2. Update of the carrier density at position z_{i+1}.
3. Update of the gain for TE and TM.

To calculate the light propagation from z to $z+\Delta z$ the Ansatz

$$\vec{E}_{\mathrm{t}}(z,t) = \underbrace{U \begin{pmatrix} e^{ik_1 z} & 0 \\ 0 & e^{ik_2 z} \end{pmatrix} U^{\mathrm{T}}}_{\equiv\Psi(z)} \underbrace{\begin{pmatrix} \phi_1(z) & 0 \\ 0 & \phi_2(z) \end{pmatrix}}_{\equiv\Phi(z)} \vec{E}_{\mathrm{t},0} e^{-i\omega t} \tag{5.60}$$

for the solution of (4.61) is introduced with the complex permittivity tensor (5.59). This Ansatz is motivated as follows: The envelope $\Phi(z)$ accounts for the amplification of the light field and the remaining parts govern the fast oscillating part of the field including rotations of the electric field vector. Based on the solution found in Section 5.2.3 the change of the electric field in propagation direction is found by insertion of the Ansatz (5.60) into the Helmholtz equation (4.61)

$$\begin{aligned}
&\left(\partial_z^2 + k_0^2\varepsilon_{\mathrm{r,t}} + ik_0^2\varepsilon_{(\mathrm{i}),\mathrm{r,t}}\right)\vec{E}_{\mathrm{t}}(z,t) = 0 \\
\Leftrightarrow\ &\left((\partial_z^2\Psi)\Phi + 2\partial_z\Psi\partial_z\Phi + \Psi\partial_z^2\Phi + k_0^2\varepsilon_{\mathrm{r,t}}\Psi\Phi + ik_0^2\varepsilon_{(\mathrm{i}),\mathrm{r,t}}\Psi\Phi\right)\vec{E}_{\mathrm{t},0} = 0 \\
\Leftrightarrow\ &\Big(\underbrace{\left(\partial_z^2\Psi + k_0^2\varepsilon_{\mathrm{r,t}}\Psi\right)}_{=0}\Phi + 2\partial_z\Psi\partial_z\Phi + ik_0^2\varepsilon_{(\mathrm{i}),\mathrm{r,t}}\Psi\Phi\Big)\vec{E}_{\mathrm{t},0} = 0 \\
\Leftrightarrow\ &U \begin{pmatrix} k_1 e^{ik_1 z} & 0 \\ 0 & k_2 e^{ik_2 z} \end{pmatrix} U^{\mathrm{T}}\partial_z\Phi\vec{E}_{\mathrm{t},0} = -\frac{k_0^2\varepsilon_{(\mathrm{i}),\mathrm{r,t}}}{2}\Psi\Phi\vec{E}_{\mathrm{t},0}
\end{aligned} \tag{5.61}$$

where the fast oscillating part of the envelope is neglected in the second step, and the solution of the Helmholtz equation for the real part of the permittivity tensor is utilized in the third step. The remaining equation is a coupled system of two equations for the envelopes ϕ_1 and ϕ_2. To approximate the solution of this equation analytically, the term Ψ is evaluated for $(k_1-k_2)\Delta z = \Delta k\Delta z \ll 1$

$$\Psi \simeq e^{i\tilde{k}z}\mathbb{1} \tag{5.62}$$

and k_1 and k_2 are replaced by the average wave number $\tilde{k} = (k_1+k_2)/2$. The approximation is valid if the longitudinal step size Δz is sufficiently small or the wave numbers are nearly equal, which corresponds to the case of low birefringence. To obtain the solution for the field envelopes, the approximation (5.62) is inserted into (5.61)

$$\begin{pmatrix} \phi_1(z+\Delta z) \\ \phi_2(z+\Delta z) \end{pmatrix} = \begin{pmatrix} e^{g_1\Delta z} & 0 \\ 0 & e^{g_2\Delta z} \end{pmatrix} \cdot \begin{pmatrix} \phi_1(z) \\ \phi_2(z) \end{pmatrix}, \tag{5.63}$$

where the terms $g_1 = -k_0^2 \varepsilon_{(\mathrm{i}),\mathrm{r},xx}/2\tilde{k}$ and $g_2 = -k_0^2 \varepsilon_{(\mathrm{i}),\mathrm{r},yy}/2\tilde{k}$ are used. In the case of edge-emitting diode lasers, $g_1 = g_{\mathrm{TM}}$ and $g_2 = g_{\mathrm{TE}}$ are identified as the TM- and TE-gain.

To illustrate the influence of the shear strain s_{xy} and the initial polarization ρ_0 on the evolution of the polarization state, plots are shown in Fig. 5.6 for a shear strain of $0.01 \cdot 10^{-4}$ in the left column, and for a shear strain of $1.00 \cdot 10^{-4}$ in right column, for the initial polarization degrees of -1 (purely TM-polarized) in the top row, 0 in the central row, and 1 (purely TE-polarized) in the bottom row. The strains in the vertical and lateral direction are set to $s_{xx} = 1.5 \cdot 10^{-4}$ and $s_{yy} = -3.3 \cdot 10^{-4}$. The axis orientation of 0 corresponds to an electric field vector pointing along the vertical direction (TM-polarized) and orientation of $\pm\pi/2$ to an electric field vector oscillating in the lateral direction (TE-polarized). The anisotropic gains are $g_{\mathrm{TE}} = 2g_{\mathrm{TM}} = 3 \cdot 10^5\,\mathrm{m}^{-1}$, and the transparency carrier densities are $N_{\mathrm{tr,TE}} = N_{\mathrm{tr,TM}}/2 = 2 \cdot 10^{24}\,\mathrm{m}^{-3}$. Although the initial conditions and strain states are equal, the results obtained by propagation with medium interaction (Fig. 5.6) differ from the ones obtained from propagation in a passive waveguide (Fig. 5.3). Even for a low shear strain, the polarization state changes significantly with propagation. Absorption of TM light due to the high transparency carrier density leads to (additional) inversion of the medium. Since the gain coefficient for TE light is higher than the one for TM stimulated recombination into the TE-mode is also higher so that the power is transferred from the TM-mode to the medium and than to the TE light (top row in Fig. 5.6). After a transition phase (below 4 mm in Fig. 5.6 top right) an equilibrium between power rotated from the TE into the TM modes due to birefringence and power transferred from TM light into the medium and back to TE light is reached, and the polarization state does not change anymore with propagation distance. Although the polarization becomes linear, it is not purely TE polarized for a non-vanishing shear component. The trend of the DOP as a function of the strain components is similar for the case with and without gain, see Fig. 5.7. The resulting DOP is higher for the model with gain compared to the one without. In the following, the results of an experimental study are presented where the emitted beam from one diode laser is injected into a second diode laser. No current is injected into the second device [2]. The two diode lasers have an equal built up and emit at the same wavelength 970 nm. Before entering the second diode laser the emitted beam with an initial polarization purity of 98% for the TE-mode passes through a half-wave plate, a polarizing beam splitter and a second half-wave plate, which is rotated to adjust the beam to be TE-, TM- or 45°-polarized with respect to the second diode laser. The results, which are drawn from the experiment (see Fig. 5.8) support the above statements: The magnitude of the gain for the TM mode is much smaller compared to the TE-gain at the TE emission wavelength λ_{TE}, so that the interaction (in terms of stimulated absorption and stimulated emission) of the QW with TM-polarized light at λ_{TE} is small compared to the interaction with TE-polarized light. For injection of TM-polarized light in the first case, nearly completely TM-polarized light comes back out of the waveguide, which supports the fact that the interaction cross-section (gain) of TM light (at the TE wavelength) is small. In the second case, the injection of 45°-polarized light, TE polarization components are absorbed by the gain medium, since the diode is not biased so that mainly TM components remain in the output light. The power decreases because the TE components are absorbed. The same argument holds for the third case: Injection of TE polarized light. The reduced DOP occurs due to

[2] The author would like to thank Simon Rauch, with TRUMPF Laser GmbH, Schramberg, for the conduction of the experimental work.

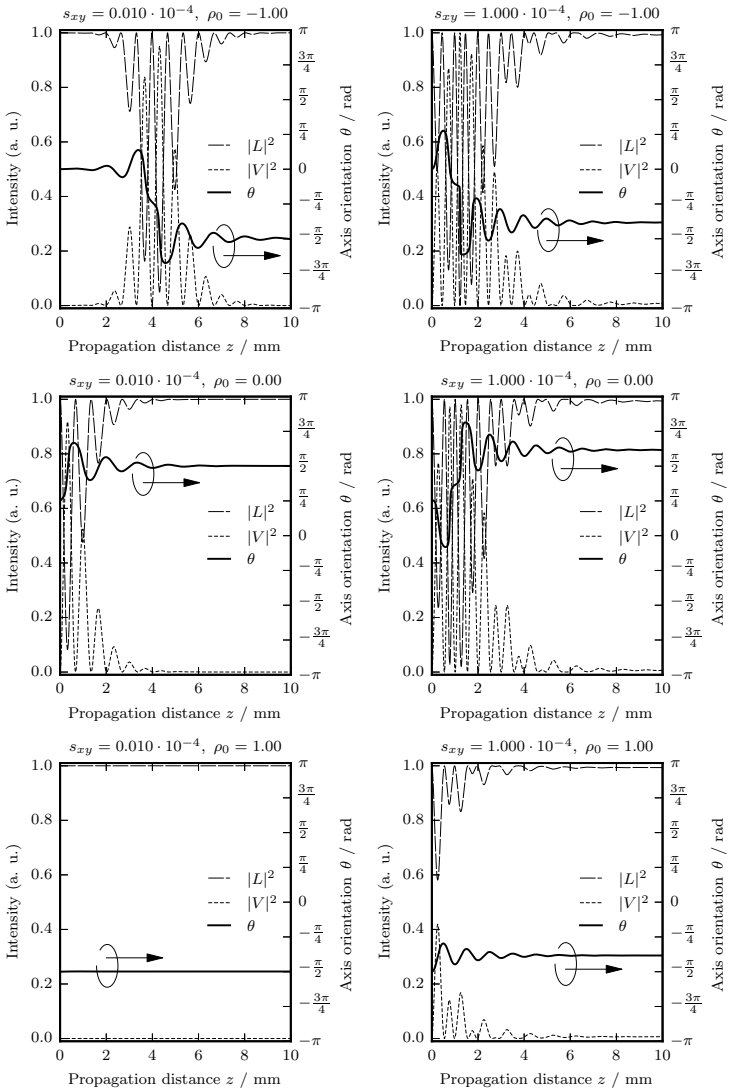

FIGURE 5.6: Relative intensities of linear $|L|^2$ and circular $|V|^2$ polarized light and orientation of polarization ellipses over propagation distance with photo-elastic properties of GaAs A.1. Definition of Stokes parameters and $|L|^2$, $|V|^2$ and θ are given in Appendix C.4.

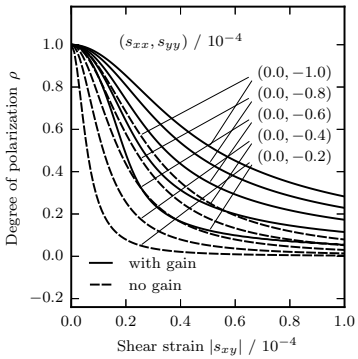

FIGURE 5.7: Propagation through the birefringent semiconductor leads to a rotation from TE-polarized to TM-polarized light. The initial field is purely TE-polarized. For comparison, the case for a medium with no gain is plotted as dashed lines. The anisotropic gains are $g_{\mathrm{TE}} = 2g_{\mathrm{TM}} = 3 \cdot 10^5\,\mathrm{m}^{-1}$ and the transparency carrier densities are $N_{\mathrm{tr,TE}} = N_{\mathrm{tr,TM}}/2 = 2 \cdot 10^{24}\,\mathrm{m}^{-3}$.

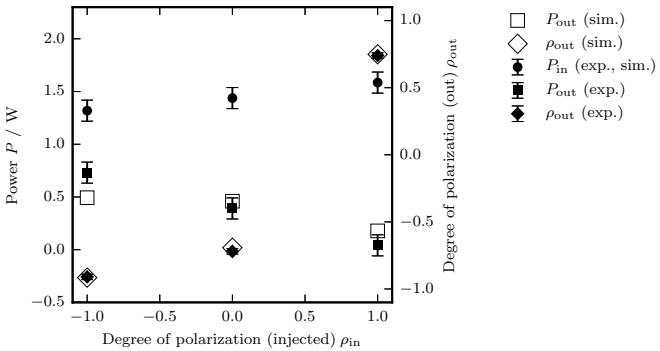

FIGURE 5.8: Results for optical injection study with different polarization states of the injected light. The device under test is not turned on.

birefringence accompanied by polarization rotations in the waveguide. For the model, the values for the strain components (Tb. 5.1) are calibrated to match the experimental results for the specific device. Evaluation of the applied strains (from Tb. 5.1) yields $s_{11}(P'_{11} - P'_{12})/(P'_{22} - P'_{12}) - s_{22} = 3.906 \cdot 10^{-4}$.

5.3 Beam Propagation in Anisotropic Medium

The vectorial BPM is employed to study the polarization rotation in a waveguide (without gain) with a homogeneous shear strain of $1 \cdot 10^{-4}$ and a (compressive) lateral strain of $-0.8 \cdot 10^{-4}$. As initial field, a Gaussian distribution in both vertical and lateral direction with widths $w_{0,x} = 1\,\mu\mathrm{m}$ and $w_{0,y} = 30\,\mu\mathrm{m}$ is launched into the waveguide. At

Parameter	Symbol	Value
Front facet refl.	R_l	2%
Gain coeff. for TE	$g_{\mathrm{TE},0}$	$3 \cdot 10^5\,\mathrm{m}^{-1}$
Gain coeff. for TM	$g_{\mathrm{TM},0}$	$0.03 \cdot 10^5\,\mathrm{m}^{-1}$
Trans. carrier density for TE	$N_{\mathrm{tr,TE}}$	$1.7 \cdot 10^{24}\,\mathrm{m}^{-1}$
Trans. carrier density for TM	$N_{\mathrm{tr,TM}}$	$5 \cdot 10^{24}\,\mathrm{m}^{-1}$
Waveguide strain (vertical)	s_{11}	$-2.533 \cdot 10^{-4}$
Waveguide strain (lateral)	s_{22}	$-2.776 \cdot 10^{-4}$
Photo-elastic coeff.	P_{11}	-0.193
	P_{12}	-0.164
	P_{44}	-0.051

TABLE 5.1: Parameters for injection study. The photo-elastic coefficients are calculated for $Al_{0.2}Ga_{0.8}As$. It is assumed that the waveguide consists entirely of this material and all parameters, including the gain coefficient and transparency carrier densities are determined for a wavelength of $\lambda = 970\,\mathrm{nm}$.

the borders of the domain, an absorbing boundary layer is applied to prevent reflections back into the waveguide. The observed polarization rotation, compare Fig. 5.9 and 5.10, for the strain state, is in agreement with the analytically predicted one, see Fig. 5.5. In this figure, the marked points are simulation results obtained with the anisotropic BPM. Starting from a Gaussian distribution in the vertical direction, during propagation the vertical mode profile resembles the fundamental mode calculated with the vertical eigenmode solver, Fig. 4.7. The lateral profile remains Gaussian. In agreement to the analytical findings, higher shear strain leads to decreased DOP. This trend also resembles with the help of BPM. The modulation of the power components over length increases and additionally the periodicity of the modulation changes. For a larger shear strain component (with the same lateral strain) more light is rotated into the TM mode within a shorter distance, see Fig. 5.10.

The opto-mechanical model is derived under the assumption that the structure is invariant in the z-direction, there is no strain along the propagation direction, and the shear strain components $s_{yz} = s_{xz} = 0$ vanish or are small enough to be neglected. This is not always the case in real applications. The longitudinal strain components can lead to a walk off of the beam in the birefringent medium as known from nonlinear crystals. The extension of the BPM including strain and therefore perturbations of the permittivity tensor also in the components, which are not solely related to the transverse components, has to be investigated in future studies. The results of the analytical and numerical analysis of propagation in an anisotropic medium are:

- For $s_{xy} \neq 0$ and $s_{xx} = s_{yy} = 0$ the entire power oscillates between TE and TM polarization.
- For $s_{xy} \neq 0$, $s_{xx} \neq 0$ and $s_{yy} \neq 0$ fractions of the total power oscillate between TE and TM polarization.
- If a plane wave is launched with the polarization vector aligned to the principal frame of the medium also for $s_{xy} \neq 0$, $s_{xx} \neq 0$ and $s_{yy} \neq 0$, there is no oscillation between the power in TE and TM modes. In this case orientation of the polarization does not change during propagation.

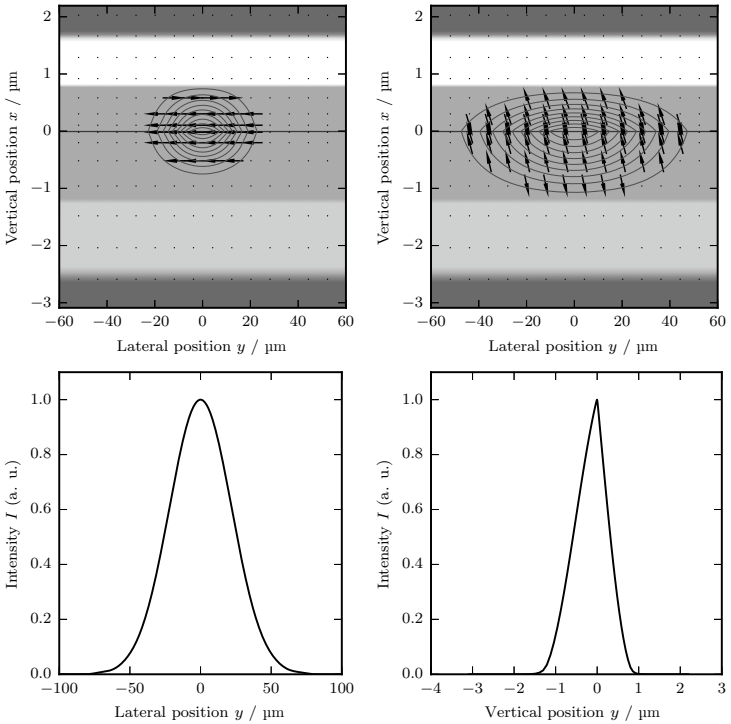

FIGURE 5.9: Polarization directions at longitudinal position $z = 0\,\mu\text{m}$ (left) and $z = 10\,\text{mm}$ (right). The background color illustrates the waveguides permittivity and the contour lines show the intensity of the field. Lateral and vertical cross-sections through the intensity at $z = 10\,\text{mm}$ are displayed in the bottom row.

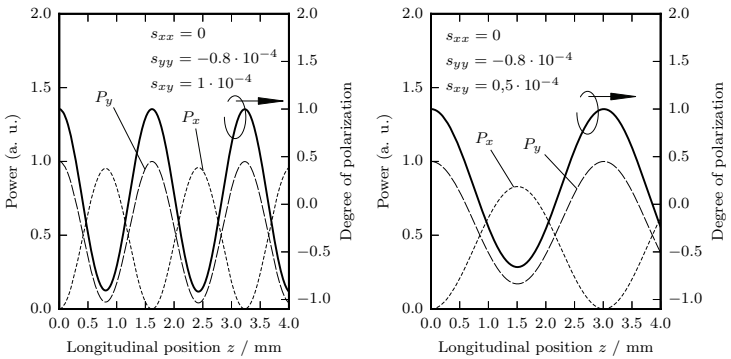

FIGURE 5.10: Degree of polarization over propagation length for two different strain states. The resulting DOP (averaged over the 4 mm distance) for state 1 (left) is 0.050, the one for state 2 (right) is 0.255.

- For $s_{xy} \neq 0$, $s_{xx} = 0$ and $s_{yy} = 0$ the angle between the principal axis and the original frame is $\pi/4$.

5.4 Influence of Thin-Film Stress on Polarization

During fabrication of semiconductor lasers, multiple stacks of thin-films are deposited on a (GaAs) substrate. These films are epitaxial layers, ohmic contacts, insulating layers, and metallizations, see Fig. 5.11. According to the respective growth processes, the films introduce mechanical stresses to the device. The stresses occur due to lattice mismatch, for example, for InGaAs quantum wells or differences in CTEs, for example, for the sputtered metallic layers. As described previously shear strain in the waveguide cause polarization rotations and should, therefore, be reduced for highly polarized output light. Shear strains emerge especially around geometric features which introduce

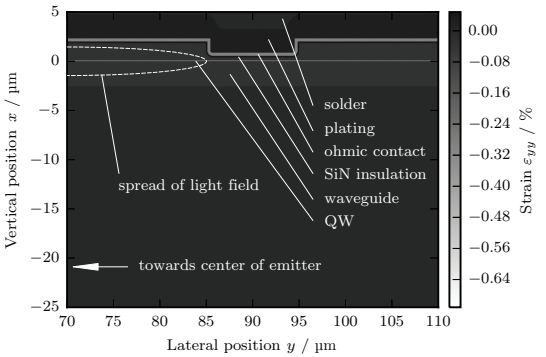

FIGURE 5.11: Overview of mechanical structure around a trench. The field plotted in the background is the initial strain for configuration 1, see Tb. 5.2. The area shown is just a fraction of the entire simulation domain.

discontinuities in stiffness of the mechanical domain. Strain and polarization patterns around v-grooves are measured and modeled by Cassidy et al. [84]. High shear strains occur at corners or material interfaces since initial stresses relax in these regions. The trenches adjacent to the contact opening are accompanied by areas of relatively large shear strains, see Fig. 5.12. However, the strength of the strain components depend on the stress state of the individual thin-films. In this section, the influence of the stress state of the thin-films on the polarization is investigated. The goal is to approximate the depolarization as a function of the thin-film stress. Two factors mainly influence the resulting depolarization: The magnitudes of the stresses applied to the individual layers and the spatial distribution of the light field. The lateral width of the latter plays an essential role in the study since large shear strains occur near the trench. So if the near-field reaches all the way to the trenches the interaction is larger than for smaller near-field widths. For each location in the two-dimensional mechanical domain, the local DOP (distributions are shown in Fig. 5.14) is evaluated concerning the computed strain from the mechanical problem and the local material parameters. Thus, after the solution of the mechanical problem the resulting strain components are inserted into (5.55), and with the help of (5.53) the longitudinally averaged DOP is determined for

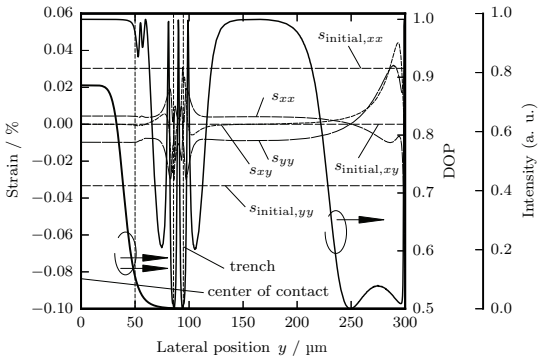

FIGURE 5.12: Degree of polarization and strain state for a lateral cross-section through the active region. The thin-film stresses are applied according to configuration 6 in Tb. 5.2.

each transverse location. This model resembles the polarization rotation of a purely TE polarized plane wave propagating through the strained waveguide for at least one period of polarization rotation. In this simplified model, the BPM is not applied so that diffraction of the light field is neglected. The overall DOP is determined by averaging the local DOP and employing the intensity distribution as a weighting function. For this study, the intensity distribution equals the eigenmode in the vertical direction and in the lateral direction two distributions are utilized: A super-Lorentzian distribution with a width of 100 µm and a top-hat distribution with a width of 170 µm. The latter is the extreme case for the near-field width since the field reaches all the way up to the trenches and therefore, reveals an upper limit for the expected depolarization. The stress in a thin film is not directly measured but are extracted from wafer-bow measurements. After the deposition of each layer the entire wafer bows according to the stress induced by the (latest) applied film, see Fig. 5.13. Based on Stoney's model [85] the in-plane (lateral direction) stress in a deposited film is

$$\sigma_{\mathrm{f}} = \frac{E_{\mathrm{s}} d_{\mathrm{s}}^2}{6\,(1-\nu_{\mathrm{s}})\,d_{\mathrm{f}}} \left(\frac{1}{R_{i-1}} - \frac{1}{R_i} \right), \tag{5.64}$$

where $\nu_{\mathrm{s}} = 0.31$, $E_{\mathrm{s}} = 85.5\,\mathrm{GPa}$, $d_{\mathrm{s}} = 450\,\mu\mathrm{m}$ are Poisson's ratio, elastic modulus, and thickness of the substrate, d_{f} is the film thickness, R_i is the radius of curvature of the wafer after application of the film and R_{i-1} the one before. The radius at process step i is determined from the (measured) wafer bow Δx_i

$$R_i = \frac{r_{\mathrm{w}}^2 + \Delta x_i^2}{2\Delta x_i}, \tag{5.65}$$

with the wafer radius $r_{\mathrm{w}} = 30\,\mathrm{mm}$. The strain in each thin-film is assumed to be constant. In Stoney's model, the strain in the substrate is linearly proportional to the distance from the neutral fiber x

$$\sigma_{\mathrm{s}} = \left(\frac{E_{\mathrm{s}}}{1-\nu_{\mathrm{s}}} \right) \frac{x}{R_i}. \tag{5.66}$$

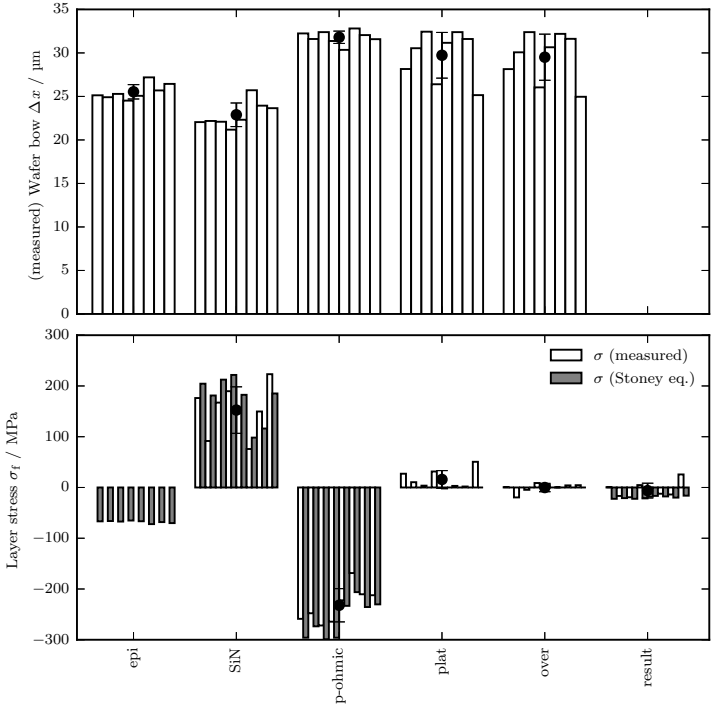

FIGURE 5.13: Top: Wafer bow after each process step. The bow is measured with p-side up, so that a positive bow indicates a compressive stress in the thin-film. Bottom: Stress in thin-film calculated by wafer measurement apparatus and evaluated from wafer bow and nominal layer thickness based on Stoney's Eq. (5.64). Measurements are performed on 8 wafers (each value indicated by individual bar). Markers indicate the average over the dataset. Additionally the spread is given by the error bars.

The neutral fiber is positioned in the center of the substrate so that the maximum stress values in the substrate are at $x_{\max} = \pm\frac{d_s}{2}$. The determined stresses are used as baseline values for the DOP study. Findings from wafer production suggest that these stresses can vary significantly in magnitude and even sign based on process parameters or production variations. Various combinations of stresses in the respected layers are taken into account to find the correlation to the resulting DOP reduction. The configurations, which are summarized in Tb. 5.2, with different magnitudes and even flips of the signs of the stresses are investigated and resulting DOP patterns are determined, see Fig. 5.14. Regardless of the sign of the resulting stress for the entire layer stack, a larger overall magnitude of the resulting stress leads to a wider spread of the regions with low polarization, compare configurations 2, 3 (top row) with 4, 5 (bottom row) in Fig. 5.14 and the difference between DOP for configuration 1, 4 and 6 in Fig. 5.15. The overlap of the light field with the region close to the trench, where the depolarization is mainly induced is a crucial property for the analysis. If the light field does not extend all the way laterally to the trenches (see the intensity and DOP in Fig. 5.12) the

	Thick. / µm	Configuration 1	2	3	4	5	6	7
		Lateral stress / MPa						
Epitaxy		intr.	intr.	intr.	intr.	intr.	intr.	intr.
SiN	0.15	150	300	-150	150	150	150	300
Ohmic con.	0.32	-230	-460	-230	230	-230	-230	-230
Plating	2.28	20	40	20	20	200	-200	20
Resulting	2.75	-2.04	-4.08	-18.43	51.59	147.14	-184.37	6.16
Avg. polarization		0.998	0.998	0.996	0.987	0.975	0.919	0.997

TABLE 5.2: Parameters for thin-film stress study. Lateral width of light field for integration $w = 170\,\mu\text{m}$.

expected polarization decrease is smaller compared to a field distribution which reaches the trench region. In summary, the correlation (obtained by linear regression) between the magnitude of the resulting layer (stack) stress $|\sigma_{\text{res}}|$ and the (averaged) change in polarization is $\Delta\rho = -1 \cdot 10^{-5}\,\text{MPa}^{-1}|\Delta\sigma_{\text{res}}|$ and $\Delta\rho = -3 \cdot 10^{-4}\,\text{MPa}^{-1}|\Delta\sigma_{\text{res}}|$ for a 100 µm and a 170 µm wide near-field. If the resulting stress $|\sigma_{\text{res}}|$ stays below 50 MPa the DOP decrease (for an unmounted laser) is smaller than 1.5 % even in the case of a wide near-field.

5.5 Packaging Influence on Polarization

The investigated HPDL arrays are packaged with hard solder (AuSn) on CuW submounts (first interface). The submount is subsequently soldered, also with AuSn for the second interface, on an electrically isolated cooler. The cooler is made of copper sheets which embody micro-channel cooling structures. This copper sheet stack is sandwiched between two ceramics layers, and additional layers of copper are plated on top of the ceramic layers to provide a mounting surface for the submount, see schematic drawing in Fig. 5.16. Requirements on the coolers are high thermal conductivity and tailored CTE for expansion matched heatsinks [86]. The goal in this section is to explain possible causes for the local reduction of DOP in LAs and investigate the influence of submount thickness, CTE and thermal state of the device on the resulting DOP.

In the mechanical model of a packaged SE or LA, it is distinguished between two types of sources: The first kind include stresses which emerge from sources, which can be modeled (with a reasonable amount of effort) or analytically described. Those sources, for example, include CTE mismatch between two materials which are bonded together in the soldering process, the intrinsic lattice mismatch of semiconductors, heating during device operation or film-stress introduced during chip processing. If material parameters are known, or assumptions can be made, the stress state of an emitter or LA is computed by application of a mechanical model as presented in Section 5.1. However, in reality, there are more contributors to the mechanical state, which, for example, emerge from microscopic properties of materials, like grain boundaries, voids or other inhomogeneities in the solder or from variations of process parameters, for example, during plating or in the packaging process. Colbourne and Cassidy present measurements of

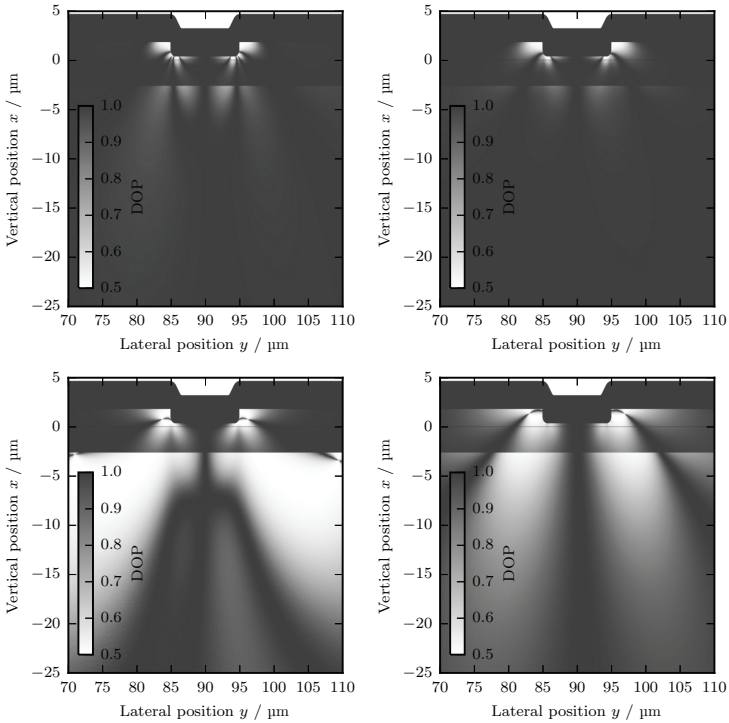

FIGURE 5.14: Local DOP around trench features for thin-film stress configurations 2 (top left), 3 (top right), 4 (bottom left), and 5 (bottom right).

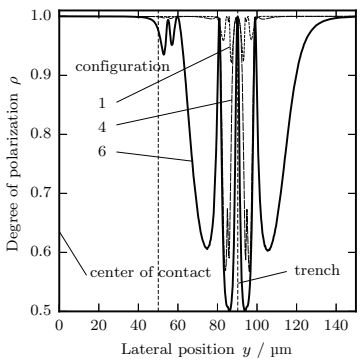

FIGURE 5.15: DOP over lateral position for cross-section through the active region. The results shown are computed with thin-film stresses given in Tb. 5.2 for configurations 1, 4, and 6.

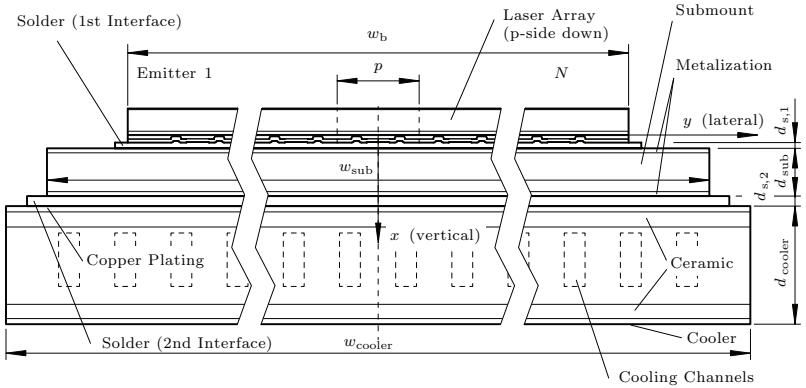

FIGURE 5.16: Schematic of high-power diode laser device packaged p-side down on submount and micro-channel cooler.

stress distributions for GaAs-based diodes obtained by scanned polarization-resolved photoluminescence [87]. They report bonding stresses (in the case of AuSn solder) up to $\sigma_{yy} = -200\,\text{MPa}$ and demonstrate the significant amount of stress introduced to the device in the bonding process. In their measurements, the peak stresses in the unmounted device are about one order of magnitude smaller compared to the mounted case. An example of polarization resolved near-field measurements of a LA A1 (details in Tb. C.3) packaged on a 350 µm thick CuW submount is displayed in Fig. 5.17. In this case, the spatial variation of the emitter resolved DOP does not follow a trend along the lateral direction. Even the emitters at the edge (the outer emitter is number one) do not show more decrease than some emitters in the central parts of the array, for example, emitter number 20 in Fig. 5.17. The local DOP is evaluated individually for each emitter by averaging the intensities over the respective emitter width. [3] The DOP variations obey a statistical nature and are not predictable by models presented in this work. However, the contributions are not excluded but treated as perturbations of the stress or strain in addition to the sources of the first kind. Neither the form of these perturbations (spatial distribution) nor the magnitude is predicted. Nevertheless, the latter is estimated by comparing numerical results with measurements. If a structure in the simulations is robust against mechanical perturbations (of arbitrary form), this fact also reflects in real applications. In the simulations presented in Fig. 5.21, an arbitrary strain perturbation is added to the initial strain. The analysis is a stability analysis of the opto-mechanical system with respect to the polarization state, in which the resilience against depolarization is evaluated. The simulation domain includes: A GaAs substrate with epitaxial layers (waveguide and QW), the thin-film layers (SiN, ohmic contact, p-metallization), AuSn solder (1st interface), submount metallization, CuW submount, AuSn solder (2nd interface), simplified model of cooler (bulk copper blocks and two ceramic layers), see schematic drawing in Fig. 5.16. The material parameters are listed in the Appendix in Tb. C.5. The finite-element sizes of the triangular mesh are locally adjusted to include microscopic features like the several nanometer thin QW (see dense meshing in Fig. 5.18 around QW), thin-film layers of submicrometer thickness

[3] The author would like to thank Udai Bhanu and Stefan Heinemann both with TRUMPF Photonics, Inc., Cranbury, for providing these measurements.

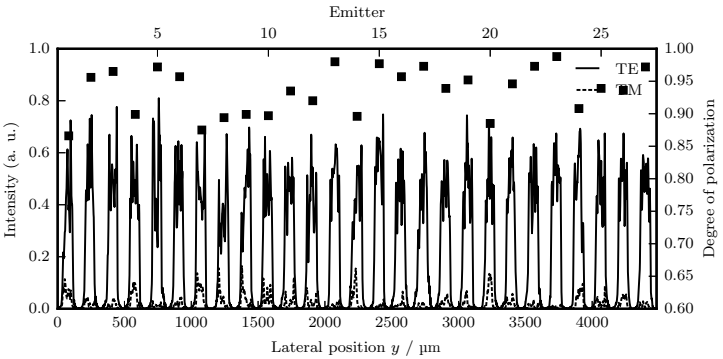

FIGURE 5.17: Measured near-field intensity of TE and TM polarized light. The DOP per emitter displayed by markers. Starting from the left edge of the laser array with emitter one a total of 27 emitters out of the 55 emitter array are displayed. The diode array is soldered on a CuW submount with 350 µm thickness, which is subsequently soldered on to a micro-channel cooler [86].

and geometrical details around the trenches (contour of p-Metal in Fig. 5.18). For the

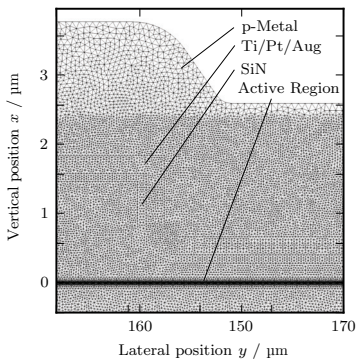

FIGURE 5.18: Detailed view of the triangular mesh around the active region at a trench.

thin-films on top of the epitaxial layers, an average force density of $455\,\mathrm{Nm}^{-1}$ is applied. Stress arising from the cooling of the materials from solidification temperature down to room temperature is computed with the CTE for each material layer to simulate the soldering process. More sophisticated numerical models for the bonding process include temperature profiles over time, creep of the solder material and plastic deformation. In this scope all materials are treated by the linear elastic theory and the final state is computed based on a loaded structure (with initial stresses), which relaxes into the equilibrium state. All the stress contributions are added and applied to the mechanical structure as initial stresses (5.9). In the initial state, all deformations are zero. When the structure relaxes the initial stresses lead to deformation of materials until local force equilibrium is reached. The relaxation is computed by the solution of (5.7). The local

polarization rotation is computed from (5.53), and the spatial averaged DOP is evaluated by integration of local DOP weighted by a predefined near-field intensity. For the intensity, the waveguide eigenmode in the vertical direction and a top-hat distribution with near-field width corresponding to the contact opening width is assumed in the lateral direction. The NF profile does not reach to the trenches so that the DOP reduction directly around the trenches does not significantly influence the spatial averaged DOP. Of course, the near-field distribution can be different in real devices so that the effect may contribute more than it is accounted for here. In the first case, no additional per-

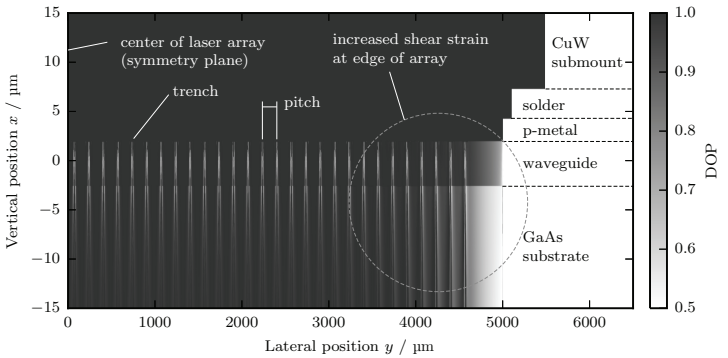

FIGURE 5.19: Polarization purity in transverse plane for the relaxed structure with no additional perturbation applied. The plot shows a fraction of the simulation domain with a focus on the waveguide. The QW is located at vertical position zero, and the axis of symmetry is at lateral position zero. The calculated polarization is only valid in the semiconductor regions. The regions with solder or metal have a default value of one assigned for the polarization.

turbation is added, and only initial stress due to lattice mismatch, the bonding process, thin-film forces, and self-heating is applied. Local DOP-decreases, particularly in the optical waveguide (Fig. 5.19), emerge from two effects: A local decrease around trench or ridge features and a decrease towards the outer edges of the array caused by an accumulation of shear strain from the bonding process (the encircled region in Fig. 5.19). Despite periodic patterns induced by the trenches, the shear strain is close to zero up to a distance of 4 mm away from the center of the array. Towards the edge of the array, shear strain decreases to about $-0.01\,\%$ accompanied by a DOP reduction to about $70\,\%$, see Fig. 5.20. Despite the edges and regions around the trenches, the local DOP is close to $100\,\%$, which is higher than the experimentally observed local DOP in Fig. 5.17. The measured DOP over the lateral direction shows a more random distribution with values below $90\,\%$. This suggests that additional sources of (initial) stresses are built into the structure during the soldering process. The (arbitrary) perturbations which are employed are

$$s_{yy,\mathrm{pert}} = A_{\mathrm{pert}}(x - x_{0,\mathrm{pert}}) \sum_{n=1}^{3} \sin(\frac{y}{k_{\mathrm{pert}} n}), \tag{5.67}$$

with the values for the parameters $A_{\mathrm{pert}}, x_{0,\mathrm{pert}}$ and k_{pert} defined in Tb. 5.3. The perturbation is added to the initial strain in the semiconductor materials. Exemplary, for the case of perturbation (2) plus initial strains, the calculated local DOP is displayed in Fig. 5.21 and Fig. 5.22. The perturbation introduces regions into the waveguide with

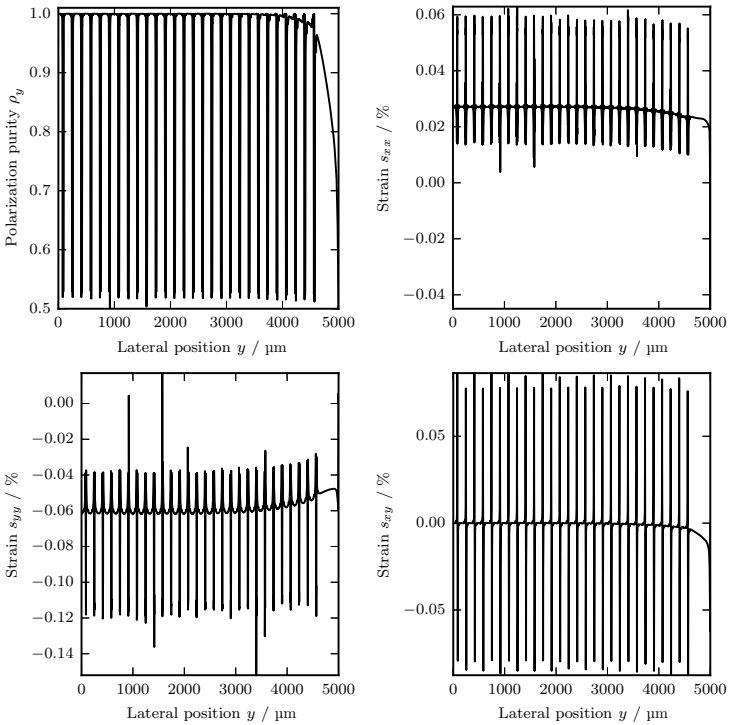

FIGURE 5.20: Lateral cross-sections through the QW ($x = 0\,\mu\text{m}$) of polarization purity and strain components in vertical s_{xx}, lateral s_{yy} direction and the in-plane shear strain s_{xy} for the relaxed structure with no additional perturbation applied. The plot shows a fraction of the simulation domain with a focus on the waveguide. The axis of symmetry is at lateral position zero.

Perturbation	A_{pert} / m^{-1}	k_{pert} / m	$x_{0,\text{pert}}$ / m
1	10	-50	$5 \cdot 10^{-5}$
2	10	-50	$1 \cdot 10^{-5}$
3	5	-50	$5 \cdot 10^{-5}$

TABLE 5.3: Parameters for strain perturbations.

local reduced DOP. The state-of-the-art knowledge is that the overall CTE of the packaged stack consisting of submount, solder, and cooler should be as close to the CTE of the diode laser as possible to match thermal expansion and therefore reduce induced packaging stress when cooling down the structure from solidification temperature. If the level of shear strain induced in the packaging process is small, an expansion matched package provides the optimum solution to ensure both high DOP and high reliability. However, if due to process variations, solder impurities or geometrical features the shear

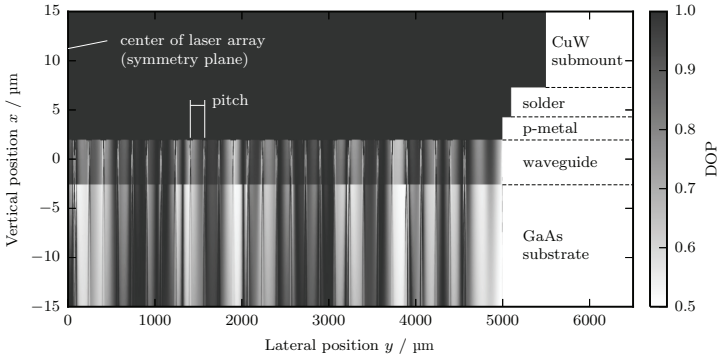

FIGURE 5.21: Polarization purity in transverse plane for the relaxed structure with perturbation (2) applied. The plot shows a fraction of the simulation domain with a focus on the waveguide. The QW is located at vertical position zero, and the axis of symmetry is at lateral position zero. The calculated polarization is only valid in the semiconductor regions. Regions with solder or metal have a default value of one assigned for the polarization.

strain in the optical waveguide increases, an introduction of compressive lateral strain buffers the decrease of polarization due to the presence of shear strain, and maintains high DOP. For a fixed magnitude of shear strain, the higher the compressive strain in the lateral direction (negative sign for s_{yy}) the higher the DOP. Under the assumption that the structure can expand in the vertical direction, based on Poisson's ratio lateral compression results in a positive value for the vertical strain component s_{xx}. Although increasing the DOP, the drawback of additional lateral stress applied to the semiconductor is a reduction of reliability [88, 84]. The spatial averaged van Mises stress, Fig. 5.23 evaluates the overall stress in the semiconductor. With thinner submount, the higher CTE of the cooler's copper becomes more dominant so that higher lateral compressive strain is induced into the device. The same occurs if the material properties of the submount are changed. Variation of the submount CTE from $6.5 \cdot 10^{-6}\,\mathrm{K}^{-1}$ (literature value) to $7.5 \cdot 10^{-6}\,\mathrm{K}^{-1}$ introduces higher lateral compressive strain. If the magnitude of the shear strain in the waveguide remains unchanged in both cases the DOP increases (Fig. 5.5). Therefore, if perturbations induce shear strains into the waveguide, see case (1), (2), (3) in Fig. 5.17, the model predicts decreasing DOP with increasing submount thickness (Fig. 5.23) and increasing DOP with increasing submount CTE (Fig. 5.24). The experimental values for submount thicknesses of 300 µm and 1000 µm show DOP magnitudes in the same order as modeling results for perturbation (3), see triangular markers in Fig. 5.17. Due to self-heating during operation of the laser array, the temperature increase can partially reverse the strain built in by cooling of the structure in the soldering process. In the study higher polarizations are computed for devices with self-heating.

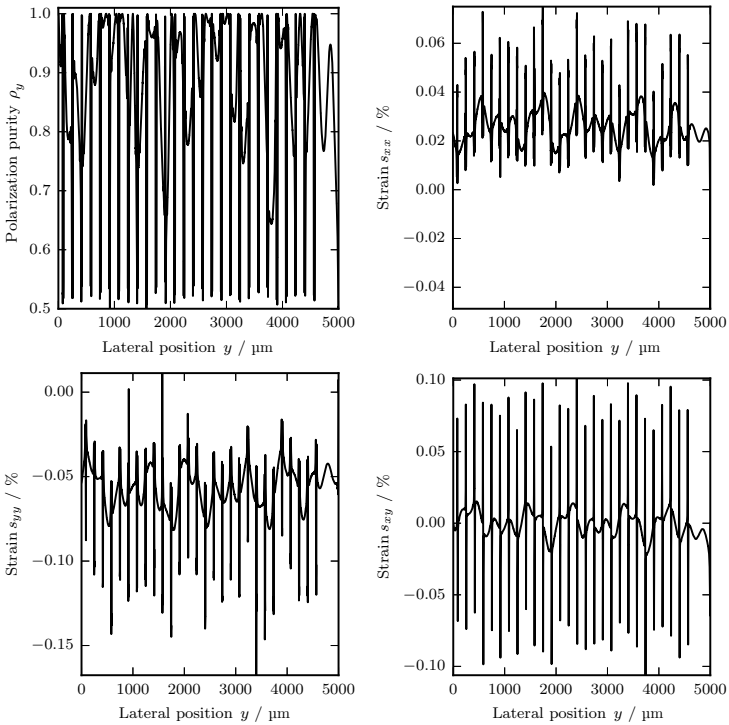

FIGURE 5.22: Lateral cross-sections through the QW ($x = 0\,\mu\text{m}$) of polarization purity and strain components in vertical s_{xx}, lateral s_{yy} direction and the in-plane shear strain s_{xy} for the relaxed structure with perturbation (2) applied. The plot shows a fraction of the simulation domain with a focus on the waveguide. The axis of symmetry is at lateral position zero.

5.6 Chapter Summary

Based on the photo-elastic model, an expression for the (longitudinally) averaged DOP for a plane wave in (transverse) birefringent media is derived as a function of the vertical strain, lateral strain, and shear strain components. The analytical results agree with the ones obtained with the vectorial FD-BPM (see Chapter 4) which are performed for a two-dimensional birefringent waveguide, compare Fig. 5.5. In addition to anisotropies in the refractive index, the DOP is influenced by an anisotropic gain and interaction with a gain medium, see Fig. 5.7. The extension of the BPM for the inclusion of strain and therefore perturbations of the permittivity tensor also in the components not solely related to the transverse components are investigated in future studies. Both (local) isotropic variations of the refractive index and birefringence potentially influence the evolution of the light field and the SAD. However, at this point, these perturbations are not included in the edge-emitting laser models but solely for the DOP studies in this chapter.

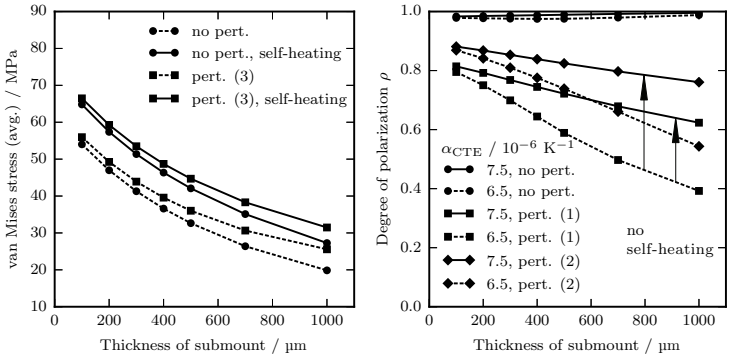

FIGURE 5.23: Left: Resulting (average) van Mises stress in the domain as a function of submount thickness. Right: DOP over submount thickness for different submount CTE and stress perturbations. The arrows indicate the change of DOP due to a change of the submount CTE.

The influence of the stress state of the thin-films on the polarization is investigated for the example of the SE-device D1. Trenches adjacent to the contact opening are accompanied by areas of relatively large shear strains, see Fig. 5.12. If the light field does not extend all the way laterally to the trenches (see the intensity and DOP in Fig. 5.12) the expected polarization decrease is smaller compared to a field distribution which reaches the trench region. If the resulting stress $|\sigma_{res}|$ stays below 50 MPa the DOP decrease (for the unmounted laser D1) is smaller than 1.5 % even in the case of a wide near-field.

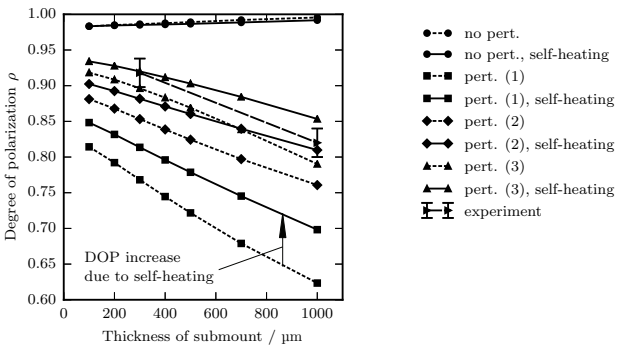

FIGURE 5.24: Results for averaged DOP for different perturbations defined in (5.67) and Tb. 5.3 over the thickness of the CuW submount. Simulations without self-heating are indicated by dashed lines.

Besides the analysis of an SE, the DOP for a transverse cross-section of a packaged LA is computed. The investigated example is a LA with 55 emitters on a CuW submount

packaged onto a micro-channel heatsink. A stability analysis of the opto-mechanical system is performed with respect to the polarization state, in which the resilience against depolarization is evaluated. If, due to process variations, solder impurities or geometrical features, the shear strain in the waveguide increases, an introduction of compressive lateral strain (in combination with free expansion of the structure in the vertical direction) buffers the decrease of polarization due to the presence of shear strain and maintains high DOP. The experimental values for submount thicknesses of 300 µm and 1000 µm show DOP magnitudes in the same order as modeling results for a specific perturbation, see triangular markers in Fig. 5.24.

Chapter 6

Electronic Properties of Semiconductors

In this chapter, a model for the electronic transport of carriers in semiconductor heterostructures is presented. The drift-diffusion model [89] is utilized to calculate the electronic properties of semiconductor lasers, as such as carrier concentrations, band edge energies, quasi-Fermi energies, current density, temperature and interaction with the QW. The focus lies on the calculation of one- and two-dimensional structures. Commercial software is available for the calculation of electronic properties of semiconductors based either on the Finite-Differences Method (FDM), Finite-Element Method (FEM) or Finite-Volume Method (FVM). Nevertheless, the underlying source code is not editable or extendable (to account for additional physical effects in future applications), and the seamless coupling (fast and standardized interfaces) to the remaining *SEMSIS* software modules is not guaranteed. The required outputs of the electrical model are:

1. Transverse current profile and spatial carrier distribution in QW,
2. optical power and voltage over current for laser devices,
3. determination of (modal) free-carrier absorption for the active device,
4. determination of heat sources (Joule, radiative and non-radiative).

The current flow through the transverse cross-section influences the carrier distribution inside the QW. The spatial profile of these carriers determines the gain and refractive index perturbation in the QW, and thus influences the optical modes. The chapter is structured as follows: First, the theoretical background for the drift-diffusion model is recited and the governing equations for the electric potential, carrier densities, and the quasi-Fermi potentials are derived. In Section 6.2, a formulation based on the Scharfetter-Gummel discretization on structured meshes, and in Section 6.3 an approach for the discretization of the drift-diffusion equations in the scope of the FEM is presented. The electrical problem is coupled to the photon rate equation, and the example of SE device D1 presents the results of electro-optical calculations for a one-dimensional (vertical) and two-dimensional (transverse) domain.

6.1 Drift-Diffusion Model

To model charge carrier transport, the electric potential and quasi-Fermi potentials of a heterostructure, the semiconductor equations for semi-classical transport of free electrons and holes under the drift-diffusion approximation are employed. The DDM consists of a system of three nonlinear coupled partial differential equations, which in this form have been proposed by van Roosbroeck [90] and describe the semiconductor properties on a macroscopic scale. Background on the semiconductor electronics equations are given in [30] and [91]. In the scope of this work, carrier densities are described by Boltzmann statistics. Extension of the Scharfetter-Gummel scheme for Fermi-Dirac statistics or other constitutive laws for the carrier densities is presented in [92]. In the drift-diffusion model (see for example [89, 38, 93, 94, 95, 96]), the fluxes arise from two contributions: Drift due to a gradient of the electric field and diffusion of carriers due to carrier density gradients. The DDM consists of a set of three nonlinear coupled differential equations, which in the stationary case read

$$\nabla \cdot \vec{J}_\phi = \rho, \tag{6.1}$$

$$\nabla \cdot \vec{J}_n = q_{\mathrm{el}} R, \tag{6.2}$$

$$\nabla \cdot \vec{J}_p = -q_{\mathrm{el}} R \tag{6.3}$$

for the dielectric displacement $\vec{J}_\phi$ in Cm^{-2}, the electron $\vec{J}_n$ and hole $\vec{J}_p$ current densities in Am^{-2}, the charge density ρ in Cm^{-3}, and the recombination rate density R in $\mathrm{m}^{-3}\mathrm{s}^{-1}$. The equations are conservation laws for the respective current densities, which are related to associated gradients of scalar potentials

$$\vec{J}_\phi = -d_\phi \nabla \phi, \tag{6.4}$$

$$\vec{J}_n = -d_n \nabla \phi_n, \tag{6.5}$$

$$\vec{J}_p = -d_p \nabla \phi_p, \tag{6.6}$$

the electric potential ϕ, quasi-Fermi potential for electrons ϕ_n, and quasi-Fermi potential for holes ϕ_p, all in units V. For intrinsic semiconductors, the Fermi level lies in the center of the bandgap. The coefficients in (6.4), (6.5), and (6.6) are

$$d_\phi = \varepsilon_{\mathrm{stat}}, \tag{6.7}$$

$$d_n = q_{\mathrm{el}} D_n \beta n, \tag{6.8}$$

$$d_p = q_{\mathrm{el}} D_p \beta p, \tag{6.9}$$

with the static permittivity $\varepsilon_{\mathrm{stat}}$, the diffusion coefficients for electrons D_n and holes D_p in $\mathrm{m}^2\mathrm{s}^{-1}$, and the electron n and hole p densities in m^{-3}. Additionally, the inverse of the thermal voltage

$$\beta = \frac{q_{\mathrm{el}}}{k_{\mathrm{B}} T} \tag{6.10}$$

is introduced. Under the assumption that the Einstein relation holds the diffusion coefficient

$$D_{n/p} = \frac{k_{\mathrm{B}} T}{q_{\mathrm{el}}} \mu_{n/p}, \tag{6.11}$$

is related to the carrier mobility for the electrons μ_n and holes μ_p in $\mathrm{m}^2\mathrm{V}^{-1}\mathrm{s}^{-1}$. The carrier mobilities are functions of temperature, doping, and material composition. The mobility models employed for GaAs and the ternary alloys AlGaAs and InGaAs are

summarized in Appendix A.3. Applying a voltage or illumination with light leads to a non-equilibrium between electrons and holes, though the carrier distributions are still in equilibrium with themselves. The non-equilibrium distributions are associated with the quasi-Fermi energies $E_{\mathrm{F},n}$ for electrons and $E_{\mathrm{F},p}$ for holes, both in units J, which are related to the quasi-Fermi potentials via

$$E_{\mathrm{F},n} = -q_{\mathrm{el}}\phi_n, \tag{6.12}$$

$$E_{\mathrm{F},p} = -q_{\mathrm{el}}\phi_p. \tag{6.13}$$

and the limit of low carrier densities is assumed so that Fermi-Dirac distributions are approximated with Boltzmann statistics. In this scope, the charge densities are related to the electric potential and quasi-Fermi potentials

$$n = N_{\mathrm{c}} \exp\left(\beta(\phi - \phi_n - \frac{\Delta E_{\mathrm{c}}}{q_{\mathrm{el}}})\right), \tag{6.14}$$

$$p = N_{\mathrm{v}} \exp\left(\beta(\phi_p - \phi + \frac{\Delta E_{\mathrm{c}}}{q_{\mathrm{el}}} - \frac{E_{\mathrm{g}}}{q_{\mathrm{el}}})\right), \tag{6.15}$$

where N_{c} and N_{v} are the effective density of states for electrons and holes, E_{g} is the bandgap and ΔE_{c} in J accounts for band edge offsets in heterostructures. A schematic of the band edges is shown in Fig. 6.1. The equation (6.1) is Poisson's equation, which determines the electric potential ϕ based on a spatial distribution of the charge density ρ

$$\nabla\left(\varepsilon_{\mathrm{stat}}\nabla\phi\right) = -\rho = -q_{\mathrm{el}}\left(p - n + N_{\mathrm{D}}(n) - N_{\mathrm{A}}(p)\right). \tag{6.16}$$

The charge density consists of the electron density n, the hole density p and the densities of donators $N_{\mathrm{D}}(n)$ and acceptors $N_{\mathrm{A}}(p)$. Inserting equations (6.14) and (6.15) into Poisson's equation (6.16)

$$\nabla\left(\varepsilon_{\mathrm{stat}}\nabla\phi\right) = -q_{\mathrm{el}}\left(n_{\mathrm{i}}\exp\left(q_{\mathrm{el}}\frac{\phi_p - \phi}{k_{\mathrm{B}}T}\right) - n_{\mathrm{i}}\exp\left(q_{\mathrm{el}}\frac{\phi - \phi_n}{k_{\mathrm{B}}T}\right) + N_{\mathrm{net}}\right), \tag{6.17}$$

eliminates the carrier densities and reveals the nonlinearity in the electric potential. This form is used in Gummel's map [97], where the equation is solved iteratively with Newton's method. The total net doping density $N_{\mathrm{net}} = N_{\mathrm{D}} - N_{\mathrm{A}}$ is introduced for abbreviation. For incomplete ionization the donator and acceptor impurity concentrations as functions of the carrier densities and potentials are

$$N_{\mathrm{D}}(n) = \frac{N_{\mathrm{D}}^{(0)}}{1 + \frac{n}{N_{\mathrm{c}}} g_{\mathrm{D}} \exp\left(\frac{\Delta E_{\mathrm{D}}}{k_{\mathrm{B}}T}\right)}, \tag{6.18}$$

and

$$N_{\mathrm{A}}(p) = \frac{N_{\mathrm{A}}^{(0)}}{1 + \frac{p}{N_{\mathrm{v}}} g_{\mathrm{A}} \exp\left(\frac{\Delta E_{\mathrm{A}}}{k_{\mathrm{B}}T}\right)}, \tag{6.19}$$

where $N_{\mathrm{D}}^{(0)}$, $N_{\mathrm{A}}^{(0)}$ are reference donator and acceptor impurity concentrations, $g_{\mathrm{D}} = 2$, $g_{\mathrm{A}} = 4$ are ground state degeneracy factors of the donor and acceptor level and ΔE_{D}, ΔE_{A} are donator and acceptor activation energies [98]. The total recombination rate

$$R = R_{\mathrm{sp}} + R_{\mathrm{A}} + R_{\mathrm{SRH}} \tag{6.20}$$

consists of contributions from the spontaneous R_{sp}, Auger R_{A} and Shockley-Read-Hall (SRH) R_{SRH} recombination. The recombination rates [96] dependent on the carrier densities

$$R_{\mathrm{SRH}} = \frac{np - n_{\mathrm{i}}^2}{\tau_n (n + n_1) + \tau_p (p + p_1)}, \tag{6.21}$$

$$R_{\mathrm{sp}} = C_{\mathrm{sp}} \left(np - n_{\mathrm{i}}^2\right), \tag{6.22}$$

$$R_{\mathrm{A}} = \left(C_n n + C_p p\right) \left(pn - n_{\mathrm{i}}^2\right), \tag{6.23}$$

where τ_n and τ_p are the non-radiative lifetimes ins, C_{sp} is the coefficient of spontaneous recombination, and C_n and C_p are the coefficients for Auger recombination. The intrinsic carrier density (see Appendix C.2 for the definition) is

$$n_{\mathrm{i}} = \sqrt{N_{\mathrm{c}} N_{\mathrm{v}}} \exp\left(\frac{-E_{\mathrm{g}}}{2 k_{\mathrm{B}} T}\right). \tag{6.24}$$

In addition, the SRH recombination rate depends on the band edges and trap energy level E_{T} with

$$n_1 = N_{\mathrm{c}} \exp\left(\frac{-E_{\mathrm{c}} + E_{\mathrm{T}}}{k_{\mathrm{B}} T}\right),$$

$$p_1 = N_{\mathrm{v}} \exp\left(\frac{E_{\mathrm{v}} - E_{\mathrm{T}}}{k_{\mathrm{B}} T}\right). \tag{6.25}$$

In the following, the approximation $\Delta E_{\mathrm{T}} = E_{\mathrm{T}} - E_{\mathrm{i}} = 0$ [96] is made so that the trap energy equals the intrinsic energy E_{i}, which leads to $n_1 = n_{\mathrm{i}}$ and $p_1 = n_{\mathrm{i}}$ in (6.23). The relation between the intrinsic energy and intrinsic carrier density is given in the Appendix C.2 in (C.9). Rearranging (6.14) and (6.15) for the quasi-Fermi potentials

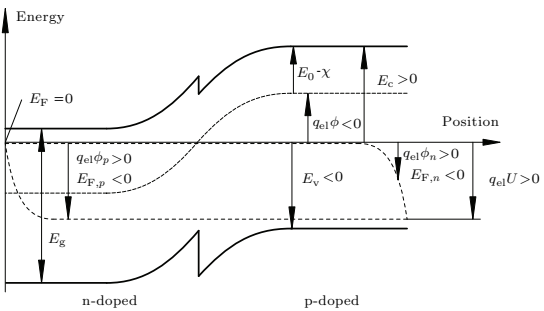

FIGURE 6.1: Schematic of band edges, quasi-Fermi energies and potentials for a heterostructure.

$$\phi_n = \phi - \frac{\Delta E_{\mathrm{c}}}{q_{\mathrm{el}}} - \frac{1}{\beta} \ln\left(\frac{n}{N_{\mathrm{c}}}\right), \tag{6.26}$$

$$\phi_p = \phi - \frac{\Delta E_{\mathrm{c}}}{q_{\mathrm{el}}} + \frac{E_{\mathrm{g}}}{q_{\mathrm{el}}} + \frac{1}{\beta} \ln\left(\frac{p}{N_{\mathrm{v}}}\right) \tag{6.27}$$

and insertion into (6.5), and (6.6) gives expressions for the current densities

$$\begin{aligned}\vec{J}_n &= q_{\mathrm{el}} D_n \nabla n - q_{\mathrm{el}} D_n \beta n \nabla \left(\phi + \frac{1}{\beta} \ln \left(\frac{N_{\mathrm{c}}}{N_0} \right) - \frac{\Delta E_{\mathrm{c}}}{q_{\mathrm{el}}} \right) \\ &= q_{\mathrm{el}} D_n \nabla n - q_{\mathrm{el}} D_n \beta n \nabla \left(\phi + \phi_{\mathrm{c}} \right), \end{aligned} \tag{6.28}$$

$$\begin{aligned}\vec{J}_p &= -q_{\mathrm{el}} D_p \nabla p - q_{\mathrm{el}} D_p \beta p \nabla \left(\phi - \frac{\Delta E_{\mathrm{c}}}{q_{\mathrm{el}}} + \frac{E_{\mathrm{g}}}{q_{\mathrm{el}}} - \frac{1}{\beta} \ln \left(\frac{N_{\mathrm{v}}}{N_0} \right) \right) \\ &= -q_{\mathrm{el}} D_p \nabla p - q_{\mathrm{el}} D_p \beta p \nabla \left(\phi + \phi_{\mathrm{v}} \right), \end{aligned} \tag{6.29}$$

where N_0 is a scale in units m^{-3}, introduced to make the argument of the logarithm dimensionless. Note that after application of the gradient-operator the scale N_0 vanishes from the expressions. The form (6.29) reveals the driving mechanisms for carrier fluxes in the DDM, which are diffusion by gradients in the carrier densities, drift by gradients in electric potential and drift by gradients in the band structure properties (bandgap, DOS and band edge offsets). The conduction and valence band edges are determined by

$$E_{\mathrm{c}} = E_0 - \chi_{\mathrm{el}} - q_{\mathrm{el}} \phi, \tag{6.30}$$

$$E_{\mathrm{v}} = E_{\mathrm{c}} - E_{\mathrm{g}} = E_0 - \chi_{\mathrm{el}} - q_{\mathrm{el}} \phi - E_{\mathrm{g}} \tag{6.31}$$

where E_0 is a reference energy in the unit J (corresponding to the vacuum level) and χ_{el} is the electron affinity in J. The reference level is aligned so that $\Delta E_{\mathrm{c}} = E_0 - \chi_{\mathrm{el}}$.

6.1.1 Boundary Conditions

For ideal Ohmic-contacts thermal equilibrium and charge neutrality is assumed [89]

$$p_\sigma - n_\sigma + \underbrace{N_{\mathrm{D}} - N_{\mathrm{A}}}_{=N_{\mathrm{net}}} = 0, \quad p_\sigma n_\sigma = n_{\mathrm{i}}^2, \tag{6.32}$$

and the carrier densities obey the mass action law. Insertion of the latter into the charge neutrality condition yields

$$n/p_\sigma = \pm \frac{N_{\mathrm{net}}}{2} + \sqrt{\frac{N_{\mathrm{net}}^2}{4} + n_{\mathrm{i}}^2}. \tag{6.33}$$

At Ohmic boundaries, the metals quasi-Fermi level aligns with the semiconductors quasi-Fermi level so that it equals the applied voltage at the contact ϕ_{ext}. The electrostatic potential at the boundary is evaluated from (6.14) and (6.15)

$$\phi_\sigma = \phi_{\mathrm{ext}} + \begin{cases} \frac{\Delta E_{\mathrm{c}}}{q_{\mathrm{el}}} + \frac{1}{\beta} \ln \left(\frac{n_\sigma}{N_{\mathrm{c}}} \right) & , \quad N_{\mathrm{net}} \geq 0, \\ \frac{\Delta E_{\mathrm{c}}}{q_{\mathrm{el}}} - \frac{E_{\mathrm{g}}}{q_{\mathrm{el}}} - \frac{1}{\beta} \ln \left(\frac{p_\sigma}{N_{\mathrm{v}}} \right) & , \quad N_{\mathrm{net}} < 0 \end{cases}. \tag{6.34}$$

Dirichlet boundary conditions enforce the values on the Ohmic boundaries so that for $\vec{x} \in \delta\Omega_{\mathrm{Ohmic}}$

$$\phi(\vec{x}) = \phi_\sigma, \quad \phi_n(\vec{x}) = \phi_p(\vec{x}) = \phi_{\mathrm{ext}}, \quad n(\vec{x}) = n_\sigma, \quad p(\vec{x}) = p_\sigma, \tag{6.35}$$

holds. The remaining boundaries are insulating Neumann boundaries. At insulating boundaries, the fluxes are tangential to the boundary so that for $\vec{x} \in \delta\Omega_{\text{Insulating}}$

$$\vec{n} \cdot \vec{J}_\phi = 0, \quad \vec{n} \cdot \vec{J}_n = 0, \quad \vec{n} \cdot \vec{J}_p = 0, \tag{6.36}$$

where $\vec{n}$ is the vector normal to the boundary.

6.1.2 Scaling Scheme

Since both material parameters and variables in the DDM differ by orders of magnitude for typical cases the quantities in the DDM equations are scaled to avoid overflow, underflow or loss of accuracy in the numerical solution. The scaled quantities become

Parameter	Definition	Unit
Potential	$\phi_0 = k_\text{B}T_\text{max}/q_\text{el}$	V
Energy	$E_0 = q_\text{el}\phi_0$	J
Diffusion coefficient	$D_0 = \max[D_n(\vec{x}), D_p(\vec{x})]$	m^2s^{-1}
Mobility	$\mu_0 = D_0/\phi_0$	$\text{m}^2\text{V}^{-1}\text{s}^{-1}$
Carrier density	$N_0 = \max[N_\text{D}(\vec{x}), N_\text{A}(\vec{x})]$	m^{-3}
Recombination rate	$R_0 = D_0N_0/l_0^2$	$\text{m}^{-3}\text{s}^{-1}$
Current density	$J_0 = N_0D_0q_\text{el}/l_0$	Am^{-2}
Photon flux density	$S_0 = D_0N_0/l_0$	$\text{m}^{-2}\text{s}^{-1}$
Power density	$I_0 = D_0q_\text{el}\phi_0N_0/l_0^2$	Wm^{-2}

TABLE 6.1: Scaling scheme for drift-diffusion model [37]. For scaling of the potential the maximum temperature in the domain $T_\text{max} = \max[T(\vec{x})]$ is used.

$$\begin{aligned}
\tilde{\vec{x}} &= \frac{\vec{x}}{l_0}, & \tilde{\nabla} &= l_0\nabla, & \tilde{n} &= \frac{n}{N_0}, & \tilde{p} &= \frac{p}{N_0}, \\
\tilde{\phi} &= \frac{\phi}{\phi_0}, & \tilde{\phi}_n &= \frac{\phi_n}{\phi_0}, & \tilde{\phi}_p &= \frac{\phi_p}{\phi_0}, & \tilde{\vec{J}}_{\phi/n/p} &= \frac{\vec{J}_{\phi/n/p}}{J_0}, \\
\tilde{D}_{n/p} &= \frac{D_{n/p}}{D_0}, & \tilde{\mu}_{n/p} &= \frac{\mu_{n/p}}{\mu_0}, & \tilde{R} &= \frac{R}{R_0}, & \tilde{\beta} &= \phi_0\beta.
\end{aligned} \tag{6.37}$$

After application of the scaling scheme (Tb. 6.1) the dimensionless parameter

$$\lambda^2 = \frac{\varepsilon_0\phi_0}{N_0q_\text{el}l_0^2} \tag{6.38}$$

remains in the Poisson equation.

6.2 Finite-Differences Discretization with Box-Integration

Numerical discretization of the DDM in the framework of the FDM with a centered differences scheme emerges in issues regarding stability and convergence of the solution. Due to a (local) artificial increase of the diffusion coefficient the numerical stability can be increased. A common approach is the Scharfetter-Gummel discretization of the

electron and hole currents as presented in [99]. The method is used to discretize the drift-diffusion equations on a two-dimensional unregular structured mesh with the FDM [89]. The particular discretization scheme for the current densities originally proposed by Scharfetter for a one-dimensional domain [99] and extended to two-dimensions in [89] is employed to ensure the stability of the numerical scheme. The method is straightforward to implement and is applied for simulation of optoelectronic devices for example in [37]. The discretized set of equations in the potential ϕ, and electron n and hole p densities can be solved fully coupled with Newton's method or in a decoupled iterative procedure called Gummel iteration [97]. Gummel's iteration is more robust regarding the initial state of the variable as Newton's method. A drawback is that Gummel's iteration usually takes more steps to convergence than Newton's method for an initial condition close to the solution. For the method presented in this section Gummel's map is employed and a summary of the underlying equations is given in the following. The Gummel map consists of three main steps: The nonlinear Poisson's equation is solved with Newton's method for the potential ϕ, where the quasi-Fermi potentials ϕ_n and ϕ_p are held constant. After the updated solution for the potential is obtained the current continuity equations are solved for electrons and holes. In the last step, the quasi-Fermi potentials are updated based on the new carrier densities, and the iteration is repeated until the changes in the variables are below a defined threshold. Despite the recombination terms, the current conservation equations are linear in the respective carrier densities. The nonlinearities in the recombination terms are linearized so that the discretized current continuity equations in the iteration are linear. Discretization of current densities based on the Scharfetter-Gummel scheme [99, 89, 37] leads to

$$\begin{aligned}
\tilde{J}_{\nu,x,i-1/2,j} &= \frac{\tilde{D}_{\nu,i-1/2,j}}{\Delta\tilde{x}_{i-1/2}} \left(B\left(\psi_{\nu,i,j} - \psi_{\nu,i-1,j}\right) \nu_{i,j} - B\left(\psi_{\nu,i-1,j} - \psi_{\nu,i,j}\right) \nu_{i-1,j} \right), \\
\tilde{J}_{\nu,x,i+1/2,j} &= \frac{\tilde{D}_{\nu,i+1/2,j}}{\Delta\tilde{x}_{i+1/2}} \left(B\left(\psi_{\nu,i+1,j} - \psi_{\nu,i,j}\right) \nu_{i+1,j} - B\left(\psi_{\nu,i,j} - \psi_{\nu,i+1,j}\right) \nu_{i,j} \right),
\end{aligned} \tag{6.39}$$

where $B(z) = \frac{z}{e^z - 1}$ is the Bernoulli function and the variables $\psi_n = \tilde{\beta}(\tilde{\phi} + \tilde{\phi}_\mathrm{c})$ and $\psi_p = -\tilde{\beta}(\tilde{\phi} + \tilde{\phi}_\mathrm{v})$ are substituted for the potentials. The definitions of the discretized current densities hold for both carrier species with $\nu = \tilde{n}$ for electrons and $\nu = \tilde{p}$ for holes. The mesh spacings are defined as $\Delta\tilde{x}_{i+1/2} = \tilde{x}_{i+1} - \tilde{x}_i$ and $\Delta\tilde{y}_{i+1/2} = \tilde{y}_{i+1} - \tilde{y}_i$. Analog, the current densities in the y direction are

$$\begin{aligned}
\tilde{J}_{\nu,y,i,j-1/2} &= \frac{\tilde{D}_{\nu,i,j-1/2}}{\Delta\tilde{y}_{j-1/2}} \left(B\left(\psi_{\nu,i,j} - \psi_{\nu,i,j-1}\right) \nu_{i,j} - B\left(\psi_{\nu,i,j-1} - \psi_{\nu,i,j}\right) \nu_{i,j-1} \right), \\
\tilde{J}_{\nu,y,i,j+1/2} &= \frac{\tilde{D}_{\nu,i,j+1/2}}{\Delta\tilde{y}_{j+1/2}} \left(B\left(\psi_{\nu,i,j+1} - \psi_{\nu,i,j}\right) \nu_{i,j+1} - B\left(\psi_{\nu,i,j} - \psi_{\nu,i,j+1}\right) \nu_{i,j} \right).
\end{aligned} \tag{6.40}$$

Application of Gauss' theorem to the electron continuity equation

$$\begin{aligned}
&\int_{\tilde{\Omega}} \tilde{\nabla} \cdot \tilde{\vec{J}}_{n/p} \mp \tilde{R} \, \mathrm{d}\tilde{x} = 0 \\
\Leftrightarrow &\int_{\delta\tilde{\Omega}} \tilde{\vec{J}}_{n/p} \cdot \mathrm{d}\tilde{s} \mp \int_{\tilde{\Omega}} \tilde{R} \, \mathrm{d}\tilde{x} = 0
\end{aligned} \tag{6.41}$$

and discretization for each inner box around the nodes $(i,j) \notin n_{\mathrm{gra},x^{\mp}}$ and $(i,j) \notin n_{\mathrm{gra},y^{\mp}}$ of a rectangular mesh (Fig. 6.2) yields

$$\begin{aligned} &\left(\tilde{J}_{n/p,x,i+1/2,j} - \tilde{J}_{n/p,x,i-1/2,j}\right) \tilde{A}_{x,j} \\ &+ \left(\tilde{J}_{n/p,y,i,j+1/2} - \tilde{J}_{n/p,y,i,j-1/2}\right) \tilde{A}_{y,i} \mp \tilde{A}_{y,i}\tilde{A}_{x,j}\tilde{R}_{i,j} = 0, \end{aligned} \tag{6.42}$$

with the surface areas

$$\tilde{A}_{y,i} = \frac{\Delta\tilde{x}_{i+1/2} + \Delta\tilde{x}_{i-1/2}}{2} \tag{6.43}$$

and

$$\tilde{A}_{x,j} = \frac{\Delta\tilde{y}_{j+1/2} + \Delta\tilde{y}_{j-1/2}}{2}. \tag{6.44}$$

All current densities in (6.42) are only evaluated on interior nodes. On exterior nodes, with Neumann boundaries, the respective term in (6.42) for the current density component normal to the boundary vanishes so that no current flows out of or in to the domain. The set of mesh nodes that have a defined gradient in the positive x direction are defined as

$$n_{\mathrm{gra},x^+} = \{(i,j) \in \mathbb{N}^2 | (i,j) \notin n_{\mathrm{N},x^+} \cup n_{\mathrm{excl}} | 0 \le i < N_x - 1 | 0 \le j \le N_y - 1\}, \tag{6.45}$$

and the ones which have a defined gradient in negative x direction are

$$n_{\mathrm{gra},x^-} = \{(i,j) \in \mathbb{N}^2 | (i,j) \notin n_{\mathrm{N},x^-} \cup n_{\mathrm{excl}} | 0 < i \le N_x - 1 | 0 \le j \le N_y - 1\}. \tag{6.46}$$

Analog, the nodes for the y direction are

$$n_{\mathrm{gra},y^+} = \{(i,j) \in \mathbb{N}^2 | (i,j) \notin n_{\mathrm{N},y^+} \cup n_{\mathrm{excl}} | 0 \le i \le N_x - 1 | 0 \le j < N_y - 1\}, \tag{6.47}$$

and

$$n_{\mathrm{gra},y^-} = \{(i,j) \in \mathbb{N}^2 | (i,j) \notin n_{\mathrm{N},y^-} \cup n_{\mathrm{excl}} | 0 \le i \le N_x - 1 | 0 < j \le N_y - 1\}, \tag{6.48}$$

where $n_{\mathrm{N},x^{\pm}}$ and $n_{\mathrm{N},y^{\pm}}$ are the set of mesh nodes which have Neumann boundaries in positive and negative x or y direction, respectively. To subtract specific regions from the rectangular domain, the mesh nodes n_{excl} are excluded from the computation.

To maintain high numerical accuracy for small values of the potential differences, similar to the approximation in [89], the Bernoulli function is evaluated as follows

$$B(z) \approx \begin{cases} -z & , z < -z_{\max} \\ |z| + \frac{|z|}{e^{|z|}-1} & , -z_{\max} \le z \le -z_{\lim} \\ 1 - \frac{1}{2}z + \frac{1}{6}z^2 & , -z_{\lim} \le z \le z_{\lim} \\ \frac{z}{e^z-1} & , z_{\lim} \le z \le z_{\max} \\ 0 & , z > z_{\max} \end{cases}, \tag{6.49}$$

where $z_{\lim} = 1 \cdot 10^{-3}$ and $z_{\max} = 80$ is used. The recombination terms (6.42) are nonlinear in the carrier densities and obey the form

$$R_{\mu}(n,p) = (np - n_{\mathrm{i}}^2) r_{\mu}(n,p). \tag{6.50}$$

The functions $r_{\mu}(n,p) \approx r_{\mu}(n_0,p_0)$ are approximated with values from previous Gummel iteration steps, and only the first term of R is linearized with respect to n and p. For

electrons the scaled linearized recombination rate yields

$$\tilde{R}_\mu(\tilde{n}) \approx \tilde{n}\tilde{p}_0\tilde{r}_\mu(\tilde{n}_0,\tilde{p}_0) - \tilde{n}_1^2\tilde{r}_\mu(\tilde{n}_0,\tilde{p}_0) \tag{6.51}$$

and for holes

$$\tilde{R}_\mu(\tilde{p}) \approx \tilde{n}_0\tilde{p}\tilde{r}_\mu(\tilde{n}_0,\tilde{p}_0) - \tilde{n}_1^2\tilde{r}_\mu(\tilde{n}_0,\tilde{p}_0). \tag{6.52}$$

Insertion of the linearized recombination terms into (6.42) results in a linear system of equations for the carrier densities on the grid nodes. The system matrix is a tridiagonal sparse matrix in the two-dimensional case.

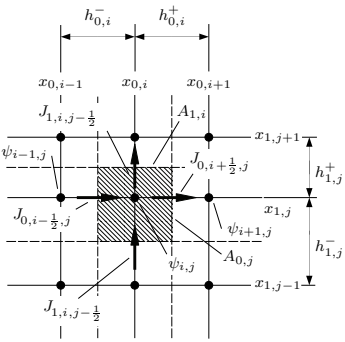

FIGURE 6.2: Definition of discretized current densities J_μ, respective mesh spacings $h_{0,i}, h_{1,j}$, integration box and mesh knots for variable ψ.

6.3 Finite-Element Formulation for Primal Mixed Method

The expressions for the current densities can be inserted into (6.1), (6.2), and (6.3) so that only the potential and quasi-Fermi potentials remain as the unknowns in the equations. However, a different approach is followed here. Both, the current densities $\vec{J}_\phi$, $\vec{J}_n$ and $\vec{J}_p$, and the potentials ϕ, ϕ_n and ϕ_p remain as unknowns in the system of equations. The benefit of this approach emerges from the explicit control of the discretization of the fluxes and the reduction of the entire system to a first order problem. The method is called Primal Mixed Method (PMM). Mathematical details about the Primal Mixed Finite-Element Method are found in [100]. For the PMM the vector of (unknown) variables is

$$u = \left(\phi, \vec{J}_\phi, \phi_n, \vec{J}_n, \phi_p, \vec{J}_p\right). \tag{6.53}$$

The system of nonlinear, coupled equations is

$$L_\phi = -\nabla \cdot \vec{J}_\phi + \rho, \tag{6.54}$$

$$\vec{L}_{\vec{J}_\phi} = \vec{J}_\phi + d_\phi \nabla \phi, \tag{6.55}$$

$$L_{\phi_n} = \nabla \cdot \vec{J}_n - q_{\mathrm{el}} R, \tag{6.56}$$

$$\vec{L}_{\vec{J}_n} = \vec{J}_n + d_n \nabla \phi_n, \tag{6.57}$$

$$L_{\phi_p} = \nabla \cdot \vec{J}_p + q_{\mathrm{el}} R, \tag{6.58}$$

$$\vec{L}_{\vec{J}_p} = \vec{J}_p + d_p \nabla \phi_p. \tag{6.59}$$

and despite the recombination terms in Eqs. (6.56) and (6.58), which are associated with the quasi-Fermi potentials, the respective currents are linear in the variables. Eq. (6.54) for the potential remains nonlinear in ϕ, ϕ_n and ϕ_p in the mixed formulation. Newton's method is employed to solve the set of nonlinear equations by iterative solution of the linearized system

$$\mathcal{L}(u, \delta u) = L(u, \delta u) + \delta L(u, \delta u) = 0 \tag{6.60}$$

for the vector of functions δu. To solve (6.60) with the FEM, the vector of test functions

$$v = \left(v_\phi, \vec{v}_{\vec{J}_\phi}, v_{\phi_n}, \vec{v}_{\vec{J}_n}, v_{\phi_p}, \vec{v}_{\vec{J}_p} \right), \tag{6.61}$$

is introduced to define the functional

$$F(u, \delta u) = \int_\Omega \mathcal{L}(u, \delta u) \cdot v \, \mathrm{d}x \tag{6.62}$$

by integration over the domain $\Omega \subset \mathbb{R}^d$, where d is the number of space dimensions. The entries of the Jacobian for Newton's method are given in Appendix C.7. By integration over the entire domain and partial integration over the terms with the divergences of vector quantities the weak form associated with (6.54) is obtained

$$\begin{aligned} F_\phi = & \int_\Omega \left(\vec{J}_\phi + \delta \vec{J}_\phi \right) \cdot \nabla v_\phi \\ & + \left(\rho - q_{\mathrm{el}}(n+p)\beta\delta\phi + q_{\mathrm{el}}\beta n \delta\phi_n + q_{\mathrm{el}}\beta p \delta\phi_p \right) v_\phi \\ & + q_{\mathrm{el}} \left(\frac{\delta N_{\mathrm{D}}}{\delta\phi}\delta\phi - \frac{\delta N_{\mathrm{A}}}{\delta\phi}\delta\phi + \frac{\delta N_{\mathrm{D}}}{\delta\phi_n}\delta\phi_n - \frac{\delta N_{\mathrm{A}}}{\delta\phi_p}\delta\phi_p \right) v_\phi \, \mathrm{d}x \\ & - \int_{\delta\Omega} \left(\vec{J}_\phi + \delta \vec{J}_\phi \right) \cdot \vec{n} v_\phi \, \mathrm{d}s. \end{aligned} \tag{6.63}$$

By partial integration, the derivatives are *shifted* from the vector currents to the scalar variables, which are the potentials and corresponding test functions. The weak form for the associated current is

$$F_{\vec{J}_\phi} = \int_\Omega \left(\vec{J}_\phi + \delta \vec{J}_\phi + d_\phi \nabla\phi + d_\phi \nabla\delta\phi \right) \cdot \vec{v}_{\vec{J}_\phi} \, \mathrm{d}x. \tag{6.64}$$

The weak form for (6.56) contains all functionals proportional to test function v_{ϕ_n}

$$\begin{aligned} F_{\phi_n} = \int_\Omega & -\left(\vec{J}_n + \delta\vec{J}_n\right)\cdot\nabla v_{\phi_n} \\ & - q_{\mathrm{el}}\left(R + \frac{\delta R}{\delta\phi}\delta\phi + \frac{\delta R}{\delta\phi_n}\delta\phi_n + \frac{\delta R}{\delta\phi_p}\delta\phi_p\right) v_{\phi_n}\,\mathrm{d}x \\ & + \int_{\delta\Omega}\left(\vec{J}_n + \delta\vec{J}_n\right)\cdot\vec{n}v_{\phi_n}\,\mathrm{d}s, \end{aligned} \tag{6.65}$$

and the weak form for (6.57) contains all functionals proportional to test function $\vec{v}_{\vec{J}_n}$

$$F_{\vec{J}_n} = \int_\Omega \left(\vec{J}_n + \delta\vec{J}_n + d_n\nabla\phi_n + d_n\nabla\delta\phi_n + \vec{b}_n\delta\phi - \vec{b}_n\delta\phi_n\right)\cdot\vec{v}_{\vec{J}_n}\,\mathrm{d}x, \tag{6.66}$$

where $\vec{b}_n = d_n\beta\nabla\phi_n$ is introduced. Analog, Eq. (6.58) holds all functionals proportional to test function v_{ϕ_p}

$$\begin{aligned} F_{\phi_p} = \int_\Omega & -\left(\vec{J}_p + \delta\vec{J}_p\right)\cdot\nabla v_{\phi_p} \\ & + q_{\mathrm{el}}\left(R + \frac{\delta R}{\delta\phi}\delta\phi + \frac{\delta R}{\delta\phi_n}\delta\phi_n + \frac{\delta R}{\delta\phi_p}\delta\phi_p\right) v_{\phi_p}\,\mathrm{d}x \\ & + \int_{\delta\Omega}\left(\vec{J}_p + \delta\vec{J}_p\right)\cdot\vec{n}v_{\phi_p}\,\mathrm{d}s, \end{aligned} \tag{6.67}$$

and with $\vec{b}_p = d_p\beta\nabla\phi_p$ the weak form

$$F_{\vec{J}_p} = \int_\Omega \left(\vec{J}_p + \delta\vec{J}_p + d_p\nabla\phi_p + d_p\nabla\delta\phi_p - \vec{b}_p\delta\phi + \vec{b}_p\delta\phi_p\right)\cdot\vec{v}_{\vec{J}_p}\,\mathrm{d}x \tag{6.68}$$

is associated with (6.59). To ensure that the integrals for the weak forms are bounded, the gradients of the scalar functions and test functions have to be square integrable and the vector currents and respective vector test functions have to be square integrable, so that the solution vector is in the mixed function space $\delta u \in V_0\times V_1\times V_0\times V_1\times V_0\times V_1 = W$ with $V_0 = \{v \in H^1(\Omega) : v = u_{\mathrm{D}}\,\mathrm{on}\,\delta\Omega_{\mathrm{D}}\}$, and $V_1 = L^2(\Omega)^d$ and the test function vector is in the mixed test function space $v \in \hat{V}_0\times\hat{V}_1\times\hat{V}_0\times\hat{V}_1\times\hat{V}_0\times\hat{V}_1 = \hat{W}$ with $\hat{V}_0 = \{v \in H^1(\Omega) : v = 0\,\mathrm{on}\,\delta\Omega_{\mathrm{D}}\}$, and $\hat{V}_1 = L^2(\Omega)^d$. The test functions vanish on the Dirichlet boundaries, as well as the normal components of the currents on the Neumann boundaries so that the surface integrals in (6.63), (6.65) and (6.67) vanish. The space $L^2(\Omega)^d$ is the set of square integrable (vector) functions on $\Omega \subset \mathbb{R}^d$. The variational problem reads: Find $\delta u \in W$ such that

$$\int_\Omega \mathcal{L}(u,\delta u)\cdot v\,\mathrm{d}x = 0 \quad \forall v \in \hat{W}. \tag{6.69}$$

Standard Galerkin (1st order Lagrange) elements are chosen for the FEM discretization of the potentials, and zero order discontinuous Galerkin elements are chosen for the current densities in the one-dimensional case. Details about the FEM discretization and respective finite-elements are summarized in [71, 77, 101]. The extension of the presented PMM for the two-dimensional case is subject to future works. A possible FE-type for discretization of the vector currents are (Discontinuous) Raviart-Thomas ((D)RT) elements since they preserve the divergence of the current densities in two-dimensions and are employed for problems in mixed formulations [101].

The introduced PMM is compared to the formulation in variables (ϕ, ϕ_n, ϕ_p), where standard 1st order Lagrange elements are employed. Details about the FE formulation in variables (ϕ, ϕ_n, ϕ_p) are given in the Appendix C.8. The PMM implementation of the DDM is demonstrated by the example of a GaAs pn-junction, with properties listed in Tb. 6.2. The terminal currents at the p- and n-side obtained with the PMM and with the FEM formulation (in the potentials as variables) are compared, Fig. 6.3. For the primal method, the total current density is conserved throughout the entire simulation domain (Fig. 6.4) even for relatively low resolutions of 20 mesh points (Fig. 6.5). In contrast, even for a resolution of 160 mesh knots the total current density shows significant numerical errors for the standard formulation, compare Fig. 6.6).

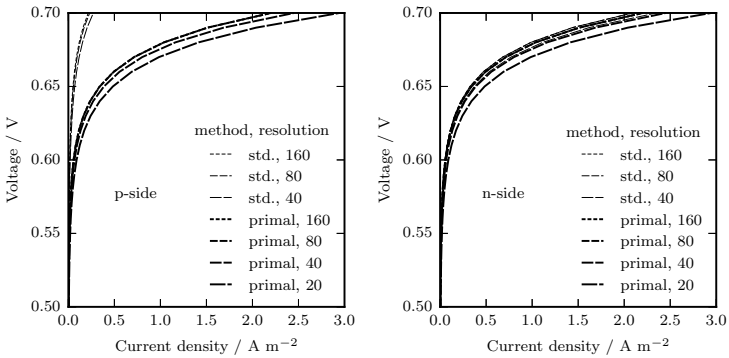

FIGURE 6.3: Comparison of calculated terminal current densities on p-side (left) and n-side (right) boundary for FEM with potentials variables and the primal method (thick lines). The large discrepancy between the current on the p-side and n-side are observable.

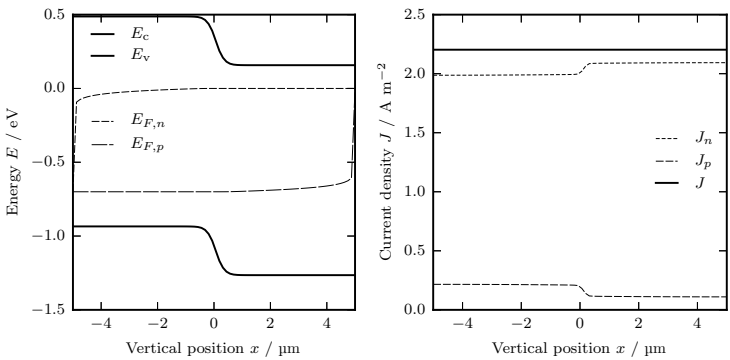

FIGURE 6.4: Energy diagram and current density calculated with PMM for the structure listed in Tb. 6.2 with 0.7 V applied. The total current density is conserved locally throughout the domain. The results displayed are calculated on 160 mesh knots.

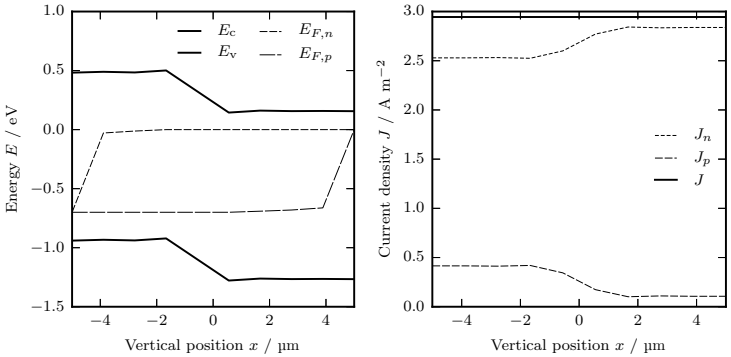

FIGURE 6.5: Energy diagram and current density calculated with PMM for the structure listed in Tb. 6.2 with 0.7 V applied. The PMM is stable, and the total current density is conserved locally throughout the domain for a resolution of 20 mesh knots.

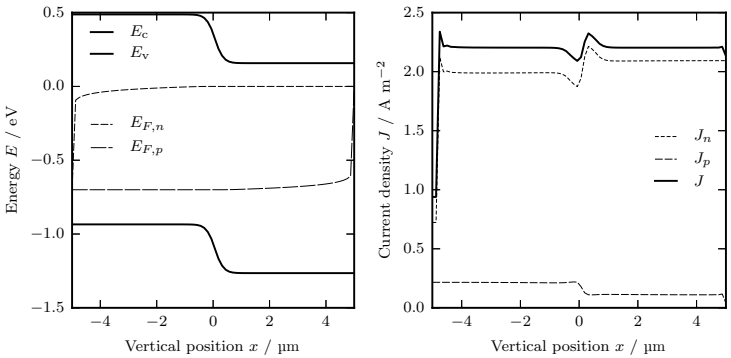

FIGURE 6.6: Energy diagram and current density calculated with the standard formulation in potentials for the structure listed in Tb. 6.2 with 0.7 V applied. The total current density is not conserved locally throughout the domain. The results displayed are calculated on 160 mesh knots.

Parameter	Value
Material	GaAs at 300 K
Domain length	10 µm
N_D (n-side)	$1 \cdot 10^{21}$ m^{-3}
N_A (n-side)	$1 \cdot 10^{19}$ m^{-3}
N_D (p-side)	$1 \cdot 10^{19}$ m^{-3}
N_A (p-side)	$1 \cdot 10^{21}$ m^{-3}

TABLE 6.2: Parameters for GaAs pn-junction.

6.4 Coupling of Active Region and Drift-Diffusion Model

In the presented model, the QW is treated as bulk semiconductor, which simplifies the implementation. But instead of applying the bulk properties of the QW material (in this case InGaAs), the effective densities $N_{\mathrm{c,QW}}, N_{\mathrm{v,QW}}$ for electrons and holes and an effective bandgap $E_{\mathrm{g,QW}}$ and conduction band offset $\Delta E_{\mathrm{c,QW}}$ are determined by fitting the change of Fermi energies with carrier density from results of a k·p band structure calculation. An example is shown in Fig. 6.7. The extracted values are inserted for the bulk properties of the QW. Therefore, the QW band structure is approximated by two parabolic bands in the DDM. Although, in this model, sub-band transitions, transition rates, incomplete quantum carrier capture, the distribution of charges determined by the quantum mechanical wavefunction (details about the inclusion of these effects are found in [102]) are neglected, the implementation is straightforward and yields a pragmatic approach to model HPDL devices. If the carriers in the quantized states are not in equilibrium with the ones in the barrier (bulk) states, carrier capture, and escape rates are introduced, and the interaction with the quantized states is treated in more elaborated models. The separate treatment of quantized and bulk carriers with capture and escape rates and two distinct carrier densities is demonstrated in [103, 104]. For an ideal two-dimensional Fermi gas, the quasi-Fermi energy is related to the carrier density by [105]

$$\pm \frac{E_{\mathrm{F},n/p}}{k_{\mathrm{B}}T} = \frac{E_{\mathrm{F},n/p,0}}{k_{\mathrm{B}}T} + \ln\left(\exp\left(\frac{n/p}{N_{\mathrm{c/v}}}\right) - 1\right), \tag{6.70}$$

where $E_{\mathrm{F},0}$ is a reference energy level. The relation between $E_{\mathrm{F},n/p}$ and n/p_{QW} is determined based on the band structure so that the effective band masses are determined by fitting the (nonlinear) function $y = b + \ln(\exp(x/a) - 1)$. For electrons and holes, the effective mass is

$$m_{n/p} = \frac{N_{\mathrm{c/v}}\pi\hbar^2 d_{\mathrm{qw}}}{k_{\mathrm{B}}T}. \tag{6.71}$$

In the limit of small carrier densities $\frac{n}{N_{\mathrm{c}}} \ll 1$ Eq. (6.70) is approximated by

$$\exp\left(\frac{E_{\mathrm{F},n} - E_{\mathrm{F},0}}{k_{\mathrm{B}}T}\right) = \exp\left(\frac{n}{N_{\mathrm{c}}}\right) - 1 \simeq \frac{n}{N_{\mathrm{c}}}, \tag{6.72}$$

and analog for holes. The approximated relation equals the expression for an ideal three-dimensional Fermi gas in the high-temperature limit [105]. To couple the optical problem to the electrical transport model, the approaches in [93, 102] are followed. On the one hand, the term for stimulated recombination depends on the optical intensity and on the other hand, the optical gain, and free-carrier absorption are determined by carrier distributions in the QW and the waveguide. For the transverse electro-optical simulation the optical problem consists of the eigenmode equation for the electric field and the photon rate equation, which determines the photon density in the cavity by equalizing losses and gain. A steady-state solution above the lasing threshold is found if the photon density and connected stimulated recombination rate equalize the modal gain and modal loss

$$G_m - \alpha_m = 0. \tag{6.73}$$

The flow-chart for the coupled iteration is displayed in Fig. 6.8, for the case that Gummel's iteration is used to solve the DDM. If Newton's method is used for the DDM the block labeled *Gummel iteration* in Fig. 6.8 is substituted. The iteration for the coupled optical-electrical problem proceeds as follows: After the applied voltage is increased the

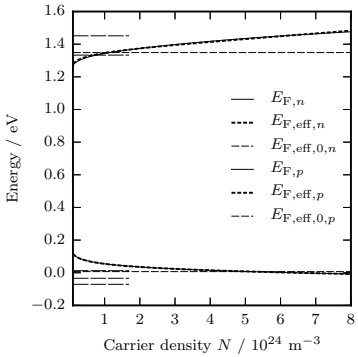

FIGURE 6.7: Fermi energy calculated from band structure of epitaxy E1 (see Tb. C.1 for details) and (fitted) with the effective model over carrier density. The horizontal lines on the left axes indicate the zone center band energies.

Gummel or Newton iteration is completed, and a consistent solution for the DDM is found. The gain and free-carrier losses are updated based on the carrier densities in the active region. The modal gain

$$G_m = \frac{\int_\Omega 2g|\phi_m|^2 \,\mathrm{d}x\,\mathrm{d}y}{\int_\Omega |\phi_m|^2 \,\mathrm{d}x\,\mathrm{d}y} \tag{6.74}$$

and modal absorption

$$\alpha_m = \frac{\int_\Omega \alpha_{\mathrm{fc}}(n,p)|\phi_m|^2 \,\mathrm{d}x\,\mathrm{d}y}{\int_\Omega |\phi_m|^2 \,\mathrm{d}x\,\mathrm{d}y} + \alpha_{\mathrm{mir}}, \tag{6.75}$$

where α_{fc} are free-carrier losses and α_{mir} are round-trip mirror losses, are determined by integration over the gain and losses weighted with the light intensity distribution $|\phi_m|^2$ of mode number m. With increasing stimulated recombination more carriers recombine in the active region so that the gain together with the carrier density decreases. For modal gain larger than the modal absorption, the stimulated recombination rate is increased. In contrast, if the modal gain is lower than the modal absorption, the recombination rate is decreased for the next iteration step. The stimulated recombination rate in the active region is updated, and the electronic transport problem is solved again for the updated recombination rate. After each update of the stimulated recombination, the residual of (6.73) should decrease, and the iteration is stopped after a defined tolerance is reached $|G_{m,i} - \alpha_{m,i}| < \varepsilon_{\mathrm{tol}}$. For each iteration step, the update of the stimulated recombination rate is estimated by

$$\delta R_{\mathrm{st},m} = \left(\frac{\partial G_m}{\partial R_{\mathrm{st},m}}\right)^{-1} (\alpha_m - G_m)\,. \tag{6.76}$$

The partial derivative at iteration step i is approximated with the values from the previous iteration steps so that the update for the recombination rate is given by

$$\delta R_{\mathrm{st},m,i} = \begin{cases} \frac{R_{\mathrm{st},m,i-1} - R_{\mathrm{st},m,i-2}}{G_{m,i} - G_{m,i-1}} (\alpha_m - G_{m,i-1}) & , G_{m,i} \neq G_{m,i-1} \\ \Delta R_{\mathrm{st},m,\mathrm{min}} & , \text{else} \end{cases} \tag{6.77}$$

and the stimulated recombination rate at iteration step i is set to

$$R_{\mathrm{st},m,i} = \begin{cases} 0 & , G_{m,i} \leq 0 \\ R_{\mathrm{st},m,i-1} + \omega_{R_{\mathrm{st},m}} \delta R_{\mathrm{st},m,i} & , G_{m,i} > 0 \end{cases} \tag{6.78}$$

The relaxation parameter $\omega_{R_{\mathrm{st},m}}$ is introduced to damp the updates and $\Delta R_{\mathrm{st},m,\mathrm{min}}$ is a parameter set to establish an initial increase of the recombination rate. The modal photon flux density S_m is calculated from the stationary photon rate equation

$$S_m = \frac{R_{\mathrm{st},m} + R_{\mathrm{sp},m}}{\alpha_m}, \tag{6.79}$$

where

$$R_{\mathrm{sp},m} = \frac{\int_\Omega \beta_{\mathrm{sp}} R_{\mathrm{sp}}(n,p) |\phi_m|^2 \,\mathrm{d}x\,\mathrm{d}y}{\int_\Omega |\phi_m|^2 \,\mathrm{d}x\,\mathrm{d}y} \tag{6.80}$$

is the fraction of the spontaneous emission coupled into the light field with the dimensionless factor β_{sp}. The photon flux density is not directly fed back into the drift-diffusion equations since the (local) stimulated recombination rate can be determined by the modal stimulated recombination and (normalized) optical mode profile

$$R_{\mathrm{st}} = \sum_m |\phi_m|^2 R_{\mathrm{st},m}. \tag{6.81}$$

Additionally to the recombination rate the temperature is updated based on local heat sources accounting for Joule heating, non-radiative recombinations, and re-absorption of light. Based on the new temperature material parameters (effective density of states, mobility, and thermal voltage) are updated. After the photon density and temperature iteration converges, the optical eigenmodes are updated (according to Section 4.5), and the inner loop is repeated until a consistent solution is found. Although the eigenmodes of the waveguide with gain and losses according to the carrier distributions can be solved, the method does not evaluate the coefficients for the coherent superposition of these modes. The modes are coupled through the connection to carrier distributions by the local gain. However, to approximate the intensity profile the calculated set of eigenmodes is incoherently superimposed. The photon flux density S in $\mathrm{m}^{-2}\ \mathrm{s}^{-1}$ is determined by

$$S = \sum_m |\phi_m|^2 S_m. \tag{6.82}$$

and it is related to the intensity I via $I = \hbar\omega S$. The approach is used for both two-dimensional transverse simulations and one-dimensional vertical simulations. In the one-dimensional case, the power in a transverse cross-section with contact width w_{c} inside the cavity is $P = w_{\mathrm{c}} d_{\mathrm{qw}} I$.

6.5 Carrier Diffusion Equation for Quantum Well

For the coupled laser model presented in Chapter 8 the electrical problem based on the drift-diffusion model is not solved in the iteration since the computation time for a voltage step is long (more than several minutes). For the FD and TD laser models, solely the (ambipolar) carrier density inside the QW is taken into account. The density of carriers $n^{\mathrm{qw}}(y,z)$ is modeled as a two-dimensional quantum gas and determined by

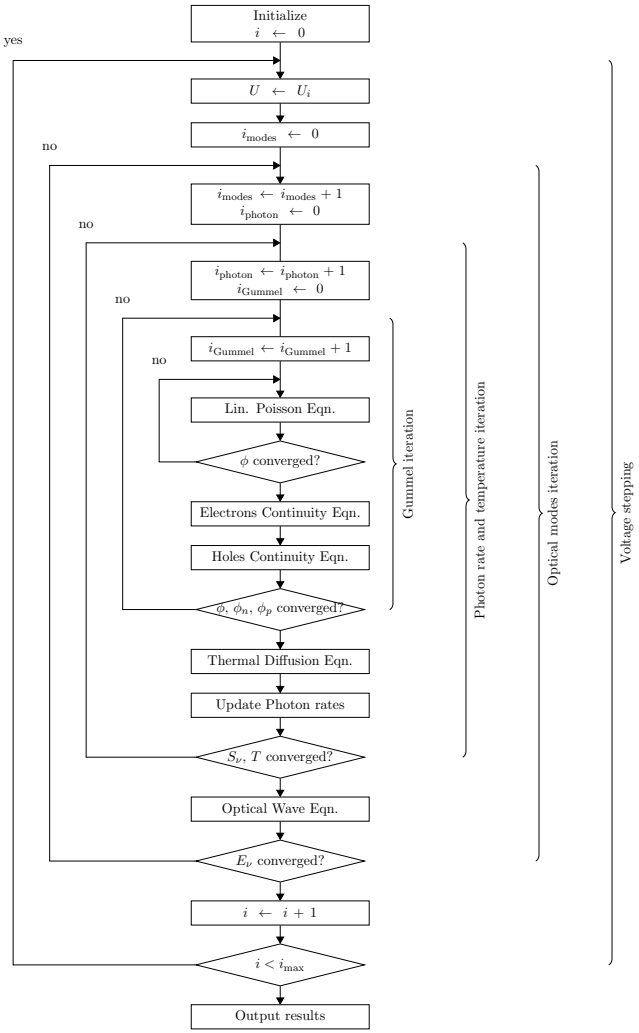

FIGURE 6.8: Flow-chart for transverse electro-optical diode laser model. The symbols used are the applied voltages U_i, temperature T, electric potential ϕ, quasi-Fermi potentials ϕ_n, ϕ_p, modal photon rates S_ν and electrical field for the optical modes E_ν with mode number ν.

the rate equation (carrier diffusion equation) [58, 36]

$$\begin{aligned}\partial_t n^{\mathrm{qw}} = &\frac{\eta_{\mathrm{tr}} J}{q_{\mathrm{el}} d_{\mathrm{qw}}} + D\partial_y^2 n^{\mathrm{qw}} + D\partial_z^2 n^{\mathrm{qw}} - A_{\mathrm{nr}} n^{\mathrm{qw}} - B_{\mathrm{sp}} \left(n^{\mathrm{qw}}\right)^2 - C_{\mathrm{A}} \left(n^{\mathrm{qw}}\right)^3 \\ &+\frac{i}{4\hbar}\left(\left(p^+_{0,\mu} + \Delta p^+_\mu\right)^* \phi^+_\mu - \left(p^+_{0,\mu} + \Delta p^+_\mu\right) \phi^{+*}_\mu\right) \\ &+\frac{i}{4\hbar}\left(\left(p^-_{0,\mu} + \Delta p^-_\mu\right)^* \phi^-_\mu - \left(p^-_{0,\mu} + \Delta p^-_\mu\right) \phi^{-*}_\mu\right), \end{aligned} \tag{6.83}$$

where $\mu, \nu = x, y$, and $\phi^\pm_\mu$, $p^\pm_\mu = p^\pm_{0,\mu} + \Delta p^\pm_\mu$ are the envelopes of the forward and backward traveling transverse components of the electric field and the material polarization[1], respectively. The equation models the distribution of confined carriers based on diffusion in the plane of the QW, and the balance of recombination rates. The polarization dependent parts enter through the SBEs [25]. The variables used in the rate equation are listed in Tb. 6.3. In general carriers diffuse in both the lateral and the longitudinal direction. However, longitudinal diffusion is neglected so that the rate equation is solved independently for individual transverse slices along the laser cavity. The static part of the polarization is expressed by the static part of the susceptibility

Parameter	Symbol	Unit
Current density	J	$\mathrm{A/m^2}$
Light intensity	I	$\mathrm{W/m^2}$
Transport efficiency	η_{tr}	
Thickness of quantum well	d_{qw}	m
Diffusion coefficient	D	$\mathrm{m^2/s}$
Non-radiative lieftime	$\tau_{\mathrm{nr}} = \frac{1}{A}$	s
Non-radiative recombination rate	A_{nr}	$\mathrm{s^{-1}}$
Coefficient of spontaneous emission	B_{sp}	$\mathrm{m^3\,s^{-1}}$
Coefficient of Auger recombination	C_{A}	$\mathrm{m^6/s}$

Table 6.3: Parameters for carrier rate equation.

$\chi_{(0),\mu\nu} = \chi_{r,(0),\mu\nu} + i\chi_{i,(0),\mu\nu}$, and by insertion of $p^\pm_{0,\mu} = \varepsilon_0 \chi_{(0),\mu\nu} \phi^\pm_\nu$, the rate equation is

[1] At this point the contribution from the linear dispersion to the polarization is neglected. The derivation including this contribution is briefly illustrated in the following: The frequency-domain relation between the linear part of the polarization and the electric field (4.23) is transformed into the time domain

$$\vec{P}_{\mathrm{L}}(t) = \varepsilon_0(\varepsilon_{\mathrm{r}} - 1 - \varepsilon'_{\mathrm{r}}\omega_{\mathrm{ref}})\vec{E}(t) + i\varepsilon_0\varepsilon'_{\mathrm{r}}\partial_t\vec{E}(t). \tag{6.84}$$

With the assumption that $\varepsilon'_{\mathrm{r}}$ is real, this relation is used to compute the term $\vec{P}^*_{\mathrm{L}} \cdot \vec{E} - \vec{P}_{\mathrm{L}} \cdot \vec{E}^* = -2i\varepsilon_0(\varepsilon_{\mathrm{r,i}}|\vec{\phi}(t)|^2 + \frac{1}{2}\varepsilon'_{\mathrm{r}}\partial_t|\vec{\phi}(t)|^2)$ which enters the carrier diffusion equation. In the equation $\varepsilon_{\mathrm{r,i}}$ denotes the imaginary part of the dielectric function. Under the assumption that amplitude fluctuations of the envelope occur at a much lower rate than, for example, the reference angular frequency, $\varepsilon'_{\mathrm{r}}\partial_t|\vec{\phi}(t)|^2$ can be neglected.

written as

$$\begin{aligned}\partial_t n^{\mathrm{qw}} &= \frac{\eta_{\mathrm{tr}} J}{q_{\mathrm{el}} d_{\mathrm{qw}}} + D\partial_y^2 n^{\mathrm{qw}} - A_{\mathrm{nr}} n^{\mathrm{qw}} - B_{\mathrm{sp}} \left(n^{\mathrm{qw}}\right)^2 - C_{\mathrm{A}} \left(n^{\mathrm{qw}}\right)^3 \\ &\quad + \frac{\varepsilon_0}{2\hbar} \left(\chi_{i,(0),\mu\nu} \phi_\mu^+ \phi_\nu^{+*} + \chi_{i,(0),\mu\nu} \phi_\mu^- \phi_\nu^{-*}\right) \\ &\quad + \frac{i}{4\hbar} \left(\Delta p_\mu^{+*} \phi_\mu^+ - \Delta p_\mu^+ \phi_\mu^{+*} + \Delta p_\mu^{-*} \phi_\mu^- - \Delta p_\mu^- \phi_\mu^{-*}\right) \\ &= \frac{\eta_{\mathrm{tr}} J}{q_{\mathrm{el}} d_{\mathrm{qw}}} + D\partial_y^2 n^{\mathrm{qw}} - A_{\mathrm{nr}} n^{\mathrm{qw}} - B_{\mathrm{sp}} \left(n^{\mathrm{qw}}\right)^2 - C_{\mathrm{A}} \left(n^{\mathrm{qw}}\right)^3 \\ &\quad + \frac{\varepsilon_0 \chi_{i,(0),xx}}{2\hbar} \left(|\phi_x^+|^2 + |\phi_x^-|^2\right) + \frac{\varepsilon_0 \chi_{i,(0),yy}}{2\hbar} \left(|\phi_y^+|^2 + |\phi_y^-|^2\right) \\ &\quad + \frac{i}{4\hbar} \left(\Delta p_\mu^{+*} \phi_\mu^+ - \Delta p_\mu^+ \phi_\mu^{+*} + \Delta p_\mu^{-*} \phi_\mu^- - \Delta p_\mu^- \phi_\mu^{-*}\right). \end{aligned} \tag{6.85}$$

In the last step, it is assumed that the complex part of the susceptibility tensor is a diagonal tensor, which means that the off-diagonal entries are zero $\chi_{i,(0),\mu\nu} = 0$ for $\mu \neq \nu$ so that there is no cross-coupling of the transverse field components via gain or loss. The field intensity $I_\mu = I_\mu^+ + I_\mu^- = \frac{c_0 \varepsilon_0 n_{\mu\mu}}{2} \left(|\phi_\mu^+|^2 + |\phi_\mu^-|^2\right)$, which is the incoherent superposition of the forward and backward intensity, together with the components of the anisotropic (amplitude) gain $g_{\mu\nu} = -\frac{\omega_{\mathrm{ref}} \chi_{i,(0),\mu\nu}}{2 c_0 n_{\mu\nu}}$ are inserted

$$\begin{aligned}\partial_t n^{\mathrm{qw}} &= \frac{\eta_{\mathrm{tr}} J}{q_{\mathrm{el}} d} + D\partial_y^2 n^{\mathrm{qw}} - A_{\mathrm{nr}} n^{\mathrm{qw}} - B_{\mathrm{sp}} \left(n^{\mathrm{qw}}\right)^2 - C_{\mathrm{A}} \left(n^{\mathrm{qw}}\right)^3 \\ &\quad - \frac{I_x}{\hbar\omega_{\mathrm{ref}}} 2 g_{xx}(n^{\mathrm{qw}}, T, \omega_{\mathrm{ref}}) - \frac{I_y}{\hbar\omega_{\mathrm{ref}}} 2 g_{yy}(n^{\mathrm{qw}}, T, \omega_{\mathrm{ref}}) \\ &\quad + \frac{i}{4\hbar} \left(\Delta p_\mu^{+*} \phi_\mu^+ - \Delta p_\mu^+ \phi_\mu^{+*} + \Delta p_\mu^{-*} \phi_\mu^- - \Delta p_\mu^- \phi_\mu^{-*}\right). \end{aligned} \tag{6.86}$$

Eq. (6.86) reveals the (dispersion free) part for stimulated recombination

$$R_{\mathrm{st}} = \frac{1}{\hbar\omega_{\mathrm{ref}}} \underbrace{2 g_{\mu\mu}}_{=G_{\mu\mu}} (n^{\mathrm{qw}}, T, \omega_{\mathrm{ref}}) I_\mu. \tag{6.87}$$

In the instationary case, the equation is linearized in the carrier density and the time derivative is discretized with the Crank-Nicolson scheme, see Appendix C.11. Dropping the time derivative and the time-dependent part of the polarization envelope in (6.86) yields the stationary carrier diffusion equation

$$\begin{aligned}0 &= \frac{\eta_{\mathrm{tr}} J}{q_{\mathrm{el}} d_{\mathrm{qw}}} + D\partial_y^2 n^{\mathrm{qw}} - A_{\mathrm{nr}} n^{\mathrm{qw}} - B_{\mathrm{sp}} \left(n^{\mathrm{qw}}\right)^2 - C_{\mathrm{A}} \left(n^{\mathrm{qw}}\right)^3 \\ &\quad - \sum_\nu \frac{I_{x,\nu}}{\hbar\omega_\nu} 2 g_{xx}(n^{\mathrm{qw}}, T, \omega_\nu) - \sum_\nu \frac{I_{y,\nu}}{\hbar\omega_\nu} 2 g_{yy}(n^{\mathrm{qw}}, T, \omega_\nu), \end{aligned} \tag{6.88}$$

where the term for the stimulated recombination rate becomes the sum over the contributions from each Fourier component $I_{\mu,\nu}$ of the light field associated with the angular frequency ω_ν. This stationary version is used in the FD models.

The dependence of the gain on the carrier density, temperature, and frequency is calculated with the methods introduced in Chapter 2. Nevertheless, the gain as a function of the carrier density can be approximated by analytical functions to simplify the implementation in the model. The gain as a function of carrier density is approximated by a

logarithmic dependence or the first order Taylor expansion of the logarithm around the transparency density, which gives a linear dependence

$$g(n^{\mathrm{qw}}, T) = g_0(T) \ln\left(\frac{n^{\mathrm{qw}}}{N_{\mathrm{tr}}(T)}\right) \approx g_0(T)\left(\frac{n^{\mathrm{qw}}}{N_{\mathrm{tr}}(T)} - 1\right). \tag{6.89}$$

The transparency carrier density N_{tr} increases and the gain coefficient g_0 decreases with increasing temperature T. The dependencies are approximated by the linear relations $g_0(T) = g_{T_0} - g_{0,T}(T - T_0)$, and $N_{\mathrm{tr}}(T) = N_{\mathrm{tr},T_0} - N_{\mathrm{tr},T}(T - T_0)$ with the parameters $g_{0,T}$ and $N_{\mathrm{tr},T}$, which are extracted from measurements or gain calculations. Evaluation of the logarithm for negative values leads to numerical instabilities in the solution process. To circumvent this problem. a Padé approximation [106]

$$\ln(x) \approx \frac{(x-1)(6+x-1)}{(6+4(x-1))} \tag{6.90}$$

is can be used instead of the logarithmic function.

6.6 Results for Vertical Electrical Simulation with Primal Mixed Method

One-dimensional simulations can be performed with higher resolutions than two-dimensional simulations in less time and with fewer resources and are suited to improve and analyze vertical epitaxial designs. In this section, the PMM is employed to simulate the electro-optical characteristics of the laser epitaxy E1 (Tb. C.1). The PMM is stable, has fast convergence and supplies results which satisfy current conservation. In the presented case the difference between both terminal currents is below $1 \cdot 10^{-12}$ A up to diode currents of 20 A. The calibration of the model to match the measured

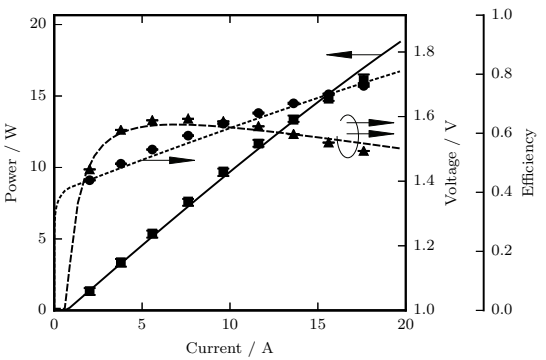

FIGURE 6.9: Power, voltage, and efficiency for one-dimensional simulation over current and experimental values (as markers). A constant voltage of 0.04 V is added to the simulated voltages to match the measured curve. A reason for this discrepancy can be a contact voltage at interfaces either at the metal-semiconductor contact or in the measurement apparatus.

electrical-optical characteristics (Fig. 6.9) is performed by adjusting the carrier transparency increase with temperature $\frac{\Delta N_{\mathrm{tr}}}{\Delta T}$ and the length of the fraction of the substrate included in the simulation domain. Since current spreads in the lateral direction the effective resistance in the substrate reduces towards the n-side. A linear model for the gain (6.89) is employed. The calculated dissipated power in conjunction with a thermal resistance of $R_{\mathrm{th}} = 3\,\mathrm{KW}^{-1}$ is used to update the temperature. Both, the mode overlap

Parameter	Symbol	Value	Source
Substrate thickness	d_{sub}	$20\,\mu\mathrm{m}$	calibration
Thermal resistance	R_{th}	$3\,\mathrm{KW}^{-1}$	experiment
Gain change	$g_{0,T}$	$-63\,\mathrm{m}^{-1}\mathrm{K}^{-1}$	band structure, gain
Transp. carrier change	$N_{\mathrm{tr},T}$	$2.74 \cdot 10^{22}\,\mathrm{m}^{3}\mathrm{K}^{-1}$	calibration

TABLE 6.4: Parameters for vertical electrical simulation.

with the doped regions (especially on the p-side) and the carrier accumulation inside the waveguide around the QW determine the modal loss (Fig. 6.10). Penetration of the mode into regions with high doping leads to large modal absorption. Besides, the carriers accumulate in the un-doped regions inside and around the QW in dependence of the operating current and lead to increased free carrier absorption, see Fig. 6.11. The mirror loss (includes the out-coupling loss) for device D1 is $4.92\,\mathrm{cm}^{-1}$, and the modal absorption of the unbiased cavity accounts to $0.48\,\mathrm{cm}^{-1}$. It is related to the overlap of the vertical mode and the doping profile and makes up 64 % of the modal free-carrier absorption at the threshold, which is $0.75\,\mathrm{cm}^{-1}$. An increase from threshold current up to 20 A, adds another $0.16\,\mathrm{cm}^{-1}$ to the modal absorption, which equals about 18 % of the modal free-carrier absorption (Fig. 6.11). The main increase of modal loss with current takes place below the threshold, where the carrier density in the QW raises significantly. The carrier density (in the QW) also increases above the threshold to maintain the modal threshold-gain for increasing temperature and corresponding decreasing material gain.

Although the most significant change in majority current takes place at the QW due to the stimulated recombination, some carriers recombine in the p-side waveguide, see Fig. 6.12. Since the highest carrier densities occur inside the QW recombination rates are largest in the active region, see Fig. 6.12. The recombination in the p-side waveguide is larger than in the n-side waveguide, which correlates to the observed leakage current.

6.7 Results for Transverse Electrical Simulation

To investigate the current density distribution in the transverse plane, electro-optical calculations are performed for device D1 (without trenches). The focus lies on the lateral spreading of the current, particularly in the p-side, and the injected current density distribution in the QW. The simulations are performed with the method presented in Sections 6.2 and 6.4 on a two-dimensional transverse domain. A maximum number of 20 eigenmodes are superimposed. However, the considered number can be smaller, depending on the number of modes found each step with positive modal gain. The results discussed in this sections are calculated for a terminal voltage of 1.43 V which results in a current of 5 A. The conduction and valence band edges in the transverse plane are

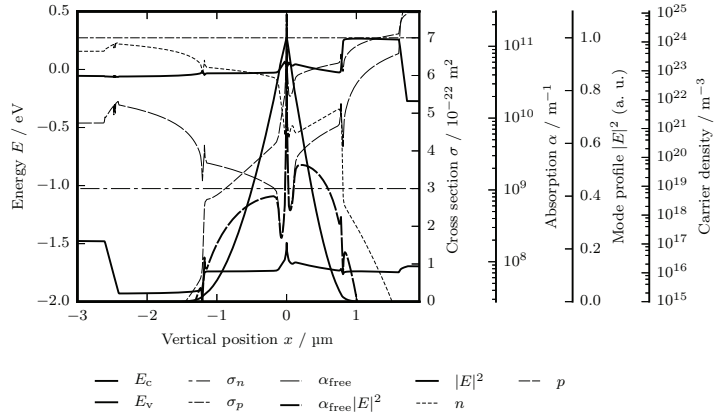

FIGURE 6.10: Optical mode profile and interplay with free carrier absorption for one-dimensional simulation with 1.7 V applied.

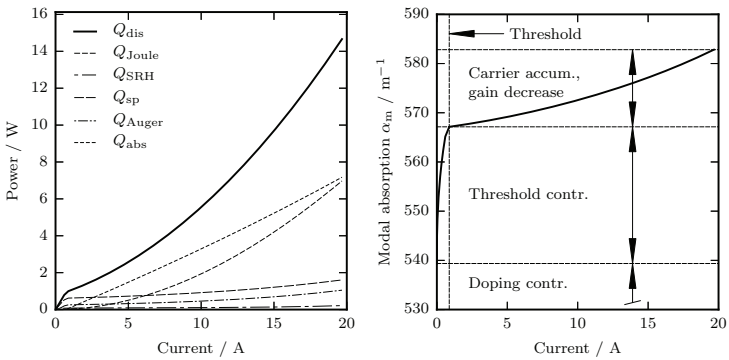

FIGURE 6.11: Results for one-dimensional simulation with 1.7 V applied.

displayed in Fig. 6.13. Under the injection stripe, the band edges are deformed so that a current-channel forms. Large lateral currents are observed mainly at interfaces between semiconductor layers with a large difference in conductivity. Due to the high doping in the GaAs p-cap layer, the current obeys significant spreading directly under the contact opening. The spreading in the p-side waveguide adds up to several micrometers on each side, see the lateral cross-section in Fig. 6.14. The largest magnitudes in lateral current density occur in the active region. The redistribution of current and carriers in the QW are results of both drift and diffusion. In the reduced model, where the carrier diffusion equation is employed for the QW-plane only contributions due to diffusion are included. The current density inside the injection stripe width is a function of the carrier distribution inside the QW and therefore also a function of the optical intensity. A minimum in the photon density leads to an increased carrier density, see the central part in the lateral cross-section for the electron density and the photon flux density

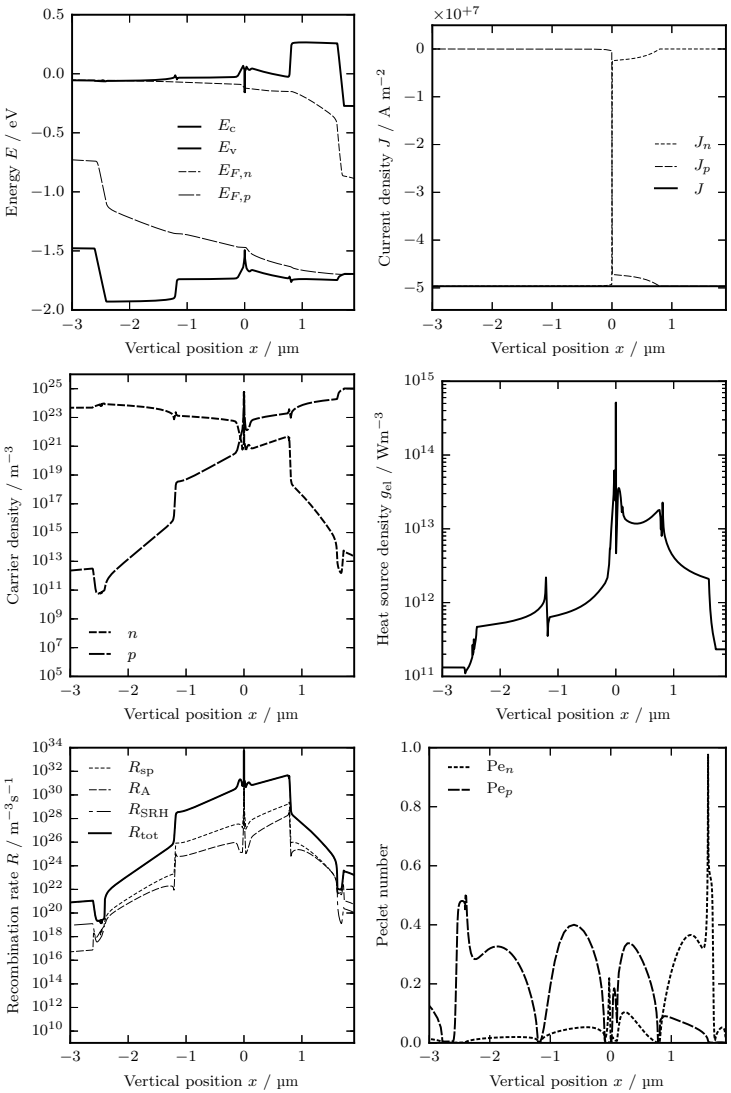

FIGURE 6.12: Results of one-dimensional electrical simulation for D1. The applied voltage is 1.7 V. The stimulated recombination is not included in the total recombination rate density.

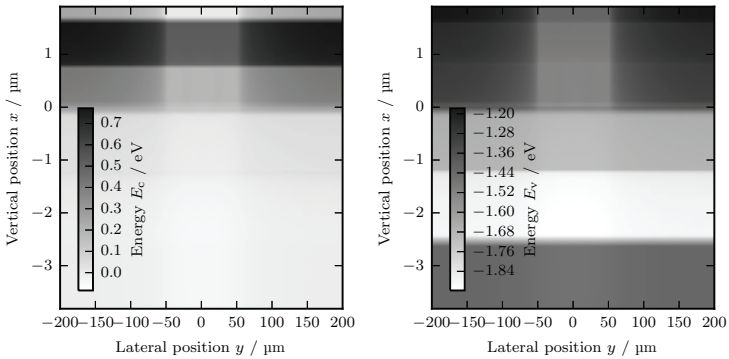

FIGURE 6.13: Conduction (left) and valence (right) band edge in transverse cross-section. The applied voltage is 1.43 V.

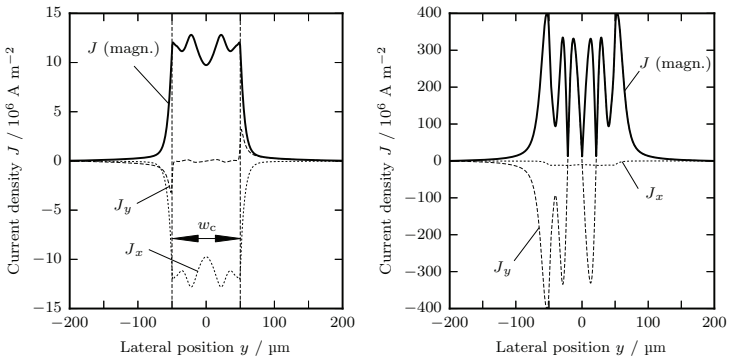

FIGURE 6.14: Current density in lateral cross-sections 0.3 µm above the QW towards the p-side (left) and inside the QW (right). The applied voltage is 1.43 V.

in Fig. 6.15. The increase in carrier density in the central region leads to increased separation of the quasi-Fermi energies in the QW. This increase reduces the injected current in this central part since the current is a function of the potential gradient from the p-contact to the QW. The lateral modulation of the current density, which correlates to the electron distribution in the QW and the optical field is observed in Fig. 6.16 and 6.15. In regions with high current densities, local thermal hotspots emerge, which lead to thermal gradients. Besides the gain distribution, which is a result of the current injection in the QW, the temperature gradients influence the optical near- and far-field characteristics. A tailored current-profile can be utilized to impact the lateral mode distribution and thus, benefit the lateral emission characteristics of diode laser devices.

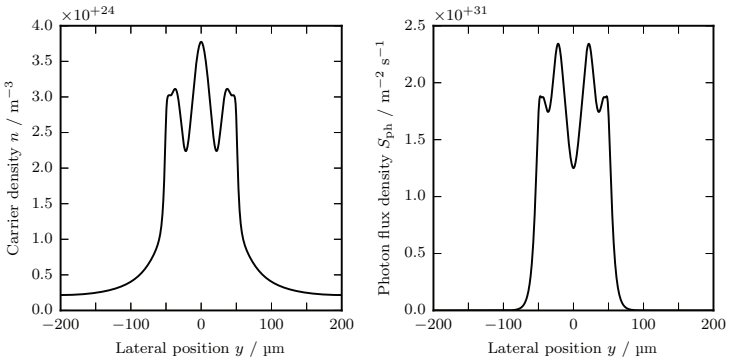

FIGURE 6.15: Electron density (left) and photon flux density (right) in lateral cross-sections through the QW. The applied voltage is 1.43 V.

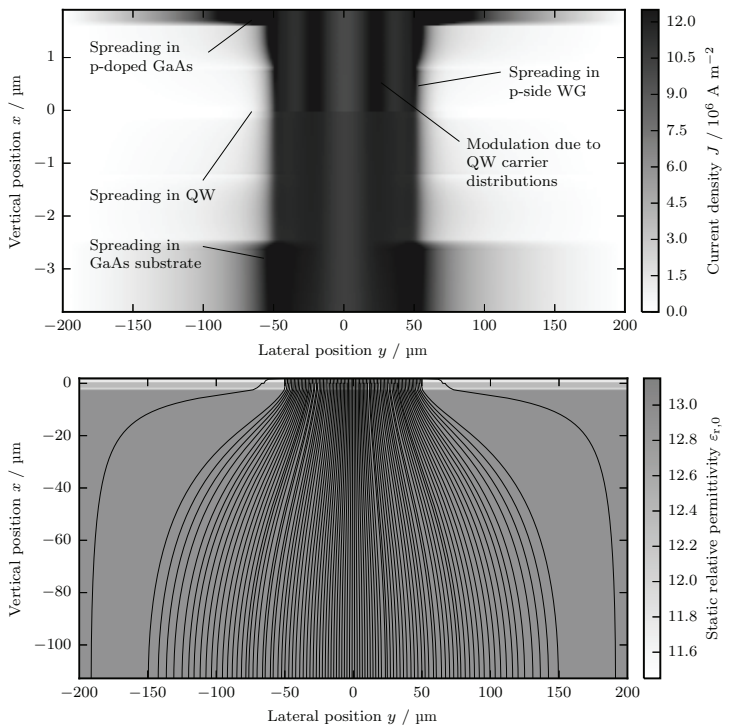

FIGURE 6.16: Current density (top) and stream (bottom) plot in transverse cross-section. The top plot displays details around the waveguide. The applied voltage is 1.43 V.

6.8 Chapter Summary

Two different discretization approaches for the DDM are presented: The Scharfetter-Gummel discretization of the current densities in combination with the FDM with box-integration (on a two-dimensional domain), and the FEM in combination with the PMM. In the PMM, the potentials and the associated current densities are treated as variables in the weak forms. So far, the PMM for the solution of the drift-diffusion equations is demonstrated on a one-dimensional domain. The extension to higher dimensions is subject to future work.

The main outputs of the electrical solver are: The transverse current profile for an active edge-emitting diode laser to quantify lateral current spreading (see the lateral cross-section in Fig. 6.14), the formulation and demonstration of a discretization scheme for an one-dimensional domain based on the FEM in conjunction with the PMM, and the calculation of output power, voltage and efficiency in agreement with experimental results for the epitaxy E1 (see Tb. C.1). Additionally, in the two-dimensional simulation the lateral modulation of the current density, which correlates to the electron distribution in the QW and the optical field is observed in Fig. 6.16 and 6.15. The modal loss, determined from the one-dimensional vertical computation for epitaxy E1 (Tb. C.1), accounts to $0.48\,\mathrm{cm}^{-1}$ for the unbiased device. This loss is related to the overlap of the vertical mode and the doping profile and makes up 64 % of the modal free-carrier absorption at the threshold of $0.75\,\mathrm{cm}^{-1}$. An increase from threshold current up to 20 A, adds $0.16\,\mathrm{cm}^{-1}$ (Fig. 6.11).

Chapter 7

Semiconductor Laser Models

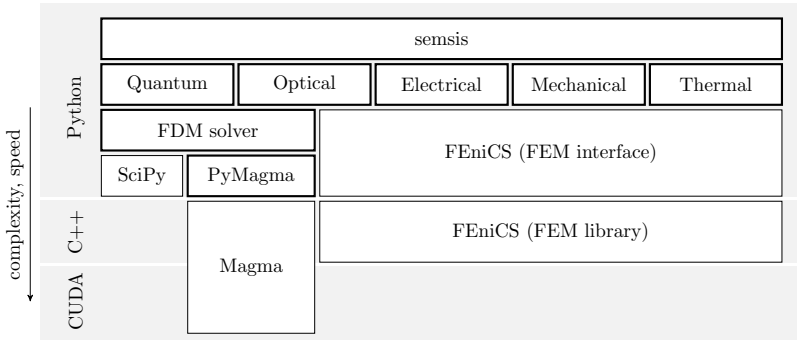

FIGURE 7.1: (Simplified) structure of programming languages, libraries, and packages used in *SEMSIS* package. The packages in the boxes with thin frames are third-party libraries.

The software package *SEMSIS* is implemented in the programming language *phython*. Some GPU accelerated modules are written in *C* and *C++* and the *pymagma* library interfaces functions of *Magma*, which offers multicore and GPU accelerated matrix-algebra including iterative sparse-matrix solvers [107]. The third party open-source library *FEniCS* [101] aims to solve partial differential equations with the FEM. Equations are defined in the weak formulation and are automatically translated into efficient finite-element code. The library consists of core modules written in the programming language *C++*, and a high-level *Python* interface. Except for the FEM package *FeniCS* and the *MAGMA* library, all modules are developed and implemented within the scope of this work. On the top level *SEMSIS* consists of a collection of modules in which the engines *Quantum* for computation of band structure and gain (Chapter 2), *Thermal* for solution of heat equations (Chapter 3), *Optical* providing BPM and TDTW methods (Chapter 4), *Mechanical* for linear-elastic mechanical problems and *Electrical* for solution of the DDM are implemented, see Fig. 7.1. The *FDM* solver module contains the implementation for the discretization scheme presented in (Chapter B). Additionally, classes for the handling of structured meshes, fields for storage and manipulation of physical properties, and domain structures, which hold material properties are included in *SEMSIS*. Material parameters for commonly used semiconductors are supplied in a

material database. In this chapter, the assembly of the individual physical problems into coupled models for edge-emitting semiconductor lasers is presented.

7.1 One-Dimensional Longitudinal Laser Model

In the one-dimensional model, the optical intensity for the forward $I_+(z)$ and backward traveling wave $I_-(z)$, and the carrier density $n^{\mathrm{qw}}(z)$ are functions of the longitudinal coordinate z. Since the gain is a function of the carrier density and the intensities are coupled to the carrier density in the rate equations the gain can saturate for higher intensities. The presented model is a steady-state model so that all time derivatives vanish. The model consists of the stationary carrier diffusion equation

$$\Lambda - A_{\mathrm{nr}} n^{\mathrm{qw}} - B_{\mathrm{sp}} \left(n^{\mathrm{qw}}\right)^2 - C_{\mathrm{st}} G(n^{\mathrm{qw}})(I_+ + I_-) = 0 \tag{7.1}$$

where any diffusion (transverse and longitudinal) is neglected. The coefficient for the stimulated term $C_{\mathrm{st}} = \frac{\lambda_0}{\hbar 2\pi c_0}$ and the pump rate $\Lambda = \frac{\eta_{\mathrm{i}} I}{q_{\mathrm{el}} d_{\mathrm{qw}} w_{\mathrm{c}} l_{\mathrm{d}}}$ with the injected current I and the internal efficiency η_{i} are introduced. With the (intensity) gain $G = 2g$ and the modal loss α_{m}, the equation governing the longitudinal evolution of the forward and backward propagating fields is

$$\partial_z I_\pm \mp (\Gamma G(n^{\mathrm{qw}}) - \alpha_{\mathrm{m}}) I_\pm = 0 \tag{7.2}$$

At the boundaries of the domain $\delta\Omega_0 = \{0\}$ and $\delta\Omega_l = \{l_z\}$, which are the back and front facet of the semiconductor laser the intensities must satisfy

$$I_+ = I_- R_0 \quad \text{on} \quad \delta\Omega_0, \tag{7.3}$$

$$I_- = I_+ R_l \quad \text{on} \quad \delta\Omega_l. \tag{7.4}$$

The gain function is approximated with the logarithmic dependence (6.89). To derive the weak form, the above equations are multiplied with test functions $v_n, v_{I_+}, v_{I_-} \in \hat{V}$, integrated over the entire domain $\Omega = \{z \in \mathbb{R}, 0 < z < l\}$ and added up

$$\begin{aligned}
F = &\int_\Omega \left(\tilde{\Lambda} - \tilde{n}^{\mathrm{qw}} - (\tilde{n}^{\mathrm{qw}})^2 \tilde{B}_{\mathrm{sp}} - C_{\mathrm{st}} \tilde{G}(\tilde{n}^{\mathrm{qw}})(\tilde{I}_+ + \tilde{I}_-)\right) v_n \,\mathrm{d}\tilde{z} \\
&+ \int_\Omega \left(\partial_{\tilde{z}} \tilde{I}_+ v_{I_+} - (\Gamma \tilde{G}(\tilde{n}^{\mathrm{qw}}) - \tilde{\alpha}_{\mathrm{m}}) \tilde{I}_+ v_{I_+}\right) \mathrm{d}\tilde{z} \\
&+ \int_\Omega \left(\partial_{\tilde{z}} \tilde{I}_- v_{I_-} + (\Gamma \tilde{G}(\tilde{n}^{\mathrm{qw}}) - \tilde{\alpha}_{\mathrm{m}}) \tilde{I}_- v_{I_-}\right) \mathrm{d}\tilde{z} \\
&+ \int_{\delta\Omega_l} \frac{\alpha}{h} \left(\tilde{I}_+ - \frac{\tilde{I}_-}{R_l}\right) v_{I_+} \,\mathrm{d}s + \int_{\delta\Omega_0} \frac{\alpha}{h} \left(\tilde{I}_- - \frac{\tilde{I}_+}{R_0}\right) v_{I_-} \,\mathrm{d}s \\
&- \int_{\delta\Omega_l} \left(\nabla v_{I_+} \cdot \vec{n} \left(\tilde{I}_+ - \frac{\tilde{I}_-}{R_l}\right) + v_{I_+} \vec{n} \cdot \tilde{\nabla} \tilde{I}_+\right) \mathrm{d}s \\
&- \int_{\delta\Omega_0} \left(\nabla v_{I_-} \cdot \vec{n} \left(\tilde{I}_- - \frac{\tilde{I}_+}{R_0}\right) + v_{I_-} \vec{n} \cdot \tilde{\nabla} \tilde{I}_-\right) \mathrm{d}s.
\end{aligned} \tag{7.5}$$

In this form, the Dirichlet boundary conditions are incorporated weakly by adding the terms with integration over the left and right boundary of the domain. In the above equation h is the local cell size of the discretized domain and α is a penalty term

chosen sufficiently large (the value is set to 10^{10}) to impose the boundary conditions. Furthermore, the scaled variables

$$\begin{aligned}
\tilde{B}_{\mathrm{sp}} &= n_0 \tau_{\mathrm{nr}} B_{\mathrm{sp}}, & \tilde{\alpha}_{\mathrm{m}} &= l_0 \alpha_{\mathrm{m}}, & \tilde{I}_{\pm} &= \frac{I_{\pm}}{I_0}, & \tilde{s}_{\pm} &= \frac{s_{\pm}}{I_0}, \\
\tilde{n}^{\mathrm{qw}} &= \frac{n^{\mathrm{qw}}}{n_0}, & \tilde{n}_{\mathrm{tr}} &= \frac{n_{\mathrm{tr}}}{n_0}, & \tilde{\nabla} &= l_0 \nabla, & \tilde{z} &= \frac{z}{l_0}, \\
\tilde{G} &= l_0 G, & \tilde{A_{\mathrm{nr}}} &= 1, & \tilde{C}_{\mathrm{st}} &= \frac{\tau_{\mathrm{nr}} I_0}{l_0 n_0}, & \tilde{\Lambda} &= \frac{\tau_{\mathrm{nr}}}{n_0},
\end{aligned} \tag{7.6}$$

with the scaling constants and parameters listed in Tb. C.4 are introduced. The variational problem to compute the finite element solution of the above problem is: Find $\tilde{I}_+, \tilde{I}_-, \tilde{n}^{\mathrm{qw}} \in V$ so that $F(\tilde{I}_+, \tilde{I}_-, \tilde{n}^{\mathrm{qw}}) = 0$ holds for all $v_{I_+}, v_{I_-}, v_{n^{\mathrm{qw}}} \in \hat{V}$. The nonlinear coupled system of equations is solved with a Newton solver. An increasing cavity

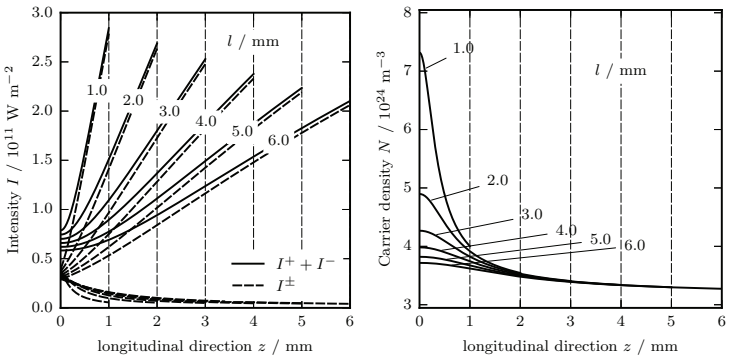

FIGURE 7.2: One-dimensional laser model results for intensity (left) and carrier density (right) for variation of cavity length l_z from 1 mm to 6 mm.

length leads to a decrease in the thermal resistance, electrical resistance, power (and slope efficiency), maximal intensity inside the cavity and an increased threshold current. For the same injection current, the maximum intensity in the cavity decreases and the effect of Longitudinal Spatial Hole Burning (LSHB), the higher carrier density in the rear part of the device, is reduced, see Fig. 7.2.

7.2 Frequency-Domain Laser Model

In the FD edge-emitting laser model (Fig. 7.4), the electric field is propagated from one transverse optical slice to the next in a Fox-Li iteration using the FD-BPM introduced in Chapter 4. The propagation can be performed with either the implicit scheme (4.72) or the explicit scheme (4.70). The total photon density is calculated based on the incoherent superposition of the forward and backward propagating fields at each longitudinal position. If the propagated field is the forward traveling one, the backward field values from the previous round-trip are taken to determine the total photon density and vice versa. Based on the carrier density and temperature distribution, the gain and carrier-induced refractive index change are calculated, and the beam-propagation matrix is updated.

The electric field is propagated through the optical slices until the next electro-thermal slice is reached and the material parameters are updated again. After iterating through the domain in the forward direction, the front facet boundary condition is applied, and the iteration is continued for the backward propagating field. Similar iterative models are reported in the literature [108, 109, 110, 111, 22, 23] and are employed to simulate output characteristics of edge-emitting diode lasers. The model can be extended with

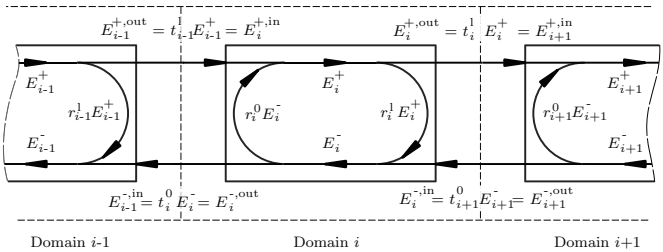

FIGURE 7.3: Schematic of the coupling scheme for multiple simulation domains. The output and input fields of each domain are passed through to the next or previous domain, respectively. Inside each domain, different methods for field propagation and computation can be applied. For example BPM, analytical approaches (for VBGs) or Fourier-based methods.

an External Optical System (EOS) [28, 29] to simulate coupled resonators, see Fig. 7.3. The EOS contains wave-optical models for optical components, for example, the fast-axis collimation lens, slow-axis collimation lens or VBGs for frequency stabilization. If an EOS is applied, the forward propagating field at the end of the chip is used as the input field for the EOS. The electric field is propagated forwards through each domain, where at each domain interface a partial reflection, according to the boundary conditions, is stored to be added to the backward propagating field at the corresponding location, when the backward propagation is performed. Within each domain, the Fox-Li iteration is performed with the difference that after each round-trip the fields of both neighboring domains are included at the domain boundaries, and thus, the domains are coupled to each other. To reduce the complexity and computational resources for the FD model (Algorithm 1) the governing partial differential equations are solved on multiple spatial domains in an iterative approach. The domains differ in dimensions, spatial extent, and the mesh discretization. The thermal domain $\Omega_{\mathrm{therm}} \subset \mathbb{R}^3$ has three-dimensions and includes the semiconductor device, the metallization, the solder, the submount and potentially a second interface and a cooler. The three-dimensional waveguide domain $\Omega_{\mathrm{wg}} \subset \mathbb{R}^3$ contains the optical waveguide and a fraction (several micrometers of the substrate in the vertical direction). To perform the BPM in the iterative approach, this domain is split up into a series of transverse cross-sections along the longitudinal direction with spacing Δz. Each transverse slice is defined on the spatial domain $\vec{x}_{\mathrm{t}} \in \Omega_{\mathrm{t}} \subset \mathbb{R}^d$, which spreads in the vertical and lateral direction, in the two-dimensional case $d = 2$, and in the lateral direction only, in the one-dimensional case $d = 1$. For the thermal solver, the temperature, intensity, (confined) carrier density, (bulk) carrier- and hole-density and the heat source densities from Joule heating, non-radiative heating, and absorption of the light field $T, I_{\mathrm{therm}}, n_{\mathrm{qw,therm}}, n_{\mathrm{therm}}, p_{\mathrm{therm}}, q_{\mathrm{el}}, q_{\mathrm{nr}}, q_{\mathrm{sp}}, q_{\mathrm{abs}} : \Omega_{\mathrm{therm}} \to \mathbb{R}$ are introduced on the three-dimensional domain. For the optical propagation, the tensor

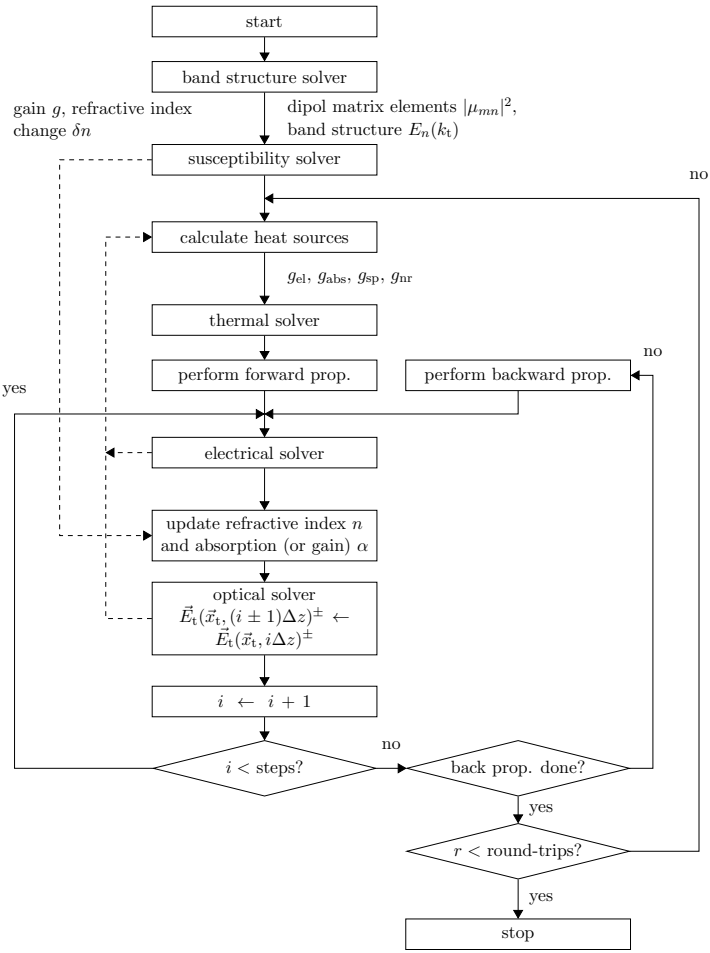

FIGURE 7.4: Flow-chart for FD edge-emitting diode laser model. Solid lines represent the sequence of tasks and quantities written next to the connection lines are outputs of the previous action. Dashed lines represent quantities passed from one particular task to another but indicate that in contrast to tasks connected by the solid lines are not performed directly after each other. The exchanged quantities are stored in temporary buffers and are supplied to the corresponding task on demand.

functions $g_{i,j}, \delta n_{i,j}, n_{i,j}, \kappa_{i,j} : \Omega_\mathrm{t} \to \mathbb{R}^{d\times d} \times \mathbb{R}^{d-1}$ for the material gain, refractive index change, refractive index, absorption and the vector function $\vec{E}_{\mathrm{t},i,j} : \Omega_\mathrm{t} \to \mathbb{C}^d$ for the transverse electric field components, and the scalar functions $n_{\mathrm{qw},i} : \Omega_\mathrm{t} \to \mathbb{R}$ are introduced. The waveguide is defined by the transverse refractive index tensor and the transverse absorption tensor $n_0, \kappa_0 : \Omega_\mathrm{wg} \times \mathbb{R} \to \mathbb{R}^{d\times d} \times \mathbb{R}^{d-1}$. These properties can, for example, account for built-in refractive index steps due to trenches or ridge waveguides. For all functions, the first index $i \in [0, 1, \ldots, N_z - 1]$ indicates the longitudinal slice number and the second index $j \in [0, 1, \ldots, N_\omega - 1]$ iterates through all frequencies used in the simulation. At each optical propagation step, a contribution $\Delta\vec{E}_\mathrm{sp}$ accounting for the spontaneous emission, which contributes to the light field is added to the electric field. The mirror reflectivities (for the amplitudes) of the front- and back-facet are r_+ and r_- and can be functions of the frequency. The number of transverse space dimensions is denoted as d, which yields $d = 2$ for the 2+1-dimensional model and $d = 1$ for the 1+1-dimensional model. For $d = 2$ the refractive index and absorption tensor has four transverse components and one longitudinal component, as introduced in (4.27) and for $d = 1$ both reduce to scalar quantities. For the 1+1-dimensional model it is assumed that the vertical mode profile is invariant so that the EIM [74] is applied to reduce the three-dimensional optical problem to a two-dimensional one, including the lateral and the longitudinal direction. In the EIM, the three-dimensional electric field is separated into a vertical profile and a lateral-longitudinal profile $\vec{E}(\vec{x}) = \psi_\mathrm{v}(x)\vec{E}_\mathrm{t}(y, z)$. The information about the overlap of the vertical field and the active region is introduced to the 1+1-dimensional model by the optical confinement factor Γ. The confinement factor is determined from the computed vertical eigenmode, see Section 4.5.2.

To reduce computation time and complexity several modifications can be made to the Algorithm 1:

1. To determine the current injection $J(y, z)$ in the QW-plane, the carrier densities n and p are calculated based on the DDM just for the first round-trip and iteration step and are not updated.

2. The electrical solver is only employed for updates of the confined carriers in the QW according to (6.88) so that the drift-diffusion equations (with coupled QW) are not solved, and a function for the current density in the QW-plane $J(y, z)$ is defined apriori.

3. The temperature is updated only each nth round-trip.

4. The confined carrier density n_qw is updated only after i_n optical propagation steps.

5. The dependencies of the gain and carrier-induced refractive index change on the carrier density and temperature are linearized or approximated by analytical formulas, compare, for example, Eqs. (6.89), and (8.2).

For the computations presented in the next chapter, modifications 2, 3, 4, and 5 are applied. The temperature is updated every 20 round-trips, and the carrier density is updated after eight optical propagation steps. For modification 2 the current density is modeled by a top-hat distribution under the contact stripe, and the current density adjacent to the stripe is estimated based on analytical approaches [112, 113, 114]. The

Algorithm 1 FD edge-emitting diode laser propagation algorithm.

procedure ITERATION($r_{\max}$)
  INITIALIZEFUNCTIONS()
  for $r \leftarrow 0$ **to** $r_{\max}$ **do**
    $n_{\mathrm{qw,therm}} \leftarrow$ INTERPOLATE($\{n_{\mathrm{qw},i}\}, \Omega_{\mathrm{wg}}, \Omega_{\mathrm{therm}}$)
    $I_{\mathrm{therm}} \leftarrow$ INTERPOLATE($\{I_{i,j}\}, \Omega_{\mathrm{wg}}, \Omega_{\mathrm{therm}}$)
    $q_{\mathrm{el}}, q_{\mathrm{nr}}, q_{\mathrm{sp}}, q_{\mathrm{abs}} \leftarrow$ HEATSOURCEDENSITIES($n_{\mathrm{qw,therm}}, I_{\mathrm{therm}}$)
    $T \leftarrow$ SOLVETHERMALEQS($q_{\mathrm{el}} + q_{\mathrm{nr}} + q_{\mathrm{sp}} + q_{\mathrm{abs}}$)
    for all $d \in \{+, -\}$ **do**
      if $d = +$ **then**
        $(i_0, i_{\mathrm{end}}) \leftarrow (0, N_z - 2)$
      else
        $(i_0, i_{\mathrm{end}}) \leftarrow (N_z - 1, 1)$
      end if
      for $i \leftarrow i_0$ **to** i_{end} **do**
        $T_{\mathrm{t},i} \leftarrow$ INTERPOLATE($T(\vec{x}_{\mathrm{t}}, i\Delta z), \Omega_{\mathrm{therm}}, \Omega_{\mathrm{t}}$)
        $n_{\mathrm{qw},i} \leftarrow$ SOLVECARRIEREQS($T_{\mathrm{t},i}, \{I_{i,j}\}$)
        for $j \leftarrow 0$ **to** $N_\omega - 1$ **do**
          $g_{i,j} \leftarrow g(\omega_j, n_{\mathrm{qw},i}, T_{\mathrm{t},i})$
          $\delta n_{i,j} \leftarrow \delta n(\omega_j, n_{\mathrm{qw},i}, T_{\mathrm{t},i})$
          $n_{i,j} \leftarrow n_{\mathrm{t},0}(\vec{x}_{\mathrm{t}}, i\Delta z, \omega_j) + \Gamma \delta n_{i,j}$
          $\kappa_{i,j} \leftarrow \kappa_0(\vec{x}_{\mathrm{t}}, i\Delta z, \omega_j) - \Gamma g_{i,j} + \kappa(n_{\mathrm{qw},i}, n_i, p_i, \omega_j)$
          $\vec{E}^{(d)}_{\mathrm{t},i+d,j} \leftarrow$ SOLVEOPTICALEQS($n_{i,j}, \kappa_{i,j}, \omega_j, \vec{E}^{(d)}_{\mathrm{t},i,j}$)
          $\vec{E}^{(d)}_{\mathrm{t},i+d,j} \leftarrow \vec{E}^{(d)}_{\mathrm{t},i+d,j} + \Delta\vec{E}_{\mathrm{sp}}(\Delta z, \omega_j, n_{\mathrm{qw},i}, T_{\mathrm{t},i})$
          $I_{i+d,j} \leftarrow$ INTENSITY($n_{i,j}, |\vec{E}^{+}_{\mathrm{t},i+d,j}|^2, |\vec{E}^{-}_{\mathrm{t},i+d,j}|^2$)
        end for
      end for
      for $j \leftarrow 0$ **to** $N_\omega - 1$ **do**
        $\vec{E}^{(-d)}_{\mathrm{t},i_{\mathrm{end}}+d,j} \leftarrow r_d(\omega_j)\vec{E}^{(d)}_{\mathrm{t},i_{\mathrm{end}}+d,j}$
      end for
    end for
  end for
end procedure

injected current density is [114]

$$J(y) = J_0 \begin{cases} 1 & \text{if } \frac{w_{\mathrm{c}}}{2} \geq |y|. \\ (1 + \frac{|y| - \frac{w_{\mathrm{c}}}{2}}{l_{\mathrm{s}}})^{-2} & \text{if } \frac{w_{\mathrm{c}}}{2} < |y|. \end{cases} \tag{7.7}$$

The current density J_0 determines the total injected current and the spreading length is determined by

$$l_{\mathrm{s}} = \sqrt{\frac{4k_{\mathrm{B}}T d_p}{q_{\mathrm{el}}\rho_p J_0}}, \tag{7.8}$$

with d_p the thickness of the p-side, and ρ_p the effective p-side resistivity. For the studied devices a thickness of 1.85 µm and the effective resistivity of $6 \cdot 10^{-3}\,\Omega\,\mathrm{m}$ is applied.

The iteration scheme is repeated until the solution converges under previously defined convergence criteria or if the solution does not converge it is stopped after a distinct

number of cavity round-trips. For the simulation of HPDL with a large number of lateral modes and filamented NF profiles, the formation of a stable electric field profile at the facet or in the FF is not defined as convergence criteria, since the profiles undergo significant changes from one round-trip to another [109]. Even up to several hundred round-trips the field profiles do not converge, and no repeating periodic patterns between round-trips are observed. However, the changes in the optical output power (Fig. 7.5), NF width (Fig. 7.6) and SAD angle (Fig. 7.7) per round-trip are considered as convergence criteria. Each round-trip inside a 4 mm long cavity corresponds to a period of about 90 ps. Integration over 50 round-trips accounts to an equivalent integration time of about 4.5 ns for averaged fields. To extract results from the model, power, NF profile and FF profile are averaged over a defined number of round-trips. The averaged simulation results are compared to real measurements of the field intensities, which are performed by detectors with typical integration times in the range of several ten µs. The integration is performed by adding up the near- and far-field intensities for the corresponding round-trips. This method is equivalent to an incoherent superposition of the fields. The superposition is performed in analogy to the real measurement, where the intensities are integrated over a distinct exposure period. Results for the SAD angle (Fig. 7.7), NF width (Fig. 7.6), and output power (Fig. 7.5) as a function of the start number r_s of the round-trip integration, and the number of round-trips being integrated Δr are analyzed by the example of a SE device with 150 µm contact width and 4 mm long cavity. The standard deviation of the fluctuations in power between round-trips is $\sigma_P = 0.214\,\mathrm{W}$. For the near- and far-field widths the standard deviation of the fluctuations between round-trips is $\sigma_{w_1} = 8.071\,\mu\mathrm{m}$, and $\sigma_{\theta_1} = 0.534°$ (both for 95% P.I.). These are the fluctuations between individual round-trips, which corresponds to $\Delta r = 1$. If the number of round-trip integrations is increased to values above 20, the spreads can be significantly reduced, see Figs. 7.5, 7.6, and 7.7. The spreads for integrated values with r_s and $\Delta r > 40$ are below or within typical measurement accuracy or spreads of characteristics between multiple devices, see experimental measurements in the next chapter in Section 8.2. In practice, the simulations are stopped after 200 round-trips, and the results are integrated over the last 50 round-trips.

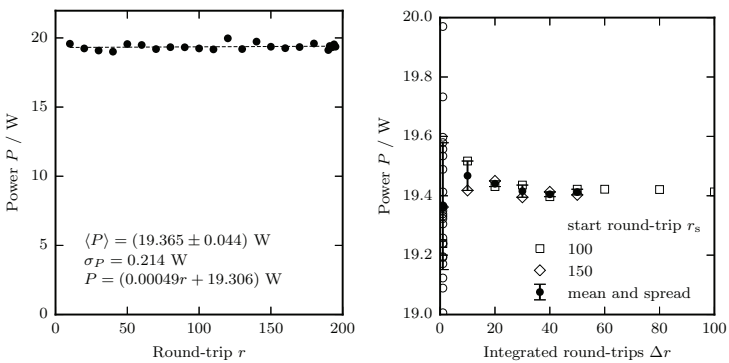

FIGURE 7.5: Study of extracted power due to round-trip integration. The exemplary study is performed for the simulation results of a 150 µm contact width SE listed as D4 in Tb. C.2.

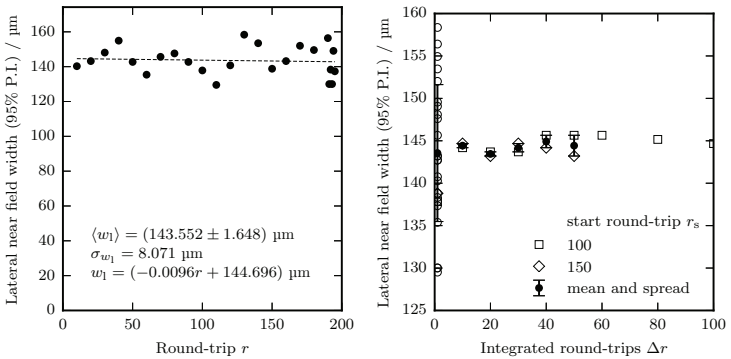

FIGURE 7.6: Study of extracted near-field width due to round-trip integration. The exemplary study is performed for the simulation results of a 150 µm contact width SE listed as SE2 in Tb. C.2.

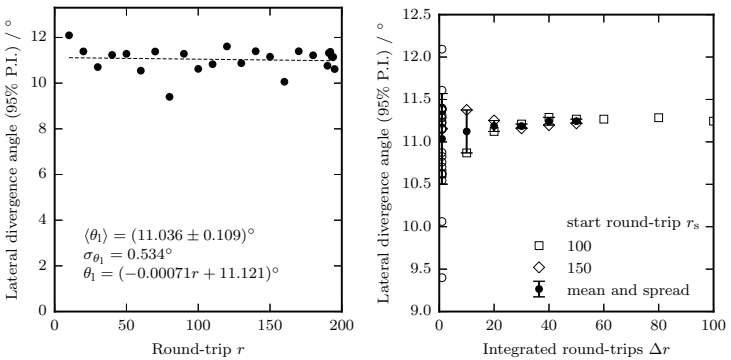

FIGURE 7.7: Study of extracted lateral far-field divergence angle due to round-trip integration. The exemplary study is performed for the simulation results of a 150 µm contact width SE listed as SE2 in Tb. C.2.

7.3 Time-Domain Laser Model

Analog to the FD laser model, the spatial domain is separated into a series of N_z transverse slices Ω_t along the propagation direction with distances Δz between two adjacent slices. For each slice $i \in [0, 1, \ldots, N_z - 1]$, the functions $\chi_{i,(0)}, \Delta\chi_i : \Omega_\mathrm{t} \to \mathbb{C}^{d\times d}$ for the static part of the susceptibility and frequency dependent part and the vector functions $\vec{E}^{\pm}_{\mathrm{t},i}, \Delta\vec{p}^{\pm}_{\mathrm{t},i} : \Omega_\mathrm{t} \to \mathbb{C}^d$ for the transverse electric field components and the scalar functions $n_{\mathrm{qw},i} : \Omega_\mathrm{t} \to \mathbb{R}$ are introduced. As introduced above d is the number of transverse space dimensions. Although the general formulation of the TD model given here accounts for two transverse dimensions and vectorial electric fields and polarization, the TD model is only applied for the 1+1 dimensional case for computation in lateral and longitudinal directions with scalar fields within the scope of this work. In contrast to the FD model, no frequency slicing is performed, but the emerge of multiple

frequencies and dispersion results from the temporal evolution of the fields. In the TD

Algorithm 2 TD edge-emitting diode laser algorithm.

procedure ITERATION($n_{\max}$)
  INITIALIZEFUNCTIONS()
  for $n \leftarrow 0$ **to** $n_{\max}$ **do**
    $n_{\mathrm{qw,therm}} \leftarrow$ INTERPOLATE($\{n_{\mathrm{qw},i}\}, \Omega_{\mathrm{wg}}, \Omega_{\mathrm{therm}}$)
    $I_{\mathrm{therm}} \leftarrow$ INTERPOLATE($\{I_i\}, \Omega_{\mathrm{wg}}, \Omega_{\mathrm{therm}}$)
    $q_{\mathrm{el}}, q_{\mathrm{nr}}, q_{\mathrm{sp}}, q_{\mathrm{abs}} \leftarrow$ HEATSOURCEDENSITIES($n_{\mathrm{qw,therm}}, I_{\mathrm{therm}}$)
    $T \leftarrow$ SOLVETHERMALEQS($q_{\mathrm{el}} + q_{\mathrm{nr}} + q_{\mathrm{sp}} + q_{\mathrm{abs}}, T$)
    for $i \leftarrow 0$ **to** $N_z - 1$ **do**
      $T_{\mathrm{t},i} \leftarrow$ INTERPOLATE($T(\vec{x}_{\mathrm{t}}, i\Delta z), \Omega_{\mathrm{therm}}, \Omega_{\mathrm{wg,t}}$)
      $\vec{E}^{+}_{\mathrm{t,new},i} \leftarrow$ SOLVEOPTICALEQS($\chi_{i,(0)}, \vec{E}^{+}_{\mathrm{t},i}, \Delta\vec{p}^{+}_{\mathrm{t},i}$)
      $\vec{E}^{-}_{\mathrm{t,new},i} \leftarrow$ SOLVEOPTICALEQS($\chi_{i,(0)}, \vec{E}^{-}_{\mathrm{t},i}, \Delta\vec{p}^{-}_{\mathrm{t},i}$)
      $\vec{E}^{+}_{\mathrm{t,avg}} \leftarrow (\vec{E}^{+}_{\mathrm{t,new},i} + \vec{E}^{+}_{\mathrm{t},i})/2$
      $\vec{E}^{-}_{\mathrm{t,avg}} \leftarrow (\vec{E}^{-}_{\mathrm{t,new},i} + \vec{E}^{-}_{\mathrm{t},i})/2$
      $\Delta\vec{p}^{+}_{\mathrm{t,new},i} \leftarrow$ SOLVEPOLARIZATIONEQS($\Delta\chi_i, \Delta\vec{p}^{+}_{\mathrm{t},i}, \vec{E}^{+}_{\mathrm{t,avg}}$)
      $\Delta\vec{p}^{-}_{\mathrm{t,new},i} \leftarrow$ SOLVEPOLARIZATIONEQS($\Delta\chi_i, \Delta\vec{p}^{-}_{\mathrm{t},i}, \vec{E}^{-}_{\mathrm{t,avg}}$)
      $\Delta\vec{p}^{+}_{\mathrm{t,avg}} \leftarrow (\Delta\vec{p}^{+}_{\mathrm{t,new}} + \Delta\vec{p}^{+}_{\mathrm{t},i})/2$
      $\Delta\vec{p}^{-}_{\mathrm{t,avg}} \leftarrow (\Delta\vec{p}^{-}_{\mathrm{t,new}} + \Delta\vec{p}^{-}_{\mathrm{t},i})/2$
      $n_{\mathrm{qw},i} \leftarrow$ SOLVECARRIEREQS($n_{\mathrm{qw},i}, \chi_{i,(0)}, \Delta\chi_i, \Delta\vec{p}^{+}_{\mathrm{t,avg}}, \Delta\vec{p}^{-}_{\mathrm{t,avg}}, \vec{E}^{+}_{\mathrm{t,avg}}, \vec{E}^{-}_{\mathrm{t,avg}}$)
      $\chi_{i,(0)} = \chi_{(0)}(\omega_{\mathrm{ref}}, n_{\mathrm{qw},i}, T_{\mathrm{t},i}, \vec{x}_{\mathrm{t}}, i\Delta z)$
      $\Delta\chi_i = \Delta\chi(\omega_{\mathrm{ref}}, n_{\mathrm{qw},i}, T_{\mathrm{t},i}, \vec{x}_{\mathrm{t}}, i\Delta z)$
      $\vec{E}^{+}_{\mathrm{t,new},i} \leftarrow \vec{E}^{+}_{\mathrm{t,new},i} + \Delta\vec{E}_{\mathrm{sp}}(n_{\mathrm{qw},i}, T_{\mathrm{t},i})$
      $\vec{E}^{-}_{\mathrm{t,new},i} \leftarrow \vec{E}^{-}_{\mathrm{t,new},i} + \Delta\vec{E}_{\mathrm{sp}}(n_{\mathrm{qw},i}, T_{\mathrm{t},i})$
      $I_i \leftarrow$ INTENSITY($n_i, |\vec{E}^{+}_{\mathrm{t,new},i}|^2, |\vec{E}^{-}_{\mathrm{t,new},i}|^2$)
    end for
    for $i \leftarrow 0$ **to** $N_z - 2$ **do**
      $\vec{E}^{+}_{\mathrm{t},N_z-1-i} \leftarrow \vec{E}^{+}_{\mathrm{t,new},N_z-2-i}$
      $\vec{E}^{-}_{\mathrm{t},i} \leftarrow \vec{E}^{-}_{\mathrm{t,new},i+1}$
    end for
    $\vec{E}^{+}_{\mathrm{t},0} \leftarrow r_{-}(\omega_{\mathrm{ref}})\vec{E}^{-}_{\mathrm{t},0}$
    $\vec{E}^{-}_{\mathrm{t},N_z} \leftarrow r_{+}(\omega_{\mathrm{ref}})\vec{E}^{+}_{\mathrm{t},N_z-1}$
  end for
end procedure

model, Eq. (4.59) or (4.57), (4.50), and (C.87) are solved iteratively (see Algorithm 2) to find the spatial and temporal evolution for the electric field envelope, polarization envelope, and the carrier density. In an outermost loop, a total number of $n_{\max}$ time steps is performed, which corresponds to a simulated time-interval of $n_{\max}\Delta t$. At every time step for each longitudinal slice i $\vec{E}_{\mathrm{t},i}$, $\Delta\vec{p}_{\mathrm{t},i}$, $n_{\mathrm{qw},i}$, and the complex susceptibility $\chi_i = \chi_{(0),i} + \Delta\chi_i$ are updated in the following order: The TDTW equation is solved based on the optical field, polarization and susceptibility values from the previous time step n for the forward and backward propagating wave. This results in new values for the forward (backward) traveling wave at the border of each slice (a slab, which extends along the propagation direction) in positive (negative) direction for the next time step $n+1$ based on the initial field given at the opposite border at time step n. To update the polarization envelopes the electric field values at the intermediate time step $n + 1/2$ and

in the center of the slice are approximated by averaging the initial value from time step n and the new one from $n+1$. Similar, the values for the polarization and the electrical field are needed to step the carrier density forward in time. Therefore, analog to the electrical field, the polarization (defined in the center of the slab) at the intermediate step is approximated by averaging the initial value from time step n and the new one from $n+1$. The new values for the carrier density are used to update the static and frequency dependent part of the susceptibility. A built-in refractive index profile due to index trenches or ridges are incorporated into the static susceptibility. Additionally, the free-carrier absorption is calculated based on the carrier density. A random-number generator is used to emulate contributions of spontaneous emission to the light field. These contributions are added to the field values at each time step. For the described steps only local values are needed in each slice so that the loop over the slices can be performed in parallel as described in the following. To decrease the computation

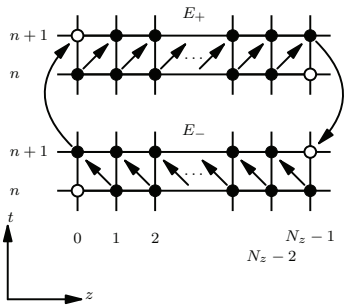

FIGURE 7.8: Schematic of TDTW stepping algorithm.

time for the TDTW method, the simulation domain is split up into subdomains along the longitudinal direction. Each subdomain contains a certain number of transverse slices and handles a specific task, like material updates and initialization, solving the propagation equation (time-stepping) and synchronization with the other subdomains. This implementation allows efficient distribution of the workload to a number of Central Processing Units (CPUs) or to different server nodes. For one time step, all fields in a subdomain can be computed without the need to communicate with the adjacent subdomains. After each step, the field values at the subdomain boundaries are exchanged with the two neighboring subdomains. When the forward propagation is performed, the (new) field value at time step $n+1$ and slice $k+1$ (longitudinal position) only depends on the (initial) value at time step n and slice k, see illustration in Fig. 7.8. The field value at the last z-slice $k = N_z-1$ (for the forward direction) and the one at the first $n = 0$ (for the backward direction) is not used to compute any of the new values at time step $n+1$. For each slice, one field value for each direction is stored. Each subdomain sends the forward propagating field from the last local slice to the following subdomain and receives the backward propagating field from the first local slice also from the following subdomain. The boundary conditions are applied so that the remaining values at the first and last slice, which are not updated in the field exchange (indicated by circles without filling in Fig.7.8), are defined, and the next time step can be performed. To efficiently run the time stepping algorithm in parallel, on multiple workers, for each process, represented

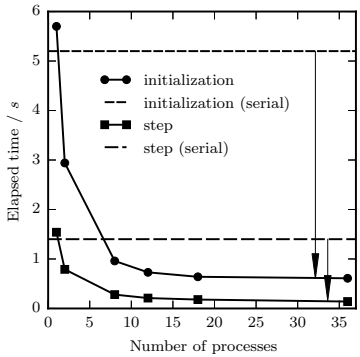

FIGURE 7.9: Execution time of initialization and step procedure for the TDTW model as a function of the number of processes. The benchmark values are averaged over multiple executions. The domain has a resolution of 200 lateral grid knots times 1000 longitudinal grid nodes with a size of 200 µm × 1000 µm. For the optical model, explicit time stepping is applied. The dashed lines indicate the execution times for the serial implementation as references. The computation is performed on an *Intel Xeon* CPU with 18 cores (36 virtual cores) and 256 GigaByte (GB) of Random Access Memory (RAM). The execution time for stepping is reduced by a factor of 10 and the one for the initialization of the slices by a factor of 8.5.

by an object of class *SliceProcess*, a *Queue* object is used for communication. The task queues decouple the main process from the workers and allow asynchronous execution of tasks on each process. The general procedure is: Until a process is stopped at the end of its lifetime, it polls the corresponding task queue, to get the next task from the buffer. After the task is performed, it tells the queue that the task is removed from the queue and is done. To synchronize all processes, the queues are *joined*. The main process (or process which calls the join command for a queue) waits until the corresponding queue is empty, which means that all previous tasks have been executed. The parallel execution of the time stepping algorithm is illustrated in the sequence diagram Fig 7.10. For each time step, the main process (*tdtw* object) puts one *step* task in each worker queue. The worker gets the task from the queue and then performs the computations for one time step for each slice contained in this worker. The computations include the update of material properties and the solution of the respective equations for the update of the electric field, polarization, and carrier density. After the step is performed, the processes need to exchange data with neighboring workers. Therefore, after the *step()* loop (over all slices in the worker) is executed, the process sends the forward field of the last slice (via *recv* task) to the queue of the following worker and the backward field of the first slice to the previous worker. After sending out the data to the neighboring queues, the *step* task is finished for the worker, and it polls the queue again. In the meantime, a *recv* task (containing field data) is put into its queue. The *recv* task is executed by receiving the send data and storing it in the corresponding first or last slice of the subdomain. After each processed received the new field values, all fields are up to date for the new time step, and the program execution continues after joining with the main process. A significant performance increase is gained from the parallel execution. By using a pool of 36 workers the execution time for one time step is reduced by a factor of 10 and the execution time for initialization of the slices by a factor of 8.5, see Fig. 7.9.

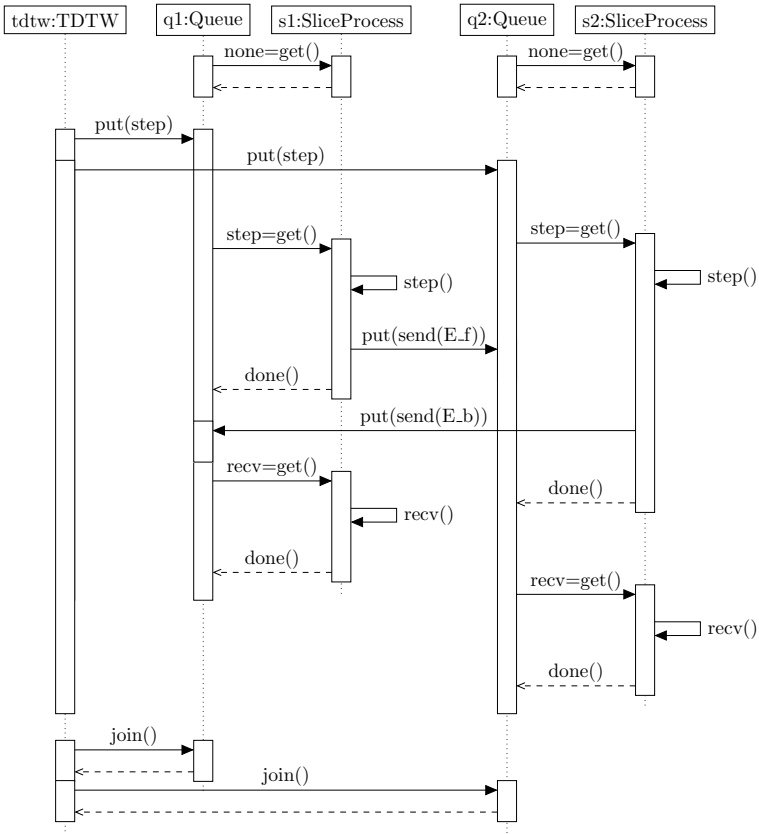

FIGURE 7.10: Sequence diagram of TDTW parallel time stepping.

If a discretization size of $\Delta z = 1\,\mu\text{m}$ is chosen with a group refractive index of $n_\text{g} = 3.9$ the time step is $\Delta t = 1.3 \cdot 10^{-14}\,\text{s}$ and for a 4 mm long cavity the round-trip time of an optical pulse is 104 ps. Therefore, for 100 round trips, the simulation duration is reduced from approximately 38 hours to 3.8 hours with the help of the parallel implementation.

7.4 Chapter Summary

The individual physical models from Chapters 2 to 6 are combined into a FD and a TD edge-emitting semiconductor laser model. Additionally, a stationary one-dimensional longitudinal model is presented, which is utilized to compute spatial hole burning in the longitudinal direction. In both, the FD and TD model the optical field is approximated with the SVEA and is separated into a forward and backward propagating part. The optical problem and material interactions are solved iteratively for transverse slices along the longitudinal direction. Despite the carrier density, and material polarization (in

the TD model), which are computed on transverse cross-sections, the temperature is determined on a three-dimensional domain. Due to the strong coupling between the electric field and the material properties, a convergence of the fields in the FD model is not observed after a number of round trips > 200. Although the fields do not converge, conclusions on the output characteristics (power, divergence, near-field width) of the device can be drawn from the FD Fox-Li method. To extract results, power, NF profile and FF profile are averaged over a defined number of round-trips. In the TDTW model, polarization dynamics are included by a Lorentzian pole, and the polarization update, carrier diffusion equation, and optical propagation are computed self-consistent for each time step. To decrease the computation time for the TDTW method, the simulation domain is split up into subdomains along the longitudinal direction and distributed to a number of CPUs. By using a pool of 36 workers, in an example, the execution time for one time-step is reduced by a factor of 10 compared to the serial execution, see Fig. 7.9.

For both the FD and TD model, the three-dimensional problem is reduced to a two-dimensional simulation domain (except for the temperature) including the lateral and the longitudinal direction based on the EIM. It is assumed that the vertical field profile is invariant and equals the dominant waveguide eigenmode computed in Chapter 3. The results presented in the next chapter are obtained with the 1+1 dimensional model under application of the EIM.

Chapter 8

Simulation of Edge-Emitting Diode Lasers

This chapter is organized as follows: First, the formation of the lateral field, and the correlation to the refractive index perturbations for gain-guided edge-emitting diode lasers is illustrated by investigation of a SE device with 90 µm contact opening and 4 mm cavity length. To identify the general interplay between carrier-induced lensing and thermal-induced lensing, and the influence on the light propagation inside the device, and the resulting FF divergence, simulations are performed with different magnitudes of the carrier- and temperature-induced lensing. In the two following sections, results for simulations performed with the FD laser model for LAs and SEs are presented. The focus lies on the comparison between simulation and experimental measurements. Simulations are performed for individual emitters out of LAs which vary in the emitter pitch, contact width or epitaxial structure (change in optical confinement factor). The SE results include devices with a change in the emitter width, the cavity length, and the facet coating (comparison between asymmetric and symmetric coated cavity). Additionally, simulations with a reduced thermal refractive index coefficient, which are compared to measurements of a device in pulsed operation, for the suppression of the thermal lensing are presented.

For each device, the total dissipated power is extracted from measurements and the heat sources obtained in the simulation are re-scaled so that the total power matches the measured dissipated power. This step is performed to circumvent uncertainties in the prediction of the electro-optical efficiency and to ensure a thermal profile close to the one in the real device for quantitative comparison of FF and NF data. For new designs or if measurements are not available, the electro-optical properties are calculated as described in Chapter 6.

The final section of this chapter closes with results obtained by the TDTW model for a 100 µm and 4 mm long device. The filamentation and field distributions inside the cavity, and the extracted FF profiles are similar to the ones generated with the FD model.

8.1 Lateral Anti-Guiding and Guiding Mechanisms and Influence on Slow-Axis Divergence Angle

The perturbations of the refractive index in the waveguide arise primarily from the carrier-induced refractive index change and the thermal-induced index change. Increases in the local refractive index lead to focusing, decreases to de-focusing of the light. The filamentation of the light field emerges from perturbations of the refractive index due to the density of carriers N in the active region, and the temperature profile T, in particular from the profiles along the lateral direction. The refractive index $n(\omega, N, T)$ of a semiconductor is dependent on the frequency of the light field ω, carrier density N and temperature T. Methods for the calculation of the refractive index and gain as a function of those three variables are presented in Chapter 2. Although the computed gain can be provided in a data table for the FD model, linearized dependencies for the refractive index are employed for the following analysis. The effective refractive index (besides the optical confinement factor) is primarily determined by the waveguides vertical and lateral refractive index profile. The perturbed effective refractive index is

$$n_{\text{eff}}(\omega, N, T) = n_{\text{eff}}(\omega, N_0, T_0) + \delta n_{\text{eff}}(N, T) = n_{\text{eff},0} + \Gamma \delta n_N(N) + \delta n_T(T), \tag{8.1}$$

where the background effective refractive index is evaluated at the constant reference carrier density N_0 and temperature T_0. The optical confinement factor Γ is inserted to account for the overlap of the mode and the QW in the vertical direction, where the carrier-induced perturbation δn_N is induced. The refractive index change δn_N is determined by the linearization

$$\delta n_N(N) = \frac{\partial \delta n}{\partial N}|_{N=N_0,T=T_0}(N - N_0) = \alpha_N \Delta N \tag{8.2}$$

and analog, the thermal-induced refractive index change δn_T is

$$\delta n_T(T) = \frac{\partial \delta n}{\partial T}|_{N=N_0,T=T_0}(T - T_0) = \alpha_T \Delta T. \tag{8.3}$$

Local strain potentially influences the waveguides refractive index (as presented in Chapter 5) and thus, the intra-cavity propagation, not only with respect to polarization rotations. However, the inclusion of this perturbation is not (yet) done for the study of the lateral emission but solely to explain polarization rotations. For the study of emitter D0 (Tb. C.2) a literature value for the refractive index change with temperature of $\alpha_T = 3 \cdot 10^{-4}\,\text{K}^{-1}$ [115] and for the carrier-induced one a value of $\alpha_N = -2 \cdot 10^{-26}\,\text{m}^3$ is used, which is in the range obtained from band structures calculated with the 8-band $k \cdot p$-method. In general, α_N is also a function of the frequency. A high field intensity leads to local depletion of carriers (due to stimulated recombination), while low intensities lead to the accumulation of carriers. This effect is called lateral spatial hole burning - it can be observed in the lateral cross-section in Fig. 8.1 for 10 A. In regions with high intensities, the decrease in the carrier density leads to a local refractive index increase, and consequently to a further concentration of the electric field. The effect is called self-focusing and results, among other effects, in filamentation of the lateral light field. In particular at low currents, where the thermal lensing does not dominate, the refractive index perturbation due to carriers becomes more prominent compared to the case of higher injection currents, see refractive index perturbations in QW plane in Fig. 8.3 and lateral cross section for 20 A in Fig. 8.2. Besides the refractive index change, variations

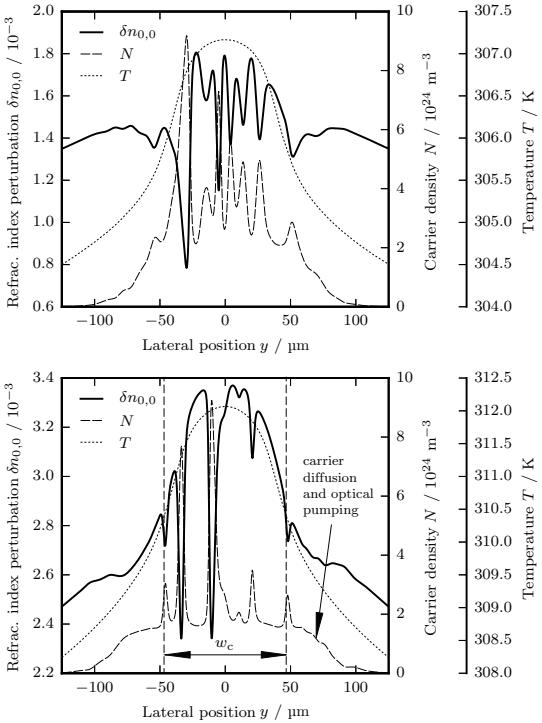

FIGURE 8.1: Lateral profile of refractive index perturbation, carrier density, and temperature for currents $I = 10\,\mathrm{A}$ at the longitudinal position $z = 0\,\mu\mathrm{m}$ (top), and $z = 4\,\mathrm{mm}$ (bottom). The snapshots are from round-trip 200.

in the local carrier density, around the threshold density, lead to gain or absorption and consequently to an additional spatial modulation of the light field due to inhomogeneous amplification. Since the spatial distributions of the heat sources for reabsorbed light, and non-radiative recombination are results of the filamented field and the carrier density, the local variations imprint on the temperature. Two features of the thermal profile influence the light propagation in particular: As described in Chapter 3, the curvature of the temperature under the injection stripe results in refractive index profile equivalent to the one in a GRIN lens. The lateral width of a field distribution launched into such a waveguide follows a cosine-like function. Even for moderate operation currents around 10 A the index curvature in a 100 µm wide emitter results in a focal point, which lies inside the cavity. Consequently, the combination of this thermal focusing in combination with the self-focusing due to carrier lensing increases filamentation. A second influence of the thermal profile emerges from the transition regions at the lateral edges of the contact opening where the gradient of the temperature reaches its maximal values, see Fig. 3.6. The resulting gradients in the refractive index manifest in high spatial frequencies of the light field. Since the intensity increases towards the front facet (for a asymmetrically coated device), the temperature also increases along the cavity length. Additionally, the SE is mounted on a submount which extends the chip length at the

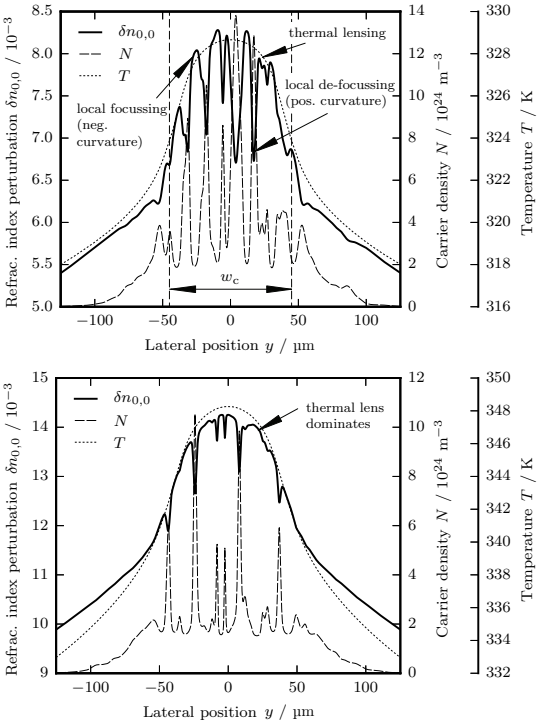

FIGURE 8.2: Lateral profile of refractive index perturbation, carrier density and temperature for currents $I = 20\,\mathrm{A}$ at longitudinal position $z = 0\,\mu\mathrm{m}$ (top), and $z = 4\,\mathrm{mm}$ (bottom). The snapshots are from round-trip 200.

rear facet, so that heat is spread more towards the rear part. This longitudinal gradient (Fig. 8.4) emerges in different characteristic refractive index profiles for the rear and front of the device. Compare the plots in both Fig. 8.1 and Fig. 8.2. The modulation of the refractive index due to the lateral spatial hole burning is more pronounced in the rear than in the front of the device where the thermal lens dominates. The widening of the NF at injection currents below 10 A cannot be solely explained by lateral current spreading. The magnitude of the lateral current spreading amounts to several microns. However, outside of the contact width, the current density decreases exponentially [114] (and Chapter 6) and so does the carrier density, so that at a smaller width the carrier density is below the transparency value and the field would not spread out as much as observed in experiments. Due to the sign of α_N, with increasing carrier density the refractive index decreases. At low operating currents and low temperatures, the accumulation of carriers leads to reduced refractive index under the injection stripe. The reduced refractive index in combination with diffraction due to spatial in-homogeneities leads to anti-guiding. Light propagates away from the center towards the outside of the device. A filament which travels off the longitudinal axis and leaves the region under the contact stripe enters material which is not inverted and is highly absorptive due to interband transitions. The light which enters these un-pumped regions is absorbed by

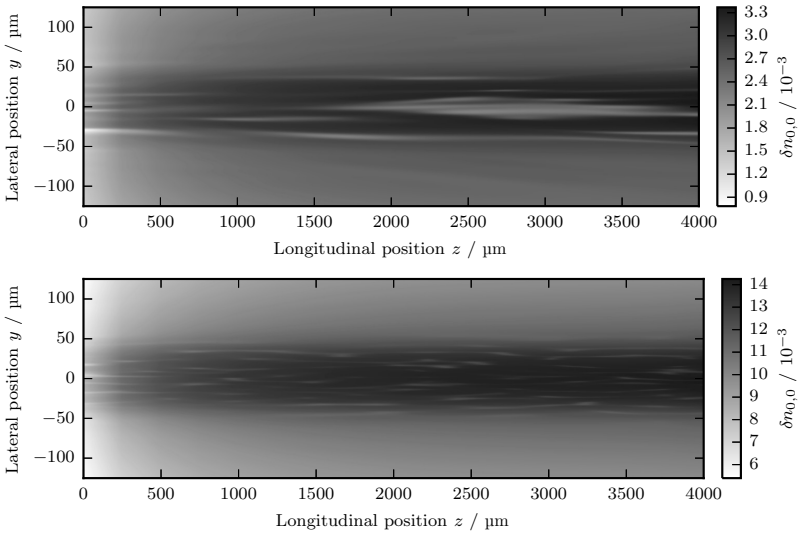

FIGURE 8.3: Refractive index perturbation in QW due to temperature and carrier density for currents of $I = 10\,\mathrm{A}$ (top) and $I = 20\,\mathrm{A}$ (bottom). The snapshots are from round-trip 200.

stimulated absorption, and carriers are excited, see carrier density in Fig. 8.4. The optically pumped regions can even become transparent. Nevertheless, carriers are subject to non-radiative recombination in addition to stimulated recombination, so that filaments outside the pumped regions decay. Overall, the adjacent medium outside of the contact stripe becomes partially transparent due to carriers which diffuse laterally and due to optically pumped regions, so that the NF widens, see the carriers in lateral cross-section in Fig. 8.1 and NF width at 5 A in Fig. 8.6. At a particular operational point, the temperature induced perturbations and the carrier-induced perturbations have the same magnitude so that they can cancel out each other partially. Although the potentially large spatial variations of the carrier density remain, the average refractive index perturbation is reduced at this point, and the increase of the SAD with current shows a minimum value (around 10 A for the presented devices). For higher currents (Fig. 8.5) the thermal guidance dominates which leads to a furtherNF reduction and FF widening. The reduction of the NF with thermal lensing is also investigated in [11]. Although the thermal perturbation dominates compared to the average carrier-induced perturbations, local peaks in the carrier density lead to local regions of guiding (negative curvature of refractive index profile in the lateral direction) and anti-guiding (positive curvature of refractive index profile in the lateral direction). In addition to the first case where $\alpha_T = 3 \cdot 10^{-4}\,\mathrm{K}^{-1}$ and $\alpha_N = -2 \cdot 10^{-26}\,\mathrm{m}^3$, three cases with an alternating influence of the perturbations are investigated, see Fig. 8.6. In the second case $\alpha_T = 3 \cdot 10^{-4}\,\mathrm{K}^{-1}$ and $\alpha_N = 0$, carrier-induced perturbations are suppressed. The SAD is correlated to the temperature increase in the cavity and monotonically increases with the current. The NF remains flat with the current with a width corresponding to the contact opening. In the third case, the thermal lens is suppressed with parameters $\alpha_T = 0$, and $\alpha_N = -2 \cdot 10^{-26}\,\mathrm{m}^3$. The NF does not narrow at high currents but remains increasing

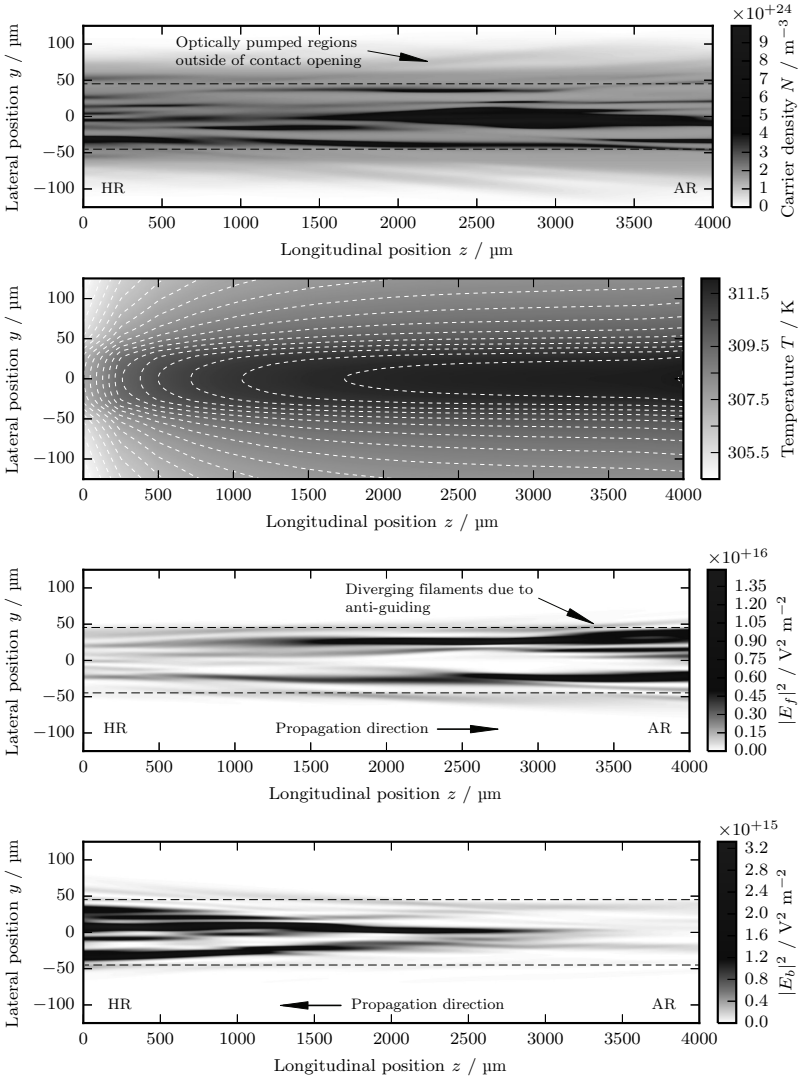

FIGURE 8.4: Carrier density, temperature, forward and backward propagating electric field (amplitude) in QW for a current of $I = 10\,\mathrm{A}$ for device D0. The average temperature in the QW is $T = 309\,\mathrm{K}$. The snapshots are from round-trip 200.

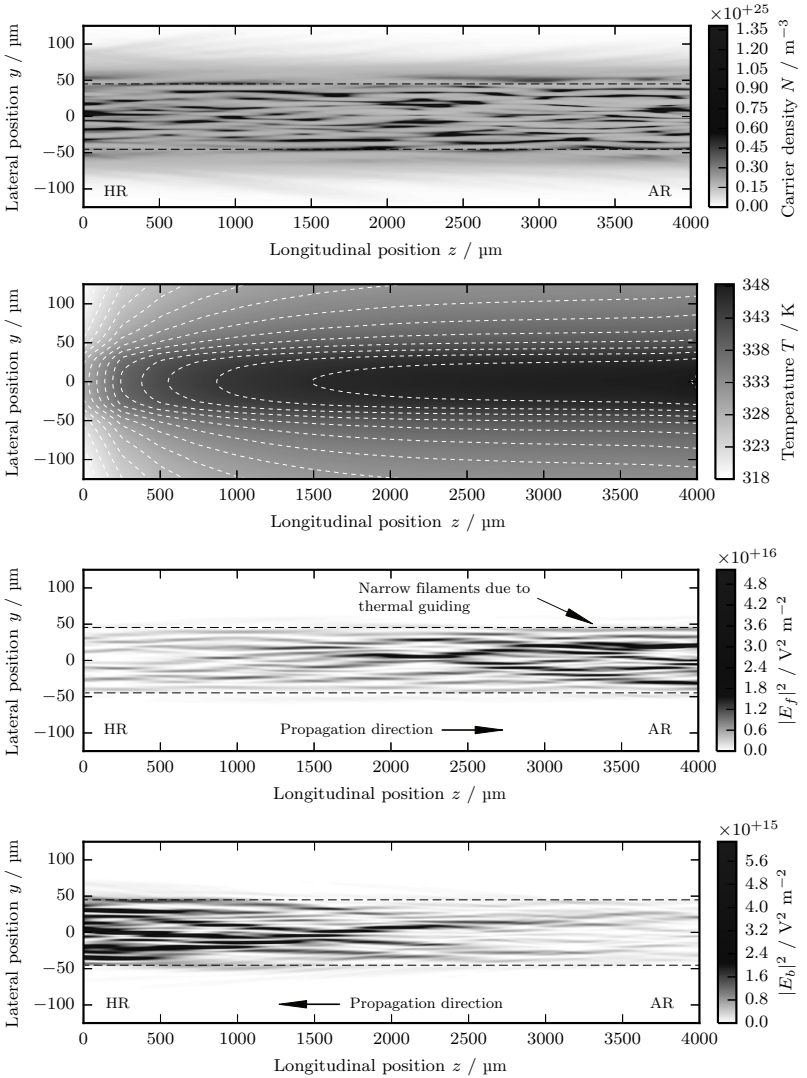

FIGURE 8.5: Carrier density, temperature, forward and backward propagating electric field (amplitude) in QW for a current of $I = 20\,\mathrm{A}$ for device D0. The average temperature in the QW is $T = 337.23\,\mathrm{K}$. The snapshots are from round-trip 200.

with current, and the SAD monotonically increases with a decreasing slope over current. In the case that both perturbations are suppressed $\alpha_T = 0$ and $\alpha_N = 0$, NF and SAD remain flat and nearly independent of injection current. Based on the investigation of these extreme cases, the conclusion is drawn that the lateral emission characteristics for $\alpha_T = 3 \cdot 10^{-4}\,\mathrm{K}^{-1}$ and $\alpha_N = -2 \cdot 10^{-26}\,\mathrm{m}^3$ follow the case without thermal lensing at low currents and the case without carrier lensing at high currents (where the thermal lens dominates). The transition region represents a merge between both states. This argumentation is supported by the investigation of SAD and NF under pulsed operation in Section 8.3, which emulates the suppression of the thermal lens $\alpha_T = 0$.

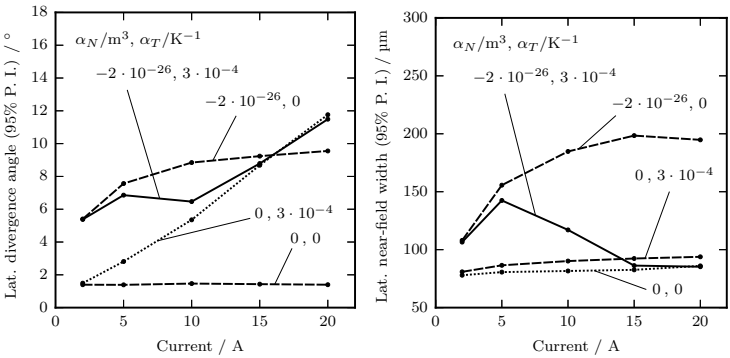

FIGURE 8.6: Lateral divergence angle (left), near-field width (right), for 1+1 dimensional FD simulations with different values of α_T, α_N accounting for the linearized perturbation coefficients for thermal-induced and carrier-induced refractive index perturbations. The values are averaged over round-trips 150 to 200.

8.2 Modeling Lateral Emission Characteristics of Laser Array Emitters

Deterioration of diode laser beam quality at high currents results from the refractive index gradient introduced by the lateral thermal profile. This profile is a function of the emitter pitch of the LA. If the individual emitters are closer (smaller pitch) even though (for the same dissipated power), the overall temperature increases the thermal lens across each emitter decreases, since temperature profiles from neighboring emitters overlap. Therefore, the resulting SAD trend is also a function of the emitter pitch. In this section two LAs D5 and D6 with an emitter pitch of 166 µm and 400 µm are compared, see Fig. 8.9. High fill-factor laser bars (device D5) are operated in regimes where the current per emitter is typically below 6 A. In this regime, the thermal-induced refractive index change does not dominate. For the investigated laser bar with a fill-factor of 55% up to 3 A, the SAD rises to values of typically 6° and remains below 7° up to currents (per emitter) below 6 A, see measured data in Fig. 8.9. Above 6 A the SAD increases rapidly due to the dominance of the thermal lensing. Measurements are performed for individual elements of a 55% fill factor bar directly mounted onto an isolated microchannel cooler with 29° cooling temperature. At low operation currents the thermal

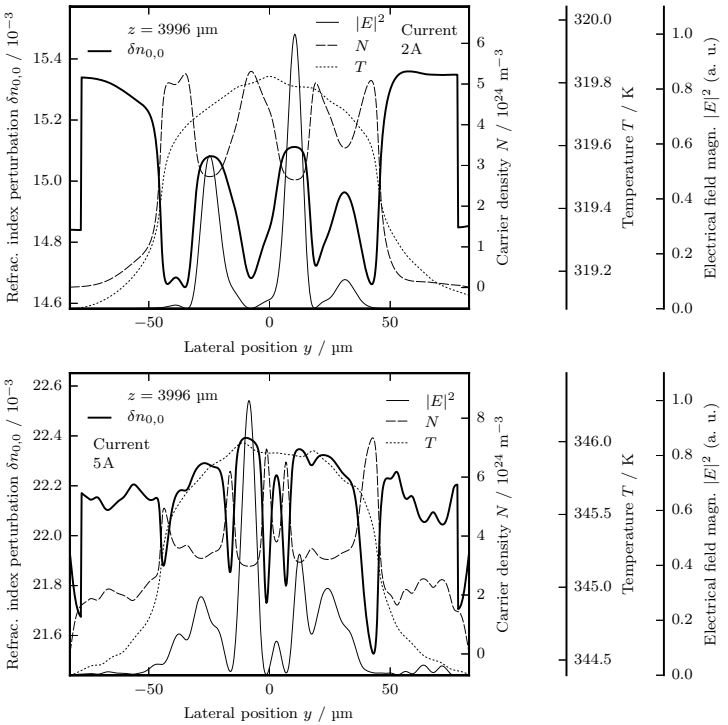

FIGURE 8.7: Lateral profile of refractive index perturbation, carrier density, and temperature for currents of 2 A (top) and 5 A (bottom) at the front facet for the device D5. The snapshots are from round-trip 180. Results are published in [5].

influence is small compared to the carrier-induced perturbation, see the lower refractive index in the central part in Fig. 8.7 for 2 A, which lead to the widening of the NF. At a particular operation point, the thermal- and the carrier-induced perturbations have the same magnitude, so that they can cancel out each other. In the case of D5, this transition regime occurs around 6 A. In contrast to the high-fill factor array D5, the device D6 (lateral profiles are shown in Fig. 8.8) with lower fill-factor, and higher pitch, but equal epitaxy shows a different SAD trend. Below a current of 6 A per emitter, the SAD is slightly lower for D6 compared to D5. Nevertheless, the slope of the SAD over current is higher for D6 than for D5. This suggests that, in this case, the different thermal profile reduces the SAD for low currents but leads to increased divergence above 6 A. A change of the confinement factor leads to a change in the modal gain $g_\mathrm{m} = \Gamma g$ and the modal carrier-induced refractive index perturbation, see (8.1). Based on the simulations and the experimental data for devices D7 and D8 with 200 µm contact opening it is suggested that a reduction of the optical confinement factor leads to a reduction of the carrier-induced perturbations and therefore, to a reduction of the local perturbations and smaller SAD angles. This dependence is shown in the comparison between the devices D7 (with epitaxial structure E2) and D8 (with epitaxial structure E3), with $\Gamma_\mathrm{E1} < \Gamma_\mathrm{E2}$. Although the simulated values are overall slightly lower than the

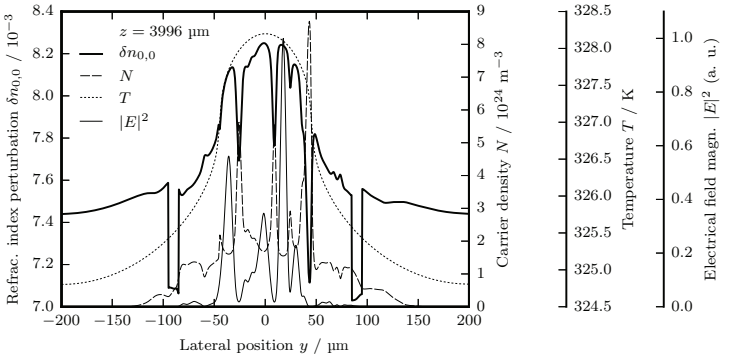

FIGURE 8.8: Lateral profile of refractive index perturbation, carrier density, and temperature for a current of 6 A at the front facet for the device D6. The snapshots are from round-trip 200.

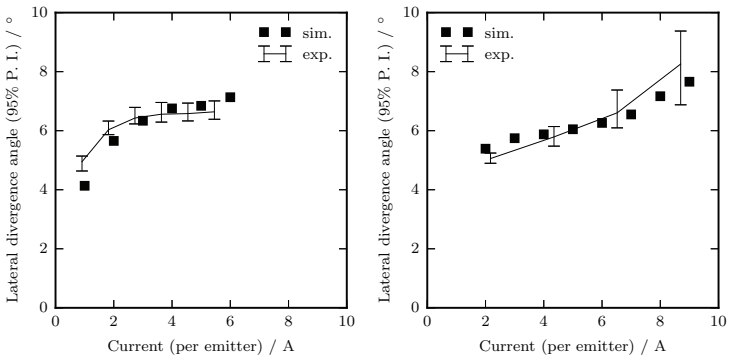

FIGURE 8.9: SAD (95% P.I.) from experimental data and modeling over current for the laser designs D5 (left) (as presented in [5]) and D6 (right). Details of the structures are listed in Tb. C.3. For D5 experimental results are an average over three sets of devices and for D6 over a total of four sets. The simulation results are averaged over round-trips 150 to 200.

measured ones, the change in divergence angle with confinement, see Fig. 8.10 (left), is reproduced. The hypothesis is not that the confinement factor alone is determining the SAD but based on the presented experimental data, and the numerical model it is concluded that it is an influencing factor and that the magnitude of the lateral divergence angle in general increases with increasing confinement. Additionally, other properties of the diode laser as such as gain spectra, internal absorption and efficiency influence temperature, threshold current, threshold carrier density and the corresponding average carrier density in the device.

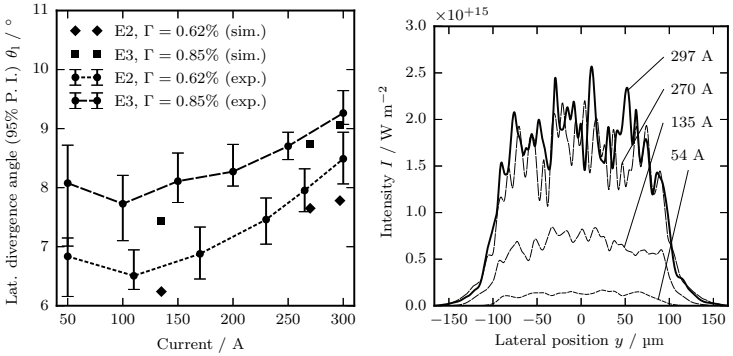

FIGURE 8.10: Left: SAD (95% P.I.) from experimental data and modeling over current for laser designs D7 and D8 as presented in [6] and [86]. The diamonds and squares mark the predicted SAD from numerical simulations. Device D8 with epitaxy E3 has a larger confinement factor than structure D7 with epitaxy E2. Right: Simulated near-field intensities for design D7 for currents (per emitter) I =2, 5, 10, 11 A. The simulation results shown in the plots are for one emitter (of the array) with a 200 µm contact opening and are published in [6]. Field intensities are averaged over round-trips 150 to 200.

8.3 Modeling Lateral Emission Characteristics of Single Emitters

A value of $2.67 \cdot 10^{-4}\,\mathrm{K}^{-1}$ is reported in [116] for the thermal-induced refractive index change in GaAs. For modeling of lasers with AlGaAs waveguides, a coefficient for the modal thermal-induced refractive index change of $3 \cdot 10^{-4}\,\mathrm{K}^{-1}$ (the value is obtained from data presented in [115]) is applied in [117, 11], and a value of $4.9 \cdot 10^{-4}\,\mathrm{K}^{-1}$ is applied in [118]. The value depends on the specific waveguide and QW compositions. To match the measured FF and NF profiles of the device D1, the parameters α_T and α_N are adjusted. The calibration results in $\alpha_T = 4 \cdot 10^{-4}\,\mathrm{K}^{-1}$ and $\alpha_N = -1.7 \cdot 10^{-26}\,\mathrm{m}^3$ for the SE devices D1-D4. The calibration is summarized as follows: α_N is adjusted to match the low current regime, in particular the increase in the NF width and α_T is increased until the FF divergence matches for high currents. The NF and FF intensity profiles are successfully resembled by the model. A comparison of measured and simulated lateral intensity profiles for device D1 with 100 µm contact width is displayed in Fig. 8.11. With an increase in injection current, both NF and FF profiles show increased filamentation and the FF width increases. Parts of the NF intensity spread outside of the contact opening width. The spread of those side-wings is a function of α_N, the profile of the current density distribution and the recombination coefficients A_{nr}, B_{sp} and C_{A}. The lower the recombination coefficients, the higher the carrier density in the regions adjacent to the contact opening, see Fig. 8.13 and Fig. 8.14. These regions can be optically pumped and form channels of gain or at least transparency, so that the light field spreads towards the outside of the emitter and the NF width increases. The computed results for the D1 device are compared to three sets of measurements (Fig. 8.12), which in total amount to 37 tested devices. The simulated FF width follows the experimental results. The change in slope of SAD over current due to the onset of thermal lensing for

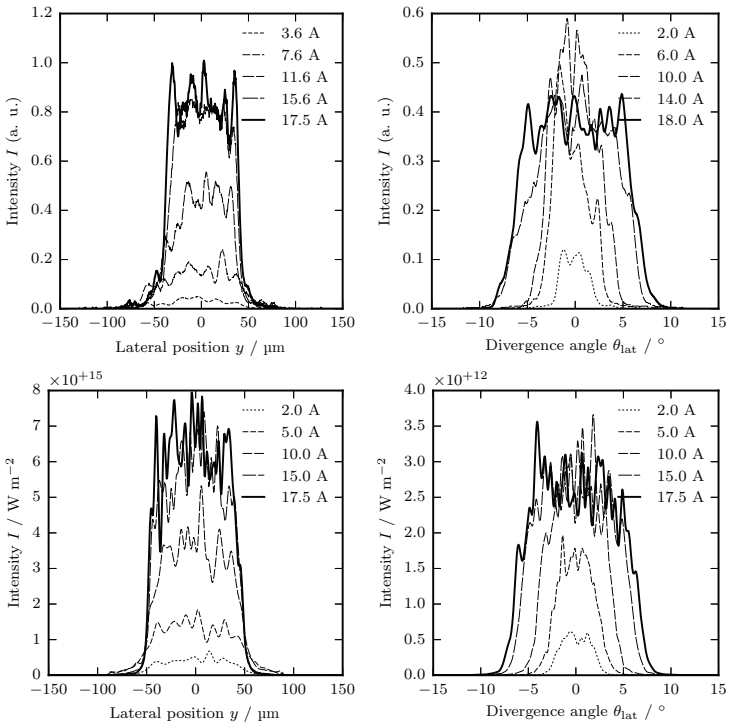

FIGURE 8.11: Near-field (left) and far-field (right) measurement (top row) and simulation (bottom) of 100 µm single emitter D1 with 1.45 µm deep trench.

currents above 10 A is reproduced. The measured NF widths for the highly filamented profiles show variations up to ±10 µm between devices out of one set of measurements and offsets of the averaged NF widths up to 10 µm between data sets. The simulated NF widths lie within the range of the measured widths, although the NF narrowing for high currents seems to be slightly overestimated by the simulation. The calculated output power matches the measured values, and the (averaged) temperature over current aligns with the measured one, which is a result of the adjustment of the heatsink coefficient for the thermal boundary condition. With the same parameters as used for D1, except for the change in the contact width to 150 µm and electro-optical efficiency (dissipated heat), the emission characteristics of device D4 are modeled. Due to the larger contact area of D4 compared to D1, at the same injection current the current density is lower for D4. To compare SAD and NF width at equal current densities, for D4 the range up to 20 A, and for D1 the current range below 13 A are considered. The dip in the SAD for D1 around 10 A is not observed for the wider device D4, and the increase in the slope of SAD over current due to thermal lensing is pushed to higher currents, see SAD in Fig. 8.17. The lower thermal lensing also manifests in the NF trend for D4. The trend of the NF width for D4 is similar to the trend for D1 below 10 A. The model is capable of predicting changes due to modifications of the contact width.

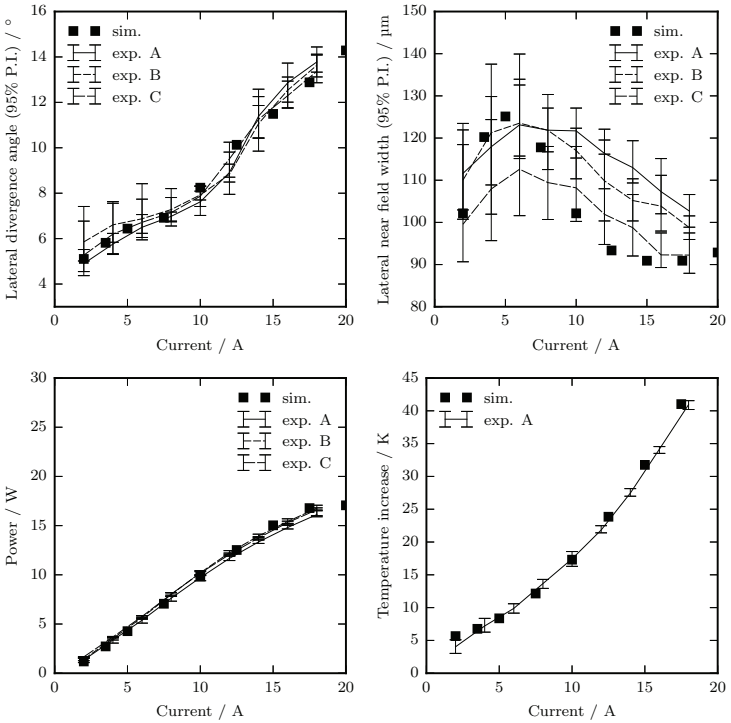

FIGURE 8.12: SAD, NF width, both (95% P.I.) and power, temperature from experimental data and modeling over current for the laser design D1. Exp. A, B and C consist of data sets of 8, 10 and 19 devices respectively. The error bars indicate the extremal values from the data set. Details of the structures are listed in Tb. C.2. The simulation results are averaged over round-trips 150 to 200.

In the following, devices with two additional modifications are investigated. Device D2 has a 140 µm contact opening and a cavity length of 5 mm so that both contact width and cavity length are changed compared to D1, which is 4 mm long. Devices D1, D2, and D4 are asymmetrically coated with an AR coating with 2 % reflectivity at the front facet and an HR coating with 98 % at the rear facet. The ratio between the reflectivities results in an asymmetric intensity distribution along the laser cavity. This distribution is observed in the averaged intensity in Fig. 8.15. If the reflectivities are equalized the longitudinal intensity (and temperature) profile changes. The averaged intensity becomes symmetric with respect to the center of the device, see Fig. 8.21. Device D3 equals device D2 despite the change in facet reflectivities, which are both set to $R_0 = R_l = 10\%$ for D3. Additionally, to capture the output power at the rear facet the submounts for the symmetric devices D3 are 5 mm long, those for the (standard) asymmetric devices are 5.4 mm long. The experimental comparison of the asymmetrically and symmetrically coated devices D2 and D3 is presented in [4]. The symmetric device provides a higher optical power (for the sum out of both facets) and (nearly) symmetric longitudinal gain and intensity profiles compared to standard asymmetrically coated devices.

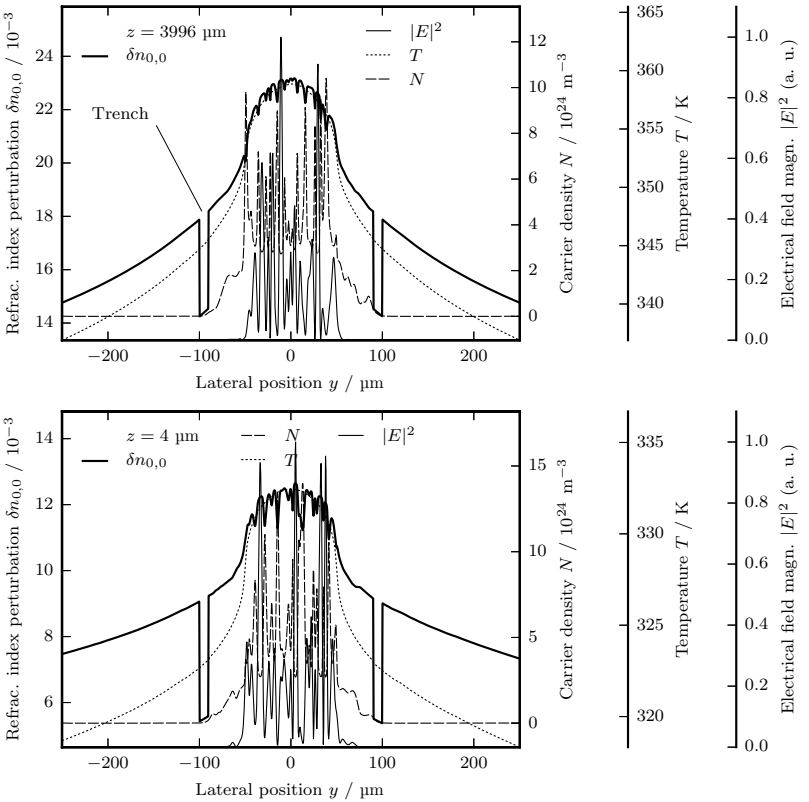

FIGURE 8.13: Lateral profile of refractive index perturbation, carrier density, intensity and temperature for current $I = 20\,\mathrm{A}$ at longitudinal position $z = 3.996\,\mu\mathrm{m}$ (top) and $z = 4\,\mu\mathrm{m}$ (bottom). The snapshots are from round-trip 200 for the laser design D1, as listed in Tb. C.2.

These differences are captured by the numerical model, see lateral averaged intensities over the longitudinal direction in Fig. 8.21. The thermal roll-over (compare power in Fig. 8.20) occurs for lower currents for the asymmetric design D2. The more pronounced LSHB for the asymmetric cavity, due to an asymmetric intensity distribution, leads to accumulation of carriers in the rear side of the device, see Fig. 7.2, which manifest in higher non-radiative recombination and higher optical absorption. Both lead to power decrease and increased dissipated heat.

The FF width and NF width of the symmetric devices increase more linear with current and do not show an increase in SAD-slope due to thermal *blooming*. These trends are contrary to the asymmetric case. For currents below 15 A, the near-field widths for the symmetric devices are smaller than for the asymmetric ones (Fig. 8.19). The average temperature for D3 at 20 A is about 332 K with dissipated heat of 11.6 W, while for D2 it amounts to about 335 K for the same dissipated heat at 18.5 A. Although for D2

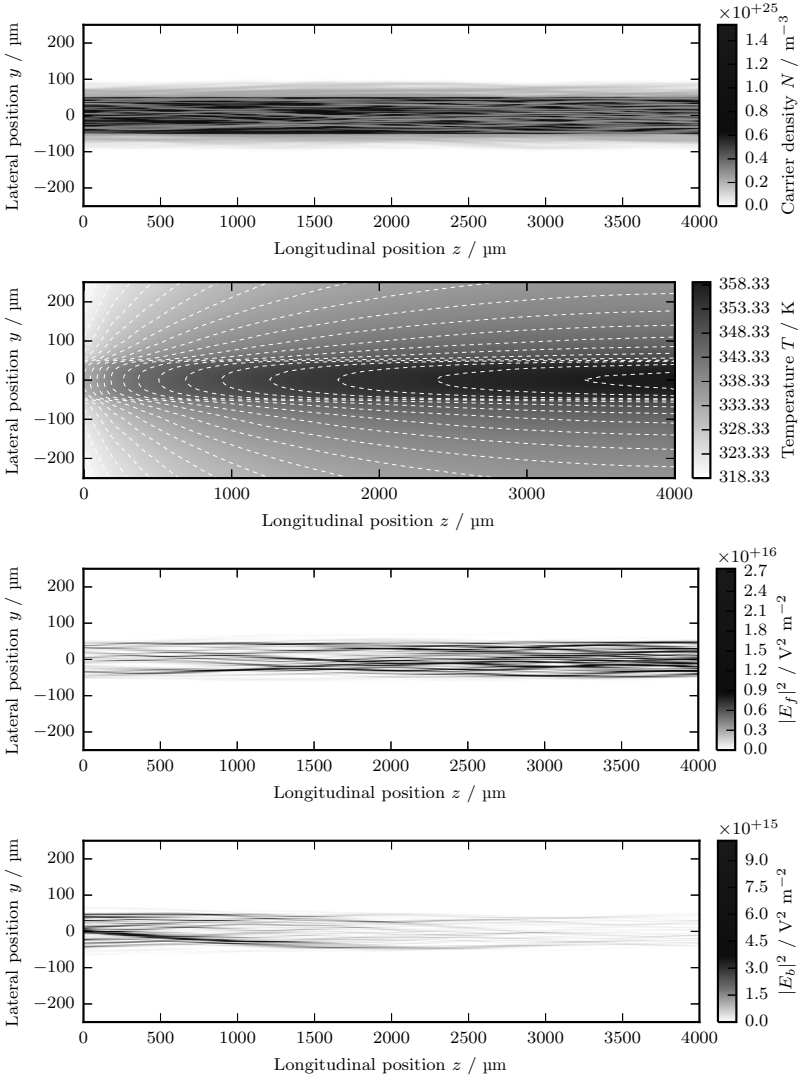

FIGURE 8.14: Carrier density, temperature, forward and backward propagating electric field (amplitude) in QW for a current of $I = 20\,\mathrm{A}$ for device D1. The snapshots are from round-trip 200.

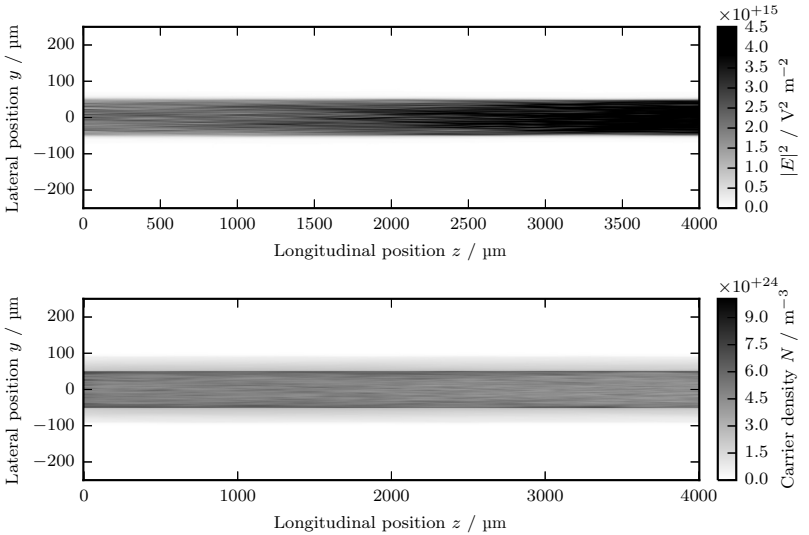

FIGURE 8.15: Averaged light intensity and carrier density in QW for a current of $I = 20\,\mathrm{A}$ for device D1. Results are averaged values over round-trips 150 to 200.

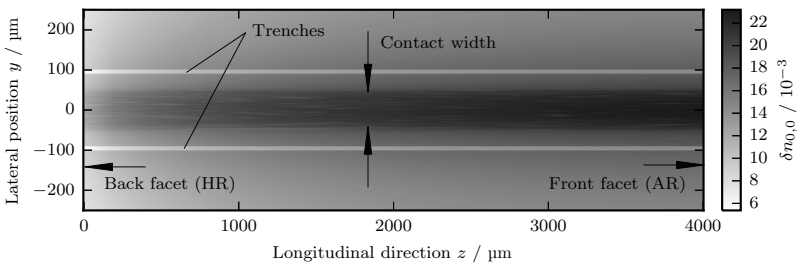

FIGURE 8.16: Refractive index perturbation in QW for a current of $I = 20\,\mathrm{A}$ for device D1. Snapshot taken at roundtrip 200.

and D3 the dissipated powers, and the averaged temperatures are in the same range, due to the different distribution of the heat sources, see temperature profile in QW in Fig. 8.22, the SAD trends for D2 and D3 differ. This suggests that by symmetrization of the thermal profile along the cavity length the onset of the thermal *blooming* is shifted to higher currents. On top, the increase in the NF width for low currents is suppressed. This trend is partially captured by the model. An explanation for the effect can be the lower peak intensities inside the cavity accompanied by a lower modulation of the carrier density profile. Under the assumption of the same current spreading in the p-side of the devices, the near-field widening in the asymmetric case suggests a larger spread of carriers besides the contact width. The $\mathrm{BPP}_{95\%,\mathrm{lat}}$ for the symmetric design D3 is about 1 mm mrad lower across the investigated current range than the one for the asymmetric design. For the symmetric design, the emission area is doubled since it includes both

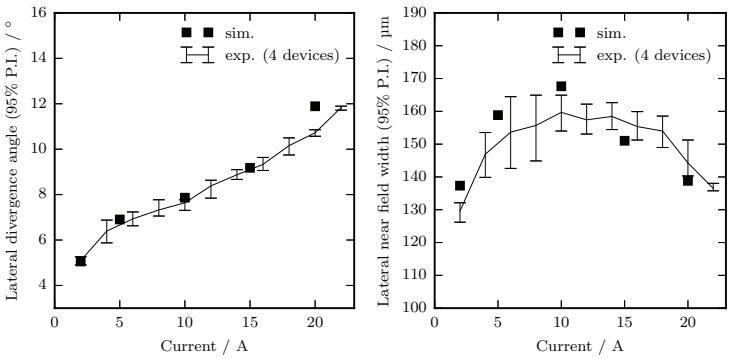

FIGURE 8.17: SAD and NF width (both 95% P.I.) over current from experimental data and modeling for laser design D4. Details of the structure are listed in Tb. C.2. The error bars indicate the extremal values from the data set. The simulation results are averaged over round-trips 150 to 200.

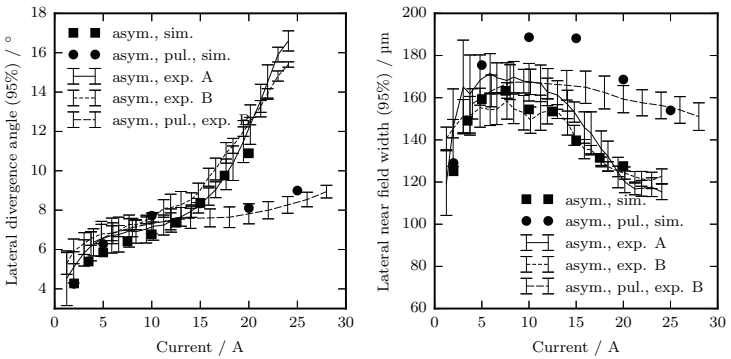

FIGURE 8.18: SAD and NF width (both 95% P.I.) over current from experimental data (presented in [4]) and modeling for the laser design D2 (asym.). Exp. A and B consist of data sets of 6 and 4 devices, respectively. The pulsed measurements are performed with 4 µs pulse width and 50 Hz repetition rate. The pulsed measurements consist of a data set of 5 devices. The error bars indicate the extremal values from the data set. Details of the structures are listed in Tb. C.2. The simulation results are averaged over round-trips 150 to 200.

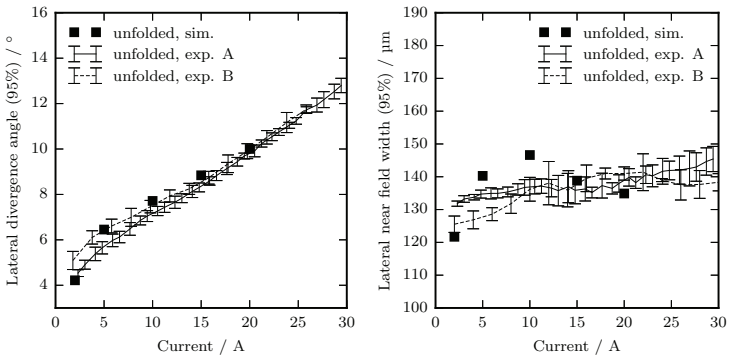

FIGURE 8.19: SAD and NF width (both 95% P.I.) over current from experimental data (presented in [4]) and modeling for the laser design D3 (sym.). Exp. A and B consist of data sets of 4 and 3 devices, respectively. The error bars indicate the extremal values from the data set. Details of the structures are listed in Tb. C.2. The simulation results are averaged over round-trips 150 to 200.

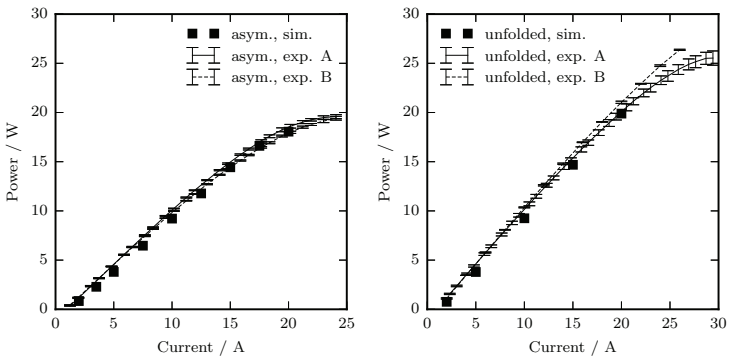

FIGURE 8.20: Power over current from experimental data (presented in [4]) and modeling for the laser designs D2 (left) with asymmetric cavity and D3 (right) with a symmetric cavity. The power for the symmetric cavity is the total output power collected from both facets. Details of the structures are listed in Tb. C.2. The simulation results are averaged over round-trips 150 to 200.

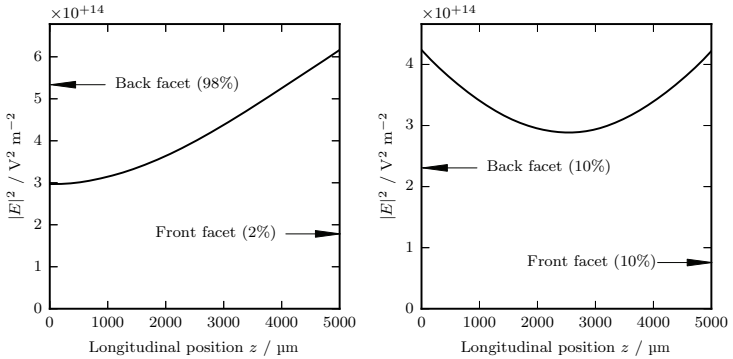

FIGURE 8.21: Laterally averaged electric field amplitude over cavity length for device D2 with symmetric coating (left) and asymmetric coatings (right) at $I = 20\,\mathrm{A}$. Details of the structures are listed in Tb. C.2. The simulation results are averaged over roundtrips 150 to 200.

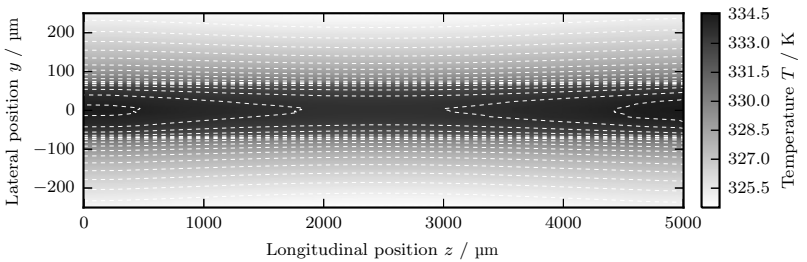

FIGURE 8.22: Temperature in QW for a current of $I = 20\,\mathrm{A}$ for device D3. Snapshot taken at roundtrip 200.

facets. Therefore, the brightness of the device is only increased if the BPP is reduced by one half for an output power (out of two facets) equal to the output power of the asymmetrically coated device. In the presented case the symmetric device indeed has a reduced BPP but a decreased brightness.

Fig. 8.18 includes a set of measurements for SAD and NF width for D2 operated in pulsed mode [1]. In pulsed operation, the temperature rise in the device is significantly reduced, and the increase in SAD for currents above 15 A is suppressed for D2, see Fig. 8.18. To emulate the pulsed mode with a reduced thermal lens, the factor α_T is reduced from $4 \cdot 10^{-4}\,\mathrm{K}^{-1}$ to $1.75 \cdot 10^{-4}\,\mathrm{K}^{-1}$ in the model to match the measured characteristics. The temperature rise is not entirely suppressed. In particular at high currents above 25 A, an increase in the SAD slope over current is observed, which suggests the formation of the thermal lens. The reduction of the thermal influence at high currents leads to both a reduced SAD and an increased NF width, compare to Fig. 8.18. Both effects are predicted by the model, although the increase in NF width is over-estimated for currents

[1] The author would like to thank Simon Rauch, with TRUMPF Laser GmbH, Schramberg, for providing the experimental data on the pulsed measurements.

around 10 A. The results from the pulsed measurements support the explanation of the SAD and NF trends based on the interplay between the carrier and thermal-induced refractive index perturbations as presented in Section 8.1.

8.4 Results of Time-Domain Simulation

In this section, the TD edge-emitting laser model (Section 7.3) is employed to simulate the field dynamics in the cavity. The model is demonstrated by the example of device D1 (since it represents a *standard* SE device), and resulting near- and far-field profiles, and the filamentation pattern inside the cavity are compared to the results obtained with the FD model. For the TD simulation, the thermal profile is obtained in the same way as for the FD model. For the TD model in this study, the temperature is obtained from the steady-state solution of the heat equation, and the temperature is calculated once at the initial time step. This circumvents the need for long simulation times to ensure the built up of the thermal profile. The temperature increase from the initial to the steady-state operating temperature takes place over time scales of several hundred nanoseconds [119]. The longitudinal resolution is $\Delta z = 4\,\mu\text{m}$ and the effective group refractive index is determined to $n_\text{g} = 3.9$. Therefore, the temporal discretization accounts to $\Delta t = 5.204 \cdot 10^{-2}\,\text{ps}$. The Lorentzian pole is modeled with amplitude $A = {}^{2\gamma\Delta g_0 n_\text{ref}}/_{k_\text{ref}}$, $\omega_\text{ref} = {}^{2\pi c_0}/_{\lambda}$ and $\gamma = {}^{\Delta\lambda c_0}/_{\lambda^2}$, where the central wavelength is $\lambda = 950\,\text{nm}$, $\Delta\lambda = 100\,\text{nm}$, the differential gain is $\Delta g_0 = 0.55 \cdot 10^4\,\text{m}^{-1}$, and the coefficient of the static gain is $g_0 = 0.55 \cdot 10^4\,\text{m}^{-1}$. The differential gain is a function of the carrier density and obeys the same logarithmic dependency as the static gain (6.89). Lateral resolution and other simulation parameters are the same as for the FD simulation for D1, listed in Tb. C.2.

The initial carrier density is set to the transparency carrier density value under the injection stripe so that the period in which the carrier density increases but is below transparency is skipped in the simulation. The simulation starts at $t = 0\,\text{s}$ with zero electric field in the cavity, and the light field builts from contributions from the random spontaneous emission source, followed by amplification of those. Since the light intensity is low, the gain is not saturated and the optical power inside the cavity growths exponentially until the first pulse forms and the carrier density is depleted. The TD model obeys the known ring-in behavior which occurs when a diode laser is switched on or operated in pulsed mode. After about 400 ps the output power fluctuates around a value of 10 W for 10 A injection current. The snapshots of the electric field in Fig. 8.23 show the formation of mode patterns and the evolution of the filamented fields. At this early times, the profile is still symmetric in the lateral direction. However, once the contributions from un-symmetric field patterns emerge with increasing perturbations, the entire field profile becomes un-symmetric. The un-symmetric patterns are displayed in Fig. 8.23 where the field intensity averaged over a period of 1 ps is shown. After several nanoseconds, the field is highly filamented with lengths of the filaments partially below 500 µm. The patterns result in sub-picosecond intensity fluctuations on the diode facet. These fluctuations are numerically and experimentally observed by Adachihara et al. in [120] and Fischer et al. in [121] and (experimentally) in [122].

If the electric field amplitudes are incoherently added and averaged over certain periods, filaments, which extend along the propagation direction are observed. An example of an integration time of 10 ps is shown in Fig. 8.24 (top) with the corresponding averaged

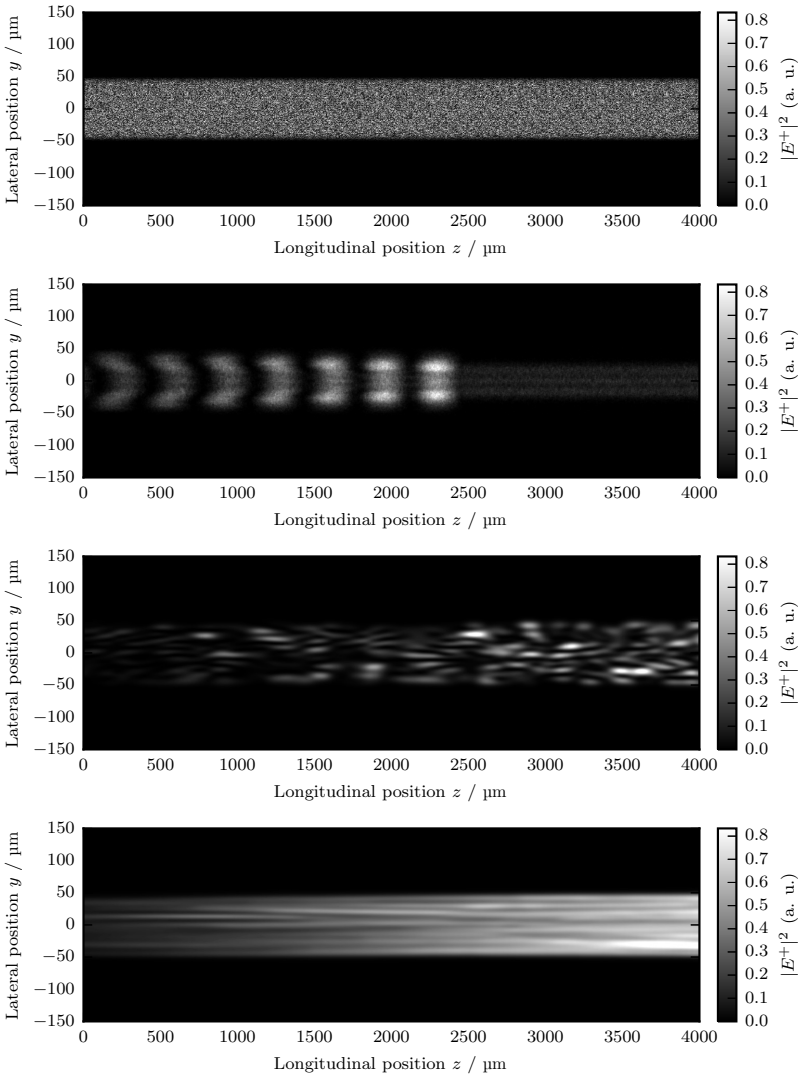

FIGURE 8.23: Snapshots and incoherent averages of electrical field magnitude in QW. Snapshots are taken after first time step (top) and at time 32 ps (2nd row). For the plots in the 3rd and bottom row integration is performed over a period of 1 ps (3rd row) and 52 ps (bottom) starting after simulated time of 4 ns.

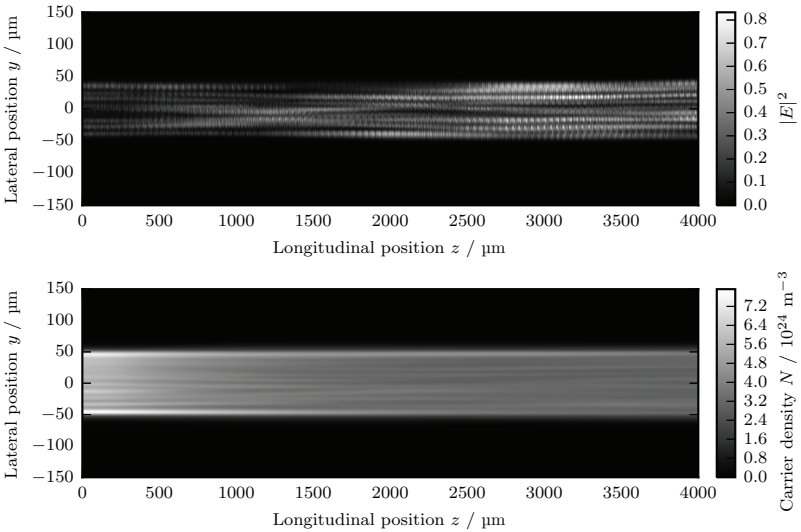

FIGURE 8.24: Averaged electrical field magnitude and carrier density in QW for a current of $I = 10$ A for device D1. Results are averaged over 10 ps starting at time 4 ns. In contrast to the results displayed in Fig. 8.23 this simulation is performed without gain dispersion.

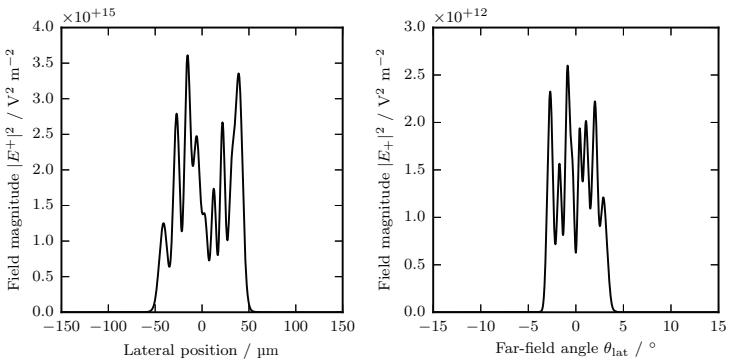

FIGURE 8.25: Averaged electrical field magnitude in near- (left) and far-field (right) for a current of $I = 10$ A for device D1. Results are averaged over 10 ps.

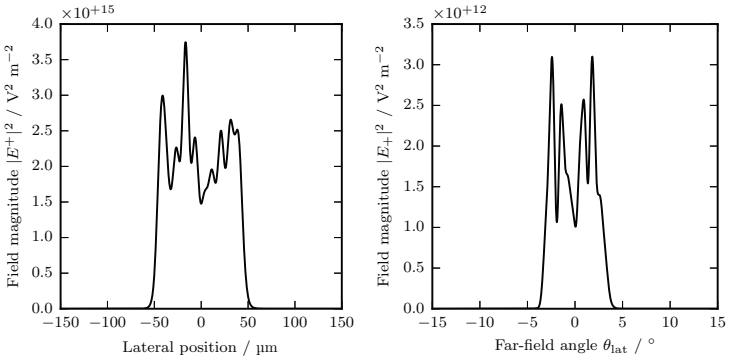

FIGURE 8.26: Averaged electrical field magnitude in near- (left) and far-field (right) for a current of $I = 10\,\mathrm{A}$ for device D1. Results are averaged over 52 ps.

carrier density (bottom). The carrier density exhibits the imprint of the filamented field and shows higher densities at the rear facet due to LSHB. The resulting averaged field in the QW-plane shows a similar structure to the one obtained by the FD model. Compare Fig. 8.14 and Fig. 8.24. For longer integration times (52 ps in Fig. 8.23 in the bottom row) the asymmetric intensity profile along the longitudinal cavity is observed in the averaged results. Again the resulting distribution obtained by the TD model equals the one calculated by the FD model (Fig. 8.15). The NF intensity profiles and FF intensity profiles for a short integration time (Fig. 8.25) show higher lateral modulation than the ones obtained by longer integration times (Fig. 8.26). The NF and FF profiles obtained for larger integration times are similar to measured profiles (Fig. 8.11). NF width and SAD for 10 A have the right magnitudes compared to measurements for device D1. In the scope of this work, the TD model is demonstrated for one device with an injection current of 10 A. The extraction of SAD and NF width over operating current and different device geometries as demonstrated with the FD model is subject to future studies.

8.5 Chapter Summary

The FD model for edge-emitting semiconductor lasers (Chapter 7), which describes the multi-mode lateral emission characteristics is employed to compute NF width, FF width, temperature, and output power over current for the SE devices D0–D4 and the LAs D5–D8. The numerical results are in agreement with the experimental data. By the example of the SE device D0 with 90 µm contact opening and 4 mm cavity length, the influences of the thermal-induced and carrier-induced refractive index changes on the NF and FF evolution over current are investigated (Fig. 8.6). When carrier-induced perturbations are suppressed the SAD correlates with the temperature increase and thus, monotonically increases with current. The NF remains flat with current with a width corresponding to the contact opening. If the thermal lens is suppressed, the NF does not narrow at high currents but remains increasing with current, and the SAD monotonically increases with a decreasing slope over current. In the case that both carrier- and thermal-induced perturbations are suppressed, NF and SAD remain flat

and nearly independent of the injection current. Based on the investigation of these extreme cases, the conclusion is drawn that the lateral emission characteristics with both perturbations follow the case without thermal lensing at low currents and the case without carrier lensing at high currents (where the thermal lens dominates). The transition region represents a merge between both cases, see Fig. 8.6. These observations reflect in the characteristics of the experimental investigated devices D1–D8 which are summarized in Fig. 1.1. The agreement between measurements and simulation for the pulsed operation supports the interpretation of the contributing factors to SAD and NF evolution.

The TD edge-emitting laser model (Section 7.3) is employed to simulate the field dynamics in the cavity. The model is demonstrated by the example of device D1 (since it represents a *standard* SE device) for an injection current of 10 A, and resulting near- and far-field profiles and the filamentation pattern inside the cavity show a similar structure to the ones generated with the FD model.

Chapter 9

Conclusion and Outlook

Numerical methods for the simulation of broad-area edge-emitting semiconductor lasers are presented in this work. Frequency-domain and time-domain models are employed to predict the propagation of the filamented optical field in the semiconductor laser and determine emission characteristics including near-field and far-field profiles, beam width, divergence angle, and power over current. The models utilize wave-optical beam propagation and account for the interaction of the optical field with the spatial (and temporal) varying carrier and temperature distributions inside the semiconductor laser cavity.

To compute gain and refractive index change of strained quantum wells, 8-band $k \cdot p$-calculations are performed to derive the band structure and dipole matrix elements. The change of the gain for the transverse-electric and transverse-magnetic transitions as a function of the externally applied stress is investigated in Chapter 2. Based on the drift-diffusion model, the electro-optical properties of the diode laser are calculated. To evaluate lateral current spreading the current density is computed in the transverse plane of a single emitter with 100 µm contact opening. For the two-dimensional simulations, the Scharfetter-Gummel discretization is applied on a structured mesh. The finite-element implementation of the drift-diffusion equations with the primal-mixed method on a one-dimensional mesh is successfully demonstrated in Chapter 6. The extension of this scheme for two-dimensional meshes is subject to continuing research. As a side product of this work, a *python*-wrapper *pymagma* [123] for the *MAGMA* library [107] is produced which offers top-level access to accelerated sparse matrix operations, including iterative solvers on Graphics Processing Units (GPUs). The library is used to perform the beam-propagation with massive-parallelization on a GPU. All numerical methods presented throughout this work, are integrated into the multi-physics semiconductor simulation-software *SEMSIS*. (Objective 1)

Once calibrated, the frequency-domain model is utilized to predict emission characteristics of single emitters and laser arrays, which differ in geometrical properties (contact width, cavity length or emitter pitch), epitaxial structure or facet reflectivity. By comparison with experimental data for eight laser designs D1-D8 it is demonstrated that the frequency-domain model allows computation of lateral far-field angles and near-field widths as a function of current and thermal state for edge-emitting diode lasers. (Objective 2)

The carrier- and temperature-induced refractive index changes are calibrated to match the near-field and far-field of one laser device, in this case, a device with 100 µm contact opening and 4 mm cavity length. With the parameters obtained from the calibration, emission characteristics of three other single-emitter lasers with equal epitaxy but different contact opening width, cavity length or facet reflectivities are computed. By decreasing the thermally induced refractive index change in the simulation, the measured change in slow-axis divergence in pulsed operation of a single-emitter device resembles in the model. The thermally induced increase of the far-field angle is shifted to higher currents in both experiment and model. The investigated devices include broad-area lasers with 4 and 5 mm cavity length and contact openings of 100, 140 and 150 µm. The differences in thermal *blooming* due to different heat loads and device geometries are reproduced in the model, simultaneously to the near-field widening at low and narrowing at high currents. The increase in beam quality due to the application of equal reflectivities for front- and rear-facet coatings are captured as well. Besides, emission characteristics for laser arrays with a variation of fill factor and epitaxial structure, with a change in the confinement factor, are successfully computed. For gain-guided diode lasers, the evolution of the lateral field with current is in particular determined by the balance and interplay of carrier- and temperature-induced refractive index perturbations. At low currents, the carrier-induced perturbations dominate, which lead to anti-guiding and an increase in the near-field width. For higher currents the thermal lens dominates, and the far-field angle increases significantly, while the near-field contracts. Other properties of the diode laser such as gain dispersion or refractive index perturbations due to strain have a potential influence on the lateral emission. (Objective 2, 3)

So far, the coupled frequency-domain laser model is employed for scalar fields, although the implementation allows vectorial beam propagation. It is planned to employ this feature to link the findings from Chapter 5 with the coupled model and investigate the effects on slow-axis divergence.

The opto-mechanical model (Chapter 5) is derived to compute the degree of polarization for packaged single emitter or laser arrays. Depolarization of the transverse electric field-components is induced by the presence of shear strain. The ratio of the shear strain and the lateral (and vertical) strain component(s) determines the degree of polarization. The larger the shear strain component is relative to the lateral strain component the larger is the depolarization. Under the assumption that the structure is invariant in the longitudinal direction the model is reduced to the transverse plane and applied to evaluate local depolarization in a packaged laser array. The mechanical strains, induced by the soldering process, heating of the device during operation and intrinsic lattice mismatch in the device, are considered. The transverse domain consists of the laser array, metallization, solder, submount, and the heatsink. A stability analysis of the opto-mechanical system is performed, in which the resilience against depolarization of a structure under introduction of strain perturbations is evaluated. The computed degree of polarization is in the range of the experimental data. (Objective 4, 5)

In addition to the frequency-domain model, a time-domain model based on the traveling-wave method is implemented and employed to compute the optical propagation in the QW-plane of an edge-emitting diode laser, including carrier- and temperature-induced refractive index changes. The evolution of the optical field along the cavity is computed iteratively for transverse slices. Alongside with the optical propagation, the carrier diffusion equation and an auxiliary equation for the material polarization are solved. The

dynamic response of the polarization, which is approximated by a Lorentzian pole, accounts for gain and refractive index dispersion. The model is implemented in a parallel algorithm, which distributes the workload among the available processing units or computing nodes. The parallelization on an 18-core processor leads to a reduction of the time-step execution-duration by a factor of 10. In the scope of this work, the time-domain model is demonstrated for a device with 100 µm contact width and 4 mm cavity length. The results obtained with the time-domain model obey similar filamented field profiles like the ones obtained with the frequency-domain (Fox-Li) model. The congruence in the obtained results suggests that it is justified to use the frequency-domain model to compute the multi-mode field distributions. (Objective 6)

The investigation of the lateral emission with the time-domain model, which includes analysis of different device designs as demonstrated with the frequency-domain model is subject to future studies.

The focus of this work lies on the implementation of multi-physics models and demonstration of phenomena observed for existing devices. In summary, the simulated far-field divergence, near-field widths, temperatures, and output powers are in agreement with the measured values obtained from experiments. A quantitative prediction of the lateral emission characteristics (for various devices) including the far-field divergence angle, and the near-field width in conjunction with the output power, and the temperature for gain-guided broad-area semiconductor lasers has not been reported before. The computations include the prediction of the filamented light field inside the cavity. In addition, the prediction of the degree of polarization for a packaged single emitter or laser array based on a computed mechanical strain field is novel with respect to the state-of-the-art.

Outlook:
The understanding and reproduction of characteristics from existing devices is the first milestone towards predictions for (lateral) laser designs with higher brightness. Suggested strategies for novel devices with increased brightness by reduction of slow-axis divergence angle or near-field width include:

1. Designs with modified vertical structures and active regions which, for example, have quantum wells with reduced carrier-induced refractive index change.
2. A reduction of the (lateral) thermal gradients by control of the (transverse) current injection profile or by variation of the emitter pitch or width on laser arrays.
3. Control of the lateral gain profile by design of the (lateral) current injection into the QW.
4. The introduction of index trenches for a lateral near-field constraint.
5. Designs with additional lateral features adjacent to the current injection region which filter higher-order transverse modes. The lateral filters can, for example, be introduced by variation of the contour of the contact opening, by an alternating effective refractive index in the lateral or longitudinal direction which act as gratings or introduction of absorbing elements.

In the design process, the numerical model acts as a *digital-twin* of the real device to understand experimental findings and predict new outcomes. With the simulation tools presented in this work the lateral emission characteristics for such novel, edge-emitting laser devices can be predicted to the extent needed to make design decisions.

Appendix A

Material Properties

A.1 Bandgap

The temperature dependent bandgap energies for the conduction band minima at the Γ, X and L point of the binary compounds GaAs, AlAs and InAs are modeled with the Varshni formula [124]

$$E_{\mathrm{g},k}(T) = E_{\mathrm{g},0,k} - \frac{\alpha_k T^2}{\beta_k + T}, \quad \text{with} \quad k = \Gamma, X, L. \tag{A.1}$$

Here $E_{\mathrm{g},0,k}$ are the bandgap energies at the reference temperature of $T_0 = 0\,\mathrm{K}$. According to [125] the temperature dependent bandgap is calculated by taking the smallest energy

$$E_{\mathrm{g}}(T) = \min\left(E_{\mathrm{g},\Gamma}(T), E_{\mathrm{g},X}(T), E_{\mathrm{g},L}(T)\right) \tag{A.2}$$

out of the bandgap energies of the conduction band minima. The material properties for the bandgap energies of GaAs, AlAs and InAs are taken from [126] and are listed in Tb. A.1, A.3 and A.4. The temperature dependent bandgap of a ternary compound $\mathrm{A}_x\mathrm{B}_{1-x}\mathrm{C}$ is calculated based on the interpolation scheme

$$E_{\mathrm{g},k}^{\mathrm{ABC}}(T) = E_{\mathrm{g},k}^{\mathrm{AC}}(T)\cdot x + E_{\mathrm{g},k}^{\mathrm{BC}}(T)\cdot(1-x) - C_{E_{\mathrm{g},k}}^{\mathrm{ABC}}\cdot x\cdot(1-x) \quad \text{with} \quad k = \Gamma, X, L \tag{A.3}$$

between the bandgap energies $E_{\mathrm{g},k}^{\mathrm{AC}}(T)$ and $E_{\mathrm{g},k}^{\mathrm{BC}}(T)$ of the binary compounds AC and BC. The bowing parameters $C_{E_{\mathrm{g},k}}^{\mathrm{ABC}}$ are determined from measurements for the specific ternary compound ABC. Analogue to the binary case the bandgap is determined by evaluating the minimum of the interpolated bandgap energies of the conduction band minima Γ, X and L according to (A.1). The bowing parameters for AlGaAs are listed in Tb. A.5 and for InGaAs in Tb. A.6.

For AlGaAs or InGaAs with bandgap $E_{\mathrm{g}}(T)$ the offset of the conduction band edge is determined based on

$$\Delta E_c(T) = c_{\Delta E_c}\left(E_{\mathrm{g}}(T) - E_{\mathrm{g}}^{\mathrm{GaAs}}(T)\right). \tag{A.4}$$

The offsets are evaluated for the case of a heterointerface of AlGaAs or InGaAs to GaAs ($\Delta E_c^{\mathrm{GaAs}} = 0$).

A.2 Effective Density of States and Effective Mass

Effective Density of States (DOS) in semiconductors are exponentially dependent on temperature

$$N_{\mathrm{c/v}} = N_{\mathrm{c/v},T_0} \left(\frac{T}{T_0} \right)^{\frac{3}{2}} \tag{A.5}$$

the effective density of states for the conduction and valence band are denoted as N_{c} and N_{v}, respectively. A value of $T_0 = 300\,\mathrm{K}$ is taken as the reference temperature. For the ternary alloys $\mathrm{Al}_x\mathrm{Ga}_{1-x}\mathrm{As}$ and $\mathrm{In}_x\mathrm{Ga}_{1-x}\mathrm{As}$ the effective density of states $N_{\mathrm{c/v},T_0}$ at the reference temperature is evaluated with the interpolation scheme [127]

$$N_{\mathrm{c/v},T_0} = N_{\mathrm{c/v},T_0,0} \left(1 + c_{N_{\mathrm{c/v},T_0},1} x + c_{N_{\mathrm{c/v},T_0},2} x^2 \right)^{\frac{3}{2}} . \tag{A.6}$$

For $\mathrm{Al}_x\mathrm{Ga}_{1-x}\mathrm{As}$ the interpolation coefficients for the conduction bands density of states changes for concentrations below $x < x_0 = 0.41$ and above $x \geq x_0$, as listed in Tb. A.5. With known effective DOS the effective masses of the conduction and valence band

$$m^*_{n/p}(T) = \frac{h^2}{2\pi k_{\mathrm{B}} T} \left(\frac{N_{\mathrm{c/v}}(T)}{2} \right)^{\frac{2}{3}} \tag{A.7}$$

are determined.

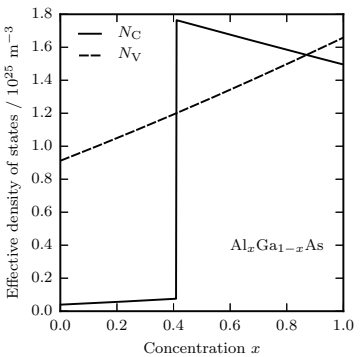

FIGURE A.1: Electron and hole effective DOS $\mathrm{Al}_x\mathrm{Ga}_{1-x}\mathrm{As}$ calculated based on parameters from Tb. A.5.

A.3 Carrier Mobility

To calculate the mobilities of electrons and holes a model presented by Sotoodeh is applied for the binary and ternary semiconductor alloys AlAs, GaAs, InAs, InP, GaP, AlGaAs, InAlAs, InGaAs and InGaP. Carrier mobilities are calculated based on the empirical model

$$\mu(T) = \mu_{\min} + \frac{\mu_{\max}(T) - \mu_{\min}}{1 + \left(\frac{N}{N_{\mathrm{ref}}(T)} \right)^{\alpha}} \tag{A.8}$$

described in [128]. The temperature dependence of the maximal mobility value is

$$\mu_{\max}(T) = \mu_{\max,T_0} \left(\frac{T_0}{T}\right)^{\beta} \tag{A.9}$$

and the reference carrier concentration is modeled via

$$N_{\mathrm{ref}}(T) = N_{\mathrm{ref},T_0} \left(\frac{T}{T_0}\right)^{\gamma}, \tag{A.10}$$

where for both the reference temperature is $T_0 = 300\,\mathrm{K}$. The carrier concentration inserted in (A.8) is the total carrier concentration, the sum of the acceptor and donator concentrations $N = N_{\mathrm{A}} + N_{\mathrm{D}}$. The remaining parameters $\mu_{\max,T_0}, N_{\mathrm{ref},T_0}, \alpha, \beta$ and γ in (A.8) are fit parameters, which all have positive values. Several facts emerge from the analysis of (A.8):

1. For small doping concentrations the mobility converges to the maximal value $\mu_{\max}(T)$.
2. The maximal mobility decreases with raising temperature.
3. For large carrier concentrations the mobility converges to the minimal value $\mu_{\min}$.
4. For high temperatures the term $N/N_{\mathrm{ref}}(T)$ decreases, so that it only results in relevant contributions for higher carrier concentrations. The physical explanation is, that scattering at ionized defects, which lead to a reduction of the mobility, takes effect at higher doping concentrations with higher temperatures.

The minimum carrier mobility is nearly independent of temperature, as confirmed by experimental measurements presented in [129]. The presented model is subject to some restrictions: The mobility after Sotoodeh describes the mobility of the majority charge carriers only and does not include the mobility for the minority charge carriers since for the latter, no experimental data is available. For small temperatures, the mobility for the Sotoodeh model deviates significantly from the measured values, so that it is only applied for temperatures above 150 K. Additionally, it is not distinguished between the type of doping - acceptors or donators - nor between the dopant atoms, for example, silicon (Si) or carbon (C).

For the ternary alloy $\mathrm{Al}_x\mathrm{Ga}_{1-x}\mathrm{As}$ the electron mobility rapidly varies with the concentration around a value of $x \approx 0.4$, since the semiconductor changes from a direct to an indirect bandgap and the effective electron mass increases significantly. To adequately reproduce this dependence a more complex interpolation scheme for the electron mobility parameters $\mu_{n,\max,T_0}, N_{n,\mathrm{ref},T_0}, \alpha_n, \beta_n$ and γ_n is employed. The value for $\mu_{n,\min}$ is calculated as proposed by Daubenschuez [130] with $x_0 = 0.45$

$$\mu_{n,\min} = \begin{cases} \mu_{n,\min}^{\mathrm{GaAs}} + (\mu_{n,\min,x_0} - \mu_{n,\min}^{\mathrm{GaAs}}) \frac{x}{x_0} & \text{if } x < x_0. \\ \mu_{n,\min,x_0} + (\mu_{n,\min}^{\mathrm{InAs}} - \mu_{n,\min,x_0}) \frac{x-x_0}{1-x_0} & \text{else.} \end{cases} \tag{A.11}$$

Based on [131, 130] $\mu_{n,\max}$ is determined with the quadratic dependence given in Tb. A.5. Sotoodeh suggests interpolation formulas of the form

$$N_{n,\mathrm{ref}} = \left(N_{n,\mathrm{ref}}^{\mathrm{GaAs}}\right)^{1-x} \left(N_{n,\mathrm{ref}}^{\mathrm{AlAs}}\right)^{x} \tag{A.12}$$

and

$$\beta_{n/p} = \frac{(1-x)\beta_{n/p}^{\mathrm{GaAs}} + x\beta_{n/p}^{\mathrm{AlAs}}}{1+x(1-x)} \tag{A.13}$$

and linear interpolation for γ_n and α_n. For the parameters $\mu_{p,\min}$, $\mu_{p,\max}$, $N_{p,\mathrm{ref}}$, α_p quadratical interpolation between AlAs, GaAs and $\mathrm{Al}_{x_0}\mathrm{G}_{1-x_0}\mathrm{C}$ is used to obtain the values for $\mathrm{Al}_x\mathrm{Ga}_{1-x}\mathrm{As}$. For $\gamma_p = \gamma_p^{\mathrm{GaAs}}$ the GaAs value is inserted. Sotoodeh [128]

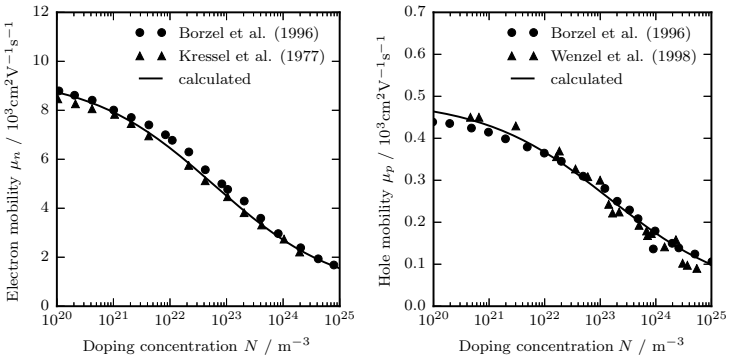

FIGURE A.2: Electron (left) and hole (right) mobility for binary alloy GaAs calculated after [128]. The markers indicate experimental values taken from literature [132] and [133] as references.

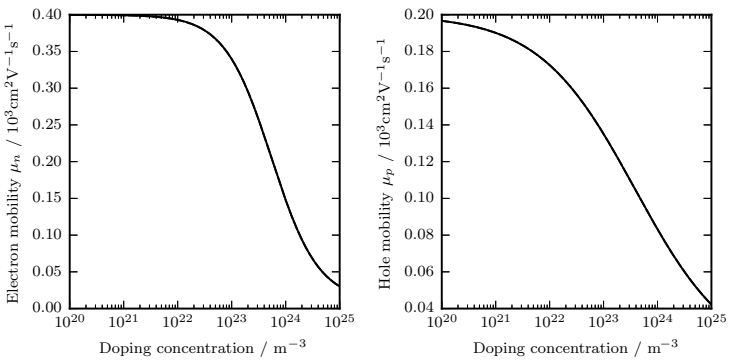

FIGURE A.3: Electron (left) and hole (right) mobility for binary alloy AlAs calculated after [128].

defines an interpolation scheme for the mobility parameters of $\mathrm{In}_x\mathrm{Ga}_{1-x}\mathrm{As}$ based on given values for $\mathrm{In}_{0.53}\mathrm{Ga}_{0.47}\mathrm{As}$. To determine the values for $N_{\mathrm{ref},n/p}$ the logarithm of $N_{\mathrm{ref},n/p}$ is quadratically interpolated using the values of InAs, GaAs and $\mathrm{In}_{0.53}\mathrm{Ga}_{0.47}\mathrm{As}$ with (C.118). The parameter $\gamma_p = \gamma_p^{\mathrm{GaAs}}$ is set to the value of GaAs. Other parameters are quadratically interpolated utilizing the values given for $x = 0.53$. Finally, (A.8) is employed to calculate the mobility.

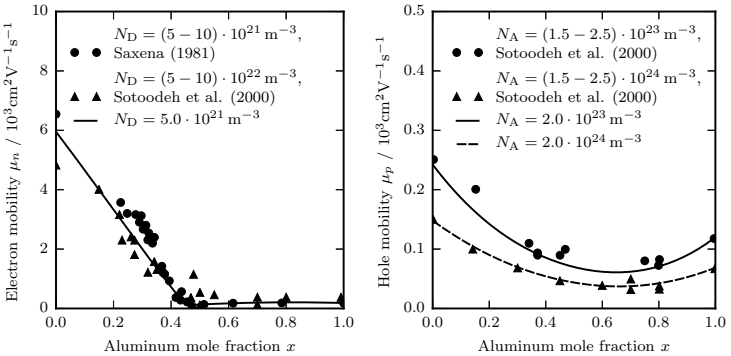

FIGURE A.4: Electron (left) and hole (right) mobility for ternary alloy $\mathrm{Al}_x\mathrm{Ga}_{1-x}\mathrm{As}$ in dependence of the aluminum concentration. The values are calculated after [128] with the interpolation scheme taken from [130]. As references experimental values are indicated by markers taken from [134] and [128] for electron mobility and form [128] for hole mobility.

A.4 Permittivity

To predict the relative permittivity for the ternary alloy $\mathrm{Al}_x\mathrm{Ga}_{1-x}\mathrm{As}$ in dependence of the mole fraction x of the compound, the temperature T and the wavelength λ, the models presented by Gehrsitz [115] or Adachi [80] are utilized. Adachi's model can also be employed for $\mathrm{In}_x\mathrm{Ga}_{1-x}\mathrm{As}$.

In Gehrsitz's model the coefficients A, C_i and B_i are extracted as fitting parameters from experimental measurements as presented in [115] to approximate the relative permittivity based on Sellmeier's equation [135]

$$\varepsilon_\mathrm{r}(\lambda) = n^2(\lambda) = A + \sum_{i=1}^{N} \frac{B_i}{1 - \frac{C_i}{\lambda^2}}. \tag{A.14}$$

The coefficients A and B_i are dimensionless, and C_i are in units m^2. Gehrsitz utilizes a total of $N = 4$ poles to match the dispersion characteristics of $\mathrm{Al}_x\mathrm{Ga}_{1-x}\mathrm{As}$.

An alternative model is presented by Adachi [80], where the refractive index of a zinc-blende material below the direct bandgap is expressed due to a simplified interband-transition model. According to [80] for $\mathrm{Al}_x\mathrm{Ga}_{1-x}\mathrm{As}$ the approximation of the relative permittivity is

$$\varepsilon_\mathrm{r}(\lambda, T) = A_\mathrm{Ad} \cdot \left(f(\chi) + \frac{1}{2} f(\chi_\mathrm{SO}) \cdot \left(\frac{E_0}{E_0 + \Delta_0} \right)^{\frac{3}{2}} \right) + B_\mathrm{Ad} \tag{A.15}$$

with

$$\chi = \frac{hc}{\lambda E_0},$$
$$\chi_{\mathrm{SO}} = \frac{hc}{\lambda\left(E_0 + \Delta_{\mathrm{SO}}\right)},$$
$$f\left(\chi\right) = \frac{2 - \sqrt{1+\chi} - \sqrt{1-\chi}}{\chi^2}. \tag{A.16}$$

The parameters are the split-off energy Δ_{SO} and the direct bandgap energy E_0. Parameters A_{Ad} and B_{Ad} are linear interpolated for ternary alloys.

As an alternative to Adachi's model the refractive index for the ternary alloy $\mathrm{In}_x\mathrm{Ga}_{1-x}\mathrm{As}$ can be calculated based on Sellmeier's equation (A.14) with the modified parameter [136]

$$C_0 = \left(\frac{C_{\mathrm{InGaAs}} E_{\mathrm{g,GaAs}}(T)}{E_{\mathrm{g,InGaAs}}(T)}\right)^2. \tag{A.17}$$

The parameters for Sellmeier's equation are $A = 8.950$, $B_0 = 2.054$, $C_{\mathrm{InGaAs}} = 0.6245 \cdot 10^{-6}\,\mathrm{m}$. The calculated refractive index of $\mathrm{In}_x\mathrm{Ga}_{1-x}\mathrm{As}$ for wavelengths between 900 and 1200 nm and concentration between 0 and 0.25 is displayed in Fig. A.5.

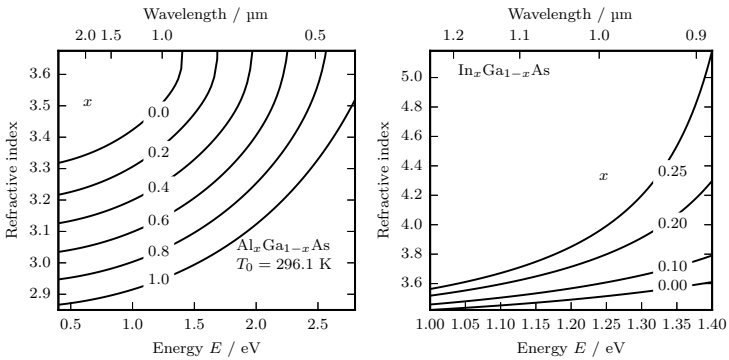

FIGURE A.5: Refractive index of $\mathrm{Al}_x\mathrm{Ga}_{1-x}\mathrm{As}$, calculated according to [115] (left) and $\mathrm{In}_x\mathrm{Ga}_{1-x}\mathrm{As}$, calculated according to [136] (right) dependent on wavelength and mole fractions.

A.5 Photo-Elastic Coefficients

The approximation of the photo-elastic coefficients (either $P_{11} - P_{12}$ or P_{44}) based on the wavelength λ are calculated according to Adachi [80]. The model is applied to calculate the properties for GaAs, AlAs, InAs, $\mathrm{Al}_x\mathrm{Ga}_{1-x}\mathrm{As}$ and $\mathrm{In}_x\mathrm{Ga}_{1-x}\mathrm{As}$.

$$\alpha_\mu(\lambda) = C_\mu(x)\left(-g(\chi) + \frac{4E_0}{\Delta_{\mathrm{SO}}}\left(f(\chi) - f(\chi_{\mathrm{SO}})\left(\frac{E_0}{E_0 + \Delta_{\mathrm{SO}}}\right)^{3/2}\right)\right) + D_\mu(x), \tag{A.18}$$

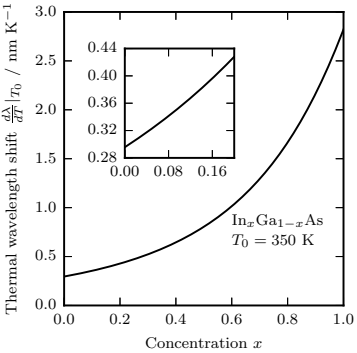

FIGURE A.6: Linearized thermal wavelength shift of $\mathrm{In}_x\mathrm{Ga}_{1-x}\mathrm{As}$ dependent on Indium concentration. Typical ranges of Indium concentrations for wavelengths around 1 µm are shown in inlet.

where μ is either $\langle 100 \rangle$ or $\langle 111 \rangle$ to calculate $p_{\langle 100 \rangle} = P_{11} - P_{12}$ or $p_{\langle 111 \rangle} = P_{44}$ with $S_{\langle 100 \rangle} = S_{11} - S_{12}$ or $S_{\langle 111 \rangle} = S_{44}$. The coefficients are related via

$$p_\mu(\lambda) = -\frac{\alpha_\mu(\lambda)}{\varepsilon_\mathrm{r}^2(\lambda) S_\mu} \tag{A.19}$$

and

$$\chi = \frac{hc_0}{\lambda E_0}, \tag{A.20}$$

$$\chi_\mathrm{SO} = \frac{hc_0}{\lambda (E_0 + \Delta_\mathrm{SO})}, \tag{A.21}$$

$$f(\chi) = \chi^{-2} \left(2 - (1+\chi)^{\frac{1}{2}} - (1-\chi)^{\frac{1}{2}} \right), \tag{A.22}$$

$$g(\chi) = \chi^{-2} \left(2 - (1+\chi)^{-\frac{1}{2}} - (1-\chi)^{-\frac{1}{2}} \right), \tag{A.23}$$

with vacuum wavelength λ in meter, the experimental parameter C_μ in $\mathrm{m^2N^{-1}}$, experimental parameter D_μ in $\mathrm{m^2N^{-1}}$, energy of direct band-gap E_0 in Joule, split-off energy Δ_SO in Joule, frequency depended relative permittivity ε_r (without perturbation), elastic compliance component S_μ in $\mathrm{m^2N^{-1}}$, speed of light in vacuum c_0 and the Planck constant h. For ternary alloys the parameters C_μ and D_μ are linear interpolated between the values of the two binary alloys.

A.6 Thermal Conductivity

The thermal conductivity k_T is given in units $\mathrm{W\,m^{-1}\,K^{-1}}$. Temperature dependent thermal conductivity is determined with an exponential temperature dependence

$$k_T(T) = k_{T_0} \cdot \left(\frac{T}{T_0} \right)^{a_k} \tag{A.24}$$

based on the value given at $T_0 = 300\,\mathrm{K}$. For alloys $\mathrm{A}_{1-x}\mathrm{B}_x$ the conductivity is determined based on the interpolation scheme

$$k_{AB,300} = \left(\frac{1-x}{k_{A,300}} + \frac{x}{k_{B,300}} + \frac{(1-x)x}{C_k} \right)^{-1}, \tag{A.25}$$

where C_{k_T} is the thermal conductivity bowing factor for ternary compounds in $\mathrm{W\,m^{-1}\,K^{-1}}$ and a_k is the exponent for temperature dependence of thermal conductivity. The exponent is linear interpolated between the values for the two compounds. See [125] for more details on thermal conductivity. For $\mathrm{Al}_x\mathrm{Ga}_{1-x}\mathrm{As}$ the thermal conductivity is minimal around $x = 0.5$, see Fig A.7.

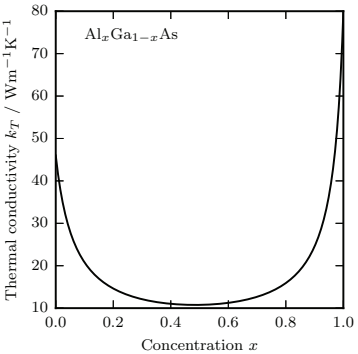

FIGURE A.7: Thermal conductivity of $\mathrm{Al}_x\mathrm{Ga}_{1-x}\mathrm{As}$ calculated based on parameters from Tb. A.3, Tb. A.1 and Tb. A.5.

A.7 Material parameters

Parameter	Symbol	Value	Unit	Reference
Static rel. permittivity	$\varepsilon_{\mathrm{r,s}}$	13.18		[80]
Relative permittivity	ε_{r}	10.89		[80]
Free-carrier abs. cross sec.	$\sigma_{\mathrm{fc},n}$	$3 \cdot 10^{-22}$	m^2	[43, 44]
Free-carrier abs. cross sec.	$\sigma_{\mathrm{fc},p}$	$7 \cdot 10^{-22}$	m^2	[43, 44]
Thermal conductivity	k_{T_0}	46	$\mathrm{Wm^{-1}K^{-1}}$	[91]
CTE	α_T	6.86	$1 \cdot 10^{-6}\,\mathrm{K}$	[137]
Thermal cond. inter. exp.	a_k	-1.25		[125]
Bandgap energy	$E_{\mathrm{g},0,\Gamma}$	1.519	eV	[126]
	α_Γ	$0.5405 \cdot 10^{-3}$	$\mathrm{eV\,K^{-1}}$	[126]
	β_Γ	204	K	[126]

TABLE A.1: Material parameters for GaAs.

Parameter	Symbol	Value	Unit	Reference
Bandgap energy	$E_{\mathrm{g},0,X}$	1.981	eV	[126]
	α_X	$0.460 \cdot 10^{-3}$	$\mathrm{eV\,K^{-1}}$	[126]
	β_X	204	K	[126]
	$E_{\mathrm{g},0,L}$	1.815	eV	[126]
	α_L	$0.605 \cdot 10^{-3}$	$\mathrm{eV\,K^{-1}}$	[126]
	β_L	204	K	[126]
Lattice constant	a_0	$5.65325 \cdot 10^{-10}$	m	[126]
Interband matrix element	E_{P}	28.8	eV	[126]
Effective mass electrons	$m_{\mathrm{c,r}}/m_{\mathrm{el}}$	0.067		[126]
Eff. DOS electrons	N_{c,T_0}	$4.7 \cdot 10^{23}$	$\mathrm{m^{-3}}$	[138]
Eff. DOS holes	N_{v,T_0}	$9.0 \cdot 10^{24}$	$\mathrm{m^{-3}}$	[138]
Luttinger parameters	γ_1	6.98		[126]
	γ_2	2.06		[126]
	γ_3	2.93		[126]
Spin-orbit split-off energy	Δ_{SO}	0.341	eV	[126]
Stiffness constants	C_{11}	122.1	GPa	[126]
	C_{12}	56.6	GPa	[126]
	C_{44}	60.0	GPa	[126]
Deformation potentials	a_c	-7.17	eV	[126]
	a_v	1.16	eV	[126]
	b	-2.0	eV	[126]
	d	-4.8	eV	[126]
Electron mobility	$\mu_{n,\max,T_0}$	9400	$\mathrm{cm^2V^{-1}s^{-1}}$	[128]
	$\mu_{n,\min}$	500	$\mathrm{cm^2V^{-1}s^{-1}}$	[128]
	N_{n,ref,T_0}	$0.6 \cdot 10^{23}$	$\mathrm{m^{-3}}$	[128]
	α_n	0.394		[128]
	β_n	2.1		[128]
	γ_n	3.0		[128]
Hole mobility	$\mu_{p,\max,T_0}$	491.5	$\mathrm{cm^2V^{-1}s^{-1}}$	[128]
	$\mu_{p,\min}$	20	$\mathrm{cm^2V^{-1}s^{-1}}$	[128]
	N_{p,ref,T_0}	$1.48 \cdot 10^{23}$	$\mathrm{m^{-3}}$	[128]
	α_p	0.38		[128]
	β_p	2.2		[128]
	γ_p	3.0		[128]
Permittivity coeff.	A_{Ad}	6.3		[80]
	B_{Ad}	9.4		[80]
Photo-elastic coeff.	$C_{\langle 100\rangle}$	$-0.46 \cdot 10^{-10}$		[80]
	$C_{\langle 111\rangle}$	$-0.21 \cdot 10^{-10}$		[80]
	$D_{\langle 100\rangle}$	$2.22 \cdot 10^{-10}$		[80]
	$D_{\langle 111\rangle}$	$2.12 \cdot 10^{-10}$		[80]
Photo-elastic parameters	P_{11}	-0.165		[80]
	P_{12}	-0.140		[80]
	P_{44}	-0.072		[80]

TABLE A.2: Material parameters for GaAs (continued). For the recombination rate parameters τ_{nr}, B_{sp} and $C_{n/p}$ for electrical simulations the values for GaAs are taken from AlGaAs.

Parameter	Symbol	Value	Unit	Reference
Static rel. permittivity	$\varepsilon_{\mathrm{r,s}}$	10.06		[80, 128]
Relative permittivity	ε_{r}	8.16		[80, 128]
Thermal conductivity	k_{T_0}	80	$\mathrm{W m^{-1} K^{-1}}$	[125]
Thermal cond. inter. exp.	a_k	-1.37		[125]
Bandgap energy	$E_{\mathrm{g},0,\Gamma}$	3.099	eV	[126]
	α_Γ	$0.885 \cdot 10^{-3}$	$\mathrm{eV\,K^{-1}}$	[126]
	β_Γ	530	K	[126]
	$E_{\mathrm{g},0,X}$	2.24	eV	[126]
	α_X	$0.70 \cdot 10^{-3}$	$\mathrm{eV\,K^{-1}}$	[126]
	β_X	530	K	[126]
	$E_{\mathrm{g},0,L}$	2.46	eV	[126]
	α_L	$0.605 \cdot 10^{-3}$	$\mathrm{eV\,K^{-1}}$	[126]
	β_L	204	K	[126]
Lattice constant	a_0	$5.6611 \cdot 10^{-10}$	m	[126]
Interband matrix element	E_{P}	21.1	eV	[126]
Effective mass of electrons	$m_{c,\Gamma}/m_{\mathrm{el}}$	0.15		[126]
Luttinger parameters	γ_1	3.76		[126]
	γ_2	0.82		[126]
	γ_3	1.42		[126]
Spin-orbit split-off energy	Δ_{SO}	0.28	eV	[126]
Stiffness constants	C_{11}	125.0	GPa	[126]
	C_{12}	53.4	GPa	[126]
	C_{44}	54.2	GPa	[126]
Deformation potentials	a_c	-5.64	eV	[126]
	a_v	2.47	eV	[126]
	b	-2.3	eV	[126]
	d	-3.4	eV	[126]
Electron mobility	$\mu_{n,\max,T_0}$	400	$\mathrm{cm^2 V^{-1} s^{-1}}$	[128]
	$\mu_{n,\min}$	10	$\mathrm{cm^2 V^{-1} s^{-1}}$	[128]
	N_{n,ref,T_0}	$5.46 \cdot 10^{23}$	$\mathrm{m^{-3}}$	[128]
	α_n	1.00		[128]
	β_n	2.1*		
	γ_n	3.0*		
Hole mobility	$\mu_{p,\max,T_0}$	200	$\mathrm{cm^2 V^{-1} s^{-1}}$	[128]
	$\mu_{p,\min}$	10	$\mathrm{cm^2 V^{-1} s^{-1}}$	[128]
	N_{p,ref,T_0}	$3.84 \cdot 10^{23}$	$\mathrm{m^{-3}}$	[128]
	α_p	0.488		[128]
	β_p	2.24		[128]
	γ_p	3.0		[128]
Photo-elastic coeff.	$C_{\langle 100\rangle}$	$-0.04 \cdot 10^{-10}$		[80]
	$C_{\langle 111\rangle}$	$-0.02 \cdot 10^{-10}$		[80]
	$D_{\langle 100\rangle}$	$0.17 \cdot 10^{-10}$		[80]
	$D_{\langle 111\rangle}$	$0.17 \cdot 10^{-10}$		[80]
Permittivity coeff.	A_{Ad}	25.3		[80]
	B_{Ad}	-0.8		[80]

Table A.3: Material parameters for AlAs. *Value is taken from material GaAs from Tb. A.1 since no reference is found in literature.

Parameter	Symbol	Value	Unit	Reference
Static rel. permittivity	$\varepsilon_{\mathrm{r,s}}$	15.15		[128]
Relative permittivity	ε_{r}	12.25		[128]
Thermal conductivity	k_{T_0}	27.3	$\mathrm{Wm^{-1}K^{-1}}$	[125]
Thermal cond. inter. exp.	a_k	-1.1		[125]
Bandgap energy	$E_{\mathrm{g},0,\Gamma}$	0.417	eV	[126]
	α_Γ	$0.276 \cdot 10^{-3}$	$\mathrm{eV\,K^{-1}}$	[126]
	β_Γ	93	K	[126]
	$E_{\mathrm{g},0,X}$	1.433	eV	[126]
	α_X	$0.276 \cdot 10^{-3}$	$\mathrm{eV\,K^{-1}}$	[126]
	β_X	93	K	[126]
	$E_{\mathrm{g},0,L}$	1.133	eV	[126]
	α_L	$0.276 \cdot 10^{-3}$	$\mathrm{eV\,K^{-1}}$	[126]
	β_L	93	K	[126]
Lattice constant	a_0	$6.0583 \cdot 10^{-10}$	m	[126]
Interband matrix element	E_{P}	21.5	eV	[126]
Effective mass of electrons	$m_{\mathrm{c},\Gamma}/m_{\mathrm{el}}$	0.026		[126]
Luttinger parameters	γ_1	20.0		[126]
	γ_2	8.5		[126]
	γ_3	9.2		[126]
Spin-orbit split-off energy	Δ_{SO}	0.39	eV	[126]
Stiffness constants	C_{11}	83.3	GPa	[126]
	C_{12}	45.3	GPa	[126]
	C_{44}	39.6	GPa	[126]
Deformation potentials	a_c	-5.08	eV	[126]
	a_v	1.00	eV	[126]
	b	-1.8	eV	[126]
	d	-3.6	eV	[126]
Electron mobility	$\mu_{n,\max,T_0}$	34000	$\mathrm{cm^2V^{-1}s^{-1}}$	[128]
	$\mu_{n,\min}$	1000	$\mathrm{cm^2V^{-1}s^{-1}}$	[128]
	N_{n,ref,T_0}	$11.0 \cdot 10^{23}$	$\mathrm{m^{-3}}$	[128]
	α_n	0.32		[128]
	β_n	1.57		[128]
	γ_n	3.0		[128]
Hole mobility	$\mu_{p,\max,T_0}$	530	$\mathrm{cm^2V^{-1}s^{-1}}$	[128]
	$\mu_{p,\min}$	20	$\mathrm{cm^2V^{-1}s^{-1}}$	[128]
	N_{p,ref,T_0}	$1.1 \cdot 10^{23}$	$\mathrm{m^{-3}}$	[128]
	α_p	0.46		[128]
	β_p	2.3		[128]
	γ_p	3.0		[128]
Photo-elastic coeff.	$C_{\langle 100\rangle}$	$-2.58 \cdot 10^{-10}$		[80]
	$C_{\langle 111\rangle}$	$-1.48 \cdot 10^{-10}$		[80]
	$D_{\langle 100\rangle}$	$2.19 \cdot 10^{-10}$		[80]
	$D_{\langle 111\rangle}$	$2.32 \cdot 10^{-10}$		[80]
Permittivity coeff.	A_{Ad}	4.36		[82]
	B_{Ad}	10.52		[82]

Table A.4: Material parameters for InAs.

Parameter	Symbol	Value	Unit	Reference
Static rel. permittivity	$\varepsilon_{\mathrm{r,s}}$	$12.90 - 2.84x$		[136]
Relative permittivity	ε_{r}	$10.919 - 3.33x$ $+0.576x^2$		[115]
Cond. band offset ratio**	$c_{\Delta E_c}$	0.67		[139]
Bowing parameters	$C_{E_{\mathrm{g},\Gamma}}$	$-0.127 + 1.310x$	eV	[126]
	$C_{E_{\mathrm{g},X}}$	0.055	eV	[126]
Eff. DOS conduction band				
	C_{k_T}	3.3		[125]
$x < 0.41$	N_{c,T_0}	$3.96 \cdot 10^{23}$	m^{-3}	[138]
	$c_{\mathrm{c},T_0,1}$	1.317		[138]
	$c_{\mathrm{c},T_0,2}$	0		[138]
$x \geq 0.41$	N_{c,T_0}	$1.96 \cdot 10^{25}$	m^{-3}	[138]
	$c_{\mathrm{c},T_0,1}$	-0.165		[138]
	$c_{\mathrm{c},T_0,2}$	0		[138]
Eff. DOS valence band	N_{v,T_0}	$9.12 \cdot 10^{24}$	m^{-3}	[138]
	$c_{\mathrm{v},T_0,1}$	0.490		[138]
	$c_{\mathrm{v},T_0,2}$	0		[138]
Electron mobility				
$x \leq 0.3$	$\mu_{n,\max,T_0}$	$1 - 2.2x + 0.8x^2$	$\mathrm{cm}^2\mathrm{V}^{-1}\mathrm{s}^{-1}$	[131, 130]
$x > 0.3$	$\mu_{n,\max,T_0}$	$-0.025 + 0.116x$ $-0.0720x^2$	$\mathrm{cm}^2\mathrm{V}^{-1}\mathrm{s}^{-1}$	[131, 130]
Hole mobility*	$\mu_{p,\max,T_0}$	240	$\mathrm{cm}^2\mathrm{V}^{-1}\mathrm{s}^{-1}$	[128]
	$\mu_{p,\min}$	5	$\mathrm{cm}^2\mathrm{V}^{-1}\mathrm{s}^{-1}$	[128]
	N_{p,ref,T_0}	$1.0 \cdot 10^{23}$	m^{-3}	[128]
	α_p	0.324		[128]
	β_p			[128]
	γ_p			[128]
Non-radiative lifetime	$\tau_{n/p}$	1	ns	[98]
Spontaneous-emission coeff.	B_{sp}	$2 \cdot 10^{-16}$	$\mathrm{m}^3\mathrm{s}^{-1}$	[94]
Auger recombination	$C_{n/p}$	$2.1 \cdot 10^{-42}$	$\mathrm{m}^6\mathrm{s}^{-1}$	[94]

TABLE A.5: Material parameters for $\mathrm{Al}_x\mathrm{Ga}_{1-x}\mathrm{As}$. *Mobility values are given for $x = 0.3$. **Band edge offset ratios ranging from 0.62 to 0.88 eV are reported in [140]. All parameters without given bowing parameter or special interpolation scheme are linear interpolated between values of AlAs and GaAs.

Parameter	Symbol	Value	Unit	Reference
Static rel. permittivity	$\varepsilon_{\mathrm{r,s}}$	$12.9 + 1.53x$ $0.67x^2$		[128]
Relative permittivity	ε_{r}	$10.9 + 1.4x$		[128]
Cond. band offset ratio***	$c_{\Delta E_c}$	0.67		
Bowing parameters	$C_{E_{\mathrm{g},\Gamma}}$	0.477	eV	[126]
	$C_{E_{\mathrm{g},X}}$	1.4	eV	[126]
	$C_{E_{\mathrm{g},L}}$	0.33	eV	[126]
	$C_{\Delta_{\mathrm{SO}}}$	0.15	eV	[126]
	$C_{\gamma_3-\gamma_2}$	0.481		[126]
	C_{E_P}	-1.48	eV	[126]
	C_F	1.77		[126]
	C_{a_c}	2.61	eV	[126]
	C_{k_T}	1.4		[125]
Eff. DOS	N_{C,T_0}	$3.96 \cdot 10^{23}$	m^{-3}	[127]
	$c_{\mathrm{C},T_0,1}$	-0.683		[127]
	$c_{\mathrm{C},T_0,2}$	0.0476		[127]
Eff. DOS	N_{V,T_0}	$4.32 \cdot 10^{24}$	m^{-3}	[127]
	$c_{\mathrm{V},T_0,1}$	0.32		[127]
	$c_{\mathrm{V},T_0,2}$	0		[127]
Electron mobility*	$\mu_{n,\max,T_0}$	14000	$\mathrm{cm}^2\mathrm{V}^{-1}\mathrm{s}^{-1}$	[128]
	$\mu_{n,\min}$	300	$\mathrm{cm}^2\mathrm{V}^{-1}\mathrm{s}^{-1}$	[128]
	N_{n,ref,T_0}	$1.3 \cdot 10^{23}$	m^{-3}	[128]
	α_n	0.48		[128]
	β_n	1.59		[128]
	γ_n	3.68		[128]
Hole mobility*	$\mu_{p,\max,T_0}$	320	$\mathrm{cm}^2\mathrm{V}^{-1}\mathrm{s}^{-1}$	[128]
	$\mu_{p,\min}$	10	$\mathrm{cm}^2\mathrm{V}^{-1}\mathrm{s}^{-1}$	[128]
	N_{p,ref,T_0}	$4.9 \cdot 10^{23}$	m^{-3}	[128]
	α_p	0.403		[128]
	β_p	1.59		[128]
	γ_p**	3.0		[128]

TABLE A.6: Material parameters for $\mathrm{In}_x\mathrm{Ga}_{1-x}\mathrm{As}$. *Mobility values are given for $x = 0.53$. **Value from GaAs. ***Band edge offset ratios ranging from 0.36 to 0.83 eV are reported in [140], however the ratio from AlGaAs is taken. All parameters without given bowing parameter or special interpolation scheme are linear interpolated between values of InAs and GaAs.

Parameter	Symbol	Value	Unit	Reference
Thermal conductivity	k_{T_0}	195	$\mathrm{Wm^{-1}K^{-1}}$	[141]
Thermal cond. inter. exp.	a_k	0		
CTE	α_T	6.5 (6.4)	$1 \cdot 10^{-6}\,\mathrm{K^{-1}}$	[142, 143], ([141])
Young's modulus	E	330	GPa	[142, 141]
Poisson's ratio	ν	0.24		
Stiffness constants	C_{11}	389	GPa	
	C_{12}	123	GPa	
	C_{44}	133	GPa	

TABLE A.7: Material parameters for CuW with 90 % tungsten. The Stiffness constants are calculated from Young's modulus and Poisson's ratio. Values in brackets are alternative values reported in literature.

Parameter	Symbol	Value	Unit	Reference
Thermal conductivity	k_{T_0}	57	$\mathrm{Wm^{-1}K^{-1}}$	[144, 145]
Thermal cond. inter. exp.	a_k	0		
CTE	α_T	13.9	$1 \cdot 10^{-6}\,\mathrm{K^{-1}}$	[144]
Young's modulus	E	59	GPa	[144]
Poisson's ratio	ν	0.4		[144]
Stiffness constants	C_{11}	126	GPa	
	C_{12}	84	GPa	
	C_{44}	21	GPa	
Solidification temperature*	T_s	280	°C	[10]

TABLE A.8: Material parameters for AuSn (80/20). The Stiffness constants are calculated from Young's modulus and Poisson's ratio. *The mechanical package bonds at solidification temperature and cools down to room temperature so that a temperature difference of $\Delta T_\mathrm{s} = 255\,\mathrm{K}$ results.

Parameter	Symbol	Value	Unit	Reference
Thermal conductivity	k_{T_0}	315 (318)	$\mathrm{Wm^{-1}K^{-1}}$	[146] ([145])
Thermal cond. inter. exp.	a_k	0		
CTE	α_T	14.2	$1 \cdot 10^{-6}\,\mathrm{K^{-1}}$	[147, 148]
Young's modulus	E	79	GPa	[149]
Poisson's ratio	ν	0.4 (0.42)		[149] ([148])
Stiffness constants	C_{11}	169	GPa	
	C_{12}	113	GPa	
	C_{44}	28	GPa	

TABLE A.9: Material parameters for Gold. The Stiffness constants are calculated from Young's modulus and Poisson's ratio. Values in brackets are alternative values reported in literature.

Parameter	Symbol	Value	Unit	Reference
Thermal conductivity	k_{T_0}	18.5	$\mathrm{Wm^{-1}K^{-1}}$	[]
Thermal cond. inter. exp.	a_k	0.33		
CTE	α_T	3.3 (3.0)	$1 \cdot 10^{-6}\,\mathrm{K^{-1}}$	[150] ([148])
Young's modulus	E	310 (150)	GPa	[150] ([148])
Poisson's ratio	ν	0.27 (0.3)		[150] ([148])
Stiffness constants	C_{11}	387	GPa	
	C_{12}	143	GPa	
	C_{44}	122	GPa	

Table A.10: Material parameters for SiN. The Stiffness constants are calculated from Young's modulus and Poisson's ratio.

Parameter	Symbol	Value	Unit	Reference
Thermal conductivity	k_{T_0}	400 (394, 398)	$\mathrm{Wm^{-1}K^{-1}}$	([151], [144])
Thermal cond. inter. exp.	a_k	0		
CTE	α_T	16.5 (16.8)	$1 \cdot 10^{-6}\,\mathrm{K^{-1}}$	[152] ([151])
Young's modulus	E	110 (114)	GPa	[151] ([144])
Poisson's ratio	ν	0.34 (0.33)		[151] ([144])
Stiffness constants	C_{11}	169	GPa	
	C_{12}	87	GPa	
	C_{44}	41	GPa	

Table A.11: Material parameters for Cu. The Stiffness constants are calculated from Young's modulus and Poisson's ratio.

Parameter	Symbol	Value	Unit	Reference
Thermal conductivity	k_{T_0}	230* (160)	$\mathrm{Wm^{-1}K^{-1}}$	([144])
Thermal cond. inter. exp.	a_k	0		
CTE	α_T	4.5 (4.4)	$1 \cdot 10^{-6}\,\mathrm{K^{-1}}$	[150] ([144])
Young's modulus	E	330	GPa	[150, 144]
Poisson's ratio	ν	0.24 (0.31)		[150] ([144])
Stiffness constants	C_{11}	389	GPa	
	C_{12}	123	GPa	
	C_{44}	133	GPa	

Table A.12: Material parameters for AlN. The Stiffness constants are calculated from Young's modulus and Poisson's ratio. *Value is supplied by vendor.

Appendix B

Finite-Differences Discretization with Box-Integration

In this chapter, a finite-difference discretization scheme with box integration on structured unregular meshes is presented. The scheme is developed for differential operators up to the second order. It is applied to transform sets of linear partial differential equations with first and (mixed) second-order partial derivatives on structures with spatial varying material values into algebraic equations. The expressions result in (sparse) matrix-vector equations for the solution vector. This solution vector contains the approximations to the fields values at the location of the mesh knots. The sparse matrix system is solved with standard linear algebra libraries, for example, *SciPy* [153], or more sophisticated solvers which utilize a massive parallel implementation on GPUs like *MAGMA* [107] and reduce the computation time significantly. The *MAGMA* toolbox is a library written in *C++* and builts onto the *NVIDIA CUDA* [154] framework to accelerate matrix and vector operations, for dense and sparse matrices and offers iterative solvers for sparse matrix equations. To seamlessly integrate the *MAGMA* library to the *Python* code an interface library, *pymagma* [123], has been written and published by the author. This package is developed to provide a python interface to GPU accelerated matrix and vector operations - especially the *sparse-iter* functions from *MAGMA*. It provides easy access to iterative sparse solvers on the GPU. Therefore, two classes *magma_matrix* and *magma_vector* are implemented. Objects of these classes can be created with a *SciPy* sparse matrix or *NumPy* array, and the class can be used to transfer a *MAGMA* matrix to the GPU memory space and internally call functions corresponding to the present data types (complex and real numbers for both 32- and 64-bit floating point numbers). The library handles the transfer of data and function-calls between *Python* and the *C++* code. To discretize differential operators of second order the box-integration method, a finite-volume method, based on the finite-differences approximation, is used [31]. The main difference compared to the standard FDM schemes is that the operators are not directly discretized, but instead, the operators are averaged by integration over a control volume, a cell of the mesh. The remaining derivatives are discretized with the FDM in the next step. The benefit of this box-integration method is that flux densities are conserved even if material values have discontinuous jumps at interfaces [31]. The application of the box-integration scheme for multi-band $k \cdot p$ Schrödinger equations is presented and discussed in [31]. The notation used for the scheme in this thesis is mainly adopted from [31].

The general form of a coupled set of N linear partial differential equations of second order with inhomogeneous coefficients is a matrix equation

$$\sum_{\nu} \hat{H}^{\mu\nu}(\vec{x})\,\psi^{\nu}(\vec{x}) = b^{\mu}(\vec{x}), \tag{B.1}$$

with the components of the solution vector ψ^{ν} and the components of a *source* vector b^{μ}. The indices run over all components $\mu,\nu = 0,1,\ldots,N-1$ with the total number of the components N. The terms of the differential matrix-operator $\hat{H}^{\mu\nu}(\vec{x})$ are separated with respect to the orders of the derivatives

$$\hat{H}^{\mu\nu}(\vec{x}) = \sum_{i,j=1}^{d} \partial_i \tilde{H}_{ij}^{\mu\nu}(\vec{x})\,\partial_j + \sum_{i=1}^{d}\left[\partial_i \tilde{H}_{i\rightarrow}^{\mu\nu}(\vec{x}) + \tilde{H}_{i\leftarrow}^{\mu\nu}(\vec{x})\,\partial_i\right] + \tilde{H}_{0}^{\mu\nu}(\vec{x}) \tag{B.2}$$

for a d dimensional space. The matrices for the coefficients $\tilde{H}_{ij}^{\mu\nu}, \tilde{H}_{i\rightarrow}^{\mu\nu}, \tilde{H}_{i\leftarrow}^{\mu\nu}, \tilde{H}_{0}^{\mu\nu}$ with $i,j = 0,1,\cdots,d-1$ contain the spatially varying parameters and in the context of physical equations are also entitled as material parameters. Due to the general formulation of the presented scheme for the numerical solution of the system of differential equations, it can be applied to a variety of physical problems which can be written in the form (B.1). In the scope of this work, it is utilized to solve the $k\cdot p$ Schrödinger equation for semiconductor nanostructures and perform the TD or FD optical calculations. Besides, it can be applied to solve the equations of continuum mechanics (see Chapter 5) or the thermal diffusion equation (see Chapter 3).

B.1 Structured Unregular Meshes

The FDM scheme is applied to a structured unregular mesh. The mesh knots in a structured unregular mesh are arranged in the form of a grid so that the cells of the mesh are rectangular cubes and the knot can have variable distances along each direction. For a d-dimensional structured grid each point with coordinates $\vec{x} = (x_0, x_1, \cdots, x_{d-1})^{\mathrm{T}}$ is uniquely identifiable through a vector containing d indices $\vec{n} = (n_0, n_1, \cdots, n_{d-1})^{\mathrm{T}}$. A mesh with d dimensions is defined through points with coordinates $X_j^{(i)}$ with $i = 0,1,\ldots,d-1, \quad j = 0,1,\ldots,N_i-1$, where N_i is the number of grid knots along direction i. Based on this definition, the vector of coordinates $\vec{x}(\vec{n})$ of the knot with indices $\vec{n}$ is given by

$$\vec{x}(\vec{n}) = \sum_{i=0}^{d-1} X_{n_i}^{(i)} \vec{e}_i, \tag{B.3}$$

where $\vec{e}_i$ is the unit-vector along dimension i. The components of the solution vector ψ^{ν} are discretized on the knots of the mesh so that the values of the fields $\psi^{\nu}(\vec{x}(\vec{n}))$ are given for each knot in the mesh. It is assumed that the solution at other positions is a linear interpolation between the knot-values. On the other hand, the coefficients of the differential equation (B.1), labeled by H, are assumed to be constant within each cell of the mesh. When discretizing the differential equation their values are evaluated at the center point of each cell (Fig. B.1), so that for example on a one-dimensional mesh the evaluation points for the coefficients lie half way between the knots of the mesh. The differential equation models a physical problem, and the coefficients take over the role of the material properties of the domain. A benefit arising from this formulation is that interfaces between different materials, which are discontinuities in the coefficients of the

differential equation can be rigorously handled and do not lead to numerical instabilities [31]. The distances $h_{i,\sigma_i}(n_i)$ between the grid knots along the dimension i in direction

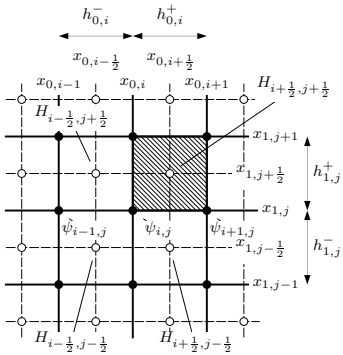

FIGURE B.1: Illustration of structured irregular box grid. The mesh knots at which field values are stored are displayed as filled circles and the locations where coefficients (material values) are stored are displayed as circles with white fillings.

$\vec{\sigma} = (\sigma_0, \sigma_1, \cdots, \sigma_{d-1})^{\mathrm{T}}$ with the components $\sigma_i = \pm 1$, where $+1$ indicates the direction of the positive coordinate, are calculated according to

$$h_{i,\sigma_i}(n_i) = x_i\left(\vec{n} + \frac{\sigma_i + 1}{2}\vec{e}_i\right) - x_i\left(\vec{n} + \frac{\sigma_i - 1}{2}\vec{e}_i\right). \tag{B.4}$$

B.2 Discretized Differential Operators

As previously introduced, values of the coefficients of the differential equation (the *material* parameters) are given for the volumes (mesh cells) in between the grid knots. The centers of the cells are located halfway between the knots in the corresponding directions. Therefore, the value of the coefficients $H(\vec{n})$ at the knots $\vec{n}$ are evaluated by interpolation of the values of the surrounding cells

$$\begin{aligned} H(\vec{n}) &= \frac{1}{V(\vec{n})} \sum_{\sigma_1=\pm 1} \cdots \sum_{\sigma_d=\pm 1} \left[\prod_{i=1}^{d} \frac{h_{i,\sigma_i}(n_i)}{2}\right] H(\vec{n} + \vec{\sigma}/2) \\ &= \frac{1}{2} D(\vec{n}) \sum_{\sigma_1=\pm 1} \cdots \sum_{\sigma_d=\pm 1} \left[\prod_{i=1}^{d} h_{i,\sigma_i}(n_i)\right] H(\vec{n} + \vec{\sigma}/2), \end{aligned} \tag{B.5}$$

where the sums $\sum_{\sigma_1=\pm 1} \cdots \sum_{\sigma_d=\pm 1}$ result in a total of 2^d terms, which contain all permutations of $\vec{\sigma}$. The factor

$$D(\vec{n}) = \frac{1}{2^{d-1} V(\vec{n})} = \frac{2}{\prod_{i=1}^{d} \sum_{\sigma_i=\pm 1} h_{i,\sigma_i}(n_i)} \tag{B.6}$$

is expressed with the help of the volume $V(\vec{n})$ of the individual cell. To discretize second order derivatives of the form

$$\partial_i \left[H(\vec{x})\, \partial_j \psi(\vec{x})\right] \tag{B.7}$$

with the box integration method expression (B.7) is averaged over a mesh cell, the control volume $V(\vec{x})$

$$\begin{aligned}&\frac{1}{V(\vec{x})}\int_{V(\vec{x})}\partial_i\left[H(\vec{x})\,\partial_j\psi(\vec{x})\right]\mathrm{d}\tilde{V}\\&=\frac{1}{V(\vec{x})}\sum_{\sigma_i}\sigma_i\left[\int_{S_i(\vec{x})}H(\vec{x})\,\partial_j\psi(\vec{x})\prod_{k\neq i}\mathrm{d}x_k\right]_{\vec{x}\left(\vec{n}+\frac{\sigma_i}{2}\vec{e}_i\right)},\end{aligned}\tag{B.8}$$

where S_i is the $(d-1)$-dimensional surface perpendicular to direction i, which is evaluated at the locations $x_i = n_i + \frac{\sigma_i}{2}$. By partial integration, the integral is written as the sum over integrals in $d-1$ dimensions of 2^{d-1} surfaces which are the facets of the mesh cell the control volume is covering. These surface integrals are approximated by the product of each facets area $\prod_{j\neq i}\frac{h_{i,\sigma_i}(n_i)}{2}$ of the $d-1$-dimensional surface with the corresponding average value of the integrals kernel. The derivative remaining in (B.8) is discretized with the FDM. To discretize (B.7) for $i=j$ the following expression is utilized

$$\begin{aligned}\partial_i\left[H(\vec{x})\,\partial_j\psi(\vec{x})\right]\;\rightarrow\;&D(\vec{n})\sum_{\sigma_1=\pm1}\cdots\sum_{\sigma_d=\pm1}H(\vec{n}+\vec{\sigma}/2)\,\frac{\prod_{j\neq i}h_{j,\sigma_j}(n_j)}{h_{i,\sigma_i}(n_i)}\\&\times\left[\psi(\vec{n}+\sigma_i\vec{e}_i)-\psi(\vec{n})\right].\end{aligned}\tag{B.9}$$

and for $i\neq j$

$$\begin{aligned}\partial_i\left[H(\vec{x})\,\partial_j\psi(\vec{x})\right]=D(\vec{n})\sum_{\sigma_1=\pm1}\cdots\sum_{\sigma_d=\pm1}\sigma_i\sigma_j\frac{1}{2}H(\vec{n}+\vec{\sigma}/2)\left[\prod_{k\neq i,j}h_{k,\sigma_k}(n_k)\right]\\\cdot\left[\psi(\vec{n}+\sigma_i\vec{e}_i+\sigma_j\vec{e}_j)-\psi(\vec{n}+\sigma_i\vec{e}_i)+\psi(\vec{n}+\sigma_j\vec{e}_j)-\psi(\vec{n})\right]\end{aligned}\tag{B.10}$$

is applied. The discretization for first-order derivatives in expressions of the form

$$H^{\alpha}(\vec{x})\,\partial_i\left[H^{1-\alpha}(\vec{x})\,\psi(\vec{x})\right]\tag{B.11}$$

with $\alpha\in\{0,1\}$ leads to the central differences scheme

$$H^{\alpha}(\vec{x})\,\partial_i\left[H^{1-\alpha}(\vec{x})\,\psi(\vec{x})\right]\rightarrow\frac{H}{2h}\left[\psi(\vec{n}+\vec{e}_i)-\psi(\vec{n}-\vec{e}_i)\right]\tag{B.12}$$

for uniform grid spacing h and constant material values H. This discretization scheme is prone to spurious solutions, which manifests in fields which oscillate between two envelope functions from one mesh knot to the other. These solutions are valid in the scheme since the derivatives in (B.12) at grid point n_i is only dependent on function values evaluated at grid locations n_i+1 and n_i-1. Therefore, this scheme is *blind* for jumps of function values between to neighboring grid knots. To circumvent this disadvantage expressions of the form (B.11) are discretized with forward and backward

differences without application of box-integration. The forward derivative is defined as

$$\begin{aligned} H(\vec{x})\,\partial_i[\psi(\vec{x})] &\rightarrow D(\vec{n})\prod_{j\neq i}[h_{j,+}(n_j)+h_{j,-}(n_j)] \\ &\quad\times[H(\vec{n})\,\psi(\vec{n}+\vec{e}_i)-H(\vec{n})\,\psi(\vec{n})] \\ &= \frac{D(\vec{n})}{h_{i,+}(n_i)+h_{i,-}(n_i)}\sum_{\sigma_1=\pm1}\cdots\sum_{\sigma_d=\pm1}\left[\prod_{j=1}^{d}h_{j,\sigma_j}(n_j)\right] \\ &\quad\times H(\vec{n}+\vec{\sigma}/2)\,[\psi(\vec{n}+\vec{e}_i)-\psi(\vec{n})]\,, \end{aligned} \tag{B.13}$$

where for the evaluation of the material coefficients $H(\vec{n})$ the interpolation (B.5) is inserted. Analogue

$$\begin{aligned} \partial_i[H(\vec{x})\,\psi(\vec{x})] &\rightarrow D(\vec{n})\prod_{j\neq i}[h_{j,+}(n_j)+h_{j,-}(n_j)] \\ &\quad\times[H(\vec{n})\,\psi(\vec{n})-H(\vec{n}-\vec{e}_i)\,\psi(\vec{n}-\vec{e}_i)] \\ &= \frac{D(\vec{n})}{h_{i,+}(n_i)+h_{i,-1}(n_i)}\sum_{\sigma_1=\pm1}\cdots\sum_{\sigma_d=\pm1}\left[\prod_{j=1}^{d}h_{j,\sigma_j}(n_j)\right] \\ &\quad\times[H(\vec{n}+\vec{\sigma}/2)\,\psi(\vec{n})-H(\vec{n}+\vec{\sigma}/2-\vec{e}_i)\,\psi(\vec{n}-\vec{e}_i)]\,. \end{aligned} \tag{B.14}$$

is applied for the backward derivatives.

B.3 Discretized System of Differential Equations

By insertion of the substitutions (B.10), (B.9), (B.13), and (B.14) the operator (B.2) is discretized on a mesh introduced in section B.1 and therefore, each block with indices μ,ν is transformed into a sparse matrix $H^{\mu\nu}_{mn}$. The ordering of the elements is carried out in a way that in each block ν of the solution vector $F^{\nu}(\vec{n})$ the values at the grid knots are listed row-wise (in *Fortran* order) for each dimension in a vector F^{ν}_{n} with $n=\sum_{i=1}^{d}\prod_{k=1}^{i-1}N_k n_i$. The matrices $H^{\mu\nu}_{mn}$ (sub-matrices of the block matrix) resulting from the discretization are banded matrices, where the number of bands depends on the number of dimensions of the differential equation, see Fig. B.2. In general, if the corresponding coefficients are not zero, the non-vanishing diagonals are one main diagonal, $2d$ off-diagonals of the first kind and $2d(d-1)$ off-diagonals of the second kind. The indices of the diagonal, which are indicating the location of the diagonal with respect to the main diagonal are

$$a_i=\sigma_i\cdot\prod_{k=1}^{i-1}N_k \quad i=1,...,d \quad \text{with} \quad \sigma_i=\pm1 \tag{B.15}$$

for the off-diagonals of the first kind. Whereby a positive value of the diagonals index labels diagonals in the upper triangle and a negative value labels diagonals in the lower triangle of the matrix. Analogue, the indices

$$b_{ij}=a_i+\sigma_j\cdot\prod_{k=1}^{j-1}N_k \quad i=1,...,d, \quad j<i, \quad \text{with} \quad \sigma_i=\pm1,\,\sigma_j=\pm1. \tag{B.16}$$

label the positions of the diagonals of the second type. The entries of the main diagonal

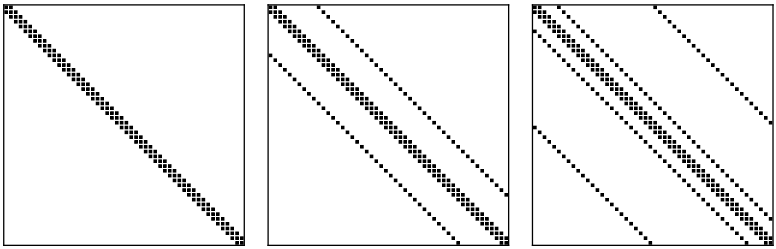

FIGURE B.2: Illustration of the non-vanishing entries (indicated by markers) of the discretized operator matrix for a one (left), two (center) and three (right) dimensional problem.

of the blocks with $\mu < \nu$ are

$$\begin{aligned}\frac{1}{D(\vec{n})}H^{\mu\nu}_{mm} = \sum_{\sigma_1=\pm1}\cdots\sum_{\sigma_d=\pm1}\Bigg[&\sum_{i=1}^{d}-\tilde{H}^{\mu\nu}_{ii}\left(\vec{n}+\frac{\vec{\sigma}}{2}\right)\frac{\prod_{j\neq i}^{d}h_{j,\sigma_j}(n_j)}{h_{i,\sigma_i}(n_i)}\\ &+\sum_{\substack{j\\ i\neq j}}^{d}-\sigma_i\sigma_j\frac{1}{2}\tilde{H}^{\mu\nu}_{ij}\left(\vec{n}+\frac{\vec{\sigma}}{2}\right)\prod_{k\neq i,j}^{d}h_{k,\sigma_k}(n_k)\\ &+\sum_{i=1}^{d}-\left[\tilde{H}^{\mu\nu}_{i\rightarrow}\left(\vec{n}+\frac{\vec{\sigma}}{2}\right)-\tilde{H}^{\mu\nu}_{i\leftarrow}\left(\vec{n}+\frac{\vec{\sigma}}{2}\right)\right]\frac{\prod_{j=1}^{d}h_{j,\sigma_j}(n_j)}{h_{i,+}(n_i)+h_{i,-}(n_i)}\\ &+\frac{1}{2}\tilde{H}^{\mu\nu}_{0}\left(\vec{n}+\frac{\vec{\sigma}}{2}\right)\prod_{i=1}^{d}h_{i,\sigma_i}(n_i)\Bigg].\end{aligned}\tag{B.17}$$

In the case of Hermitian problems (for example the solution of the $k\cdot p$ Schrödinger equation), the blocks with indices $\mu > \nu$ are determined by Hermitian conjugation $H^{\mu\nu}_{mn} = (H^{\nu\mu}_{nm})^*$. The entries of the off-diagonals of the first kind are

$$\begin{aligned}\frac{1}{D(\vec{n})}H^{\mu\nu}_{m_in_i} = \sum_{\sigma_1=\pm1}\cdots\sum_{\sigma_{i-1}=\pm1}\sum_{\sigma_{i+1}=\pm1}\cdots\sum_{\sigma_d=\pm1}\Bigg[&\tilde{H}^{\mu\nu}_{ii}\left(\vec{n}+\frac{\vec{\sigma}}{2}\right)\frac{\prod_{j\neq i}h_{j,\sigma_j}(n_j)}{h_{i,\sigma_i}(n_i)}\\ &+\sum_{j\neq i}\frac{-1}{2}\sigma_i\sigma_j\left[\tilde{H}^{\mu\nu}_{ij}\left(\vec{n}+\frac{\vec{\sigma}}{2}\right)-\tilde{H}^{\mu\nu}_{ji}\left(\vec{n}+\frac{\vec{\sigma}}{2}\right)\right]\prod_{k\neq i,j}h_{k,\sigma_k}(n_k)\Bigg]\\ &+\delta_{\sigma_i,1}\sum_{\sigma'_1=\pm1}\cdots\sum_{\sigma'_d=\pm1}\Bigg[\tilde{H}^{\mu\nu}_{i\rightarrow}\left(\vec{n}+\sigma_i\vec{e}_i+\frac{\vec{\sigma'}}{2}\right)\\ &\times\frac{h_{i,\sigma'_i}(n_i+1)\prod_{j\neq i}^{d}h_{j,\sigma'_j}(n_j)}{h_{i,+}(n_i+1)+h_{i,-}(n_i+1)}\\ &+\tilde{H}^{\mu\nu}_{i\leftarrow}\left(\vec{n}+\frac{\vec{\sigma'}}{2}\right)\frac{\prod_{j=1}^{d}h_{j,\sigma'_j}(n_j)}{h_{i,+}(n_i)+h_{i,-}(n_i)}\Bigg],\quad i=1,...,d.\end{aligned}\tag{B.18}$$

The entries of the off-diagonals of the second kind are given by

$$\begin{aligned}\frac{1}{D\left(\vec{n}\right)}H_{m_i n_i}^{\mu\nu} = &\sum_{\sigma_1=\pm1}\cdots\sum_{\sigma_{i-1}=\pm1}\sum_{\sigma_{i+1}=\pm1}\cdots\sum_{\sigma_{j-1}=\pm1}\sum_{\sigma_{j+1}=\pm1}\cdots\sum_{\sigma_d=\pm1}\frac{1}{2}\sigma_i\sigma_j\\ &\times\left[\tilde{H}_{ij}^{\mu\nu}\left(\vec{n}+\frac{\vec{\sigma}}{2}\right)+\tilde{H}_{ji}^{\mu\nu}\left(\vec{n}+\frac{\vec{\sigma}}{2}\right)\right]\prod_{k\neq i,j}h_{k,\sigma_k}\left(n_k\right),\\ &i=1,...,d\quad\text{for}\quad j<i.\end{aligned}\tag{B.19}$$

Since problems with Hermitian matrices, for example in case of eigenvalue problems, benefit the numerical solution in terms of stability and convergence, the matrices $H_{mn}^{\mu\nu}$ can be separated in diagonal matrices D and remaining parts $H_{mn}^{\prime\mu\nu}$, so that in the eigenvalue problem with eigenvalue E

$$\begin{aligned}H\psi &= E\psi\\ \Leftrightarrow DH'\psi &= E\psi\\ \Leftrightarrow \underbrace{D^{\frac{1}{2}}H'D^{\frac{1}{2}}}_{\equiv S}\psi' &= E\psi'.\end{aligned}\tag{B.20}$$

the matrix of the system $S\in\mathbb{C}^{AN\times AN}$ becomes Hermitian. Additionally, the solution vector is modified $\psi'=D^{-\frac{1}{2}}\psi$. The number of blocks of the system of differential equations is A and $N=\prod_i^d N_i$ is the total number of knots of the mesh. Note that computation of the inverse or square root of the matrix D is carried out straightforward since the matrix has only entries on the main diagonal.

Appendix C

Miscellaneous

C.1 Model Parameters

Epitaxy	E0	E1	E2	E3
Γ / %	0.683	0.721	0.62	0.85
n_{eff}	3.424	3.400	3.366	3.383
G_0 / $1 \cdot 10^5\,\text{m}^{-1}$	2.43	2.20	2.35	2.35
$G_{0,T}$ / $\text{m}^{-1}\text{K}^{-1}$		-63		
N_{tr} / $1 \cdot 10^{24}\,\text{m}^{-3}$	1.48	2.00	2.08	2.08
$N_{\text{tr},T}$ / $1 \cdot 10^{22}\,\text{m}^{-3}\text{K}^{-1}$		1.01		
λ_0 / nm	972	950	950	950
β_{sp} / $1 \cdot 10^{-3}$	1	1	1	1
α_{int} / m^{-1}	38	20	20	20
α_N / $1 \cdot 10^{-26}\,\text{m}^3$	-2.00	-1.70	-2.19	-2.19
α_T / $1 \cdot 10^{-4}\,\text{K}^{-1}$	3	4	3	3
τ_{nr} / ns	5 [48]	5 [48]	10	10
B_{sp} / $1 \cdot 10^{-16}\,\text{m}^3\text{s}^{-1}$	1.7	1.4 [48]	1.4 [48]	1.4 [48]
C_{A} / $1 \cdot 10^{-42}\,\text{m}^6\text{s}^{-1}$	3.5	3.5	3.5	3.5
$D_{n/p}$ / $1 \cdot 10^{-4}\,\text{m}^2\text{s}^{-1}$	26.0	19.6*	20.3*	20.3*

TABLE C.1: Parameters for the model of the active region for the epitaxial structures E0–E3. The values in the first section are extracted from band structure and vertical eigenmode calculations. The values in the second section are set to match experimental results for the emission characteristics or are literature values. *Calculated ambipolar diffusion coefficient based on $D_{n/p} = 2D_nD_p/(D_n + D_p)$, with hole D_n and electron D_p diffusion coefficient determined from p- and n- mobility in QW from model presented in the Appendix A.3.

Device	D0	D1	D2	D3	D4
Epitaxy	E0	E1	E1	E1	E1
Geometry	S0	S1	S2	S4	S3
w_d / µm	600	600	600	600	600
w_c / µm	90	100	140	140	150
w_r / µm		180	220	220	230
w_t / µm		10	10	10	10
l_d / mm	4	4	5	5	4
R_0	0.96	0.98	0.98	0.10	0.98
R_l	0.02	0.02	0.02	0.10	0.02
δn_t^* / $1 \cdot 10^{-4}$		-38.4	-38.4	-38.4	-38.4
α_t / m^{-1}		0	0	0	0
T_hs / K	300	300	300	300	300
g_hs^{**} / $1 \cdot 10^5\,\mathrm{Wm^{-2}K^{-1}}$		0.550	0.275	0.350	0.860
$l_{y,\mathrm{sim.}}$ / µm	250	500	500	500	500
$N_{y,\mathrm{sim.}}$	500	1024	1024	1024	1024
$N_{z,\mathrm{sim.}}$	4000	4000	5000	5000	4000

TABLE C.2: List of HPDL device designs and parameters for SE. The values in the lower group are parameters for the simulation domain. *Extracted from vertical eigenmode calculation for corresponding ridge / trench depth. **Determined by calibration of calculated (average) temperature in QW with measured values.

Device	D5	D6	D7	D8
Epitaxy	E2	E2	E2	E3
Geometry	A1	A2	A3	A3
w_d / µm	166*	400*	334*	334*
w_c / µm	90	90	200	200
w_r / µm	156	170	324	324
w_t / µm	10	10	10	10
l_d / mm	4	4	4	4
N_emitter	55	23	27	27
R_0	0.98	0.98	0.98	0.98
R_l	0.02	0.02	0.02	0.02
δn_t^* / $1 \cdot 10^{-4}$	-5	-5	-5	-5
α_t / m^{-1}	0	0	0	0
T_hs / K	300	300	300	300
g_hs^{***} / $1 \cdot 10^5\,\mathrm{Wm^{-2}K^{-1}}$	1.60	1.20	1.35	1.35
$l_{y,\mathrm{sim.}}$ / µm	166	400	334	334
$N_{y,\mathrm{sim.}}$	512	1024	1024	1024
$N_{z,\mathrm{sim.}}$	512	1024	1024	1024

TABLE C.3: List of HPDL device designs and parameters for LA. The values in the lower group are parameters for the simulation domain. *For the simulation of the laser arrays A1, A2, A3 the width is equal to the pitch of the emitters. **Extracted from vertical eigenmode calculation for corresponding ridge or trench depth. ***Determined by calibration of calculated (average) temperature in QW with measured values.

Parameter	Symbol	Value
Intensity scale	I_0	$1 \cdot 10^{11}\,\mathrm{Wm}^{-2}$
Carrier density scale	n_0	$1 \cdot 10^{24}\,\mathrm{m}^{-3}$
Length scale	l_0	$1 \cdot 10^{-6}\,\mathrm{m}$
Transparency carrier density	n_{tr}	$3.11 \cdot 10^{24}\,\mathrm{m}^{-3}$
Gain coefficient	g_0	$3.043 \cdot 10^{5}\,\mathrm{m}^{-1}$
Gain decrease with temperature	$g_{0,T}$	$5 \cdot 10^{3}\,\mathrm{K}^{-1}\,\mathrm{m}^{-1}$
Front facet reflectivity	R_l	0.98
Rear facet reflectivity	R_0	0.02
QW thickness	d_{qw}	6.3 nm
Injection contact width	w_{c}	90 µm
Confinement factor	Γ	0.0067
Internal absorption	α_{int}	$38\,\mathrm{m}^{-1}$
Central wavelength	λ_0	910 nm
Spontaneous emission	B_{sp}	$1.4 \cdot 10^{-16}\,\mathrm{m}^3\mathrm{s}^{-1}$ [48]
Longitudinal resolution	N_z	200
Non-radiative recombination	τ_{nr}	5 ns [48]
Spontaneous Emission contribution to light field	β_{sp}	$1 \cdot 10^{-4}$ [48]
Internal efficiency	η_{i}	0.9
Reference device length	$l_{z,0}$	4 mm

Table C.4: Parameters for one-dimensional laser model.

Parameter	Value
CTE submount / $1 \cdot 10^{-6}\,\mathrm{K}^{-1}$	6.5, 7.5
Submount material	CuW
Solder (1st)	AuSn
Solder (2nd)	AuSn
Thickness submount / µm	380
Thickness solder (1st) / µm	2
Thickness solder (2nd) / µm	15
Thickness p-metal / µm	2.3
Thickness submount metal / µm	10
Thickness metal on cooler / µm	1
Thickness cooler / mm	3
Thin-film line force / Nm^{-1}	455
Emitters	55
Pitch / µm	166

Table C.5: Parameters for opto-mechanical simulations.

Parameter	Value
Submount material	AlN
Material for submount metal	Au
Solder	AuSn
Material for p-metal	Au
Thickness submount / µm	380
Thickness submount metal / µm	10
Thickness solder / µm	4
Thickness p-metal / µm	2.3
Thickness substrate / µm	110
Thickness n-metal / µm	0.3

Table C.6: Parameters for thermal simulation of SEs.

Parameter	Value
Submount material	CuW
Material for submount metal	Au
Solder	AuSn
Material for p-metal	Au
Thickness submount / µm	380
Thickness submount metal / µm	10
Thickness solder / µm	2
Thickness p-metal / µm	2.3
Thickness substrate / µm	110
Thickness n-metal / µm	0.3

Table C.7: Parameters for thermal simulation of emitters out of LAs.

C.2 Equilibrium Carrier Distributions

The number of occupied states per unit volume and energy E is

$$\delta n(E) = g_{\mathrm{c}}(E) f\left(\frac{E - E_{\mathrm{F}}}{k_{\mathrm{B}} T}\right) \tag{C.1}$$

where the Fermi-Dirac probability distribution is

$$f(x) = \frac{1}{1 + \exp(x)} \tag{C.2}$$

and $g_{\mathrm{c}}(E)$ is the density of states in the conduction band and E_{F} is the Fermi energy. The density of occupied states for holes is

$$\delta p(E) = g_{\mathrm{v}}(E)\left(1 - f\left(\frac{E - E_{\mathrm{F}}}{k_{\mathrm{B}} T}\right)\right), \tag{C.3}$$

where $g_{\mathrm{v}}(E)$ is the density of states in the valence band. For a free electron with effective mass m^* the densities

$$g_{\mathrm{c}}(E) = \frac{8\pi\sqrt{2}}{h^3} m_e^{*\frac{3}{2}} \sqrt{E - E_{\mathrm{c}}}, \quad E \geq E_{\mathrm{c}} \tag{C.4}$$

$$g_{\mathrm{v}}(E) = \frac{8\pi\sqrt{2}}{h^3} m_h^{*\frac{3}{2}} \sqrt{E_{\mathrm{v}} - E}, \quad E \leq E_{\mathrm{v}}. \tag{C.5}$$

The total particle densities per unit volume are

$$n = \int_{E_{\mathrm{c}}}^{\infty} \delta n(E)\, \mathrm{d}E, \tag{C.6}$$

$$p = \int_{-\infty}^{E_{\mathrm{v}}} \delta p(E)\, \mathrm{d}E. \tag{C.7}$$

Intrinsic semiconductors do not contain impurities and are usually non-degenerate. The intrinsic electron and hole densities are n_{i} and p_{i} with $n_{\mathrm{i}} = p_{\mathrm{i}}$. The Fermi-energy of the intrinsic material is E_{i} and thus [91]

$$n_{\mathrm{i}} = N_{\mathrm{c}} \exp\left(\frac{E_{\mathrm{i}} - E_{\mathrm{c}}}{k_{\mathrm{B}} T}\right), \tag{C.8}$$

$$p_{\mathrm{i}} = n_{\mathrm{i}} = N_{\mathrm{v}} \exp\left(\frac{E_{\mathrm{v}} - E_{\mathrm{i}}}{k_{\mathrm{B}} T}\right). \tag{C.9}$$

Multiplying the intrinsic electron and hole density and using $E_{\mathrm{g}} = E_{\mathrm{c}} - E_{\mathrm{v}}$ leads to the definition of the intrinsic carrier density

$$n_{\mathrm{i}} = \sqrt{N_{\mathrm{c}} N_{\mathrm{v}}} \exp\left(\frac{-E_{\mathrm{g}}}{2 k_{\mathrm{B}} T}\right). \tag{C.10}$$

If both carrier densities equal this number the recombination terms vanish.

C.3 Order of Differential Operators

The material parameters applied to a heterostructure can change rapidly at heterojunctions or with an arbitrary spatial gradient for example due to concentration profiles. The substitution

$$k_\alpha \to -i\partial_\alpha, \tag{C.11}$$

which is performed when discretizing derivatives along direction x_α evokes that the Hamilton operator is not hermitian anymore, because the material coefficients and the derivatives do not commute anymore. The order of the operators is chosen to circumvent this and result in a hermitian Hamilton operator. The order of the operators defines the sequence in which material parameters and differential operators occur in the equations. Parameters which are defined by matrix elements of the form

$$A \propto \sum_\beta \langle u_\alpha | p_\mu | u_\beta \rangle \langle u_\beta | p_\nu | u_\gamma \rangle \tag{C.12}$$

are substituted by

$$A k_\nu k_\mu \to -\partial_\mu A(\vec{x}) \partial_\nu \tag{C.13}$$

in the Hamiltonian [155]. The order of p_μ and p_ν therefore corresponds to the order of the differential operators in (C.13). First order differential operators are not symmetrized, so that they occur in the Hamiltonian as

$$\begin{pmatrix} \ddots & B\partial_\alpha \\ \partial_\alpha B & \ddots \end{pmatrix}. \tag{C.14}$$

Differential operators in the upper triangle of the Hamiltonian are discretized with forward derivatives (B.13) in Chapter B and operators in the lower triangle of the Matrix are discretized with backward differences (B.14) in Chapter B). In contrast to the symmetrization of first order derivatives according to

$$B(\vec{x}) k_\alpha \to -\frac{i}{2} \left[B(\vec{x}) \partial_\alpha + \partial_\alpha B(\vec{x}) \right] \tag{C.15}$$

the former introduced scheme surpresses jumps of the numerically calculated envelope functions and un-physical solutions at heterointerfaces [31].

C.4 Stokes Parameters

The Stokes parameters

$$\begin{aligned} S_0 &= |E_x|^2 + |E_y|^2, \\ S_1 &= \left(|E_x|^2 - |E_y|^2 \right) / S_0, \\ S_2 &= 2\Re \left(E_x E_y^* \right) / S_0, \\ S_3 &= -2\Im \left(E_x E_y^* \right) / S_0. \end{aligned} \tag{C.16}$$

encode information about the polarization state of a light field with (complex) transverse components E_x and E_y. For further information and details on measurement see [156].

The intensity in linear polarized fraction of the light is

$$|L|^2 = |S_1|^2 + |S_2|^2, \tag{C.17}$$

the intensity in circular polarized light is

$$|V|^2 = |S_3|^2, \tag{C.18}$$

and the orientation of the polarization ellipse is defined by

$$\theta = \text{angle}(S_1 + iS_2) \tag{C.19}$$

All three properties are calculated based on the Stokes parameters.

C.5 Gateaux Differential

For a functional F of the function u the Gateaux differential is defined as

$$\delta F(u, \delta u) = \frac{\mathrm{d}}{\mathrm{d}\varepsilon} F(u + \varepsilon \delta u)|_{\varepsilon=0} = \frac{\delta F(u)}{\delta u} \delta u. \tag{C.20}$$

C.6 Linearization for Formulation in Variables (ϕ, ϕ_n, ϕ_p)

The entries of the Jacobian (C.63) are

$$\begin{aligned}
\delta L_\phi(u, \delta\phi) &= \nabla \cdot (d_\phi \nabla \delta\phi) - q_{\mathrm{el}} \beta n \delta\phi - q_{\mathrm{el}} \beta p \delta\phi \\
&\quad + q_{\mathrm{el}} \delta N_{\mathrm{D}}(u, \delta\phi) - q_{\mathrm{el}} \delta N_{\mathrm{A}}(u, \delta\phi), && \text{(C.21)} \\
\delta L_\phi(u, \delta\phi_n) &= q_{\mathrm{el}} \beta n \delta\phi_n + q_{\mathrm{el}} \delta N_{\mathrm{D}}(u, \delta\phi_n), && \text{(C.22)} \\
\delta L_\phi(u, \delta\phi_p) &= q_{\mathrm{el}} \beta p \delta\phi_p - q_{\mathrm{el}} \delta N_{\mathrm{A}}(u, \delta\phi_p), && \text{(C.23)}
\end{aligned}$$

and

$$\begin{aligned}
\delta L_{\phi_n}(u, \delta\phi) &= -\nabla \cdot \left(\vec{b}_n \delta\phi \right) - q_{\mathrm{el}} \delta R(u, \delta\phi), && \text{(C.24)} \\
\delta L_{\phi_n}(u, \delta\phi_n) &= -\nabla \cdot \left(-\vec{b}_n \delta\phi_n + d_n \nabla \delta\phi_n \right) - q_{\mathrm{el}} \delta R(u, \delta\phi_n), && \text{(C.25)} \\
\delta L_{\phi_n}(u, \delta\phi_p) &= -q_{\mathrm{el}} \delta R(u, \delta\phi_p), && \text{(C.26)}
\end{aligned}$$

and

$$\begin{aligned}
\delta L_{\phi_p}(u, \delta\phi) &= \nabla \cdot \left(\vec{b}_p \delta\phi \right) + q_{\mathrm{el}} \delta R(u, \delta\phi), && \text{(C.27)} \\
\delta L_{\phi_p}(u, \delta\phi_n) &= q_{\mathrm{el}} \delta R(u, \delta\phi_n), && \text{(C.28)} \\
\delta L_{\phi_p}(u, \delta\phi_p) &= -\nabla \cdot \left(\vec{b}_p \delta\phi_p + d_p \nabla \delta\phi_p \right) + q_{\mathrm{el}} \delta R(u, \delta\phi_p), && \text{(C.29)}
\end{aligned}$$

where the functional derivatives are written in terms of the notation given in Eq. (C.20) in Section C.20. Linearization of the SRH recombination terms gives

$$\delta R_{\mathrm{SRH}}(u,\delta\phi_n) = -\frac{np-n_{\mathrm{i}}^2}{\left(\tau_n(n+n_{\mathrm{i}})+\tau_p(p+n_{\mathrm{i}})\right)^2} \times \left(\tau_n n - \tau_p p\right)\beta\delta\phi, \tag{C.30}$$

$$\delta R_{\mathrm{SRH}}(u,\delta\phi_n) = \left(-\frac{\beta np}{\tau_n(n+n_{\mathrm{i}})+\tau_p(p+n_{\mathrm{i}})} + \frac{(np-n_{\mathrm{i}}^2)\tau_n\beta n}{\left(\tau_n(n+n_{\mathrm{i}})+\tau_p(p+n_{\mathrm{i}})\right)^2}\right)\delta\phi_n, \tag{C.31}$$

$$\delta R_{\mathrm{SRH}}(u,\delta\phi_p) = \left(\frac{\beta np}{\tau_n(n+n_{\mathrm{i}})+\tau_p(p+n_{\mathrm{i}})} - \frac{(np-n_{\mathrm{i}}^2)\tau_p\beta p}{\left(\tau_n(n+n_{\mathrm{i}})+\tau_p(p+n_{\mathrm{i}})\right)^2}\right)\delta\phi_p, \tag{C.32}$$

linearization of the spontaneous recombination term gives

$$\delta R_{\mathrm{sp}}(u,\delta\phi) = 0, \tag{C.33}$$

$$\delta R_{\mathrm{sp}}(u,\delta\phi_n) = -\beta C_{\mathrm{sp}} np\delta\phi_n, \tag{C.34}$$

$$\delta R_{\mathrm{sp}}(u,\delta\phi_p) = \beta C_{\mathrm{sp}} np\delta\phi_p, \tag{C.35}$$

and for Auger recombination

$$\delta R_{\mathrm{A}}(u,\delta\phi) = (C_n n - C_p p)(np-n_{\mathrm{i}}^2)\beta\delta\phi, \tag{C.36}$$

$$\delta R_{\mathrm{A}}(u,\delta\phi_n) = (C_n n n_{\mathrm{i}}^2 - 2C_n n^2 p - C_p p^2 n)\beta\delta\phi_n, \tag{C.37}$$

$$\delta R_{\mathrm{A}}(u,\delta\phi_p) = (C_n n^2 p + 2C_p p^2 n - C_p p n_{\mathrm{i}}^2)\beta\delta\phi_p. \tag{C.38}$$

For models including incomplete ionization the donator and aceptor concentrations depend on the respective carrier densities (quasi-Fermi potentials) and the electric potential, so that

$$\delta N_{\mathrm{D}}(u,\delta\phi) = -\frac{N_{\mathrm{D}}(n)n\beta g_{\mathrm{D}}\exp\left(\beta\Delta E_{\mathrm{D}}\right)}{N_{\mathrm{c}}\left(1+\frac{n}{N_{\mathrm{c}}}g_{\mathrm{D}}\exp\left(\beta\Delta E_{\mathrm{D}}\right)\right)}\delta\phi, \tag{C.39}$$

$$\delta N_{\mathrm{D}}(u,\delta\phi_n) = \frac{N_{\mathrm{D}}(n)n\beta g_{\mathrm{D}}\exp\left(\beta\Delta E_{\mathrm{D}}\right)}{N_{\mathrm{c}}\left(1+\frac{n}{N_{\mathrm{c}}}g_{\mathrm{D}}\exp\left(\beta\Delta E_{\mathrm{D}}\right)\right)}\delta\phi_n \tag{C.40}$$

$$\tag{C.41}$$

and

$$\delta N_{\mathrm{A}}(u,\delta\phi) = \frac{N_{\mathrm{A}}(p)p\beta g_{\mathrm{A}}\exp\left(\beta\Delta E_{\mathrm{A}}\right)}{N_{\mathrm{v}}\left(1+\frac{p}{N_{\mathrm{v}}}g_{\mathrm{A}}\exp\left(\beta\Delta E_{\mathrm{A}}\right)\right)}\delta\phi, \tag{C.42}$$

$$\delta N_{\mathrm{A}}(u,\delta\phi_p) = -\frac{N_{\mathrm{A}}(p)p\beta g_{\mathrm{A}}\exp\left(\beta\Delta E_{\mathrm{A}}\right)}{N_{\mathrm{v}}\left(1+\frac{p}{N_{\mathrm{v}}}g_{\mathrm{A}}\exp\left(\beta\Delta E_{\mathrm{A}}\right)\right)}\delta\phi_p. \tag{C.43}$$

The derivatives with respect to the carrier densities are

$$\delta N_{\mathrm{D}}(u,\delta n) = -\frac{N_{\mathrm{D}}(n) g_{\mathrm{D}} \exp\left(\beta \Delta E_{\mathrm{D}}\right)}{N_{\mathrm{c}} \left(1 + \frac{n}{N_{\mathrm{c}}} g_{\mathrm{D}} \exp\left(\beta \Delta E_{\mathrm{D}}\right)\right)} \delta n \tag{C.44}$$

and

$$\delta N_{\mathrm{A}}(u,\delta p) = -\frac{N_{\mathrm{A}}(p) g_{\mathrm{A}} \exp\left(\beta \Delta E_{\mathrm{A}}\right)}{N_{\mathrm{v}} \left(1 + \frac{p}{N_{\mathrm{v}}} g_{\mathrm{A}} \exp\left(\beta \Delta E_{\mathrm{A}}\right)\right)} \delta p. \tag{C.45}$$

C.7 Linearization for Primal Mixed Method

In this section the entries of the Jacobian for the drift-diffusion model for the fully coupled system of equations in PMM are given. The entries of the Jacobian for the mixed formulation are

$$\begin{aligned}
\delta L_{\phi}(u,\delta \vec{J}_{\phi}) &= -\nabla \cdot \delta \vec{J}_{\phi}, && \text{(C.46)}\\
\delta L_{\phi_n}(u,\delta \vec{J}_{n}) &= \nabla \cdot \delta \vec{J}_{n}, && \text{(C.47)}\\
\delta L_{\phi_p}(u,\delta \vec{J}_{p}) &= \nabla \cdot \delta \vec{J}_{p}, && \text{(C.48)}\\
\delta L_{\phi}(u,\delta \phi) &= -q_{\mathrm{el}} \beta n \delta\phi - q_{\mathrm{el}} \beta p \delta\phi \\
&\quad + q_{\mathrm{el}} \delta N_{\mathrm{D}}(u,\delta\phi) - q_{\mathrm{el}} \delta N_{\mathrm{A}}(u,\delta\phi), && \text{(C.49)}\\
\delta L_{\phi}(u,\delta \phi_n) &= q_{\mathrm{el}} \beta n \delta\phi_n + q_{\mathrm{el}} \delta N_{\mathrm{D}}(u,\delta\phi_n) && \text{(C.50)}\\
\delta L_{\phi}(u,\delta \phi_p) &= q_{\mathrm{el}} \beta p \delta\phi_p - q_{\mathrm{el}} \delta N_{\mathrm{A}}(u,\delta\phi_p) && \text{(C.51)}\\
\delta L_{\phi_p}(u,\delta \phi) &= -\delta L_{\phi_n}(u,\delta\phi) = q_{\mathrm{el}} \delta R(u,\delta\phi) && \text{(C.52)}\\
\delta L_{\phi_p}(u,\delta \phi_n) &= -\delta L_{\phi_n}(u,\delta\phi_n) = q_{\mathrm{el}} \delta R(u,\delta\phi_n) && \text{(C.53)}\\
\delta L_{\phi_p}(u,\delta \phi_p) &= -\delta L_{\phi_n}(u,\delta\phi_p) = q_{\mathrm{el}} \delta R(u,\delta\phi_p) && \text{(C.54)}\\
\delta L_{\vec{J}_{\phi}}(u,\delta \phi) &= d_{\phi} \nabla \delta\phi && \text{(C.55)}\\
\delta L_{\vec{J}_{n}}(u,\delta \phi) &= \vec{b}_n \delta\phi && \text{(C.56)}\\
\delta L_{\vec{J}_{n}}(u,\delta \phi_n) &= -\vec{b}_n \delta\phi_n + d_n \nabla \delta\phi_n && \text{(C.57)}\\
\delta L_{\vec{J}_{p}}(u,\delta \phi) &= -\vec{b}_p \delta\phi && \text{(C.58)}\\
\delta L_{\vec{J}_{p}}(u,\delta \phi_p) &= \vec{b}_p \delta\phi_p + d_p \nabla \delta\phi_p && \text{(C.59)}
\end{aligned}$$

all other entries of the Jacobian vanish. The functional derivatives are written in terms of the notation given in Eq. (C.20) in Section C.20.

C.8 Finite-Element Formulation in Variables (ϕ, ϕ_n, ϕ_p)

The drift-diffusion model is solved for the fully coupled system of equations for the electric potential ϕ, quasi-Fermi potential for electrons ϕ_n and quasi-Fermi potential for holes ϕ_p. For the fully coupled scheme the vector of (unknown) variables is

$$u = \begin{pmatrix} \phi \\ \phi_n \\ \phi_p \end{pmatrix}. \tag{C.60}$$

The system of nonlinear, coupled equations is

$$L\left(u\right) = \begin{pmatrix} L_{\phi} \\ L_{\phi_n} \\ L_{\phi_p} \end{pmatrix} = 0, \tag{C.61}$$

with the equations L_{ϕ}, L_{ϕ_n} and L_{ϕ_p} from (6.54), (6.56) and (6.58). To solve the system with Newton's method it is linearized around a state u_0

$$J(u_0)\delta u + L(u_0) = 0 \tag{C.62}$$

where J is the Jacobian of the system

$$J = \begin{pmatrix} \frac{\delta L_{\phi}}{\delta \phi} & \frac{\delta L_{\phi}}{\delta \phi_n} & \frac{\delta L_{\phi}}{\delta \phi_p} \\ \frac{\delta L_{\phi_n}}{\delta \phi} & \frac{\delta L_{\phi_n}}{\delta \phi_n} & \frac{\delta L_{\phi_n}}{\delta \phi_p} \\ \frac{\delta L_{\phi_p}}{\delta \phi} & \frac{\delta L_{\phi_p}}{\delta \phi_n} & \frac{\delta L_{\phi_p}}{\delta \phi_p} \end{pmatrix}. \tag{C.63}$$

The entries of the Jacobian which include the linearized terms for the system of equations C.62 with respect to the variables ϕ, ϕ_n and ϕ_p are given in Section C.6. To solve the coupled set of linear equations

$$\mathcal{L}(u, \delta u) = L(u, \delta u) + \delta L(u, \delta u) = 0 \tag{C.64}$$

for the vector of functions δu (which are the unknowns in the scope of Newton's method) with the help of FEM we introduce the vector of test functions

$$v = \begin{pmatrix} v_{\phi} \\ v_{\phi_n} \\ v_{\phi_p} \end{pmatrix}, \tag{C.65}$$

where each component is an element of the test function space $v_i \in \hat{V}$

$$\hat{V} = \{v \in H^1(\Omega) : v = 0 \,\text{on}\, \delta\Omega_{\mathrm{D}}\}, \tag{C.66}$$

where $H^1(\Omega)$ is the Sobolev space [77]. The solutions for ϕ, ϕ_n and ϕ_p lie in the function space V

$$V = \{v \in H^1(\Omega) : v = u_{\mathrm{D}} \,\text{on}\, \delta\Omega_{\mathrm{D}}\}, \tag{C.67}$$

and fulfill the Dirichlet conditions at the respective boundary $\delta\Omega_{\mathrm{D}}$. The functional becomes

$$F(u, \delta u) = \int_{\Omega} \mathcal{L}(u, \delta u) \cdot v \,\mathrm{d}x \tag{C.68}$$

by integration over the domain $\Omega \subset \mathbb{R}^D$, where D is the number of space dimensions. The total functional yields

$$F = F_{\phi} + F_{\phi_n} + F_{\phi_p} \tag{C.69}$$

$$= \int_{\Omega} \mathcal{L}_{\phi} v_{\phi} \,\mathrm{d}x + \int_{\Omega} \mathcal{L}_{\phi_n} v_{\phi_n} \,\mathrm{d}x + \int_{\Omega} \mathcal{L}_{\phi_p} v_{\phi_p} \,\mathrm{d}x. \tag{C.70}$$

After partial integration the terms of the weak form proportional to test function v_ϕ are

$$\begin{aligned} F_\phi = \int_\Omega & -d_\phi \nabla\phi \cdot \nabla v_\phi - d_\phi \nabla\delta\phi \cdot \nabla v_\phi \\ & + q_{\mathrm{el}}(p - n + N_{\mathrm{D}} - N_{\mathrm{A}})v_\phi + q_{\mathrm{el}} \left(-(n+p)\beta + \frac{\delta N_{\mathrm{D}}}{\delta\phi} - \frac{\delta N_{\mathrm{A}}}{\delta\phi} \right) \delta\phi v_\phi \\ & + q_{\mathrm{el}}(\beta n + \frac{\delta N_{\mathrm{D}}}{\delta\phi_n})\delta\phi_n v_\phi + q_{\mathrm{el}}(\beta p - \frac{\delta N_{\mathrm{A}}}{\delta\phi_p})\delta\phi_p v_\phi \,\mathrm{d}x, \end{aligned} \tag{C.71}$$

all functionals proportional to the test function v_{ϕ_n} are

$$\begin{aligned} F_{\phi_n} = \int_\Omega & d_n \nabla\phi_n \cdot \nabla v_{\phi_n} - q_{\mathrm{el}} R v_{\phi_n} + \vec{b}_n \delta\phi \cdot \nabla v_{\phi_n} - q_{\mathrm{el}} \frac{\delta R}{\delta\phi}\delta\phi v_{\phi_n} \\ & - q_{\mathrm{el}} \frac{\delta R}{\delta\phi_p}\delta\phi_p v_{\phi_n} - \vec{b}_n \delta\phi_n \nabla v_{\phi_n} + d_n \nabla\delta\phi_n \cdot \nabla v_{\phi_n} - q_{\mathrm{el}} \frac{\delta R}{\delta\phi_n}\delta\phi_n v_{\phi_n} \,\mathrm{d}x, \end{aligned} \tag{C.72}$$

and all functionals proportional to the test function v_{ϕ_p} are

$$\begin{aligned} F_{\phi_p} = \int_\Omega & d_p \nabla\phi_p \cdot \nabla v_{\phi_p} + q_{\mathrm{el}} R v_{\phi_p} - \vec{b}_p \delta\phi \cdot \nabla v_{\phi_p} + q_{\mathrm{el}} \frac{\delta R}{\delta\phi}\delta\phi v_{\phi_p} \\ & + q_{\mathrm{el}} \frac{\delta R}{\delta\phi_p}\delta\phi_p v_{\phi_p} + \vec{b}_p \delta\phi_p \nabla v_{\phi_p} + d_p \nabla\delta\phi_p \cdot \nabla v_{\phi_p} + q_{\mathrm{el}} \frac{\delta R}{\delta\phi_n}\delta\phi_n v_{\phi_p} \,\mathrm{d}x. \end{aligned} \tag{C.73}$$

In Eqs. (C.72), and (C.73), as introduced above $\vec{b}_n = \beta d_n \nabla\phi_n$ and $\vec{b}_p = \beta d_p \nabla\phi_p$ is used. The test functions vanish on the Dirichlet boundaries and so do the normal components of the current densities (proportional to the gradients of the potentials) on the Neumann boundaries so that the surface integrals in (C.71), (C.72), and (C.73) vanish. The variational problem reads: Find $\delta u \in V$ such that

$$\int_\Omega \mathcal{L}(u, \delta u) \cdot v \,\mathrm{d}x = 0 \quad \forall v \in \hat{V}. \tag{C.74}$$

Standard Galerkin (1st order Lagrange) elements are chosen for the FEM discretization of the unknown functions [77].

C.9 Analytical One-Dimensional Laser Model

The analytical one-dimensional model is based on the carrier and photon rate equation and takes into account an exponential increase of the intensity along the cavity. The gain does not saturate at high intensities since the carrier density is assumed to be constant and equal to the threshold carrier density. With the current I, optical frequency ω, threshold carrier density N_{th}, contact width w_{c}, QW thickness d_{qw}, cavity length l_z, non-radiative recombination coefficient A_{nr}, spontaneous recombination coefficient B_{sp}, and the Auger coefficient C_{A} the power out of the front facet is

$$P = \frac{\hbar\omega}{q_{\mathrm{el}}} \frac{(1-R_{\mathrm{l}})\sqrt{R_0}}{(\sqrt{R_0}+\sqrt{R_{\mathrm{l}}})(1-\sqrt{R_0 R_{\mathrm{l}}})} \frac{\alpha_{\mathrm{mir}}}{\alpha_{\mathrm{mir}}+\alpha_{\mathrm{int}}} \eta_{\mathrm{i}} \left(I - I_{\mathrm{th}}\right), \tag{C.75}$$

where η_{i} is the internal quantum efficiency and I_{th} is the threshold current

$$I_{\mathrm{th}} = J_{\mathrm{th}} w_{\mathrm{c}} l_z = w_{\mathrm{c}} l_z d_{\mathrm{qw}} q_{\mathrm{el}} \left(A_{\mathrm{nr}} N_{\mathrm{th}} + B_{\mathrm{sp}} N_{\mathrm{th}}^2 + C_{\mathrm{A}} N_{\mathrm{th}}^3 \right). \tag{C.76}$$

The ouput power (out of both facets) is derived in [30] and the asymmetry factor accounting for the power out of the front facet in the case of different front and back facet reflectivities, is given in [157]. With the reflectivities R_0 and R_l the mirror loss in m^{-1} is [30]

$$\alpha_\mathrm{mir} = -\frac{\ln\left(R_0 R_\mathrm{l}\right)}{2l_z}, \tag{C.77}$$

and the threshold gain is

$$g_\mathrm{th} = \frac{\alpha_\mathrm{int} + \alpha_\mathrm{mir}}{\Gamma}, \tag{C.78}$$

where Γ is the optical confinement and α_int is the intrinsic loss. The threshold carrier density

$$N_\mathrm{th} = N_\mathrm{tr} \exp\left(\frac{g_\mathrm{th}}{g_0}\right) \tag{C.79}$$

is determined from the logarithmic gain dependence with gain coefficient g_0 and the transparency carrier density N_tr.

C.10 Numerical Evaluation of Chemical Potential in QW

To numerically evaluate the chemical potential from equation (2.83) the root of the residual

$$F(\mu_e) = n_{2d} - \frac{1}{2\pi d_\mathrm{qw}} \sum_{\sigma=\uparrow,\downarrow} \sum_m \int k_t f(x_m(k_t))\,\mathrm{d}k_t = 0. \tag{C.80}$$

is searched. The derivative of $F(\mu_e)$ is computed

$$\frac{dF(\mu_e)}{d\mu_e} = -\frac{1}{2\pi d_\mathrm{qw}} \frac{1}{k_\mathrm{B}T} \sum_{\sigma=\uparrow,\downarrow} \sum_m \int k_t \frac{\exp(x_m(k_t))}{\left(1+\exp(x_m(k_t))\right)^2}\,\mathrm{d}k_t, \tag{C.81}$$

where the derivative of the Fermi distribution $f(x)$ is

$$\frac{df(x)}{dx} = \frac{-\exp(x)}{\left(1+\exp(x)\right)^2} \tag{C.82}$$

and Newton's method is employed to find a solution for (C.80).

C.11 Implicit Scheme for Carrier Rate Equation

The diffusion of carriers in the longitudinal direction is neglected $\partial_z^2 \to 0$ so that the remaining equation can be solved (independently) for each transverse slice, which in case of the two-dimensional quantum well is the lateral direction. Therefore for each longitudinal slice of the simulation domain a time-dependent one-dimensional diffusion equation is solved. The neglection of the longitudinal derivative of second order brings significant benefits for the speed of the simulation since the decoupled slice-vise calculation fits into the TDTW parallel implementation, introduced in Section 4.3. In analogy to the discretization of the TDTW model, either the Crank-Nicolson scheme can be used to end up with an implicit equation for the carrier density update or the explicit approach is introduced with the ICN scheme, which leads to an explicit expression for the

carrier density update. Eq. (6.85) is written in a shorter form collecting all terms which are independent (or in a stricter sense not directly dependent on) the carrier density in R_0 and all remaining terms in the recombination rate $R(n^{\mathrm{qw}})$, which is a nonlinear function in n^{qw} including partial derivatives

$$\begin{aligned}\partial_t n^{\mathrm{qw}} &= R(n^{\mathrm{qw}}) + R_0 \\ &= R(n_n^{\mathrm{qw}}) + \frac{\partial R}{\partial n^{\mathrm{qw}}}|_{n_m^{\mathrm{qw}}} (n^{\mathrm{qw}} - n_m^{\mathrm{qw}}) + R_0 \\ &= \underbrace{\frac{\partial R}{\partial n^{\mathrm{qw}}}|_{n_m^{\mathrm{qw}}}}_{=H} n^{\mathrm{qw}} + \underbrace{R(n_m^{\mathrm{qw}}) - \frac{\partial R}{\partial n^{\mathrm{qw}}}|_{n_m^{\mathrm{qw}}} n_n^{\mathrm{qw}} + R_0}_{=b} \\ &= H n^{\mathrm{qw}} + b. \end{aligned} \tag{C.83}$$

To solve the rate equation the nonlinear terms are linearized around the value of the carrier density at the current time step m. The error of this approximation is small if the change of the carrier density with the time step is small. In the TD model introduced in Section 4.3 the electrical field and polarization updates are performed prior to the carrier update, so that the field values at both time steps m and $m+1$ are known. Therefore, the *source-term* b can be evaluated with the trapezoidal rule $b_{m+\frac{1}{2}} \approx \frac{b_{m+1}+b_m}{2}$ and the term dependent on n_m^{qw} yields

$$R(n_m^{\mathrm{qw}}) - \frac{\partial R}{\partial n^{\mathrm{qw}}}|_{n_m^{\mathrm{qw}}} n_m^{\mathrm{qw}} = B_{\mathrm{sp}} (n_m^{\mathrm{qw}})^2 + 2C_{\mathrm{A}} (n_m^{\mathrm{qw}})^3 . \tag{C.84}$$

The partial derivatives with respect to the transverse direction (in the case of a QW only the lateral direction) remain in H

$$H = -A_{\mathrm{nr}} - 2B_{\mathrm{sp}} n_m^{\mathrm{qw}} - 3C_{\mathrm{A}} (n_m^{\mathrm{qw}})^2 + D\partial_y^2, \tag{C.85}$$

and all terms proportional to n_n^{qw} are collected in the operator

$$H_{\mathrm{R}} = -A_{\mathrm{nr}} + D\partial_y^2 + B_{\mathrm{sp}} n_m^{\mathrm{qw}} + 2C_{\mathrm{A}} (n_m^{\mathrm{qw}})^2 . \tag{C.86}$$

Although the computational cost is higher as for the explicit scheme, due to the stability the standard Crank-Nicolson scheme is applied which leads to an implicit expression for the carrier density at the next time step

$$\left(1 - \frac{\Delta t}{2} H\right) n_{m+1}^{\mathrm{qw}} = \left(1 + \frac{\Delta t}{2} H_{\mathrm{R}}\right) n_m^{\mathrm{qw}} + \Delta t R_{0,m+\frac{1}{2}} \tag{C.87}$$

where $R_{0,m+\frac{1}{2}}$ includes the generation and stimulated recombination terms. To ensure numerical stability the scaled quantities $\tilde{D} = \frac{Dt_0}{x_0^2}$, $\tilde{n}^{\mathrm{qw}} = \frac{n^{\mathrm{qw}}}{N_0}$, $\tilde{J} = Jx_0^2 t_0$, $\tilde{A} = At_0$, $\tilde{t} = \frac{t}{t_0}$, $\tilde{x}_i = \frac{x_i}{x_0}$ are introduced. For the time scale t_0 values in the order of the magnitude of τ_{nr} which are a few nanoseconds are used and for the length scale a typical value of $x_0 = 1\,\mu\mathrm{m}$ is used. The scale for the carrier densities is set to $N_0 = 1 \cdot 10^{24}\,/\mathrm{m}^3$.

C.12 Complex-Conjugate Pole-Residue Pairs

The dispersion of the permittivity is modeled by complex-conjugate pole-residue pairs according to [64]

$$\varepsilon(\omega) = \varepsilon_0\varepsilon_\infty + \varepsilon_0 \sum_{p=1}^{P} \frac{c_p}{i\omega - a_p} + \frac{c_p^*}{i\omega - a_p^*}, \tag{C.88}$$

where P is the total number of complex pole pairs. The electric susceptibility expressed by the complex-conjugate pole-residue pairs is

$$\begin{aligned}
\chi(\omega) &= \varepsilon_\infty - 1 + \sum_{p=1}^{P} \frac{c_p}{i\omega - a_p} + \frac{c_p^*}{i\omega - a_p^*} \\
&= \varepsilon_\infty - 1 + \sum_{p=1}^{P} \frac{c_p' + ic_p''}{i\omega - a_p' - ia_p''} + \frac{c_p' - ic_p''}{i\omega - a_p' + ia_p''} \\
&= \varepsilon_\infty - 1 + 2 \cdot \sum_{p=1}^{P} \frac{i\omega c_p' - c_p' a_p' - c_p'' a_p''}{a_p'^2 + a_p''^2 - 2ia_p'\omega - \omega^2} \\
&= \varepsilon_\infty - 1 + 2 \cdot \sum_{p=1}^{P} \frac{\left(-c_p' a_p' - c_p'' a_p''\right)\left(a_p'^2 + a_p''^2 - \omega^2\right) - 2a_p'\omega^2 c_p'}{\left(a_p'^2 + a_p''^2 - \omega^2\right)^2 + 4a_p'^2\omega^2} \\
&\quad + 2i\omega \cdot \sum_{p=1}^{P} \frac{-\left(c_p' a_p' + c_p'' a_p''\right) 2a_p' + c_p'\left(a_p'^2 + a_p''^2 - \omega^2\right)}{\left(a_p'^2 + a_p''^2 - \omega^2\right)^2 + 4a_p'^2\omega^2},
\end{aligned} \tag{C.89}$$

with $a_p = a_p' + ia_p''$ and $c_p = c_p' + ic_p''$. Both a_p and c_p have the unit $\mathrm{rad\,s^{-1}}$.

C.13 Components of Matrix Operator for BPM

The entries of the matrix operator $R_{\mu\nu}$ in Eq. (4.64) are

$$\begin{aligned}
\left(R \cdot \phi_\mathrm{t}\right)_\mu &= R_{\mu\nu}\phi_\nu \\
&= \partial_{ii}\phi_\mu + k_0^2\left(n_{\mu\nu}^2 - n_{\mathrm{ref}}^2\delta_{\mu,\nu}\right)\phi_\nu - \partial_\mu\partial_i\phi_i + \partial_\mu\left(\frac{1}{n_{zz}^2}\cdot\partial_j\left(n_{j\nu}^2\phi_\nu\right)\right) \\
&= \partial_i\delta_{\mu\nu}\delta_{ij}\partial_j\phi_\nu + k_0^2\left(n_{\mu\nu}^2 - n_{\mathrm{ref}}^2\delta_{\mu\nu}\right)\phi_\nu - \partial_i\partial_j\delta_{j\mu}\delta_{i\nu}\phi_\nu \\
&\quad + \partial_i\left(\delta_{i\mu}\frac{1}{n_{zz}^2}D_\nu\phi_\nu\right) + \partial_i\left(\delta_{i\mu}\frac{1}{n_{zz}^2}n_{j\nu}^2\left(\partial_j\phi_\nu\right)\right).
\end{aligned} \tag{C.90}$$

In the last step we introduced $D_\nu = \partial_j n_{j,\nu}^2$. The components of the matrix operator written explicitly are

$$\begin{aligned} R_{xx}\phi_x &= \partial_{yy}\phi_x + \left(n_{xx}^2 - n_{\text{ref}}^2\right) \cdot \left(\frac{\omega}{c_0}\right)^2 \phi_x + \partial_x \left(\frac{1}{n_{zz}^2}\partial_x \left(n_{xx}^2\phi_x\right)\right) \\ &\quad + \partial_x \left(\frac{1}{n_{zz}^2}\partial_y \left(n_{yx}^2\phi_x\right)\right) \\ \Leftrightarrow R_{xx}\phi_x &= \partial_{yy}\phi_x + \left(n_{xx}^2 - n_{\text{ref}}^2\right) \cdot \left(\frac{\omega}{c_0}\right)^2 \phi_x + \partial_x \left(\frac{n_{xx}^2}{n_{zz}^2}\partial_x\phi_x\right) \\ &\quad + \partial_x \left(\frac{1}{n_{zz}^2} 2n_{xx} \left(\partial_x n_{xx}\right) \phi_x\right) \\ &\quad + \partial_x \left(\frac{n_{yx}^2}{n_{zz}^2}\partial_y\phi_x\right) + \partial_x \left(\frac{1}{n_{zz}^2} 2n_{yx} \left(\partial_y n_{yx}\right) \phi_x\right), \end{aligned} \tag{C.91}$$

and

$$\begin{aligned} R_{xy}\phi_y &= n_{xy}^2 \left(\frac{\omega}{c_0}\right)^2 \phi_y - \partial_{xy}\phi_y + \partial_x \left(\frac{1}{n_{zz}^2}\partial_y \left(n_{yy}^2\phi_y\right)\right) + \partial_x \left(\frac{1}{n_{zz}^2}\partial_x \left(n_{xy}^2\phi_y\right)\right) \\ \Leftrightarrow R_{xy}\phi_y &= n_{xy}^2 \left(\frac{\omega}{c_0}\right)^2 \phi_y - \partial_{xy}\phi_y + \partial_x \left(\frac{n_{yy}^2}{n_{zz}^2}\partial_y\phi_y\right) + \partial_x \left(\frac{1}{n_{zz}^2} 2n_{yy} \left(\partial_y n_{yy}\right) \phi_y\right) \\ &\quad + \partial_x \left(\frac{n_{xy}^2}{n_{zz}^2}\partial_x\phi_y\right) + \partial_x \left(\frac{1}{n_{zz}^2} 2n_{xy} \left(\partial_x n_{xy}\right) \phi_y\right). \end{aligned} \tag{C.92}$$

The equality

$$\begin{aligned} &-\partial_{xx}\phi_x + \partial_x \left(\frac{1}{n_{zz}^2}\partial_x \left(n_{xx}^2\phi_x\right)\right) \\ &= -\partial_{xx}\phi_x + \partial_x \left(\frac{1}{n_{zz}^2} 2n_{xx} \left(\partial_x n_{xx}\right) \phi_x + \frac{n_{xx}^2}{n_{zz}^2}\partial_x\phi_x\right) \\ &= \partial_x \left(\left(\frac{n_{xx}^2}{n_{zz}^2} - 1\right)\partial_x\phi_x\right) + \partial_x \left(\frac{1}{n_{zz}^2} 2n_{xx} \left(\partial_x n_{xx}\right) \phi_x\right) \end{aligned} \tag{C.93}$$

is used to rewrite the equations. The following relation is used in the derivation

$$\begin{aligned} &\partial_\mu \left(2/n_{j,j}^2 n_{\nu,l} \left(\partial_\nu n_{\nu,l}\right) \phi_l\right) \\ &\Leftrightarrow \partial_i \delta_{\mu,i} \left(1/n_{d-1,d-1}^2 n_{\nu,l} D_{\nu,l} \phi_l\right) \end{aligned} \tag{C.94}$$

with

$$D_{i,j} = \partial_i n_{i,j}. \tag{C.95}$$

C.14 Demonstration of Beam Propagation

For demonstration, the BPM is utilized to compute the propagation of a Gaussian field distribution. The propagation of a Gaussian field distribution can be described analytically so that the beam width over propagation distance obtained by the BPM is compared to the analytical one, see Fig. C.1. The power in the transverse plane is

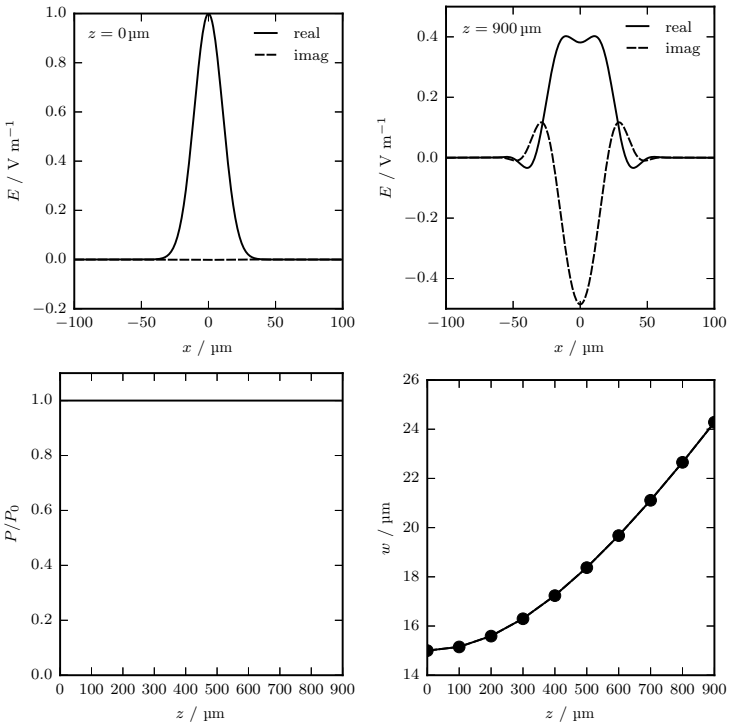

FIGURE C.1: Propagation of a Gaussian field distribution with beam waist $w_0 = 15\,\mu\text{m}$ and wavelength $\lambda = 1\,\mu\text{m}$ on a two-dimensional transverse mesh (coordinates x, y) along the z-direction. The transverse resolution is 256×256 grid points and each propagation step is $1\,\mu\text{m}$. The electrical field strength at $z = 0\,\mu\text{m}$ (top left) and $z = 900\,\mu\text{m}$ (top right) is displayed. The markers indicate the beam widths for the analytical solution $w(z) = \sqrt{1 + \left(\frac{z}{z_\text{R}}\right)^2}$. P_0 is the initial power.

constant throughout the propagation and the beam radius follows the one calculated with the analytical solution.

C.15 Complex Matrix Vector Multiplication

To reduce a complex matrix vector multiplication

$$Ax = b, \tag{C.96}$$

where $A \in \mathbb{C}^{n\times n}$ and $x, b \in \mathbb{C}^n$ to a real one with $A', A'' \in \mathbb{R}^{n\times n}$ and $x', x'', b', b'' \in \mathbb{R}^n$ and $A = A' + iA''$, $x = x' + ix''$, and $b = b' + ib''$, respectively, we write

$$\begin{aligned} &\left(A' + iA''\right) \cdot \left(x' + ix''\right) = b' + ib'' \\ \Leftrightarrow\ &A'x' + iA'x'' + iA''x' - A''x'' = b' + ib'' \\ \Leftrightarrow\ &\begin{pmatrix} A' & -A'' \\ A'' & A' \end{pmatrix} \cdot \begin{pmatrix} x' \\ x'' \end{pmatrix} = \begin{pmatrix} b' \\ b'' \end{pmatrix}. \end{aligned} \tag{C.97}$$

Note that the matrix for the real representation is an element of $\mathbb{R}^{2n\times 2n}$ and the vectors are elements of $\mathbb{R}^{2n}$, respectively.

C.16 Substitute Equations for Derivation of the Vectorial Wave Equation

For an electric field vector

$$\vec{E} = \begin{pmatrix} \vec{E}_t \\ E_z \end{pmatrix} = \begin{pmatrix} E_x \\ E_y \\ E_z \end{pmatrix}, \tag{C.98}$$

separated into transverse and longitudinal components with the separated vector

$$\vec{E}_s = \begin{pmatrix} E_x \\ E_y \\ 0 \end{pmatrix}, \tag{C.99}$$

including only the transverse components, the following equations hold

$$\begin{aligned} \nabla_s \times \vec{E}_s &= \begin{pmatrix} 0 \\ 0 \\ \partial_x E_y - \partial_y E_x \end{pmatrix}, \\ \nabla_s \times \nabla_s \times \vec{E}_s &= \begin{pmatrix} \partial_y \left(\partial_x E_y - \partial_y E_x\right) \\ -\partial_x \left(\partial_x E_y - \partial_y E_x\right) \\ 0 \end{pmatrix}, \\ \nabla_s \times \nabla_s \times \vec{E} &= \nabla_s \times \nabla_s \times \vec{E}_s - \left(\partial_x^2 + \partial_y^2\right) E_z \vec{e}_z, \\ \nabla_s \times \nabla_s \times E_z &= -\partial_z^2 \vec{E}_s, \\ \nabla_z \times \nabla_z \times \vec{E} &= -\partial_z^2 \vec{E}_s, \\ \nabla_s \times \nabla_z \times \vec{E} &= \vec{e}_z \partial_z \nabla_s \cdot \vec{E}_s, \\ \nabla_z \times \nabla_s \times \vec{E} &= \partial_z \nabla_s E_z. \end{aligned} \tag{C.100}$$

C.17 Weak Form of Wave Equation

To derive a weak form for complex functions $u, v \in \mathbb{C}^d$ the complex version of the inner product

$$\begin{aligned}\langle u, v\rangle = \langle u_\mathrm{r} + iu_\mathrm{i}, v_\mathrm{r} + iv_\mathrm{i}\rangle &= \int_\Omega uv^* \,\mathrm{d}^d x \\ &= \int_\Omega u_\mathrm{r}v_\mathrm{r} + u_\mathrm{i}v_\mathrm{i} + iu_\mathrm{i}v_\mathrm{r} - iu_\mathrm{r}v_\mathrm{i} \,\mathrm{d}^d x \end{aligned} \tag{C.101}$$

is used. Multiplication of the TD envelope wave-equation (4.26) with the test function

$$\vec{v} = \begin{pmatrix} v_x \\ v_y \\ v_z \end{pmatrix} = \vec{v}_s + v_z\vec{e}_z \tag{C.102}$$

where $\vec{e}_z$ is the unit vector in longitudinal direction and the transverse components of the test function are

$$\vec{v}_s = \begin{pmatrix} v_x \\ v_y \\ 0 \end{pmatrix}. \tag{C.103}$$

leads to

$$\begin{aligned}&\left(\nabla_s \times \nabla_s \times \vec{\phi}_s^{\pm}\right) \cdot \vec{v}_s^* - \left(\partial_x^2 + \partial_y^2\right)\phi_z^{\pm} v_z^* + \left(\partial_z\left(\nabla_s \cdot \vec{\phi}_s^{\pm}\right)\right) v_z^* \\ &\pm ik_\mathrm{ref}\left(\nabla_s \cdot \vec{\phi}_s^{\pm}\right) v_z^* + \left(\partial_z\left(\nabla_s \phi_z^{\pm}\right)\right) \cdot \vec{v}_s^* \pm ik_\mathrm{ref}\left(\nabla_s \phi_z^{\pm}\right) \cdot \vec{v}_s^* \\ &+ k_\mathrm{ref}^2 \vec{\phi}_s^{\pm} \cdot \vec{v}_s^* \mp 2ik_\mathrm{ref}\left(\partial_z \vec{\phi}_s^{\pm}\right) \cdot \vec{v}_s^* - \left(\partial_z^2 \vec{\phi}_s^{\pm}\right) \cdot \vec{v}_s^* \\ &+ \frac{1}{c_0^2}\left(\partial_t^2 - 2i\omega_\mathrm{ref}\partial_t - \omega_\mathrm{ref}^2\right)\left(\mu_r\varepsilon_r\vec{\phi}_s^{\pm} \cdot \vec{v}^* + \mu_r\varepsilon_r\phi_z^{\pm}\vec{e}_z \cdot \vec{v}_s^*\right) = 0. \end{aligned} \tag{C.104}$$

We integrate over the two dimensional transverse domain (in the x and y coordinates) and perform partial integration for terms with second order derivatives to get

$$\begin{aligned}&\int_\Omega \left(\partial_x\phi_y^{\pm} - \partial_y\phi_x^{\pm}\right)\left(\partial_x v_y^* - \partial_y v_x^*\right) + \nabla_t\phi_z^{\pm} \cdot \nabla_t v_z^* - \left(\partial_z\vec{\phi}_t^{\pm}\right) \cdot \nabla_t v_z^* \\ &\mp ik_\mathrm{ref}\vec{\phi}_t^{\pm} \cdot \nabla_t v_z^* + \nabla_t\left(\partial_z\phi_z^{\pm}\right) \cdot \vec{v}_t^* \pm ik_\mathrm{ref}\nabla_t\phi_z^{\pm} \cdot \vec{v}_t^* \\ &+ k_\mathrm{ref}^2\vec{\phi}_t^{\pm} \cdot \vec{v}_t^* \mp 2ik_\mathrm{ref}\left(\partial_z\vec{\phi}_t^{\pm}\right) \cdot \vec{v}_t^* - \left(\partial_z^2\vec{\phi}_t^{\pm}\right) \cdot \vec{v}_t^* \\ &+ \frac{\mu_r}{c_0^2}\left(\partial_t^2 - 2i\omega_\mathrm{ref}\partial_t - \omega_\mathrm{ref}^2\right) \\ &\quad\times \left(\left(\varepsilon_{r,t}\vec{\phi}_t^{\pm}\right) \cdot \vec{v}_t^* + \varepsilon_{z,t} \cdot \vec{\phi}_t v_z^* + \varepsilon_{zz}\phi_z^{\pm}v_z^* + \varepsilon_{z,t} \cdot \vec{v}_t^*\phi_z^{\pm}\right)\mathrm{d}x\,\mathrm{d}y = 0, \end{aligned} \tag{C.105}$$

where surface terms arising from partial integration vanish due to Neumann conditions, which are applied for all boundaries. Note that we used the fact that the permeability is a isotropic tensor in the last line to separate it from the tensor multiplications. The

following relations are used in the above derivation:

$$\varepsilon\vec{\phi}_s = \begin{pmatrix} \varepsilon_{xx}\phi_x - \varepsilon_{xy}\phi_y \\ \varepsilon_{yx}\phi_x - \varepsilon_{yy}\phi_y \\ \varepsilon_{zx}\phi_x - \varepsilon_{zy}\phi_y \end{pmatrix}, \tag{C.106}$$

and

$$\varepsilon\vec{e}_z\phi_z = \begin{pmatrix} \varepsilon_{xz} \\ \varepsilon_{yz} \\ \varepsilon_{zx} \end{pmatrix} \tag{C.107}$$

and

$$\left(\nabla_s \times \nabla_s \times \vec{\phi}_s\right) \cdot \vec{v}_s^* = \partial_y \left(\partial_x\phi_y - \partial_y\phi_x\right) v_x - \partial_x \left(\partial_x\phi_y - \partial_y\phi_x\right) v_y. \tag{C.108}$$

The term in the wave equation including the rotations can be rewritten in a simpler form. Partial integration (and again dropping surface integrals due to Neumann boundaries) leads to

$$\begin{aligned} &\int_\Omega \left(\nabla_s \times \nabla_s \times \vec{\phi}_s\right) \cdot \vec{v}_s^* \,\mathrm{d}x\,\mathrm{d}y \\ &= \int_\Omega -\left(\partial_x\phi_y - \partial_y\phi_x\right)\partial_y v_x + \left(\partial_x\phi_y - \partial_y\phi_x\right)\partial_x v_y \,\mathrm{d}x\,\mathrm{d}y \\ &= \int_\Omega \left(\partial_x\phi_y - \partial_y\phi_x\right)\left(\partial_x v_y - \partial_y v_x\right) \mathrm{d}x\,\mathrm{d}y \\ &= \int_\Omega \mathrm{curl}_t(\vec{\phi}_t)\mathrm{curl}_t(\vec{v}_t^*)\,\mathrm{d}x\,\mathrm{d}y. \end{aligned} \tag{C.109}$$

In the last step with the help of (C.100) the projected tangential curl operator

$$\mathrm{curl}_t(\vec{E}_t) = \partial_x E_y - \partial_y E_x \tag{C.110}$$

which returns just the non-zero parts of the previously calculated rotation is used to write the weak form of the differential equation in a more compact form. For FEM descritization the choice of two dimensional curl-conserving vector basis functions for the transverse fields $\vec{\phi}_t \in H(\mathrm{curl}, \Omega)$ and a Lagrange polynomal space for the longitudinal component $\phi_z \in H^1(\Omega)$ leads to a stable computation scheme. For the curl-conserving elements the Nédélec function space introduced in [55] is employed.

C.18 Iterated Crank-Nicolson Scheme

The ICN scheme [65] can be utilized for a parabolic differential equation of the form

$$\partial_\eta\phi = H\phi + b \tag{C.111}$$

to derive an explicit expression for the derivative with respect to η and update of the field ϕ. Operator H contains second order spatial derivatives. In a first step the derivative is approximated by

$$\frac{\phi_{n+1}^{(1)} - \phi_n}{\Delta\eta} = H\phi_n. \tag{C.112}$$

The field value at the intermediate step is approximated by a weighted average

$$\phi^{(1)}_{n+\frac{1}{2}} = a_1 \phi^{(1)}_{n+1} + (1 - a_1)\, \phi_n \tag{C.113}$$

with weighting factor a_1. The derivative for the second iteration step is approximated with the help of the averaged value from the intermediate step

$$\frac{\phi^{(2)}_{n+1} - \phi_n}{\Delta\eta} = H \phi^{(1)}_{n+\frac{1}{2}}, \tag{C.114}$$

followed by a similar estimation of the intermediate value for the second iteration step approximated by a second weighted average

$$\phi^{(2)}_{n+\frac{1}{2}} = a_2 \phi^{(2)}_{n+1} + (1 - a_2)\, \phi_n, \tag{C.115}$$

with weighting factor a_2. Finally, the discrete derivative from step n to step $n + 1$ is approximated with

$$\frac{\phi_{n+1} - \phi_n}{\Delta\eta} = H \phi^{(2)}_{n+\frac{1}{2}}. \tag{C.116}$$

The previous definitions for the first and second step can be sucsessively inserted into the equation from the previous line to get

$$\begin{aligned} \phi_{n+1} = {} & \left(1 + (\Delta\eta H) + a_2(\Delta\eta H)^2 + a_1 a_2 (\Delta\eta H)^3\right) \phi_n \\ & + \left(1 + a_2(\Delta\eta H) + a_1 a_2 (\Delta\eta H)^2\right) \Delta\eta b, \end{aligned} \tag{C.117}$$

which delivers an explicit expression for the calculation of the field at the new step. For the above derivation we assumed that the operator H and the term b are independent of the coordinate η. The weighting constants for the averages are $a_1 = a_2 = \frac{1}{2}$.

C.19 Interpolation

The quadratic interpolation between three materials AC, BC and the alloy $A_{x_0}B_{1-x_0}C$ is calculated from x the fraction of the alloy, x_0 fraction that material A has in the alloy $A_{x_0}B_{1-x_0}C$, v_{AC} value of the property of material AC, v_{BC} value of the property of material BC, v_{ABC} value of the alloy. For $A_xB_{1-x}C$

$$v_{BC} + (v_{AC} - v_{BC})x + \left(\frac{v_{ABC}}{(x_0(1-x_0))} - \frac{v_{AC}}{(1-x_0)} - \frac{v_{BC}}{x_0} \right) x(1-x) \tag{C.118}$$

is the interpolated value.

To interpolate the value of a ternary compound $A_xB_{1-x}C$ of two binary materials AC and BC with parameters v_{AC} and v_{BC} with the help of the bowing factor K_{ABC} the formula

$$v_{ABC} = x v_{AC} + (1-x) v_{BC} - x(1-x) K_{ABC} \tag{C.119}$$

is used. If the bowing factor K_{ABC} is zero, a linear interpolation is performed.

Bibliography

[1] S. Ried, S. Rauch, L. Irmler, J. Rikels, A. Killi, E. Papastathopoulos, E. Sarailou, and H. Zimer, "Next generation diode lasers with enhanced brightness," in *High-Power Diode Laser Technology XVI, Proc. SPIE*, vol. 10514, 2018.

[2] H.-D. Hoffmann, U. Witte, C. Holly, and S. Hengesbach, "Diodenlaserstrahlquellen: Technologieschub für Direktanwendungen," *Lasermagazin*, no. 1, pp. 26–28, 2015.

[3] S. O'Brien, H. Zhao, A. Schoenfelder, and R. J. Lang, "9.3 W CW (In)AlGaAs 100 µm wide lasers at 970 nm," *Electronics Letters*, vol. 33, pp. 1869–1871, Oct. 1997.

[4] S. Rauch, P. Modak, C. Holly, and H. Zimer, "Beam quality improvement of broad-area laser diodes by symmetric facet reflectivities," in *2018 IEEE International Semiconductor Laser Conference (ISLC)*, pp. 1–2, Sept. 2018.

[5] C. Holly, X. Liu, S. Heinemann, S. McDougall, and H. Zimer, "Influence of lateral refractive index profiles on the divergence angle of gain-guided broad-area laser diode bars," *31st Annual Conference of the IEEE Photonics Society*, 2018.

[6] X. Liu, C. Holly, C.-L. Jiang, Y. Xiong, S. McDougall, K. Boucke, H. Zimer, and B. Schmidt, "Electro-optical efficiency and slow axis far-field improvement of high power laser diode bars using epitaxy structure optimization," in *2017 IEEE High Power Diode Lasers and Systems Conference (HPD)*, pp. 33–34, Oct. 2017.

[7] C. Harder, "High power laser diodes," in *The 17th Annual Meeting of the IEEE-Lasers and Electro-Optics Society, 2004. LEOS 2004.*, vol. 1, pp. 3–4 Vol.1, Nov. 2004.

[8] C. Hinke, S. Merkt, F. Eibl, J. Schrage, and S. Bremen, "Additive manufacturing: perspectives for diode lasers," *2015 IEEE High Power Diode Lasers and Systems Conference (HPD)*, pp. 39–40, Oct. 2015.

[9] M. Kanskar, S. Keeney, and R. Martinsen, "Laser diodes: The power of brilliance – the past and future of high-power semiconductor lasers," *Laser Focus World*, vol. 54, 2018.

[10] F. Bachmann, P. Loosen, and R. Poprawe, eds., *High Power Diode Lasers*. Springer Science+Business Media, LLC, New York, 2007.

[11] S. Rauch, H. Wenzel, M. Radziunas, M. Haas, G. Tränkle, and H. Zimer, "Impact of longitudinal refractive index change on the near-field width of high-power broad-area diode lasers," *Applied Physics Letters*, vol. 110, no. 26, p. 263504, 2017.

[12] P. Crump, S. Hengesbach, U. Witte, H.-D. Hoffmann, G. Erbert, and G. Tränkle, "High-power diode lasers optimized for low-loss smile-insensitive external spectral stabilization," *IEEE Photonics Technology Letters*, vol. 24, pp. 703 – 705, Feb. 2012.

[13] D. Mehuys, R. Lang, M. Mittelstein, J. Salzman, and A. Yariv, "Self-stabilized nonlinear lateral modes of broad area lasers," *IEEE Journal of Quantum Electronics*, vol. 23, pp. 1909 – 1920, 1987.

[14] Crosslight Software Inc., "crosslight." `http://crosslight.com/products/pics3d`, accessed Dec. 2017.

[15] G. P. Agrawal, W. B. Joyce, R. W. Dixon, and M. Lax, "Beam-propagation analysis of stripe-geometry semiconductor lasers: Threshold behavior," *Applied Physics Letters*, vol. 43, no. 1, pp. 11–13, 1983.

[16] G. P. Agrawal, "Effect of index antiguiding on the far-field distribution of stripe-geometry lasers," *Optics Communications*, vol. 47, no. 4, pp. 283 – 287, 1983.

[17] G. P. Agrawal, "Fast-fourier-transform based beam-propagation model for stripe-geometry semiconductor lasers: Inclusion of axial effects," *Journal of Applied Physics*, vol. 56, no. 11, pp. 3100–3109, 1984.

[18] G. R. Hadley, J. Hohimer, and A. Owyoung, "Free-running modes for gain-guided diode laser arrays," *IEEE Journal of Quantum Electronics*, vol. 23, pp. 765–774, June 1987.

[19] G. R. Hadley, J. P. Hohimer, and A. Owyoung, "Comprehensive modeling of diode arrays and broad-area devices with applications to lateral index tailoring," *IEEE Journal of Quantum Electronics*, vol. 24, pp. 2138–2152, Nov. 1988.

[20] R. J. Lang, A. Hardy, R. Parke, D. Mehuys, S. O'Brien, J. Major, and D. F. Welch, "Numerical analysis of flared semiconductor laser amplifiers," *IEEE Journal of Quantum Electronics*, vol. 29, pp. 2044–2051, June 1993.

[21] R. J. Lang, D. Mehuys, A. Hardy, K. M. Dzurko, and D. F. Welch, "Spatial evolution of filaments in broad area diode laser amplifiers," *Applied Physics Letters*, vol. 62, no. 11, pp. 1209–1211, 1993.

[22] Z. Dai, R. Michalzik, P. Unger, and K. J. Ebeling, "Numerical simulation of broad-area high-power semiconductor laser amplifiers," *IEEE Journal of Quantum Electronics*, vol. 33, pp. 2240–2254, Dec. 1997.

[23] L. Borruel, S. Sujecki, P. Moreno, J. Wykes, M. Krakowski, B. Sumpf, P. Sewell, S. C. Auzanneau, H. Wenzel, D. Rodriguez, T. M. Benson, E. C. Larkins, and I. Esquivias, "Quasi-3-d simulation of high-brightness tapered lasers," *IEEE Journal of Quantum Electronics*, vol. 40, pp. 463–472, May 2004.

[24] S. Balsamo, F. Sartori, and I. Montrosset, "Dynamic beam propagation method for flared semiconductor power amplifiers," *IEEE Journal of Selected Topics in Quantum Electronics*, vol. 2, pp. 378–384, June 1996.

[25] J. V. Moloney, R. A. Indik, and C. Z. Ning, "Full space-time simulation for high-brightness semiconductor lasers," *IEEE Photonics Technology Letters*, vol. 9, pp. 731–733, June 1997.

[26] R. Čiegis, M. Radziunas, and M. Lichtner, "Numerical algorithms for simulation of multisection lasers by using traveling wave model," *Mathematical Modelling and Analysis*, vol. 13, pp. 327–348, Sept. 2008.

[27] WIAS-Berlin, "BALaser, A software tool for simulation of dynamics in broad area semiconductor lasers." `https://www.wias-berlin.de/software/balaser`, accessed Jan. 2019.

[28] C. Holly, S. Hengesbach, M. Traub, and H.-D. Hoffmann, "Simulation of spectral stabilization of high-power broad-area edge emitting semiconductor lasers," *Opt. Express*, vol. 21, pp. 15553–15567, July 2013.

[29] C. Holly, S. Hengesbach, M. Traub, and H.-D. Hoffmann, "Numerical analysis of external feedback concepts for spectral stabilization of high-power broad-area semiconductor lasers," in *High-Power Diode Laser Technology and Applications XII, Proc. SPIE*, vol. 8965, pp. 8965 – 8965 – 8, 2014.

[30] S. L. Chuang, *Physics in Optoelectronic Devices*. Wiley series in pure and applied optics, New York: John Wiley & Sons, Inc., New York, 1995.

[31] T. Andlauer, "Discretization of multiband-k·p-Schrödinger equations for multidimensional semiconductor nanostructures," Master's thesis, Technische Universität München, 2004.

[32] C. Holly, "Numerical solution of k·p-Schrödinger equations for semiconductor nano-structures using box-discretization," Bachelor's thesis, Chair for Technology of Optical Systems, RWTH Aachen University, Aachen, 2013.

[33] J. R. Chelikowsky and M. L. Cohen, "Nonlocal pseudopotential calculations for the electronic structure of eleven diamond and zinc-blende semiconductors," *Physical Review B*, vol. 14, pp. 556–580, 1976.

[34] P. Löwdin, "A note on the quantum mechanical perturbation theory," *J. Chem. Phys.*, vol. 19, no. 1396, 1951.

[35] G. Liu and S. L. Chuang, "Modeling of Sb-based type-II quantum cascade lasers," *Physical Review B*, vol. 65, no. 165220, 2002.

[36] S. W. Koch and W. W. Chow, *Semiconductor-Laser Fundamentals*. Berlin, Heidelberg: Springer, 1999.

[37] X. Li, *Optoelectronic Devices - Design, Modeling, and Simulation*. Cambridge University Press, 2009.

[38] J. Piprek, *Optoelectronic Devices - Advanced Simulation and Analysis*. Springer-Verlag New York, 2005.

[39] J. Stohs, D. J. Bossert, D. J. Gallant, and S. R. J. Brueck, "Gain, refractive index change, and linewidth enhancement factor in broad-area gaas and ingaas quantum-well lasers," *IEEE Journal of Quantum Electronics*, vol. 37, pp. 1449–1459, Nov. 2001.

[40] B. Witzigmann, A. Witzig, and W. Fichtner, "A full 3-dimensional quantum well laser simulation," *Intl. Workshop on Computational Electronics*, pp. 13 – 14, 2000.

[41] P. S. Zory, *Quantum well lasers / edited by Peter S. Zory, Jr.* Academic Press Boston, 1993.

[42] K. Bulashevich, V. F Mymrin, S. Karpov, D. M Demidov, and A. L Ter-Martirosyan, "Effect of free-carrier absorption on performance of 808 nm algaas-based high-power laser diodes," *Semiconductor Science and Technology*, vol. 22, p. 502, Mar. 2007.

[43] B. S. Ooi, K. McIlvaney, M. W. Street, A. S. Helmy, S. G. Ayling, A. C. Bryce, J. H. Marsh, and J. S. Roberts, "Selective quantum-well intermixing in gaas-algaas structures using impurity-free vacancy diffusion," *IEEE Journal of Quantum Electronics*, vol. 33, pp. 1784–1793, Oct. 1997.

[44] H. C. Casey, "Room-temperature threshold-current dependence of GaAs-$Al_xGa_{1-x}As$ double-heterostructure lasers on x and active-layer thickness," *Journal of Applied Physics*, vol. 49, no. 7, pp. 3684–3692, 1978.

[45] C. H. Henry, R. A. Logan, and K. A. Bertness, "Spectral dependence of the change in refractive index due to carrier injection in gaas lasers," *Journal of Applied Physics*, vol. 52, no. 7, pp. 4457–4461, 1981.

[46] B. R. Bennett, R. A. Soref, and J. A. D. Alamo, "Carrier-induced change in refractive index of InP, GaAs and InGaAsP," *IEEE Journal of Quantum Electronics*, vol. 26, pp. 113–122, Jan. 1990.

[47] H. Wenzel, G. Erbert, and P. M. Enders, "Improved theory of the refractive-index change in quantum-well lasers," *IEEE Journal of Selected Topics in Quantum Electronics*, vol. 5, pp. 637–642, May 1999.

[48] R. Marciante and G. Agrawal, "Controlling filamentation in broad-area semiconductor lasers and amplifiers," *Applied Physics Letters*, vol. 69, pp. 593 – 595, Aug. 1996.

[49] L. A. Coldren, M. L. Mašanović, and S. W. Corzine, *Diode Lasers and Photonic Integrated Circuits, Second Edition.* John Wiley & Sons, Inc., New York, 2012.

[50] M. Szymanski, "Mathematical models of heat flow in edge-emitting semiconductor lasers," in *Heat Transfer - Engineering Applications* (V. S. Vikhrenko, ed.), IntechOpen, Dec. 2011.

[51] S. Rauch, C. Holly, and H. Zimer, "Catastrophic optical damage in 950-nm broad-area laser diodes due to misaligned optical feedback and injection," *IEEE Journal of Quantum Electronics*, vol. 54, pp. 1–7, Aug. 2018.

[52] O. Loebich, "The optical properties of gold," *Gold Bulletin - GOLD BULL*, vol. 5, pp. 2–10, Mar. 1972.

[53] J. Souto, J. L. Pura, M. Rodríguez, J. Anaya, A. Torres, and J. Jimenéz, "Mechanisms driving the catastrophic optical damage in high-power laser diodes," in *High-Power Diode Laser Technology and Applications XIII, Proc. SPIE*, vol. 9348, pp. 93480–93480, Mar. 2015.

[54] R. Schatz and C. G. Bethea, "Steady state model for facet heating leading to thermal runaway in semiconductor lasers," *Journal of Applied Physics*, vol. 76, no. 4, pp. 2509–2521, 1994.

[55] J.-C. Nédélec, "Mixed finite elements in $\mathbb{R}^3$," *Numer. Math.*, vol. 35, p. 315–341, 1980.

[56] J. D. Jackson, *Classical electrodynamics*. New York: Wiley, 3rd ed., 1999.

[57] S. Balle, "Effective two-level-model with asymmetric gain for laser diodes," *Optics Communications*, vol. 119, no. 1, pp. 227 – 235, 1995.

[58] C. Z. Ning, R. A. Indik, and J. V. Moloney, "Effective bloch equations for semiconductor lasers and amplifiers," *IEEE Journal of Quantum Electronics*, vol. 33, pp. 1543–1550, Sept. 1997.

[59] U. Bandelow, M. Radziunas, J. Sieber, and M. Wolfrum, "Impact of gain dispersion on the spatio-temporal dynamics of multisection lasers," *IEEE Journal of Quantum Electronics*, vol. 37, pp. 183–188, Feb. 2001.

[60] C. L. Xu and W. P. Huang, "Finite-difference beam popagation method for guide-wave optics," *Progress In Electromagnetics Research*, vol. 11, pp. 1–49, 1995.

[61] C. Z. Ning, J. V. Moloney, A. Egan, and R. A. Indik, "A first-principles fully space - time resolved model of a semiconductor laser," *Quantum and Semiclassical Optics: Journal of the European Optical Society Part B*, vol. 9, no. 5, p. 681, 1997.

[62] J. Park and Y. Kawakami, "Time-domain models for the performance simulation of semiconductor optical amplifiers," *Opt. Express*, vol. 14, pp. 2956–2968, Apr. 2006.

[63] E. S. Solberg, "Simulation of electro-optic modulators by a time-domain beam-propagation method," Thesis for the degree of licentiate of philosophy, Department of Mathematical Sciences, Division of Mathematics, Chalmers University of Technology and University of Gothenburg, Gothenburg, 2015.

[64] M. Han, R. W. Dutton, and S. Fan, "Model dispersive media in finite-difference time-domain method with complex-conjugate pole-residue pairs," *IEEE Microwave and Wireless Components Letters*, vol. 16, pp. 119–121, Mar. 2006.

[65] T. V. Yioultsis, G. D. Ziogos, and E. E. Kriezis, "Explicit finite-difference vector beam propagation method based on the iterated crank-nicolson scheme," *J. Opt. Soc. Am. A*, vol. 26, pp. 2183–2191, Oct. 2009.

[66] P. C. Lee and E. Voges, "Three-dimensional semi-vectorial wide-angle beam propagation method," *Journal of Lightwave Technology*, vol. 12, pp. 215–225, Feb. 1994.

[67] K. Q. Le, "Complex padé approximant operators for wide-angle beam propagation," *Optics Communications*, vol. 282, no. 7, pp. 1252 – 1254, 2009.

[68] K. Q. Le, R. Godoy-Rubio, P. Bienstman, and G. R. Hadley, "The complex jacobi iterative method for three-dimensional wide-angle beam propagation," *Opt. Express*, vol. 16, pp. 17021–17030, Oct. 2008.

[69] R. Vahldieck and P. Leuchtmann, *Fields and Components II*. ETH, Eidgenössische Technische Hochschule Zürich, Institut für Feldtheorie und Höchstfrequenztechnik, 2002.

[70] E. Lezar, "GPU acceleration of matrix-based methods in computational electromagnetics," Master's thesis, Department of Electrical and Electronic Engineering, Stellenbosch University, 2011.

[71] R. C. Kirby, A. Logg, M. E. Rognes, and A. R. Terrel, *Common and unusual finite elements*, pp. 95–119. Berlin, Heidelberg: Springer Berlin Heidelberg, 2012.

[72] J. F. Lee, D. K. Sun, and Z. J. Cendes, "Full-wave analysis of dielectric waveguides using tangential vector finite elements," *IEEE Transactions on Microwave Theory and Techniques*, vol. 39, pp. 1262–1271, Aug. 1991.

[73] V. Hernandez, J. E. Roman, and V. Vidal, "SLEPc: A scalable and flexible toolkit for the solution of eigenvalue problems," *ACM Trans. Math. Software*, vol. 31, no. 3, pp. 351–362, 2005.

[74] C. Holly, "Numerical analysis of external resonators for high power diode lasers," Master's thesis, Chair for Laser Technology, RWTH Aachen University, Aachen, 2012.

[75] W. S. Slaughter, *The Linearized Theory of Elasticity*. Birkhäuser, Basel, 2002.

[76] J. R. Barber, *Elasticity*. Springer, Netherlands, 2010.

[77] H. P. Langtangen and A. Logg, *Solving PDEs in Python*. Springer, 2017.

[78] A. F. Bower, *Applied Mechanics of Solids*. CRC Press, Inc. , Boca Raton, FL., 2010.

[79] S. Adachi and K. Oe, "Internal strain and photoelastic effects in $Ga_{1-x}Al_xAs$/GaAs and $In_{1-x}Ga_xAsyP_{1-y}$/InP crystals," *Journal of Applied Physics*, vol. 54, no. 11, pp. 6620–6627, 1983.

[80] S. Adachi, "GaAs, AlAs, and $Al_xGa_{1-x}As$: Material parameters for use in research and device applications," *Journal of Applied Physics*, vol. 58, no. 3, pp. R1–R29, 1985.

[81] S. Adachi, "Material parameters of $In_{1-x}Ga_xAs_yP_{1-y}$ and related binaries," *Journal of Applied Physics*, vol. 53, no. 12, pp. 8775–8792, 1982.

[82] S. Adachi, "Refractive indices of III–V compounds: Key properties of InGaAsP relevant to device design," *Journal of Applied Physics*, vol. 53, no. 8, pp. 5863–5869, 1982.

[83] M. M. Mehrabadi and S. C. Cowin, "Eigentensors of Linear Anisotropic Elastic Materials," *The Quarterly Journal of Mechanics and Applied Mathematics*, vol. 43, pp. 15–41, Feb. 1990.

[84] D. Cassidy, C. Hall, O. Rehioui, and L. Bechou, "Strain estimation in III-V materials by analysis of the degree of polarization of luminescence," *Microelectronics Reliability, Elsevier*, vol. 50 (4), pp. 462–466, 2010.

[85] M. R. Ardigo, M. Ahmed, and A. Besnard, "Stoney formula: Investigation of curvature measurements by optical profilometer," in *Residual Stresses IX*, vol. 996 of *Advanced Materials Research*, pp. 361–366, Trans Tech Publications, Oct. 2014.

[86] S. Heinemann, S. D. McDougall, G. Ryu, L. Zhao, X. Liu, C. Holly, C.-L. Jiang, P. Modak, Y. Xiong, T. Vethake, S. G. Strohmaier, B. Schmidt, and H. Zimer, "Advanced chip designs and novel cooling techniques for brightness scaling of industrial, high power diode laser bars," in *High-Power Diode Laser Technology XVI, Proc. SPIE*, vol. 10514, pp. 10514 – 10514 – 9, 2018.

[87] P. D. Colbourne and D. T. Cassidy, "Imaging of stresses in GaAs diode lasers using polarization-resolved photoluminescence," *IEEE Journal of Quantum Electronics*, vol. 29, pp. 62–68, Jan. 1993.

[88] J. W. Tomm and J. Jiménez, eds., *Failure prediction of high-power laser bars*, p. 246. McGraw-Hill, New York, 2007.

[89] S. Selberherr, *Analysis and Simulation of Semiconductor Devices*. Springer, Vienna, 1984.

[90] W. V. Roosbroeck, "Theory of the flow of electrons and holes in germanium and other semiconductors," *The Bell System Technical Journal*, vol. 29, pp. 560–607, Oct. 1950.

[91] S. M. Sze, *Physics of Semiconductor Devices*. Wiley-Interscience, New York, 2nd ed., 1981.

[92] P. Farrell, N. Rotundo, D. H. Doan, M. Kantner, J. Fuhrmann, and T. Koprucki, "Numerical methods for drift-diffusion models," *WIAS Report, ISSN 2198-5855*, 2016.

[93] G. H. Song, K. Hess, T. Kerkhoven, and U. Ravaioli, "Two-dimensional simulation of quantum well lasers," *European Transactions on Telecommunications*, vol. 1, no. 4, pp. 375–381, 1990.

[94] Z.-M. Li, K. M. Dzurko, A. Delage, and S. P. McAlister, "A self-consistent two-dimensional model of quantum-well semiconductor lasers: optimization of a grin-sch sqw laser structure," *IEEE Journal of Quantum Electronics*, vol. 28, pp. 792–803, Apr. 1992.

[95] G. . Tan, N. Bewtra, K. Lee, and J. M. Xu, "A two-dimensional nonisothermal finite element simulation of laser diodes," *IEEE Journal of Quantum Electronics*, vol. 29, pp. 822–835, Mar. 1993.

[96] T. Ohtoshi, K. Yamaguchi, C. Nagaoka, T. Uda, Y. Murayama, and N. Chinone, "A two-dimensional device simulator of semiconductor lasers," *Solid State Electronics*, vol. 30, pp. 627–638, June 1987.

[97] H. K. Gummel, "A self-consistent iterative scheme for one-dimensional steady state transistor calculations," *IEEE Transactions on Electron Devices*, vol. 11, pp. 455–465, Oct. 1964.

[98] K. Yang, J. R. East, and G. I. Haddad, "Numerical modeling of abrupt heterojunctions using a thermionic-field emission boundary condition," *Solid-State Electronics*, vol. 36, no. 3, pp. 321 – 330, 1993.

[99] D. L. Scharfetter and H. Gummel, "Large-signal analysis of a silicon-read diode oscillator," *Electron Devices, IEEE Transactions on*, vol. 16, pp. 64 – 77, Feb. 1969.

[100] D. Kim and E.-J. Park, "Primal mixed finite-element approximation of elliptic equations with gradient nonlinearities," *Computers & Mathematics with Applications*, vol. 51, no. 5, pp. 793 – 804, 2006. Selected Papers Presented at the Com2Mac Conference on Computational Mathematics.

[101] M. S. Alnæs, J. Blechta, J. Hake, A. Johansson, B. Kehlet, A. Logg, C. Richardson, J. Ring, M. E. Rognes, and G. N. Wells, "The fenics project version 1.5," *Archive of Numerical Software*, vol. 3, no. 100, 2015.

[102] M. Grupen and K. Hess, "Simulation of carrier transport and nonlinearities in quantum-well laser diodes," *IEEE Journal of Quantum Electronics*, vol. 34, pp. 120–140, Jan. 1998.

[103] B. Romero, J. Arias, I. Esquivias, and M. Cada, "Simple model for calculating the ratio of the carrier capture and escape times in quantum-well lasers," *Applied Physics Letters*, vol. 76, no. 12, pp. 1504–1506, 2000.

[104] B. Witzigmann, A. Witzig, and W. Fichtner, "A multidimensional laser simulator for edge-emitters including quantum carrier capture," *IEEE Transactions on Electron Devices*, vol. 47, pp. 1926–1934, Oct. 2000.

[105] H. Haug and S. W. Koch, *Quantum Theory of the Optical and Electronic Properties of Semiconductors*. World Scientific, 5th ed., 2009.

[106] F. Topsøe, "Some bounds for the logarithmic function," *Research report collection*, vol. 7, no. 2, 2004.

[107] S. Tomov, J. Dongarra, and M. Baboulin, "Towards dense linear algebra for hybrid GPU accelerated manycore systems," *Parallel Computing*, vol. 36, pp. 232–240, June 2010.

[108] J. J. Lim, S. Sujecki, L. Lang, Z. Zhang, D. Paboeuf, G. Pauliat, G. Lucas-Leclin, P. Georges, R. C. I. MacKenzie, P. Bream, S. Bull, K. H. Hasler, B. Sumpf, H. Wenzel, G. Erbert, B. Thestrup, P. M. Petersen, N. Michel, M. Krakowski, and E. C. Larkins, "Design and Simulation of Next-Generation High-Power, High-Brightness Laser Diodes," *IEEE Journal of Selected Topics in Quantum Electronics*, vol. 15, pp. 993–1008, May 2009.

[109] J. R. Marciante and G. P. Agrawal, "Nonlinear mechanisms of filamentation in broad-area semiconductor lasers," *IEEE Journal of Quantum Electronics*, vol. 32, pp. 590–596, Apr. 1996.

[110] J. Wykes, L. Borruel, S. Sujecki, I. Esquivias, P. Sewell, T. M. Benson, E. C. Larkins, P. Moreno, and M. Krakowski, "Hot-cavity modelling of high-power tapered laser diodes using wide-angle 3d fd-bpm," *Lasers and Electro- Optics Society, LEOS, The 15th Annual Meeting of the IEEE*, 2002.

[111] S. Sujecki, L. Borruel, J. Wykes, P. Moreno, B. Sumpf, P. Sewell, H. Wenzel, T. M. Benson, G. Erbert, I. Esquivias, and E. C. Larkins, "Nonlinear properties of tapered laser cavities," *IEEE Journal of Selected Topics in Quantum Electronics*, vol. 9, pp. 823–834, May 2003.

[112] W. T. Tsang, "The effects of lateral current spreading, carrier out-diffusion, and optical mode losses on the threshold current density of GaAs-$Al_xGa_{1-x}As$ stripe-geometry DH lasers," *Journal of Applied Physics*, vol. 49, no. 3, pp. 1031–1044, 1978.

[113] W. B. Joyce, "Current-crowded carrier confinement in double-heterostructure lasers," *Journal of Applied Physics*, vol. 51, no. 5, pp. 2394–2401, 1980.

[114] X. Du, W. Guo, B. Cui, W. Li, and X. Xu, "Lateral current spreading in stripe laser diodes," *2010 OSA-IEEE-COS Advances in Optoelectronics and Micro/Nano-Optics, AOM 2010*, Dec. 2010.

[115] S. Gehrsitz, F. K. Reinhart, C. Gourgon, N. Herres, A. Vonlanthen, and H. Sigg, "The refractive index of $Al_xGa_{1-x}As$ below the band gap: Accurate determination and empirical modeling," *Journal of Applied Physics*, vol. 87, no. 11, pp. 7825–7837, 2000.

[116] J. Talghader and J. S. Smith, "Thermal dependence of the refractive index of gaas and alas measured using semiconductor multilayer optical cavities," *Applied Physics Letters*, vol. 66, no. 3, pp. 335–337, 1995.

[117] J. Piprek, "Inverse thermal lens effects on the far-field blooming of broad area laser diodes," *IEEE Photonics Technology Letters*, vol. 25, pp. 958–960, May 2013.

[118] T. Paoli, "Waveguiding in a stripe-geometry junction laser," *IEEE Journal of Quantum Electronics*, vol. 13, pp. 662–668, Aug. 1977.

[119] M. Hempel, J. W. Tomm, M. Bäumler, H. Konstanzer, J. Mukherjee, and T. Elsässer, "Near-field evolution in strongly pumped broad area diode lasers," in *Novel In-Plane Semiconductor Lasers XI, Proc. SPIE*, vol. 8277, 2012.

[120] H. Adachihara, O. Hess, E. Abraham, P. Ru, and J. V. Moloney, "Spatiotemporal chaos in broad-area semiconductor lasers," *J. Opt. Soc. Am. B*, vol. 10, pp. 658–665, Apr. 1993.

[121] I. Fischer, O. Hess, W. Elsäßer, and E. Göbel, "Complex spatio-temporal dynamics in the near-field of a broad-area semiconductor laser," *EPL (Europhysics Letters)*, vol. 35, no. 8, p. 579, 1996.

[122] S. K. Mandre, I. Fischer, and W. Elsäßer, "Control of the spatiotemporal emission of a broad-area semiconductor laser by spatially filtered feedback," *Opt. Lett.*, vol. 28, pp. 1135–1137, July 2003.

[123] C. Holly, "pymagma." `https://github.com/carloholly/pymagma`, accessed Oct. 2017.

[124] Y. Varshni, "Temperature dependence of the energy gap in semiconductors," *Physica*, vol. 34, no. 1, pp. 149 – 154, 1967.

[125] V. Palankovski, *Simulation of Heterojunction - Bipolar Transistors*. PhD thesis, Fakultät für Elektrotechnik und Informationstechnik, Technischen Universität Wien, 2000.

[126] I. Vurgaftman, J. R. Meyer, and L. R. Ram-Mohan, "Band parameters for III-V compound semiconductors and their alloys," *Journal of Applied Physics*, vol. 89, no. 11, pp. 5815–5875, 2001.

[127] Ioffe Physico-Technical Institute, "Electronic archive, New Semiconductor Materials. Characteristics and Properties." `http://www.ioffe.ru/SVA/NSM/Semicond/index.html`, accessed Nov. 2017.

[128] M. Sotoodeh, A. H. Khalid, and A. A. Rezazadeh, "Empirical low-field mobility model for III–V compounds applicable in device simulation codes," *Journal of Applied Physics*, vol. 87, no. 6, pp. 2890–2900, 2000.

[129] M. L. Lovejoy, M. R. Melloch, and M. S. Lundstrom, "Temperature dependence of minority and majority carrier mobilities in degenerately doped GaAs," *Applied Physics Letters*, vol. 67, no. 8, pp. 1101–1103, 1995.

[130] M. Daubenschuez, P. Gerlach, and R. Michalzik, "Electro-thermal characteristics of VCSELs: simulations and experiments," in *Semiconductor Lasers and Laser Dynamics VI, Proc. SPIE*, vol. 9134, pp. 9134 – 9134 – 8, 2014.

[131] M. Shur, *Physics of Semiconductor Devices*. Upper Saddle River, NJ: Prentice-Hall, Inc., 1990.

[132] M. R. Brozel and G. E. Stillman, eds., *Properties of Gallium Arsenide*. London: Institution of Engineering and Technology, 3rd ed., 1996.

[133] M. Wenzel, G. Irmer, J. Monecke, and W. Siegel, "Determination of the effective hall factor in p-type semiconductors," *Semiconductor Science and Technology*, vol. 13, no. 5, p. 505, 1998.

[134] A. K. Saxena, "Electron mobility in $Ga_{1-x}Al_xAs$ alloys," *Phys. Rev. B*, vol. 24, pp. 3295–3302, Sept. 1981.

[135] W. von Sellmeier, "Zur Erklärung der abnormen Farbenfolge im Spectrum einiger Substanzen," *Annalen der Physik*, vol. 219, no. 6, pp. 272–282, 1871.

[136] BATOP GmbH, "Refractive index." `https://www.batop.de/information.html`, accessed Nov. 2017.

[137] S. K. Ghandhi, *VLSI Fabrication Principles: Silicon and Gallium Arsenide*. John Wiley & Sons, Inc., New York, 2nd ed., 1994.

[138] M. Levinshtein, S. Rumyantsev, and M. Shur, *Handbook Series on Semiconductor Parameters*. World Scientific, 1996.

[139] H. Okumura, S. Misawa, S. Yoshida, and S. Gonda, "Determination of the conduction-band discontinuities of $GaAs/Al_xGa_{1-x}As$ interfaces by capacitance-voltage measurements," *Applied Physics Letters*, vol. 46, pp. 377–379, Feb. 1985.

[140] E. Yu, J. McCaldin, and T. McGill, "Band offsets in semiconductor heterojunctions," *Solid State Physics: Advances in Research and Applications*, vol. 46, pp. 1–146, Jan. 1992.

[141] A. Luedtke, "Thermal management materials for high-performance applications," *Advanced Engineering Materials*, vol. 6, no. 3, pp. 142–144, 2004.

[142] Torrey Hills Technologies, LLC, "Tungsten-copper heat sinks." `https://www.torreyhillstech.com/hswcu.html`, accessed Nov. 2017.

[143] Sumitomo Electric Hartmetall GmbH, "Copper-tungsten." `http://www.sumitomoelectricusa.com/products/heatsinks/copper-tungsten`, accessed Nov. 2017.

[144] T. M. Alander, P. A. Heino, and E. O. Ristolainen, "Analysis of laser bar bonding reliability on different substrates," *International Journal of Microcircuits and Electronic Packaging*, vol. 24, no. 2, pp. 160 – 172, 2001.

[145] N. Yuxi, M. Xiaoyu, J. Hongqi, and L. Suping, "Finite element analysis of expansion-matched submounts for high-power laser diodes packaging," *Journal of Semiconductors*, vol. 37, no. 6, p. 064005, 2016.

[146] Engineering ToolBox (2005), "Thermal conductivity of metals, metallic elements and alloys." `https://www.engineeringtoolbox.com/thermal-conductivity-metals-d_858.html`, accessed Nov. 2017.

[147] Engineering ToolBox (2013), "Coefficients of linear thermal expansion." `https://www.engineeringtoolbox.com/linear-expansion-coefficients-d_95.html`, accessed Nov. 2017.

[148] K. Adokanou, K. Inal, P. Montmitonnet, F. Courtade, and B. Bonnet, "Thermomechanical analysis of gaas devices under temperature-humidity-bias testing," in *2015 16th International Conference on Thermal, Mechanical and Multi-Physics Simulation and Experiments in Microelectronics and Microsystems*, pp. 1–8, Apr. 2015.

[149] P. F. Kelly, *Properties of Materials*. CRC Press, Boca Raton, FL, 1st ed., 2014.

[150] Accuratus, "Aluminum nitride, AIN ceramic properties." `http://accuratus.com/alumni.html`, accessed Nov. 2017.

[151] C. Scholz, *Thermal and Mechanical Optimisation of Diode Laser Bar Packaging*. PhD thesis, Faculty of Mechanical Engineering, RWTH Aachen University, Aachen, 2007.

[152] Y. Lu, Z. Nie, P. Zhang, Z. Wang, L. Xiong, S. Wang, D. Wu, and X. Liu, "Numerical simulation of thermo-mechanical behavior in high power diode laser arrays," in *2016 17th International Conference on Electronic Packaging Technology (ICEPT)*, pp. 76–83, Aug. 2016.

[153] E. Jones, T. Oliphant, P. Peterson, *et al.*, "SciPy: Open source scientific tools for Python," 2001. Online, accessed 2017.

[154] J. Nickolls, I. Buck, M. Garland, and K. Skadron, "Scalable parallel programming with cuda," *Queue*, vol. 6, pp. 40–53, Mar. 2008.

[155] M. G. Burt, "Fundamentals of envelope function theory for electronic states and photonic modes in nanostructures," *J. Phys.: Condens. Matter*, vol. 11, no. R53, 1999.

[156] E. Collett, *Field Guide to Polarization*, vol. FG05. Bellingham, WA: SPIE Press, 2005.

[157] K. Petermann, *Laser Diode Modulation and Noise*. Springer Netherlands, 1988.